

ABSTRACT

The process of urbanisation has a major influence in determining the microclimate condition in urban areas through physical and social developments. With the estimation of 67 % world population will be living in the urban areas in 2050, modification of urban climate through urban heating will continually occur by adapting artificial urban surfaces to accommodate the demands from urban dwellers. This thesis highlighted the mitigation strategy by applying solar collector system embedded underneath road pavements, RPSC due to the concern of heat release from the ground road surfaces to the nearby air temperature, which indirectly affects the outdoor thermal comfort and elevates the urban heat island (UHI) effect. The performance of hydronic RPSC system was determined by factoring the influence of building configurations, termed as urban canyon. 3D CFD simulation studies of Standard $k - \varepsilon$ RANS model coupled with Solar Load and DO radiation model were carried out to simulate the integration of hydronic RPSC with urban canyons. Validations of the simulation results were done against previous published works and the thesis' thermal data collections within Kuala Lumpur conurbation centre. Based on the simulation and data collection, it was found that building configurations with symmetrical canyon height had clearly increased the performance of RPSC system in surface temperature reduction and potential temperature collection as compared to other comparative settings. There was an increasing trend by changing the aspect ratio (AR) 1 to AR 2 with a slightly drop in the performance to AR 3 and AR 4 due to shadow effects. Findings from the data collection however, disagreed the trend due to a major factor from the solar intensity of the measured days affecting the temperature values. Furthermore, application of RPSC system in deep street canyons showed the potential of the system to reduce up to 4 °C air temperature at the pedestrian level; however, it was still insufficient to achieve an outdoor comfort temperature level.

PREFACE

The following outputs were produced as a result of this research:

JOURNAL PUBLICATION:

Nasir, D. S. N. M., Hughes, B. R., Calautit, J. K., Aquino, A. I. and Shahzad, S. (2017) ‘Effect of Urban Street Canyon Aspect Ratio on Thermal Performance of Road Pavement Solar Collectors (RPSC)’, *Energy Procedia*. The Author(s), 105, pp. 4414–4419. doi: 10.1016/j.egypro.2017.03.936.

Nasir, D. S. N. M., Hughes, B. R. and Calautit, J. K. (2017) ‘Influence of urban form on the performance of road pavement solar collector system: Symmetrical and asymmetrical heights’, *Energy Conversion and Management*. doi: 10.1016/j.enconman.2017.03.081.

Nasir, D. S. N. M., Hughes, B. R. and Calautit, J. K. (2015) ‘A CFD analysis of several design parameters of a road pavement solar collector (RPSC) for urban application’, *Applied Energy*. Elsevier Ltd, 186, pp. 436–449. doi: 10.1016/j.apenergy.2016.04.002.

Nasir, D. S. N. M., Hughes, B. R. and Calautit, J. K. (2015) ‘A study of the impact of building geometry on the thermal performance of road pavement solar collectors’, *Energy*. Elsevier Ltd, 93, pp. 2614–2630. doi: 10.1016/j.energy.2015.09.128.

CONFERENCE PROCEEDINGS:

Nasir, D. S. N. M., Hughes, B. R., Calautit J. K., and Aquino, A., 2016. Effect of urban street canyon aspect ratio on thermal performance of road pavement solar collectors (RPSC) In: *The 8th International Conference on Applied Energy (ICAE)*.

Nasir, D. S. N. M., Ben Richard Hughes and John Kaiser Calautit, 2016. Analysis of the Impact of Urban Configuration on Road Solar Collector In: *11th Sustainable Development of Energy, Water And Environment Systems (SDEWES)*.

Nasir, D. S. N. M., Hughes, B.R. and Calautit, J.K., 2015. The Impact of Urban Canyon on the Thermal Performance of Solar Roads, In: 3rd Sustainable Thermal Energy Management Conference (SusTEM 2011), Newcastle Upon Tyne, United Kingdom

Nasir, D. S. N. M., Hughes, B. R. and Calautit, J. K., 2015. CFD Simulation of Integration Solar Roads in Urban Canyon. In: USES 2015 – The University of Sheffield Engineering Symposium, The Octagon Centre, University of Sheffield.

Nasir, D. S. N. M., Hughes, B. R. and Calautit, J.K. 2014. The Influence of Urban Geometry Aspect Ratio on Heating the Pavement Middle Layers: Potential in Passive Energy Collection. In: RSA Early Career Conference, Regional Studies Association (RSA), Sheffield, United Kingdom.

Nasir, D. S. N. M., Hughes, B. R. and Calautit J.K., 2014. Investigating the Influence of the Urban Canyon Geometry Aspect Ratio on the Temperature of Pavement Middle Layers. In: PGR Student's Conference 2014 – University of Leeds, School of Civil Engineering, Leeds, United Kingdom.

TABLE OF CONTENTS

ABSTRACT	i
PREFACE	iii
TABLE OF CONTENTS.....	v
LIST OF FIGURES	x
LIST OF TABLES	xxi
NOMENCLATURE	xxiii
ACKNOWLEDGEMENT	xxv
CHAPTER 1	1
Introduction	1
1.1 Description on Urban Heat Island (UHI) effect	3
1.1.1 Correlation between building configuration and urban heating.....	6
1.1.2 Influence of urban street canyon on UHI effect.....	8
1.2 Correlation between urban surfaces and UHI effect	9
1.2.1 Surface based UHI mitigation techniques.....	10
1.2.2 Application of Road Pavement Solar Collector (RPSC) system	13
1.3 Problem statement	15
1.4 Aim	16
1.5 Research methodology	17
1.6 Structure of the thesis	18
CHAPTER 2	21
Literature review	21
2.0 Introduction	21
2.1 Quantifying global UHI effect and its consequences	22
2.2 Effects of built form on UHI effect	25
2.2.1 Configuration of urban canyons.....	27
2.2.1 Case studies of generic urban canyon	32
2.2.2 Case studies of multiscale and non-generic urban canyon.....	42
2.3 Research and development of RPSC system for UHI mitigation	49
2.3.1 Effect of high surface temperature on outdoor environment	50

2.3.2	Effect of flowing pipes on pavement surface and surroundings	53
2.3.3	Effect of system adjustment on extreme weather condition	55
2.3.4	Case studies of using hydronic pipes for thermal energy collection.....	60
2.4	Summary	63
2.5	Research gap.....	64
CHAPTER 3	65
	Theoretical background.....	65
3.0	Introduction	65
3.1	Theoretical effects of urban landscapes on urban atmosphere.....	66
3.1.1	Urban surfaces receive low solar radiation due to shadow	66
3.1.2	Heat reflection from sunny walls	68
3.1.3	Reduction in cooling due to buildings act as obstacle to airflow.....	72
3.2	Mechanism of heat transfer within urban area	75
3.2.1	Radiation heat transfer	76
3.2.2	Conduction heat transfer	77
3.2.3	Convection heat transfer	78
3.3.2	Heat transfer between pavement surface and air layer	79
3.3.3	Heat transfer between pavement and RPSC system	84
3.3	Summary	86
CHAPTER 4	87
	Computational method.....	87
4.0	Introduction	87
4.1	Introduction to the computational method	88
4.1.1	Solver setting: CFD based on Finite-Volume Method (FVM)	90
4.1.2	CFD governing equation.....	91
4.2	Computational geometry and domain	95
4.2.1	Description of macro domain of the study.....	97
4.2.2	Description of micro domain of the study	101
4.3	Mesh: type and setting.....	104
4.3.1	Macro domain - unstructured mesh	105
4.3.2	Macro domain - structured mesh	108
4.3.3	Micro domain.....	115

4.4	Boundary conditions.....	117
4.4.1	Macro domain	117
4.4.2	Micro domain	118
4.5	Solution convergence	120
4.6	Post-computer solution: performance calculation	121
4.7	Method validation.....	122
4.7.1	Validation for macro domain	122
4.7.2	Micro domain method	126
4.8	Summary	129
CHAPTER 5	131
	Experimental methods.....	131
5.0	Introduction	131
5.1	Rationale for experimental case studies	132
5.2	Background of study: Kuala Lumpur conurbation centre	133
5.2.1	Weather condition of Kuala Lumpur conurbation centre	135
5.2.2	Description of street canyon.....	136
5.3	Temperature measurement using infrared thermal camera	142
5.3.1	Experimental setup: mobile measuring technique	143
5.3.2	Equipment calibration based on distance	147
5.4	Data collection: input, observation and analysis	152
5.4.1	Observation of surface temperatures based on time and date	153
5.4.2	Influence of street canyon aspect ratio on surface temperatures.....	161
5.4.3	Influence of canyon configuration on road temperature	170
5.4.4	Modelling investigation and validation against data collection	176
5.5	Summary	183
CHAPTER 6	185
	Results and discussion	185
6.0	Introduction	185
6.1	CFD analysis of RPSC performance based on urban configuration	186
6.1.1	Effect of urban canyon on RPSC performance	189
6.1.2	Effect of canyon aspect ratio on RPSC performance.....	193
6.1.3	Effect of urban topologies on RPSC performance.....	202
6.2	CFD analysis of RPSC performance with system adjustment	210

6.2.1	Minimising/maximising surface area on RPSC performance.....	211
6.2.2	Minimising/maximising mass flow rate on RPSC performance.....	214
6.2.3	Combined effect of surface area and flow rate on RPSC system	217
6.3	Effect of RPSC application on outdoor temperature condition.....	226
6.3.1	Calculation of Heat Index (HI) using air temperature	230
6.3.2	Effect on energy load based on urban air temperature.....	231
6.4	Comparative analysis on experimental and simulation results	232
6.4.1	Similarities in the simulation data set and experimental data set	233
6.4.2	Differences in the simulation data set and experimental data set	234
6.4.3	Temperature results based on aspect ratio	235
6.4.4	Temperature results based on street canyon configuration	236
6.4.5	Temperature results based on wind-blocking canyon condition.....	239
6.4.6	Analysis based on the potential UHI occurrence and mitigation.....	240
6.5	Summary	242
CHAPTER 7	243
	Conclusion and future work.....	243
	Limitation of study.....	250
	Future work	251
LIST OF REFERENCES	253
APPENDICES	267
	Appendix A.1	267
	Appendix A.2	270
	Appendix A.3	273
	Appendix A.4	274
	Appendix A.5	275
	Appendix A.6	281
	Appendix A.7	282
	Appendix A.8	283
	Appendix A.9	284
	Appendix A.10	285
	Appendix A.11	290
	Appendix A.12	291
	Appendix A.13	292

Appendix A.14	294
Appendix A.15	296
Appendix A.16	298
Appendix A.17	300
Appendix A.18	302
Appendix A.19	304
Appendix A.20	305

LIST OF FIGURES

Figure 1.1 Urban land cover of three urban areas in Malaysia; Dengkil, Kajang and Cheras that evolved from 1998 to 1999 using Landsat TM (Ahmad & Hashim 2007)....	2
Figure 1.2 Significant different between diurnal surface temperature rise in urban conurbation centre and diurnal air temperature. 1 st March 2017. Retrieved from https://www.epa.gov/heat-islands	4
Figure 1.3 Statistic of the research and development involving the study of urban street canyon and its impact on urban microclimates based on downloaded journal publication before 2000, 2000-2013 and after 2014	9
Figure 1.4 Statistic of the research and development involving the study of pavement cooling based on downloaded journal publication before 2000, 2000-2013 and after 2014	14
Figure 1.5 Flow chart of the outline of the thesis' research methodology.....	17
Figure 2.1 Example from New Orleans on the plotted electrical loads which increased steadily when the temperature exceeded 68-77 F (20-25 °C) (Smith & Levermore 2008)	23
Figure 2.2 Illustration of heat transmittance and emittance (Akbari 2005; Levermore & Cheung 2012) towards (a) flat surface (b) within urban canyon	27
Figure 2.3 Illustration of 3D urban street canyon (Lemonsu & Masson 2002) with additional representation of canyon-air volume (Landsberg 1981; Arnfield & Grimmond 1998)	28
Figure 2.4 Illustration of urban topology to be determined by building height following (Vardoulakis et al. 2003) in (a) Symmetrical (b) asymmetrical	29
Figure 2.5 Illustration of urban canyon configuration to be influenced by length following (Vardoulakis et al. 2003) (a) short, (b) medium, (c) long	30
Figure 2.6 Illustration of canyon aspect ratio according to height, H against width, W (Ali-Toudert & Mayer 2006) (a) $H/W = 0.5$, (b) $H/W = 1.0$, (c) $H/W = 2.0$, (d) $H/W = 4.0$; also (e) street canyon orientation	30
Figure 2.7 Illustration of simplified multiple types of urban canyon following (Panão et al. 2006) (a) Square blocks, $L = W$ (b) Rectangular blocks, $L = 3W$, (c) Street, $L = 15W$	31

Figure 2.8 Illustration following (Hiung & Ahmad 2006) illustrating deep street canyon of Damansara urban district (b) shallow street canyon of Melawati district	32
Figure 2.9 Velocity profile plotted from ground to rooftop level showed (a) lower velocity at the lower level, thus creating warmer air temperature (Rotach 1995) (b) validation of numerical results to the measurement results (Rotach 1999)	33
Figure 2.10 Comparative variables used to investigate thermal effect in urban canyon showing high evaporative cooling due to the high moisture on air temperature and mean radiant temperature (Saneinejad et al. 2014).....	34
Figure 2.11 Perpendicular airflow across street canyon demonstrating (a) air skimming flow and 1 helical vortex for narrow canyon (Ahmad et al. 2005) (b) normalised air velocity and circulation in street canyon by (Eliasson et al. 2006).....	34
Figure 2.12 Modelling of predominant airflow cross building length from neutral to unstable Richardson bulk number comparing parallel, perpendicular and oblique flow showed highest velocity with parallel orientation (Niachou et al. 2008).....	35
Figure 2.13 Profile of mean streamwise velocity normalised by friction velocity comparing locations: a – above cube, b – behind cube, c – in front of cube and d – in between cubes (Abd Razak et al. 2013).....	36
Figure 2.14 Spatial contours of normalised temperature within urban canyon comparing four aspect ratios demonstrating higher temperature was associated with higher aspect ratio with less windy condition – 0.5 m/s (Memon et al. 2010).....	37
Figure 2.15 Results from the comparison suggested that positive natural convection due to the buoyancy effect from the ground surface temperature increased the velocity magnitude and low surface temperature (Bottillo et al. 2014).....	38
Figure 2.16 CHTC comparison between several urban configurations with and without natural convection settings (Allegrini et al. 2012).....	39
Figure 2.17 Contours inside urban canyon during even surface heating, showing higher temperature at leeward side as compared to windward side. Note that 1 - air temperature, 2 - air velocity (Memon & Leung 2011).....	40
Figure 2.18 Ground temperature comparing aspect ratio and materials (Nazarian & Kleissl 2015)	41
Figure 2.19 Selection of aspect ratio within the old Saharan city involved wide, narrow and enclosed types with symmetrical canyon height and asymmetrical canyon height (Ali-toudert et al. 2005)	42

Figure 2.20 Location of wind speed and direction and the correlation between turbulent kinetic energy (TKE) at canyon surfaces (facades and ground) wind condition (Ziehn & Tomlin 2008; Benson et al. 2008).....	44
Figure 2.21 Impact of wind speed and albedo of façade materials on air temperature (Priyadarsini et al. 2008).....	45
Figure 2.22 Thermal analysis of urban canyons; 1 – wide canyon, 2 – narrow canyon, demonstrating the validation of air-ground temperatures based on CFD prediction against data measurement (Ito et al. 2005).....	46
Figure 2.23 Low wind speed reduced the cooling effect from ground surfaces. This condition was found within the street canyon that was perpendicular to the predominant wind direction (Toparlar et al. 2015)	47
Figure 2.24 Reduction in surface IR radiation with the application of cooling materials and artificial shading devices (Stavarakakis et al. 2012).....	48
Figure 2.25 Example of hydronic pavement solar collector proposed by (a) (Wang et al. 2010; Shaopeng et al. 2011) (b) (Wang et al. 2010; Shaopeng et al. 2011)	49
Figure 2.26 Comparison of mean surface temperature between several tested pavement surfaces showed asphalt pavement scored highest (Tan & Fwa 1992).....	50
Figure 2.27 Comparative analysis between asphalt, concrete and granulite pavements have shown asphalt pavement obtained high mean surface temperature during early noon hours (Chudnovsky et al. 2004)	51
Figure 2.28 Investigation on surface temperature comparing several pavement types during summertime and winter time, with (a) shows method and site view and (b) shows the effects on air temperature and heat output (Lin et al. 2007)	52
Figure 2.29 Correlation between surface temperature and air temperature of tested pavements between two cities showed the temperature difference varies according to time with positive difference during daytimes (Qin & Hiller 2011).....	53
Figure 2.30 RTEC investigation for pavement excessive temperature mitigation; (a) shows distributed pavement temperature with RTEC and (b) shows temperature reduction with RTEC (Hasebe, M, Yamikawa, Y and Meiarashi 2006)	53
Figure 2.31 Estimated yearly thermal gain based on temperature gain showed the optimum values were during summer months (Loomans et al. 2003).....	54
Figure 2.32 Correlation between surface temperature before-after the flowing water and air temperature showed the influence of low surface temperature to reduce air temperature above 0.1 m from the surface (Mallick et al. 2009)	55

Figure 2.33 RPSC system used to fight against extreme weather during winter time. Figure (a) shows the embedment of serpentine pipe. Figure (b) shows the snow-melting time according to the embedment of pipes (Chen et al. 2011).....	56
Figure 2.34 Correlation between the set gap between pipes, water flow rate and surface temperature (a) shows highest RPSC efficiency with smallest pipe gap, and (b) shows consistency in high heat collecting capacity with 90 mm (Gao et al. 2010).....	57
Figure 2.35 Significant effect was found in the reduction of pavement temperature when (a) comparing with and without pipe layout and vice-versa when (b) comparing two large difference flow rates (Shaopeng et al. 2011)	57
Figure 2.36 The effect of change in the inlet temperature from high to low according to transient test (a) Delta T according to time (b) surface temperature according to inlet temperature (Shaopeng et al. 2011)	58
Figure 2.37 Correlation between the beginning of the time for water circulation and the obtained temperature difference, Delta T (a) after 6 hours surface radiation (b) with the beginning time for the 6 hours radiation (Shaopeng et al. 2011).....	59
Figure 2.38 Correlation between material conductivity and the effectiveness of RPSC in terms of (a) the beginning of melting time (b) comparison of Delta T between AC and CAC (Chen et al. 2011).....	60
Figure 2.39 Example of the system prototype combined GHSP, bridge deck and ground soil thermal storage (a) plan view (b) cross section view (Chiasson & Spitler 2001)....	61
Figure 2.40 Comprehensive heating system which utilises solar radiation as the main component of the energy generation (Utlu et al. 2014)	62
Figure 3.1 Illustration depicting the energy flux for ΔQ_s (a) warming condition with vertical flux convergence - Q_{in} exceeds Q_{out} , (b) cooling condition with vertical flux divergence - Q_{in} is less than Q_{out} , and (c) warming condition with horizontal flux divergence - Q_{in} exceeds Q_{out} (Oke 1987a).....	70
Figure 3.2 Illustration of energy balance comparing (a) rural area, and (b) urban area	72
Figure 3.3 Illustration demonstrating (a) streamlines and flow zone (b) wind velocity profiles with a building acts as an obstacle (Oke 1987a).....	73
Figure 3.4 Illustration of airflow patterns of (a) isolated roughness flow with $H/W < 0.4$ for cubic and < 0.3 for rows, (b) wake interference flow with $H/W = 0.7$ for cubic and $= 0.65$ for rows, and (c) skimming flow with $H/W \geq 1$ (Oke 1987a).....	74
Figure 3.5 Illustration following (Cengel & Ghajar 2015) showing (a) velocity variation of air (b) temperature variation of air.....	79

Figure 4.1 Flow chart of de-coupled CFD based on finite-volume method (FVM)	89
Figure 4.2 Representation of control volume in the form of (a) cell-centred (b) tri-dimensional four faces where the central node is in purple. 1 st April 2017. Retrieved from: http://www.iue.tuwien.ac.at/phd/heinzl/node25.html	90
Figure 4.3 A benchmark urban canyon domain configuration (Bottillo et al. 2014)....	95
Figure 4.4 Proposed diagram of de-coupled macro domain and micro domain	96
Figure 4.5 Details of domain size (a) elevation view (b) 3D perspective (c) plan view	97
Figure 4.6 Empty domain consisting fluid flow and flat ground (no buildings).....	98
Figure 4.7 Sectional elevation showing (a) AR 1 (b) AR 2 (c) AR 3 (d) AR 4. Figure (e) shows full dimension of the domain based on the tallest building height, AR 4 among the compared aspect ratios.	99
Figure 4.8 Comparison of (a) Building A is higher than Building B (b) vice-versa...	100
Figure 4.9 Description of 3D RPSC model with 1 pipe (a) size of domain, pipe and pavement body (b) pipe embedment within street canyon of urban domain	101
Figure 4.10 Configuration of RPSC domain with additional pipes (Pipe A - D) embedded beneath the surface layer.....	103
Figure 4.11 Configuration of RPSC domain with additional pipes (Pipe A - D) embedded beneath the surface layer.....	104
Figure 4.12 Mesh images by using Patch Independent Algorithm; showing (a) top view of generated mesh with finer mesh nearby street canyon and buildings (b) closed-up image of hybrid mesh (tetrahedron-hexahedral) within street canyon	105
Figure 4.13 Mesh independence study based on the three location, Point 1, 2 and 3 within street canyon zone.....	107
Figure 4.14 Temperature values plotted at Point 1, 2 and 3 according to Figure 4.13	107
Figure 4.15 Mesh generation using Automatic Meshing Method with sliced volumes	109
Figure 4.16 Mesh verification test based on 21 plotted points comparing (a) air pressure, Pa (b) air velocity magnitude, m/s	112
Figure 4.17 Mesh verification test based on 11 plotted points comparing (a) air pressure, Pa (b) air velocity magnitude, m/s	114

Figure 4.18 Mesh setting for RPSC pipe with Automatic Meshing Method	116
Figure 4.19 Mesh setting for RPSC pipe with Automatic Meshing Method	116
Figure 4.20 Location of pipes beneath ground surface (a) with buildings – urban macro domain (b) flat surface – flat/rural macro domain	118
Figure 4.21 Validation of air velocity at four locations in y-axis (a) 0 m – inlet plane (b) 20 m away from inlet (c) 40 m away from inlet (d) 60 m away from inlet	123
Figure 4.22 Macro domain validation of unstructured mesh, plotting (a) canyon wind velocity profile (b) canyon air temperature profile	123
Figure 4.23 Macro domain validation of structured mesh, plotting (a) dimensionless canyon wind velocity profile (b) dimensionless canyon air temperature profile.....	124
Figure 4.24 Validation of three temperature points at Point 1, 2 and 3 of ground surface	125
Figure 4.25 Method validation following the experimental work of (Shaopeng et al. 2011) (a) current meshing technique (b) plan dimension (c) depth dimension.....	126
Figure 4.26 Selection of surface heat flux based on experimental validation error, %	126
Figure 4.27 Trend comparison between the simulation and experimental results according to the depth from the surface of (a) 883.6 mL/min (b) 1757 mL/min.....	127
Figure 4.28 Validation of micro domain with 4 pipes against experimental results according to the depth from the surface with 1757 mL/min flow rate.....	128
Figure 5.1 Distance between the location of Sultan Aziz Shah Airport, Subang and the location of Raja Chulan road, Kuala Lumpur	135
Figure 5.2 Traffic intensity of ROAD 1 on 5th August 2015 (a) at 9 am (b) at 3 pm	137
Figure 5.3 Roadways configuration (a) ROAD 1 - yellow (b) ROAD 2 – blue. Side (a) means the left side of the canyon meanwhile Side (b) means the right side of the canyon.	138
Figure 5.4 Plan view showing 6 cross-sectional elevations; Section (a)-(f) for the street canyon studies of (a) ROAD 1 (b) ROAD 2	140
Figure 5.5 Product display of (a) one whole package of FLIR T650sc (b) infrared contours and static cursors detected temperatures on three spots	142
Figure 5.6 Mobile measuring technique of thermal imaging process for ROAD 1 and ROAD 2 based on walk and stop at both road lanes.....	144

Figure 5.7 Cycle of thermal imaging process in 30 minutes for every 1-hour interval between 09:00 hour and 16:00 hour for ROAD 1 and ROAD 2.....	144
Figure 5.8 Arrangement of thermal image according to time for ROAD 1 Section (A)	146
Figure 5.9 Process of calibration based on various distance comparing thermocouples Type K and FLIR T650sc	147
Figure 5.10 Calibration setup showing (a) heated sand paper surface with 4 thermocouples Type K stitched on surface (b) final location of where thermal image was captured. Also, thermal image at (c) 1 m distance (d) 5 m (e) 10 m	149
Figure 5.11 Comparative temperature results obtained by thermocouples and FLIR T650sc infrared thermal camera at (a) 3 m, (b) 6 m and (c) 9 m distance (d) average percentage of error, % according to the distance from the heat source	150
Figure 5.12 Average temperature values obtained against distance from the measuring points (a) at 13:30 hour (b) at 14:00 hour	151
Figure 5.13 Additional measurement spots and polylines to obtain the average of (a) façade temperature (b) road surface temperature.....	153
Figure 5.14 Average values calculated from thermal images of ROAD 1 consisting (a) façade temperature combining Side 1 and Side 2 during August 2015 (b) façade temperature combining Side 1 and Side 2 during March 2016. It should be noted that WS was indicated as wind speed in m/s and AT was indicated as ambient temperature in K.	154
Figure 5.15 Average values calculated from thermal images of ROAD 2 consisting (a) façade temperature combining Side 1 and Side 2 during August 2015 (b) façade temperature combining Side 1 and Side 2 during March 2016. It should be noted that WS was indicated as wind speed in m/s and AT was indicated as ambient temperature in K.	155
Figure 5.16 Average values calculated from thermal images of ROAD 1 consisting (a) road surface temperature combining Side 1 and Side 2 during August 2015 (b) road surface temperature combining Side 1 and Side 2 during March 2016. It should be noted that WS was indicated as wind speed in m/s and AT was indicated as ambient temperature in K.	158
Figure 5.17 Average values calculated from thermal images of ROAD 2 consisting (a) road surface temperature combining Side 1 and Side 2 during August 2015 (b) road surface temperature combining Side 1 and Side 2 during March 2016. It should be noted that WS was indicated as wind speed in m/s and AT was indicated as ambient temperature in K.	159

Figure 5.18 Mean ambient temperature and daily wind speed according to date for (a) ROAD 1 and for (b) ROAD 2. It should be noted that the mean wind speed was calculated in m/s unit.....	162
Figure 5.19 Average temperature comparing the street canyon sections of ROAD 1 (a) façade temperature (b) road surface temperature. The comparison included the data collection during August 2015 and during March 2016.	163
Figure 5.20 Average temperature comparing the street canyon sections of ROAD 2 (a) façade temperature (b) road surface temperature. The comparison included the data collection during August 2015 and during March 2016.	165
Figure 5.21 Comparison of average surface temperature between August 2015 and March 2016 for ROAD 1	167
Figure 5.22 Comparison of average surface temperature between August 2015 and March 2016 for ROAD 2	167
Figure 5.23 Comparison of average surface temperature based on different street canyon configuration and aspect ratio, ROAD 1 and ROAD 2 in August 2015	168
Figure 5.24 Comparison of average surface temperature based on different street canyon configuration and aspect ratio, ROAD 1 and ROAD 2 in March 2016	169
Figure 5.25 Influence of canyon configurations on road temperature - August 2015	171
Figure 5.26 Influence of canyon configurations on road temperature - March 2016 .	172
Figure 5.27 Influence of canyon configurations on road surface temperature.....	175
Figure 5.28 Geometry construction in Google Sketchup 2015 with Solid Inspector .	176
Figure 5.29 Dimension of the flow domain based on HTB = 300 m	177
Figure 5.30 3D simulation consists of ROAD 1 and ROAD 2 with the setting of urban airflow, solar radiation and surface properties	180
Figure 5.31 Validation of static façade temperature against thermal imaging results for (a) ROAD 1 during 9th March 2016 at 14:00 hour (b) ROAD 2 during 14th March 2016 at 11:00 hour	181
Figure 5.32 Validation of static road surface temperature against thermal imaging results for (a) ROAD 1 during 9th March 2016 at 14:00 hour (b) ROAD 2 during 14th March 2016 at 11:00 hour	182

Figure 6.1 Simulation result of static surface temperature for (a) urban street canyon of urban macro domain (b) flat surface of rural/flat macro domain. Sectional air velocity indicated as S-S(a), S-S(b) and S-S(c) is detailed in Appendix A.13	186
Figure 6.2 Air temperature at the centre of street canyon of urban macro domain	188
Figure 6.3 Area-weighted average road surface temperature 0.15m above selected pipe location at 13:00 hour for urban macro domain with street canyon AR 1 and for rural/flat macro domain without building (AR 0)	188
Figure 6.4 Surface temperature after RPSC simulation at 0.15m below pipes for (a) urban macro domain or RPSC-1 (b) rural/flat macro domain or RPSC-0	189
Figure 6.5 Effect of hourly solar intensity on the RPSC outlet water temperature	191
Figure 6.6 Result of inlet outlet temperature difference, Delta T of RPSC performance based on wind factor	192
Figure 6.7 Predicted Delta T of RPSC performance based on seasonal changes	193
Figure 6.8 Surface temperature contour of street canyon comparing its effect based on the configuration of aspect ratio (a) AR 1 (b) AR 2 (c) AR 3 (d) AR 4	194
Figure 6.9 Section S-S of centre canyon for (a) AR 1 (b) AR 2 (c) AR 3 (d) AR 4 showing (i) air velocity magnitude, m/s (ii) air temperature, K	196
Figure 6.10 Temperature contour of Leeward Wall (façade of Building A facing canyon) and 3D air streamlines of (a) AR 1 (b) AR 2 (c) AR 3 (d) AR 4	198
Figure 6.11 Details on 9 locations of average surface temperature from macro domain to be exported to micro domain	199
Figure 6.12 Performance of RPSC based on street canyon aspect ratio showing (a) Delta T (b) PTC, % (c) STR, %	201
Figure 6.13 Temperature contour of canyon road surface comparing (a) Symmetrical canyon height (b) Asymmetrical canyon height Type 1 (c) Asymmetrical canyon height Type 2	203
Figure 6.14 Air velocity contour comparing (a) Symmetrical canyon height (b) Asymmetrical canyon height Type 1 (c) Asymmetrical canyon height Type 2	205
Figure 6.15 Façade temperature comparing (a) Symmetrical canyon height – i & ii (b) Asymmetrical canyon height Type 1 – i & ii (c) Asymmetrical canyon height Type 2 – i & ii	207

Figure 6.16 RPSC performance calculated in (a) potential temperature collection (PTC) and (b) surface temperature reduction (STR).....	210
Figure 6.17 RPSC performance based on pipe depth in (a) Delta T (b) PTC and STR	212
Figure 6.18 RPSC performance based on inlet water temperature in (a) Delta T (b) PTC and STR.....	213
Figure 6.19 RPSC performance based on water velocity in (a) Delta T (b) PTC and STR	215
Figure 6.20 RPSC performance based on pipe diameter in (a) Delta T (b) PTC and STR	216
Figure 6.21 Surface temperature plotted across four locations and pipe wall surface temperature based on 0.1 m/s inlet water velocity simulation comparing (a) Type STP (b) Type SPP	218
Figure 6.22 Surface temperature plotted across four locations and pipe wall surface temperature based on 0.25 m/s inlet water velocity simulation comparing (a) Type STP (b) Type SPP	220
Figure 6.23 Average surface temperature based on hourly simulation (09:00 – 15:00) and percentage of surface temperature reduction (%) comparing: (a) Type SPP with 0.1 m/s (b) Type STP with 0.1 m/s	222
Figure 6.24 Average surface temperature based on hourly simulation (09:00 – 15:00) and percentage of surface temperature reduction (%) comparing: (a) SPP with 0.25 m/s (b) Type STP with 0.25 m/s	223
Figure 6.25 RPSC performance comparing SPP and STP based on hourly simulation (09:00 – 15:00) with 0.1 m/s and 0.25 m/s inlet velocity in (a) Delta T (b) PTC.....	225
Figure 6.26 RPSC performance comparing SPP and STP based on hourly simulation (09:00 – 15:00) with 0.1 m/s and 0.25 m/s inlet velocity in terms of STR.....	226
Figure 6.27 Performance of RPSC in dissipating heat from road surface according to street canyon aspect ratio in terms of STR	228
Figure 6.28 Temperature reduction (in °C) comparing the aspect ratio of 1, 2, 3 and 4	229
Figure 6.29 Table of Heat Index (HI) developed by NOAA’s National Weather Service. 20 th September 2017. Retrieved from:	230

Figure 6.30 Effect of canyon aspect ratio on road temperature based on (a) simulation modelling (b) thermal imaging in August 2015 (c) thermal imaging in March 2016 ..235

Figure 6.31 Effect of canyon configuration on road temperature based on (a) simulation modelling (b) thermal imaging in August 2015237

Figure 6.32 Effect of canyon configuration on road temperature based on (a) simulation modelling (b) thermal imaging in March 2016237

LIST OF TABLES

Table 2.2.1 Summary of common hypothesised causes of UCL and UBL (Oke 1987)	25
Table 3.1 Relationship between street azimuth ϵ , angle of horizon σ and street of narrowness, N (Landsberg 1981)	67
Table 3.2 Percentage loss in illumination by street canyon ratio (Landsberg 1981)	67
Table 4.1 Comparison of mesh setting for independence study	106
Table 4.2 Mesh setting for macro domain with aspect ratio (AR) of 1, 2, 3 and 4	109
Table 4.3 Mesh setting for macro domain with asymmetrical canyon height	110
Table 4.4 Cell information based on medium mesh setting for different aspect ratios	113
Table 4.5 Mesh independence study for STP and SPP	116
Table 4.6 Boundary condition applied on ground surface, soil and building walls	118
Table 4.7 Boundary condition applied on RPSC domain	119
Table 4.8 Summary of parameter values used for RPSC system	120
Table 5.1 Parameter description and value based on local weather station	136
Table 5.2 Number of vehicle passed by ROAD 1 and ROAD 2	137
Table 5.3 Canyon aspect ratio of 6 cross-sectional elevations in ROAD 1 and ROAD 2	141
Table 5.4 Object parameter using FLIR T650sc user manual	143
Table 5.5 Boundary condition for temperature validation of ROAD 1 and ROAD 2	180
Table 6.1 Calculated Delta T, PTC and STR values at 13:00 hour on 21st June	190
Table 6.2 Average surface temperature and outlet water temperature during 13:00 hour	199
Table 6.3 Calculation of average surface temperature according to pipe locations	209
Table 6.4 Exported average temperature at 0.15 m below surface to macro domain	227

Table 6.5 Exported average temperature at 0.15 m below surface to macro domain.. 233

Table 6.6 Potential UHI and mitigation comparing simulation and experiments..... 241

NOMENCLATURE

CO ₂	Carbon dioxide emissions
3D	Tri-dimensional
Albedo	A measure of reflectance or optical brightness
AR	Aspect ratio of a street canyon according to building height, H against canyon width, W (H/W)
CAC	Conductive Asphalt Concrete
CBD	Central Business District
CFD	Computational fluid dynamics
CHTC	Convective heat transfer coefficient
De-coupled simulation modelling	Separated simulation modelling combining urban domain and RPSC domain
Delta T	The difference value between the inlet temperature and the outlet temperature
Façade	Front of a building, facing a street or an open space
GHG	Greenhouse gas
GUI	Graphical user interface
HDMR	High dimensional model representations
HRES	Hybrid Renewable Heating System
Hydronic	Fluid medium such as water used for heating and cooling system
k-ε	k-epsilon
MW	Megawatts
PET	Physiologically Equivalent Temperature
PTC	Potential temperature collection in %
RANS	Reynolds-Averaged Navier-Stokes
RANS	Reynolds-Averaged Navier-Stokes equation; time-averaged equations of motion and fluid flow
RPSC	Road pavement solar collector system
STR	Surface temperature reduction in %
SVF	Low Sky View Factor
TMY	Typical meteorological year
UBL	Urban boundary layer
UCL	Urban canopy layer
UHI	Urban Heat Island effect
UHII	Urban Heat Island intensity
UTCI	Universal Thermal Climate Index

Acknowledgement

I would like to express my gratitude to Allah s.w.t. for giving me strength to be perseverance and be patient until the last moment with the research and thesis in 3 years 11 months. Here I am, still survive and alive from the struggles. At last, I can ‘breathe’.

سُبْحَانَ اللَّهِ ، وَالْحَمْدُ لِلَّهِ ، وَ لَا إِلَهَ إِلَّا اللَّهُ ، وَ اللَّهُ أَكْبَرُ

To my beloved Papa, Mama and my family members, Abang Long, Kak Irza, Abang Ngah, Kak Nina, my eldest sister Akak, Abang Wan, my little brother Chiboy Aiman and my little sister Atin Bayin, my nieces and my nephews (Nafisa, Najla, Harith, Haziq, the future Baby Ninin and the future baby in Akak’s womb); I love all of you so much and thank you for being there for me whenever I feel low. I will never forget your prayers on my success especially from Papa and Mama. Thank you for your willingness to deal with my crap stories, cries, complaints and negative thoughts within the period of being a PhD student. It was tough to me, but I made all of you feel more worried.

Alhamdulillah, it finally ends. Now I can give you this BABY BOOK to all of you! ☺

To my young, dedicated, funny and superb PhD supervisor, Dr Ben Richard Hughes; I can’t imagine any other supervisor to supervise my silly PhD works except you. I know you are the most patient person who can tolerate with my silly questions and simulations. Knowing you, your works and research group are like venturing myself into a new world I have never been experienced before coming to the UK. It was hard initially, but the endless supports from your sides have strengthen me in and out, encouraging me to keep going, be persuasive and be confident about my studies.

To Dr John Kaiser Calautit, thank you for your never ending helps in CFD lessons, conference proceedings and journal publications and for being the person who always see the silver linings out of the complexity and difficulties. Young but full of maturity!

Last but not least, those people I love the most in Sheffield, Leeds, Malaysia and anywhere; Dr Polypocket, Dr Sally, Cholo, Mohamed, Dr Dom, Dr Adam, Dr Daniel, Kak Zu, Nassya, Faten Najwa, Siti, Lucy, Maria, Wan Azliza, Suzy, Geng SOS, Rai, Intan, Raihan, Kak Fad, Cinnun, Fiqah, Nadhirah Sooyoung, Kak Ju, Kak Munirah, Teacher Sarah, Najwa, Maaruf, Wardah, Yoona, Hong Jonghyun; you guys rock!

CHAPTER 1

Introduction

The process of urbanisation plays an important role in warming the urban environment due to the increasing artificial urban surfaces which are formed into buildings, roads and other infrastructure elements in replacing natural surfaces (Akbari 2005). Urbanisation influences the changes in the environment, land cover and land use which is of the interest to policy makers and scientific research (Comarazamy et al. 2015), with both opportunities and challenges to infrastructure development, specifically to determine the types of infrastructure to be constructed based on the types of urban form (Kennedy & Corfee-Morlot 2013).

The correlation between climate and urban area can be understood based on the influence of climate on the city space and vice-versa. It was stated that a large-scale city modifies the regional climate conditions of solar radiation, precipitation, cloud cover, air temperature and air speed with a clear difference between the urban area and its surrounding area (rural). For a small-scale city, the microclimate of the city is strongly influenced by outdoor space, building configuration, orientation and spacing (Kleerekoper et al. 2012).

The United Nation has projected that 67 % of the world population will live within cities by 2050 due to rapid urbanisation (Chapman et al. 2013). With larger urban areas, the increasing urban dwellers determine and depend on the urban infrastructures; causing the modification of urban climate due to waste heat production and artificial urban surfaces. Previous study stated that cities in the world accommodate over 50 % of its total population, which the impact has both no respect towards climate change and the capability to respond towards climate change (O'Malley et al. 2015). For example, it was reported that the total urban land cover of three hot humid urban cities of Malaysia, Dengkil, Kajang and Cheras has been noticeably evolved from 1998 to 1999 (Ahmad & Hashim 2007), see Figure 1.1.

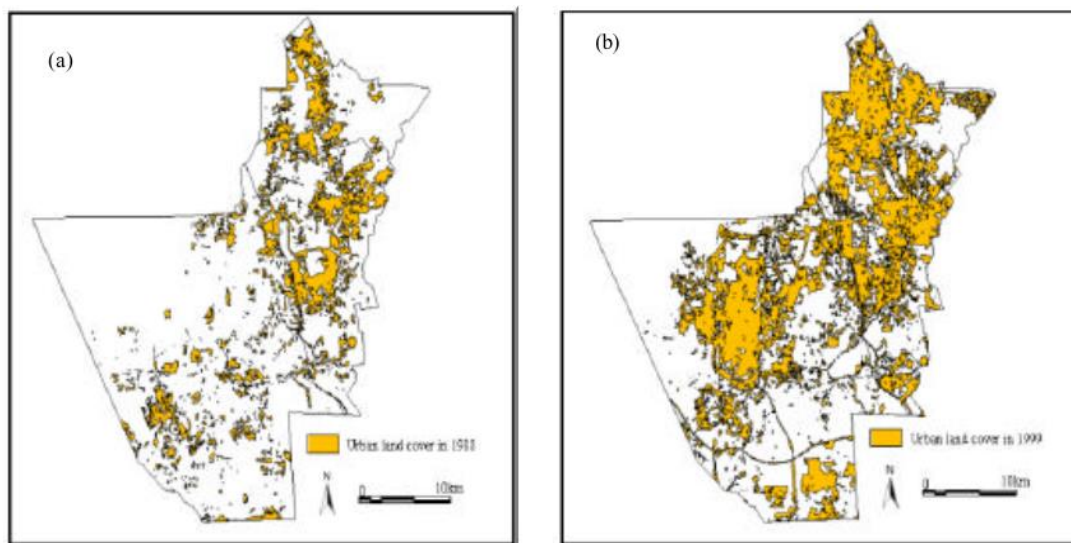


Figure 1.1 Urban land cover of three urban areas in Malaysia; Dengkil, Kajang and Cheras that evolved from 1998 to 1999 using Landsat TM (Ahmad & Hashim 2007)

It was stated that the centre of metropolitan cities in hot climates can experience elevated temperatures 2-4 °C higher than the rural area, the values which are similar to those experienced by gulf countries (Radhi et al. 2013). According to the International Panel on Climate Change, it was predicted that the increase in the global air temperature is 1.1-

6.4 °C for the 21st century, which encourages the occurrence of heat waves and extreme weather conditions, meanwhile The Royal Dutch Meteorological Institute (KNMI) predicted that the increased air temperature will cause warmer winters and dryer summers (Kleerekoper et al. 2012). Heat-wave incidence was found noticeable in urban areas due to high thermal discomfort and is projected to be a typical incidence by 2050. In 2003, it was reported that European heat-wave incidence caused thousands of death across the continent during the year's hottest summer (Chapman et al. 2013).

Additionally, high temperatures cause the generation of urban pollutants and global emissions (Kleerekoper et al. 2012). In 2009, United Nations Framework Convention on Climate Change reported that 74 % of net global greenhouse gas (GHG) emissions are from massive infrastructures including building energy use, waste management, power generation and transportation systems in developed countries (Kennedy & Corfee-Morlot 2013). To achieve low carbon climate resilience, the development of infrastructures should be ready to reduce GHG emissions and should be adaptable to extreme weather conditions and rising sea levels.

1.1 Description on Urban Heat Island (UHI) effect

The excessive urban temperatures as compared to its surroundings (rural areas) is termed as Urban Heat Island (UHI) effect, in which the effect was reported to be significant during night time due to the emitted heat from the urban surfaces. In comparison to urban areas, rural areas get warm quicker than urban areas during the daytime but get cool quicker during the night time (Kershaw et al. 2010). The term 'Urban Heat Island' (UHI) effect has been discussed in theoretical and empirical works for more than three decades. UHI effect also refers to the phenomenon of higher atmospheric and surface temperatures

that occurs in urban areas or high density urban areas as opposed to rural or less density (Voogt & Oke 2003). It was stated that the UHI effect is the annual mean air temperature of an urban area with a population of one million or more which is calculated 1-3 °C warmer than the surroundings (Oke 1981), meanwhile the nocturnal temperature intensity (night time basis) can reach as high as 12 °C (Oke 1987a). Figure 1.2 shows an example of the temperature difference between diurnal air temperature and nocturnal air temperature influenced by the complexity of surface topography and its temperature.

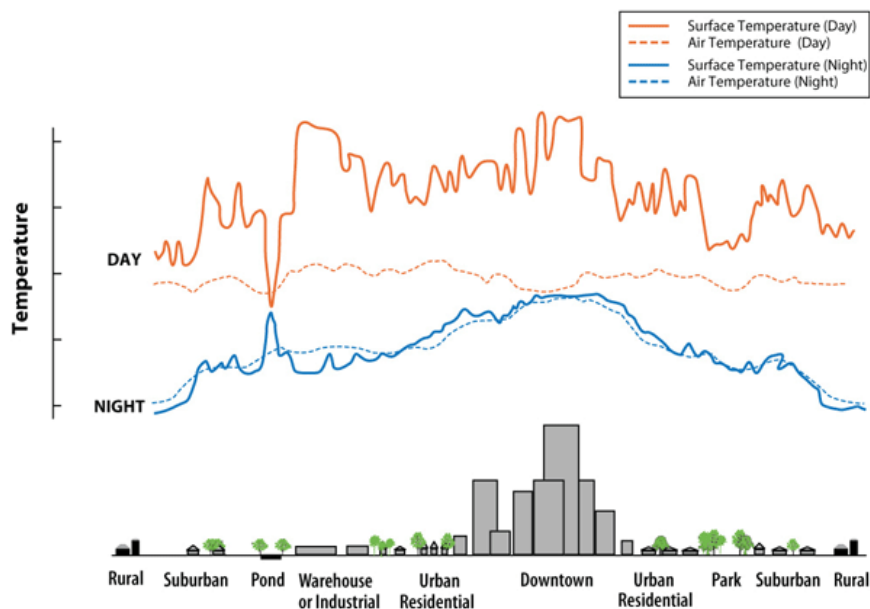


Figure 1.2 Significant different between diurnal surface temperature rise in urban conurbation centre and diurnal air temperature. 1st March 2017. Retrieved from <https://www.epa.gov/heat-islands>

In Luke Howard's 'The Climate of London' which observed the UHI intensity between several urban areas in London and the countryside since 1806, found that the average excess of temperature in London was 1.58 °C warmer than the countryside, concerning to remove the urban influence on the climate condition of London (Mills 2008). In 1941, evidence of air and surface temperature values of an urban area higher than the air and

surface temperature values of a rural area have been reported (April 1999). The UHI effect in urban areas can increase the maximum temperature by 10 °C as compared to the rural at times, which significantly affects the thermal comfort of urban dwellers (Chapman et al. 2013). An overview of the available literatures regarding UHI effect concluded that the rise in the air temperature is apparent according to time (Sani 1984; Elsayed & Ilham S. M. Elsayed 2012; Elsayed 2012b; Kolokotroni et al. 2012) and was highlighted that the increase up to 1 °C can be observed within a decade after all factors have been considered i.e. urban physical development, population, pollutants (April 1999). Nevertheless, the correlation between the rise by 1 °C air temperature and its impact on urban environment i.e. urban energy usage and human thermal comfort have been increasingly relevant to the current global concern on unpredicted climate condition and the scarcity of world non-renewable resources (Elsayed & Ilham S. M. Elsayed 2012; Elsayed 2012b; Akbari et al. 2001; Akbari & Matthews 2012).

There are seven causes to the occurrence of UHI effect within urban environment; including (a) short-wave and long-wave radiation from solar and materials, (b) obstruction from buildings to the sky, (c) anthropogenic heat release from nearby activities i.e. industries and traffic, (d) reduction in wind speed and turbulent heat transport within urban streets, (e) high absorptive materials, (f) less permeable materials and (g) air pollution (Oke 1987b). With dense infrastructures built in urban areas, more heat will be stored during the daytime from direct solar radiation and indirect anthropogenic heat i.e. waste energy and traffic exhaust (Kershaw et al. 2010; Comarazamy et al. 2015).

This comparison was termed as UHI intensity (UHII), an indicator of comparing the air and surface temperatures in both configurations (Memon et al. 2009). Under the studies of environmental and social sciences, three factors of urbanisation that influence the UHII were highlighted as (i) the application of artificial surfaces greater than natural surfaces (Ojima 1990; Berdahl & Bretz 1997; Streutker 2003; Rossi et al. 2014), (ii) rise in the energy consumption of human and production activities (Ojima 1990); and (iii) physical properties of urban elements that enhance the radiant surface temperature of the urban environment (Kolokotroni & Giridharan 2008a; Chudnovsky et al. 2004; Rossi et al. 2014). The re-emission of absorbed heat from the urban structures takes more time than in less dense areas, thus the intensity of the temperature between urban area and less dense area was observed to be noticeable.

1.1.1 Correlation between building configuration and urban heating

Complex and high dense urban structures establish ‘urban heating’ with high energy admittance and storage. With this abundant heat, the potential cooling through natural air convection in dissipating heat from the urban surface is low especially during the night-time (Lemonsu & Masson 2002). Urban heating reduces the comfort level of inhabitants to stay outdoors (Alchapar et al. 2014). Furthermore, the large span of non-evaporating impervious materials which predominantly cover the urban areas has caused a subsequent increase in the sensible heat flux at the expense of latent heat flux, thus contributes to elevating the UHI effect (Owen et al. 1998).

The UHI effect is caused by the differences in the energy budget between urban and rural area although the differences can be relatively small (Arnfield 2003). Additionally, the absorbed energy during the daytime in urban areas caused by low surface albedo will be

recovered by the radiative loss during the night time due to high surface emissivity (Christen & Vogt 2004; Giannaros & Melas 2012). For example, studies of urban heating through the intensities of air temperature and surface temperature were carried out in Hong Kong and results have demonstrated that high UHI intensity (UHII) for surface temperature was observed during solar peak time and vice-versa during solar-off peak time (Memon et al. 2009). Higher UHII for air during the night-time was due to the released heat from the source of urban heating.

Previous works have discussed on how urban built form can influence the total flux of urban energy in three ways (Harman & Belcher 2006). Firstly, the incident of direct solar radiation; where not only shadows from the horizontal building facades can cause variation in the incident solar radiation but multiple transmittance and absorption of the heat flux from surface to surface can cause small heat flux to be transmitted to the sky. Low Sky View Factor (SVF) has a significant influence in establishing surface heat island effects. Secondly, the changes in airflow within an urban canopy. Buildings cause a reduction in the average wind speed as it removes the momentum of airflow through pressure drag. With low average wind speed, the scalar of local turbulent transport is reduced, particularly air patterns that are closer to the building facades. Thirdly, urban surface area is larger as compared to a flat surface area based on the surface area in contact with air per unit plan area of ground. Due to this, the sensible heat flux per unit plan area of the urban surface increases contrarily to the reduction of turbulent transport.

1.1.2 Influence of urban street canyon on UHI effect

The arrangement of urban buildings according to the height and the width of the space in between the buildings which creates a configuration termed as ‘urban street canyon’, increases the area of heat absorption but at the same time reduces the heat loss via the convection and radiation heat transfer. The heat is trapped in between the urban spaces, and subsequently increases the nearby air and surface temperature. Urban street canyon is classified as a minimum of two building rows sat adjacent to one another, creating an empty space in between due to the blockage of the vertical facades from both buildings (Landsberg 1981; Oke 1988; Arnfield 1990). As early as 1980s, the subject of urban street canyon has been highlighted as one of major factors to determine surface temperature absorption and reflection from the abundant solar radiation.

Previous works highlighted several significant effects of street canyon configuration on microclimate conditions. It was highlighted that the increase in the air temperature was found with the decrease in the convective heat transfer coefficient (CHTC) when vertical facades become the blockage towards the predominant airflow (Rotach 1995; Toparlar et al. 2015). The next effect was based on the increase and the decrease in the solar intensity penetrating the urban street canyon caused by the vertical facades to influence the shadow effect on certain surface areas and the refraction of the solar radiation to other surfaces (Nazarian & Kleissl 2015; Stavrakakis et al. 2012). Next, the rise in the air temperature within street canyons closer to the heated ground surfaces becomes important factor on reducing pedestrian comfort (Memon et al. 2010; Memon & Leung 2011).

Literature review was carried out on the research which correlates urban street canyon with urban microclimate conditions i.e. temperature, airflow and pollutant movement has

been increasingly developed beginning in 2000s until recent years assisted by the improvement of computational technologies with graphical user interface (GUI) (Ito et al. 2005; Franke et al. 2007; Priyadarsini et al. 2008; Memon & Leung 2011; Allegrini et al. 2012; Nazarian & Kleissl 2015), see Figure 1.3. As shown in Figure 1.3, research conducted on urban street canyon between 2000 and 2013 was on average 3.8 % a year and the number increased to 10.3 % in journal publication for such topic from 2014 until the recent period.

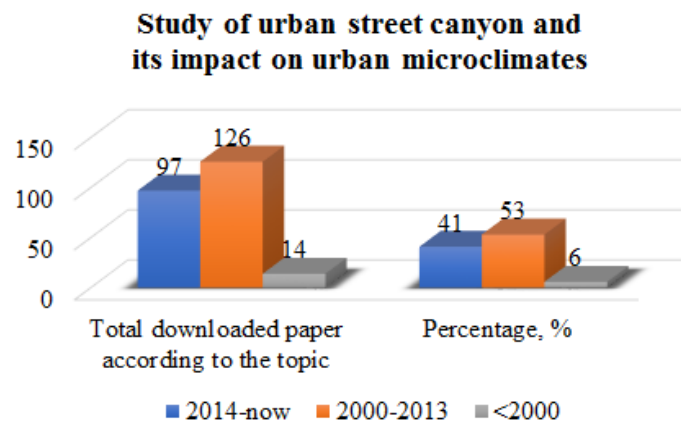


Figure 1.3 Statistic of the research and development involving the study of urban street canyon and its impact on urban microclimates based on downloaded journal publication before 2000, 2000-2013 and after 2014

1.2 Correlation between urban surfaces and UHI effect

Apart from urban geometry, the formation of UHI also includes the use of high heat absorptive materials such as asphalt, steel and concrete, which prevent precipitation penetrating the underground soils and subsequently avoid the formation of non-radiative air-cooling phenomenon (Comarazamy et al. 2015). The exposed urban surfaces influence on three aspects in determining the condition of an urban area, which are: (i) climate, (ii) thermal comfort, and (iii) electricity usage (Berdahl & Bretz 1997).

It was highlighted that during hot and summer days, artificial urban surfaces such as roofs and road pavements that are exposed to the solar radiation can be 27-50 °C warmer than the air temperature (Berdahl & Bretz 1997); meanwhile experiments on an exposed asphalt road showed the surface can be heated up to 70 °C (Bobes-Jesus et al. 2013). It was summarised that that asphaltic and dark surface materials led to excessive heat absorption more than less asphaltic an dark surface materials, thus intensify the impact on outdoor environment (Tan & Fwa 1992) especially the nearby air temperature (Berdahl & Bretz 1997).

1.2.1 Surface based UHI mitigation techniques

It was highlighted that mitigating UHI effect can be done by increasing the reflectivity and emissivity of the pavement surfaces. In the previous three decades, alternative pavements with the increased values in the solar reflectance, thermal emittance and convection coefficient for surface temperature reduction began on the investigation to replace the conventional pavement materials which lead to high excessive heat storage and release (Berdahl & Bretz 1997).

The implementation of pocket parks and vegetation types as the temperature moderators have been proposed (Elsayed 2012c; Elsayed 2012b). Two ways of tree planting can be applied. A direct approach is when the specific building benefits the improvement in the thermal effect solely and depends on how the building can achieve the said criteria. An indirect approach on the other hand is used for a city-wide range but requires time for its effectiveness (Akbari 2005). Numerous studies concluded that by promoting green approaches to city planning, more improvements can be made to reduce the thermal effect from the urban surfaces such as from buildings, roads and community spaces. This is due

to its high potential in reducing absorption of direct sunlight through shades by providing thermal comfort, although vegetation produces low surface albedo (Erell et al. 2013). In the case of hot humid climates, it was recommended that the mitigation of UHI effect should encourage more well-planned tree-planting programme (Elsayed 2012c).

Previous researchers have used several methods to improve surface albedo. Application of high albedo materials through direct and indirect methods are preferable as it is inexpensive measure to mitigate the temperature rise in both surfaces and atmosphere (Bretz et al. 1997; Synnefa et al. 2011; Santamouris 2012). Supplementary research on the properties of urban materials was carried out to determine the intensity of energy absorption and reflection (albedo) from the solar radiation in the composition of ultraviolet rays, visible light and infrared energy. The important properties to determine the intensity of the UHI effect are thermal emissivity and heat capacity of the materials (Akbari 2005).

For small-scale studies, laboratory and outdoor experimental works are commonly applied for measuring surface albedo for its effects on surface temperatures (Lin et al. 2010). Based on the investigation, results suggested that the change in the surface albedo from 0.05 to 0.12 changes the thermophysical properties of the tested surface; in this case to achieve the standard of a cement concrete which is better in terms of heat reflection and lesser in terms of heat absorption as compared to an asphalt surface (Akbari 2005). It was reported that the increased surface albedo up to 0.25 can potentially reduce approximately 10 °C in the temperature. The drawback of using high surface albedo for urban road surfaces was the glare problem, however it was reported that accidents caused by the glare are rare. Another drawback that can be considered as a strong reason to

against its application is the problem associated with the non-black road surface. With continuous vehicle movement and external dirt, the reflectivity of the non-black surface will be reduced (Akbari 2005).

The Lawrence Berkeley National Laboratory (LBNL) has developed numerous studies to mitigate UHI effect by enhancing energy saving and air-quality benefits from the application of cool roofs, cool pavements, shade trees and vegetation (Gilbert et al. 2016). A similar approach was also considered by the Environmental Protection Agency (EPA) which assists in the reduction of excessive heat absorbed by urban surfaces from the solar radiation. EPA endorses the use of cool pavement to increase the reflectivity, allow for water permeability and continue the investigation of heat storage from the pavement surface (Santamouris 2015). Furthermore, a reduction in the surface temperature by 5 °C was required to extend the lifecycle of the pavement up to 5 years meanwhile a reduction between 3 °C and 4 °C in the surface temperature or 6 °C in the total daily cycle fluctuation was predicted to significantly delay the pavement cracking and structural damage during the exposed daytime (Hall et al. 2012).

The important governing equations for empirical and numerical modelling method are mass conservation, potential temperature, momentum, water vapour and chemical species continuity. Meteorological and photochemical models are commonly applied to examine the increases in albedo and vegetation. The purpose was to enhance urban climate and air quality for large-scale studies specifically for urban areas. Several simulations were carried out in the Los Angeles basin to examine any noticeable temperature reduction from the changes in the surfaces albedo (Taha et al. 1992). A case study of California reported that with the surface albedo value 0.3 set for 25 % of the city area, at least 12 %

decrease in the ozone exceedance when 1.5 K temperature reduction was estimated based on the assumption that the albedo of all roads and roofs were improved (Akbari 2005).

Subsequently, cool pavement analysis was investigated to evaluate the influence on the external environment of one-third the city of Los Angeles by using the similar method (Taha et al. 1992). This study concluded with an estimation that by reducing 1.5°C in the air temperature, the city can save approximately 100 megawatts per hour in the demand for electricity. Thus, researches agreed with the use of light coloured asphalt or light asphalt mixtures to replace the conventional ones (Akbari 2005); however, a study of high reflective materials was found to reduce the level of external pedestrian comfort apart from its potential for UHI mitigation (Erell et al. 2013).

1.2.2 Application of Road Pavement Solar Collector (RPSC) system

The application of surface cooling was regarded a potential technique for future use in two ways: to reduce excessive heat from the urban surfaces which indirectly reduces air temperature closer to the ground level and to store and collect potential temperature as passive energy (Hasebe, M, Yamikawa, Y and Meiarashi 2006; Mallick et al. 2009). Solar collector systems embedded within the surface layer is designed to mitigate high surface temperature through the heat transfer from the surface to the surface layer and to the system, which function to collect the heat based on the flowing fluid (water) by using heat exchangers. The model of solar collector system installed underneath road pavement, termed as a 'Road Pavement Solar Collector' (RPSC) system in this thesis, became the focus of this thesis for its indirect potential to mitigate UHI effect and simultaneously can be used as urban passive energy collector.

Hydronic Road Pavement Solar Collector (RPSC) system was highlighted as the system which enhances the system performance in surface temperature reduction and in potential temperature collection based on the adjustment of the system parameters i.e. pipe depth, inlet water flow rate and conductivity of pavement materials (Bobes-Jesus et al. 2013). Previous works also highlighted the use of hydronic RPSC system to mitigate extreme weather conditions, concentrating on the pavement capability to absorb high heat from the daytime solar intensity (Qin & Hiller 2011; Wang et al. 2010). Figure 1.4 shows the comparison of the downloaded journal publication before 2000, 2000-2013 and after 2014. Based on Figure 1.4, it can be concluded that the research and development regarding pavement cooling has the same pace with the research and development on urban street canyon topic, from 3.4 % a year before 2013 to 12 % a year after 2014.

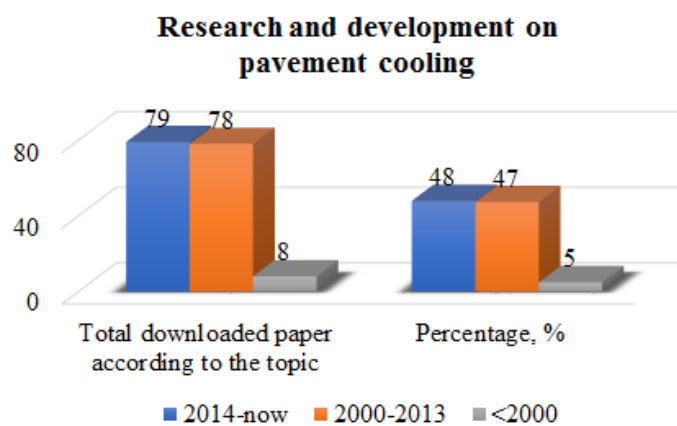


Figure 1.4 Statistic of the research and development involving the study of pavement cooling based on downloaded journal publication before 2000, 2000-2013 and after 2014

1.3 Problem statement

Research based on the application of hydronic RPSC system has identified the potential of the system as a mitigation strategy to mitigate the UHI effect, however the available literatures to correlate the two topics are found to be insufficient and require more development. Apart from the previous works which have carried out the research of RPSC system via laboratory and outdoor conditions, the conducted air speed and air temperature were usually bounded to be constant for simplification. As stated in the earlier published works, urban geometry has a major influence on microclimate conditions as compared to flat or rural geometry due to its complex shapes, causing heat to accumulate in between the urban spaces during multiple reflections of short-wave and long-wave radiations.

The configuration of urban canyon was emphasised to assist the modification of urban climate due to its obstruction towards predominant wind and low convective cooling to the ground air temperature, causing outdoor thermal discomfort. At the same time, the vertical facades of urban canyon can refract the direction of short-wave and long-wave radiations, causing some spots to receive shadow and other spots to receive higher heat. Thus, this thesis highlights the necessity to adjoin the hydronic RPSC system with larger and more complex urban conditions by including the effect of simplified urban built form, urban street canyon to carry out the investigation of hydronic RPSC system in mitigating excessive urban temperatures with more realistic urban conditions.

The research question was formed to establish the research aim and objectives based on the limitation found in the previously published works:

- i. What are the key parameters of urban canyon to support the application of hydronic RPSC system a UHI mitigation technique?

1.4 Aim

Determine the influence of a Road Pavement Solar Collector (RPSC) system as an Urban Heat Island (UHI) mitigation strategy.

OBJECTIVES

Investigate the effect of urban canyons on RPSC system/performance to:

1. Determine the effect of urban canyon on RPSC performance
2. Determine the effect of canyon aspect ratios on RPSC performance
3. Determine the effect of urban topologies on RPSC performance

Investigate the effect of RPSC system adjustment on RPSC performance to:

4. Determine the effect based on minimising/maximising surface area on RPSC performance
5. Determine the effect based on minimising/maximising mass flow rate on RPSC performance
6. Determine the effect based on minimising/maximising surface area and mass flow rate on RPSC performance

Investigate the effect of RPSC on mitigating UHI effect to:

7. Determine the condition of comfort temperature after RPSC application
8. Determine the impact on energy consumption for thermal comfort after RPSC application

1.5 Research methodology

Figure 1.5 is a flow chart of the research methodology followed in this study to investigate the RPSC system as the UHI mitigation strategy by using integrated 3D CFD ‘de-coupled’ urban domain with system domain simulation technique.

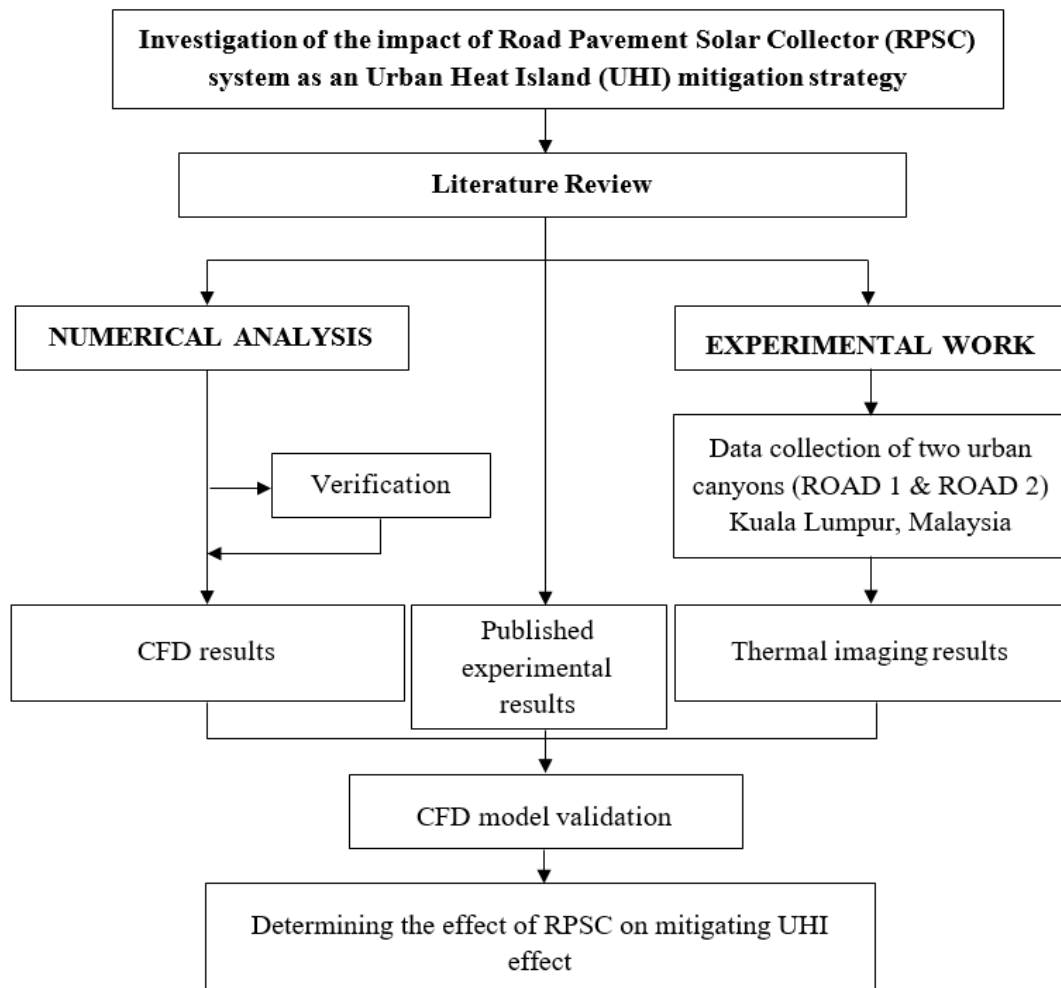


Figure 1.5 Flow chart of the outline of the thesis’ research methodology

1.6 Structure of the thesis

This thesis consists of 7 chapters. The current chapter, Chapter 1, introduced the background of the study, the problem statement and research gap. With the research motivation and questions developed for the study, the aim of the study with three main objectives were stated. The methodology of the research was designed to achieve the aim and the objectives.

Chapter 2 presents the available literature based on the effects of urbanisation in the increase of urban air-surface temperatures, highlighting the negative impact of UHI intensity in thermal comfort, global warming and energy usage. The chapter then emphasises the impacts of urban canyon towards microclimate conditions, which becomes the important reason of highlighting several surface cooling techniques for UHI mitigation. Chapter 2 also highlights the available research and development of hydronic RPSC system in encountering extreme weather condition and subsequently is potential for urban passive energy system. Based on the published literature, the research gap is identified.

Chapter 3 introduces the relevant theories and mathematical equations to relate the influence of urban built form on the occurrence of high air-surface temperatures, termed as UHI effect. The chapter highlights the absorption of heat fluxes from the urban environments (above ground level) by the pavement surface towards the pavement surface layers (below ground level). The theory of using a cooling medium to reduce heat is highlighted in the chapter.

Chapter 4 introduces the main research methodology of the thesis, which conducted a 3D Computational Fluid Dynamics (CFD) simulation to integrate the application and the performance of hydronic RPSC system with a simplified urban environment, to be specified as an urban street canyon. The simulation was based on the ‘de-coupled’ simulation technique, which the simulated temperatures of urban environment, termed as macro domain, becomes the temperature boundary condition of the hydronic RPSC system embedded inside a ground road pavement, termed as micro domain. Grid independent study and method validation were conducted to determine the optimum models used to simulate solar radiation, airflow and material conductivity of the macro domain and the micro domain.

Chapter 5 introduces the experimental method of using thermal infrared imaging data collection which was conducted in two urban street canyons in hot humid climate city, Kuala Lumpur. This is the chapter which the validation of the thermal effect from realistic building facades and road surfaces in several days of month of August 2015 and in several days of month of March 2016 was carried out. Additionally, the chapter also describes calibration tests on FLIR T650sc which were conducted via indoor and outdoor conditions against thermocouple and data reading devices. Results based on the data collection and the ANSYS Fluent CFD models which were used for the computational modelling against the data collection are also discussed in this chapter.

Chapter 6 presents the results of ‘de-coupled’ urban domain and RPSC domain including the effects of the simulation when several parameters bounded for both domains were investigated. The results of the RPSC system in mitigating UHI effect in terms of surface

temperature and air temperature are discussed with the support from the previous published literature and the data collection.

Chapter 7 summarises the investigation of the thesis based on the research outcomes against the aim and objectives and presents areas of future works that could not be carried out due to current limitations and time constraints.

CHAPTER 2

Literature review

2.0 Introduction

In this chapter, a comprehensive review correlating the Urban Heat Island (UHI) effect with urban surfaces consisting of urban built forms, infrastructure and complex surface materials has been used to define the research problem and statement of the thesis. Section 2.1 details on the global UHI effect and its consequences to the climate conditions in urban areas. Section 2.2 describes the correlation of built forms with UHI effects by introducing the previous studies which highlighted the configuration of urban canyons and example of urban canyon studies. Research and development of RPSC system for UHI mitigation are detailed in Section 2.3. The summary of Chapter 2 and the research gap in the literature review is then highlighted in Section 2.4 and Section 2.5, respectively.

2.1 Quantifying global UHI effect and its consequences

According to April (1999), an increase in air temperature was reported as 1 °C based on the measurement of 31 stations in California from 1940 to 1941. An observation study published in 1995 evidenced the intensity of air temperature in urban areas as compared to less urban areas up to 3 °C (Rosenfeld et al. 1995) meanwhile numerous studies have published the intensity in the range of 3-7 °C (Sani 1984; Wilby 2003; Elsayed & Ilham S. M. Elsayed 2012; Elsayed 2012b; Elsayed 2012a). In 2006, an evidence of UHII in Kuala Lumpur conurbation centre was found by 1.5 °C after two decades of the previous measurement studies carried out in by Sham (1986), demonstrating the correlation between UHII and urbanisation in hot humid countries over the years (Elsayed 2006). The impact of hot arid urban expansion in Bahrain under the Gulf Cooperation Council Countries (GCCC) which was studied in several decades by using Geographical Information System (GIS) given the results of 2-5 °C rise in the air temperature (Radhi et al. 2013).

In Hong Kong, 0.4-1.3 °C in nocturnal UHII was observed comparing three different residential areas (Giridharan et al. 2004) meanwhile diurnal UHII was calculated 1.5 °C and 0.4 °C, respectively for a specific urban residential area and for the comparison of three different residential areas (Giridharan et al. 2005). In Rotterdam, it was evidenced with 4.3-8 °C rise in the air temperature during summer (van Hove et al. 2015). A specific maximum UHII which was studied in London was mentioned 8.9 °C and 8.6 °C, respectively during cloudy daytime and night time (Kolokotroni & Giridharan 2008b). Additionally, higher intensity was found (12 °C) based on field observation studies of Lodz, Poland and Mexico City, Mexico (Hu et al. 2012).

Two factors are highlighted to cause the impact of heat island on an urban area: (i) The changes of natural surface on earth, and (ii) the increase in energy consumption (Ojima 1990). In the case study of Los Angeles in year 2005, there was a rise in the air temperature by 0.6 °C documented, estimating the rise in the electric demand 1.5-2 % (Akbari 2005). A significant increase in the average energy load when air temperature exceeds 20-25 °C representing the case study of New Orleans (Smith & Levermore 2008) is displayed in Figure 2.1.

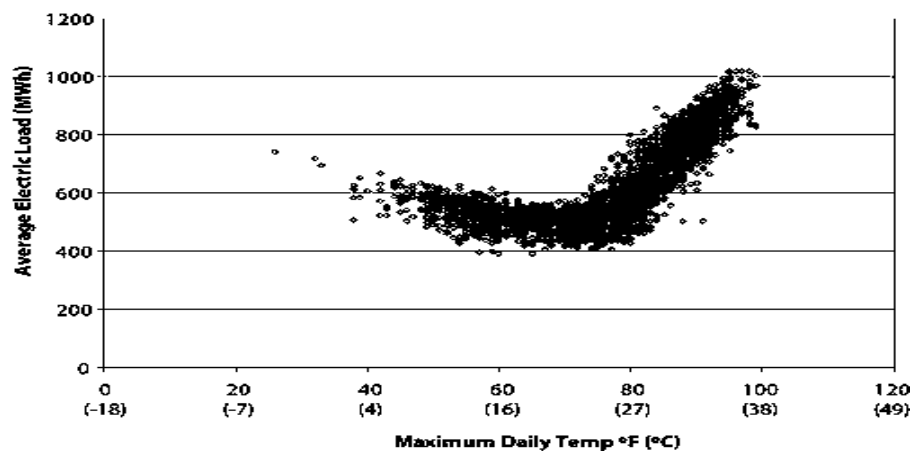


Figure 2.1 Example from New Orleans on the plotted electrical loads which increased steadily when the temperature exceeded 68-77 F (20-25 °C) (Smith & Levermore 2008)

Another study estimated that with 1 °C increase in daily maximum temperature, 2 % increase in the air-conditioning usage was reported which was equivalent to the excessive cost on electric demand reached \$100,000 per hour for the usage of 1-1.5 gigawatts (Elsayed 2012b; Elsayed & Ilham S. M. Elsayed 2012). Thus, it was suggested that to achieve comfort temperature level (22 °C), the UHI effect should be reduced as maximum as 3 °C (Rosenfeld et al. 1995). Furthermore, 1 °C increase in the air temperature was estimated to be equivalent to the rise in air-conditioning usage by 500 MW (Akbari & Matthews 2012; Akbari et al. 2001). In the case study of hot humid city of Kuala Lumpur,

a rise in the air temperature reached 1.5 °C was found within 20 years of observation (Sani 1984; Elsayed & Ilham S. M. Elsayed 2012).

It was reported that smoke formation and air pollution are also associated with high air temperature (Bretz et al. 1997). Additionally, the rise in the air temperature above 23 °C can potentially cause unfortunate events such as smoke formation, based on the probability of 24 % smoke increase by 1 °C (Rosenfeld et al. 1995). The common use of artificial cooling mechanism to encounter excessive air temperature indirectly produces waste heat and contributes to global warming (Smith & Levermore 2008), contradicting the global policies in limiting the emission of greenhouse gases.

An investigation on quantifying UHI effect was carried out by projecting overheating effects on city centre offices within 20 locations of East-West axis through London, United Kingdom comparing the effect in year 2000 to the year 2050, suggesting that a significant 200-500 % CO₂ emissions from offices is estimated to be obtained in 2050. By reducing from high to medium heat gains, the environmental impacts was estimated to be reduced from 230 % to 87 % for rural location and from 480 % to 140 % for urban location (Kolokotroni et al. 2012).

2.2 Effects of built form on UHI effect

According to Oke (1987a), investigation on urban mass and energy balances is strongly connected to three major elements: (i) surface roughness, (ii) characteristic of urban geometries, and (iii) thermal properties of urban materials. The surface roughness is determined from the geometries developed in an urban area based on the arrangement of building rows and the properties of the surfaces. To describe the energy balance of urban areas, two types of urban boundary layer were described in detail (Oke 1987a): (i) Urban Boundary Layer (UBL), and (ii) Urban Canopy Layer (UCL). Common hypothesised causes of UHI based on UCL and UBL as referred to (Oke 1987a) are summarised in Table 2.2.1.

Table 2.2.1 Summary of common hypothesised causes of UCL and UBL (Oke 1987)

ALTERED ENERGY BALANCE TERMS LEADING TO POSITIVE THERMAL ABNORMALITY		FEATURES OF URBANISATION UNDERLYING CHANGES IN ENERGY BALANCE
Urban Canopy Layer (UCL)		
1	Increased absorption of short-wave radiation	Canyon geometry - <i>increased surface area and multiple reflection</i>
2	Increased long-wave radiation from the sky	Air pollution - <i>greater absorption and re-emission</i>
3	Decreased long-wave radiation loss	Canyon geometry - <i>reduction of Sky View Factor (SVF)</i>
4	Anthropogenic heat source	Building and traffic heat losses
5	Increased sensible heat storage	Construction materials - <i>increased thermal admittance</i>
6	Decreased evapotranspiration	Construction materials - <i>increased 'water-proofing'</i>
7	Decreased total turbulent heat transport	Canyon geometry - <i>reduction of wind speeds</i>
Urban Boundary Layer (UBL)		
1	Anthropogenic heat source	Chimney and stack releases
2	Increased sensible heat input (entrainment from below)	Canopy heat island - <i>increased heat flux from canopy layer and roofs</i>
3	Increased sensible heat input (entrainment from below)	Heat island, roughness - <i>increased turbulent entrainment</i>
4	Increased absorption of short-wave radiation	Air pollution - <i>increased aerosol absorption</i>

UBL is known as the portion of planetary boundary layer above UCL which the characteristics of the climate are depending on the presence city at the surface. City landscapes provide a rougher, warmer and drier surface conditions as compared to the rural landscapes (Oke 1987a). The second type, UCL is characterised based on the complexity of the active surface units with repetition throughout urban canopy. The unit refers to the walls and ground or street between two adjacent buildings.

Building arrangements and configurations can decelerate the heat emission from the surface upward (Sailor & Fan 2002). Furthermore, the density of urban geometry and building density influences the incidence of radiation by multiple reflections between street surface and building facades where the materials can store heat (Kleerekoper et al. 2012). Vertical obstacles such as cubes and block that represent buildings in simplified forms have been used to investigate the dynamics of heat and airflow in urban areas and microclimate issues i.e. UHI effect, urban planning and urban heat flux. Dynamic flow studies relating to building rows and the surroundings emphasised the impact of the configuration on the velocity and temperature profiles (Levermore & Cheung 2012). This configuration was based on two buildings adjacent to one another that created an empty row or to be called 'street canyon' in between the two buildings.

It was reported that urban canyon causes to poor ventilation and to the increase of surface temperatures (Bottillo et al. 2014). In the study of deep street canyons, the transmitted heat in-between two buildings cause the number of photons left surrounding temperatures to elevate. Flat surfaces, the reflection of the heat to the atmosphere is indeed a simpler process (Akbari 2005; Levermore & Cheung 2012). For simplification, transmittance and

emittance of heat fluxes are depicted based on the direction of arrows in Figure 2.2(a) and Figure 2.2 (b) on flat surfaces and within urban canyons, respectively.

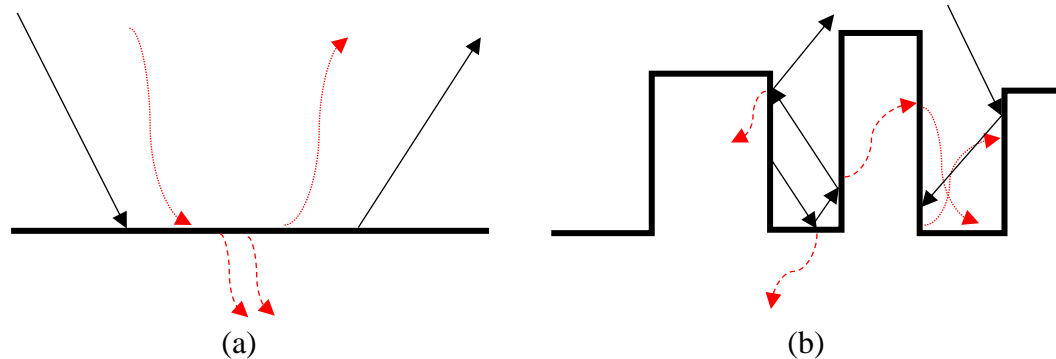


Figure 2.2 Illustration of heat transmittance and emittance (Akbari 2005; Levermore & Cheung 2012) towards (a) flat surface (b) within urban canyon

Additionally, high solar absorptivity of urban materials causes a major rise in the ambient temperature up to 30 °C (Carnielo & Zinzi 2013). Surface temperatures of a 3D urban scale street canyon are uneven due to the surface interaction to store, absorb and release heat. The instability in the surface temperature was reported due to the instability in the air circulation inside the canyon which largely influences the street pollution dispersion (Mirzaei & Haghighat 2012).

2.2.1 Configuration of urban canyons

An urban canyon is described as the ratio of average height of canyon walls (H) to the canyon width (W) termed ‘aspect ratio’ (Oke 1988; Arnfield 1990; Montávez & Jiménez 2000; Vardoulakis et al. 2003). The street orientation and aspect ratio are both significant for the studies of urban canyon and energy balance (Ali-toudert et al. 2005). In the study of Oke (1988), a 2D cross-section was used to represent a basic geometric urban unit with predominant direction of airflow across the canyon. The urban canyon is a rectangular

channel with surface materials and has the orientation based on specific angle, θ (Arnfield 1990).

Urban canyon represents the walls of adjacent buildings with the enclosed air volume (Landsberg 1981; Arnfield & Grimmond 1998), which is sandwiched between two walls. An urban canyon was created as a generic model which had identical streets within all directions and were applied on an entire urban area with several types of surfaces: roads, streets and walls (Lemonsu & Masson 2002). In this study, width of buildings, D_B was also highlighted for 3D analysis. An example of 3D generic urban canyon is specified in Figure 2.3.

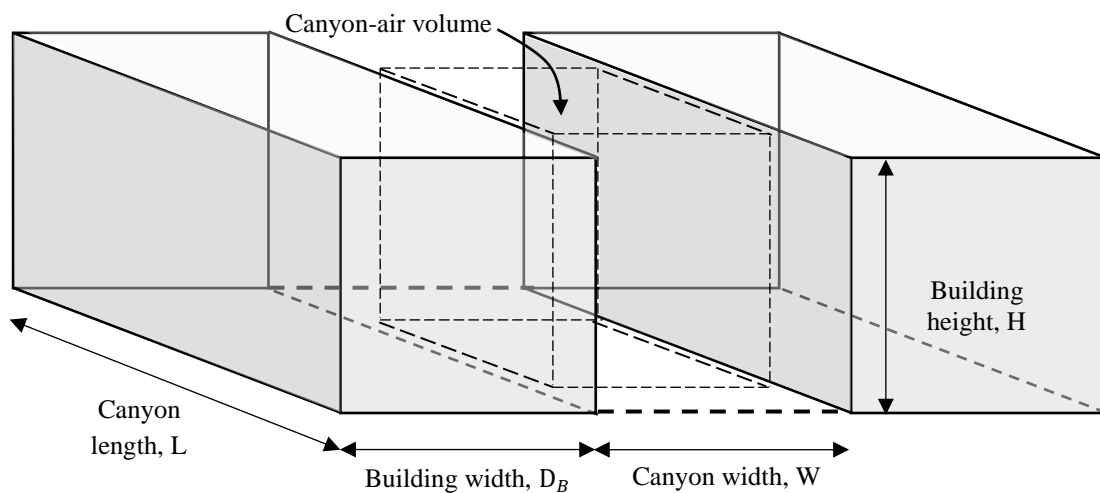


Figure 2.3 Illustration of 3D urban street canyon (Lemonsu & Masson 2002) with additional representation of canyon-air volume (Landsberg 1981; Arnfield & Grimmond 1998)

A simplified urban canyon was configured as a narrow street with building rows along both sides, realistically urban streets are not bordered with building rows on both sides due to the openings on walls of the canyons (Vardoulakis et al. 2003). However, a regular street canyon can be defined based on the height of the canyon equals to the width (an

approximate aspect ratio of 1). Additionally, the canyon streets were also made symmetrical due to approximately symmetrical building height and vice-versa for asymmetrical building height, see Figure 2.4.

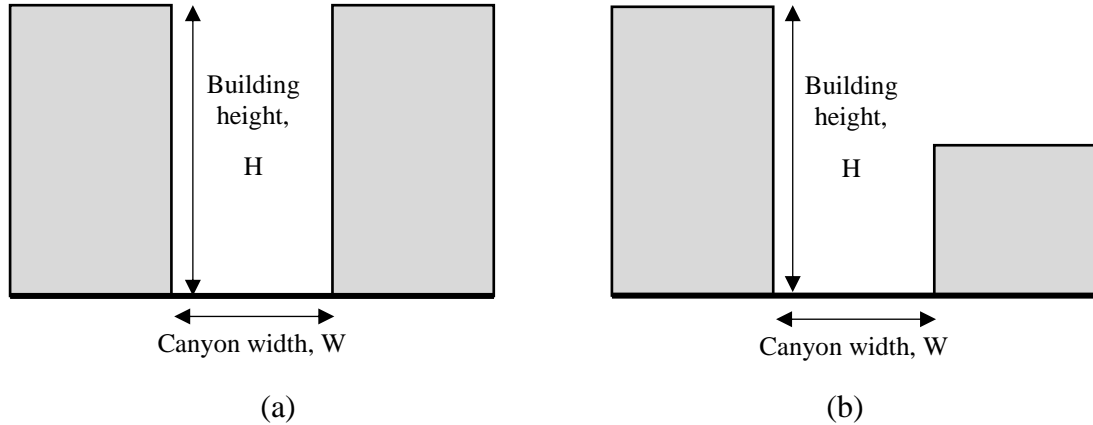


Figure 2.4 Illustration of urban topology to be determined by building height following (Vardoulakis et al. 2003) in (a) Symmetrical (b) asymmetrical

The ratio of street canyon length, L to the building height, H was highlighted in short ratio = $L/H \approx 3$, medium ratio = $L/H \approx 5$ and long ratio = $L/H \approx 7$ (Vardoulakis et al. 2003). Four cubical buildings were made in the centre of the domain; ensuring the street aspect ratio (H/W , L/W) was equal to 1 in west, south, east and north directions (Kim & Baik 2004). Thermal effect by solar irradiation within the confinement of street canyon became the focus due to its commonality to the shape of European cities (Bozonnet et al. 2005). The study was conducted by using a simplified long street canyon shape ($W/L \ll 1$ and $H/L \ll 1$) with low wind speed condition to neglect boundary effects on the street canyon, see Figure 2.5.

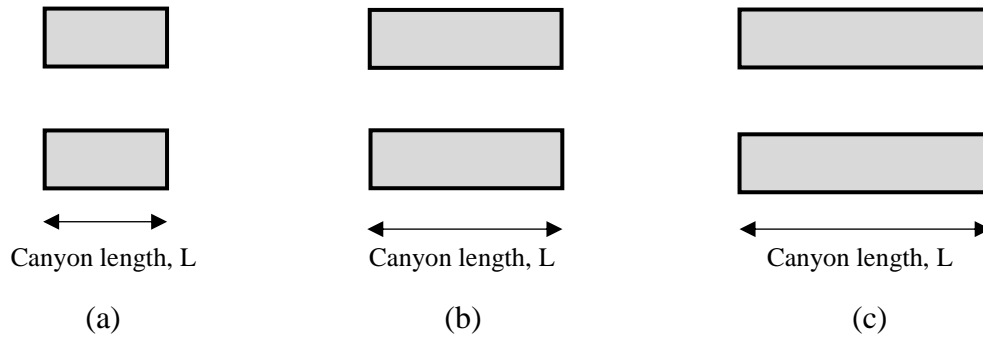


Figure 2.5 Illustration of urban canyon configuration to be influenced by length following (Vardoulakis et al. 2003) (a) short, (b) medium, (c) long

3D patterns of thermal comfort within street canyons were observed from shallow to deep street canyons (Ali-Toudert & Mayer 2006). Several aspect ratios (H/W) were determined (0.5, 1.0, 2.0 and 4.0) with East West (E-W) and North South (N-S) orientations. Northeast Southwest (NE-SW) and Northwest Southeast (NW-SE) orientations were also highlighted for comparative studies; see sectional diagrams in Figure 2.6.

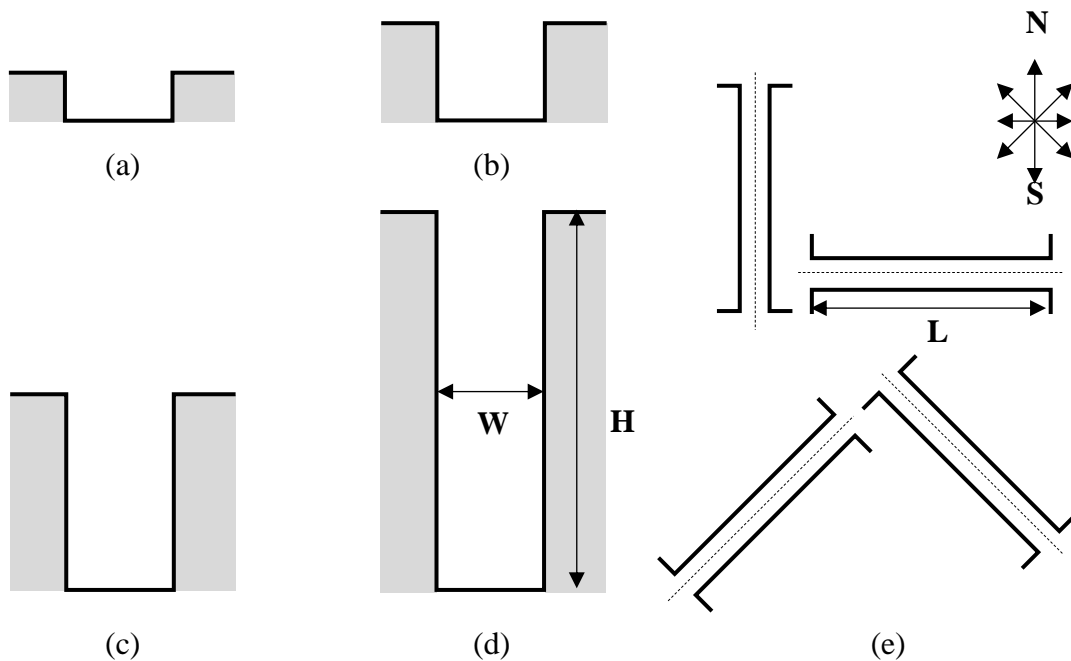


Figure 2.6 Illustration of canyon aspect ratio according to height, H against width, W (Ali-Toudert & Mayer 2006) (a) $H/W = 0.5$, (b) $H/W = 1.0$, (c) $H/W = 2.0$, (d) $H/W = 4.0$; also (e) street canyon orientation

The investigation of net radiative balance was carried out by comparing several 3D simplified urban canyon layouts (Panão et al. 2006): (i) square blocks, (ii) rectangular blocks and (iii) street type. The characterisation of the urban layouts was determined based on building length, L and the canyon width, W ; shown in Figure 2.7.

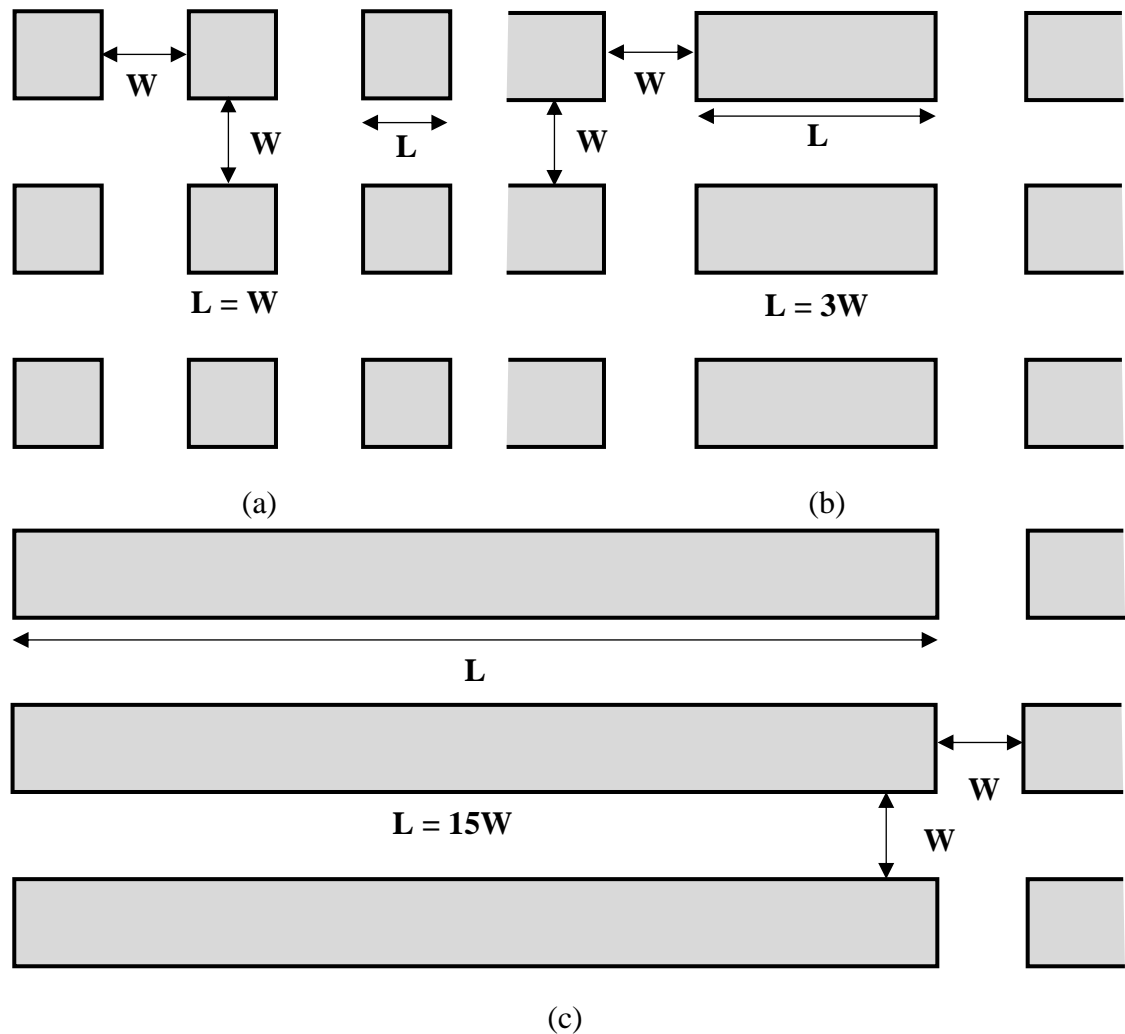


Figure 2.7 Illustration of simplified multiple types of urban canyon following (Panão et al. 2006) (a) Square blocks, $L = W$ (b) Rectangular blocks, $L = 3W$, (c) Street, $L = 15W$

Air temperature measurements within two urban canyon locations (Damansara and Melawati) between June and July 1987 were compared with the 3D simulation results developed in CFD FLOVENT (Hiung & Ahmad 2006). For Damansara, the configuration

of urban canyon was deeper as compared to the configuration of urban canyon in Melawati. Both canyons were modelled explicitly in 1:1 scale with the material properties bounded following field measurement work, see Figure 2.8.

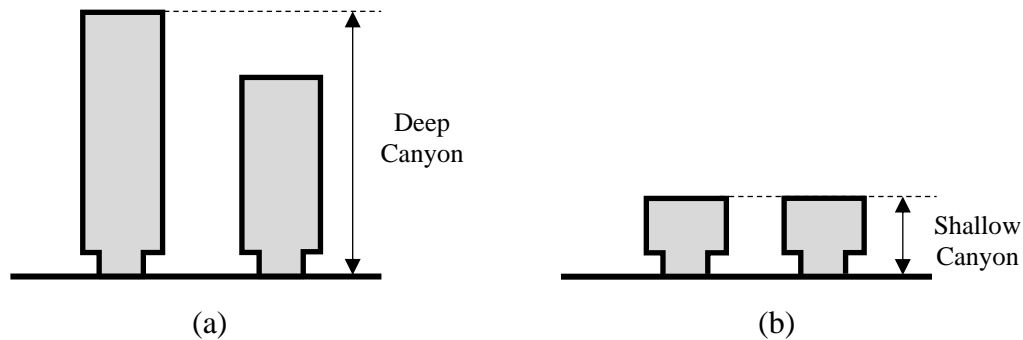


Figure 2.8 Illustration following (Hiung & Ahmad 2006) illustrating deep street canyon of Damansara urban district (b) shallow street canyon of Melawati district

Studies of urban forms were established in generic urban form and was conducted using simulations (Allegrini et al. 2015). However, the studies of urban configuration and layout based on actual measurements at specific location and climate are found more practical (Toparlar et al. 2015). A review paper published in 2005 described numerous types of modelling and experimental methods for the analysis of airflow around buildings with various shapes, orientation, arrangements (Ahmad et al. 2005). The paper emphasised on the influence of street canyon configuration on determining the microclimate changes specifically the wake effects and air swirling within the canyon.

2.2.1 Case studies of generic urban canyon

Three observational methods were included as common practice: field measurements, thermal remote sensing and small-scale modelling (Mirzaei & Haghighat 2012). Recently, computational simulation modelling is increasingly recognised to be sufficient to conduct the analysis which combines the interactions between energy and atmospheric motion

(Toparlar et al. 2015). In the works involving urban microclimate condition, modelling simplification on the geometry patterns were occasionally conducted. For example, several street canyon configurations were compared with the condition that one standard height was applied to all simulations (Allegrini, Dorer & Carmeliet 2012). However, multiple canyon geometry were also modelled and analysed (Allegrini et al. 2015). A study of urban canyon was carried out by conducting 18 months period of temperature measurements in Zurich (Rotach 1995), showing warmer air temperature at deeper part of the canyon area as compared to the upper part of roughness sublayer, see Figure 2.9.

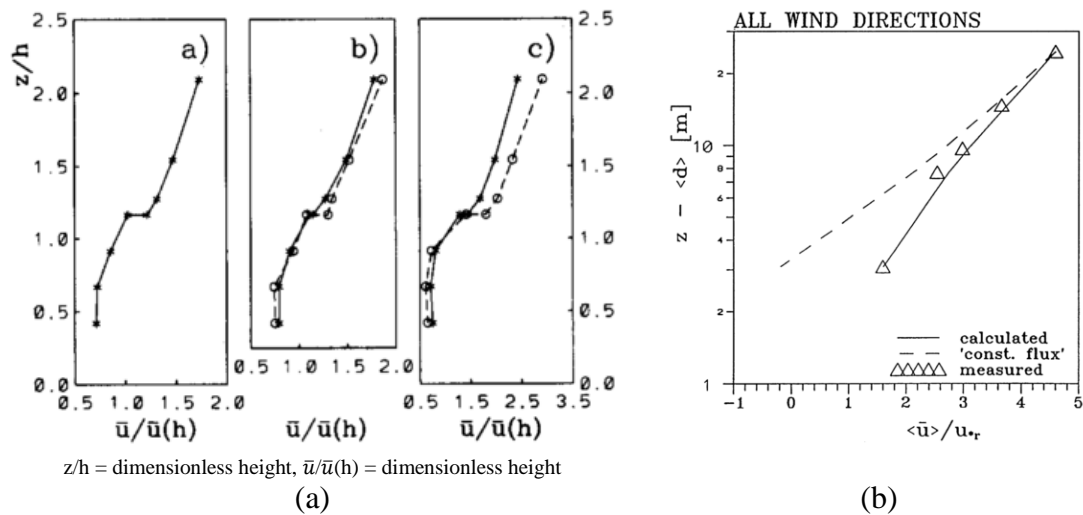


Figure 2.9 Velocity profile plotted from ground to rooftop level showed (a) lower velocity at the lower level, thus creating warmer air temperature (Rotach 1995) (b) validation of numerical results to the measurement results (Rotach 1999)

Investigation of thermal effect within an urban canyon with high moisture climate condition and evaporative cooling caused reduction in air temperature and mean radiant temperature and vice-versa (Saneinejad et al. 2014). Additionally, it demonstrated that a more prominent trend was found during the heat wave (HW) condition as compared to the results based on typical meteorological year (TMY); see Figure 2.10 below.

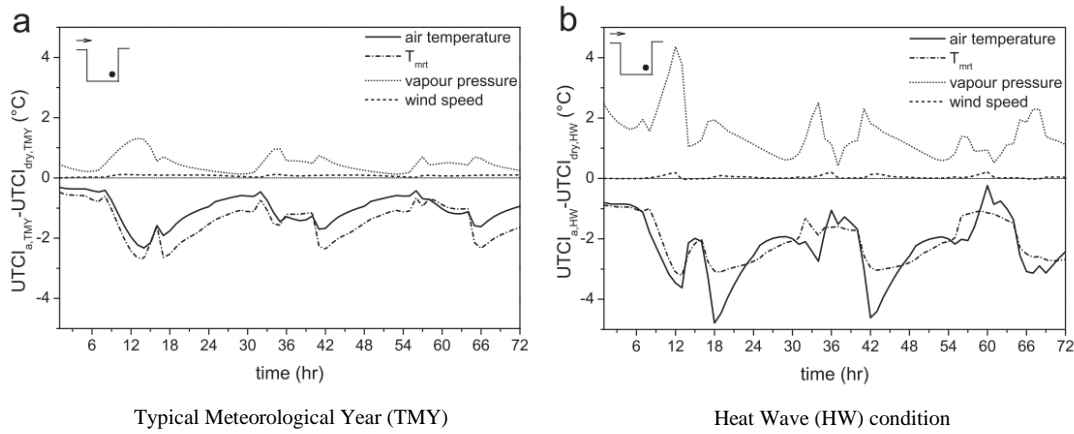


Figure 2.10 Comparative variables used to investigate thermal effect in urban canyon showing high evaporative cooling due to the high moisture on air temperature and mean radiant temperature (Saneinejad et al. 2014)

It was found that wind flow patterns were associated with the width of the canyon and the building height when wind direction is perpendicular to the building wall (Ahmad et al. 2005). For narrow street canyons (small ratio of height over width), a single vortex was observed to be established within street canyon, creating a skimming flow regime; see Figure 2.11(a).

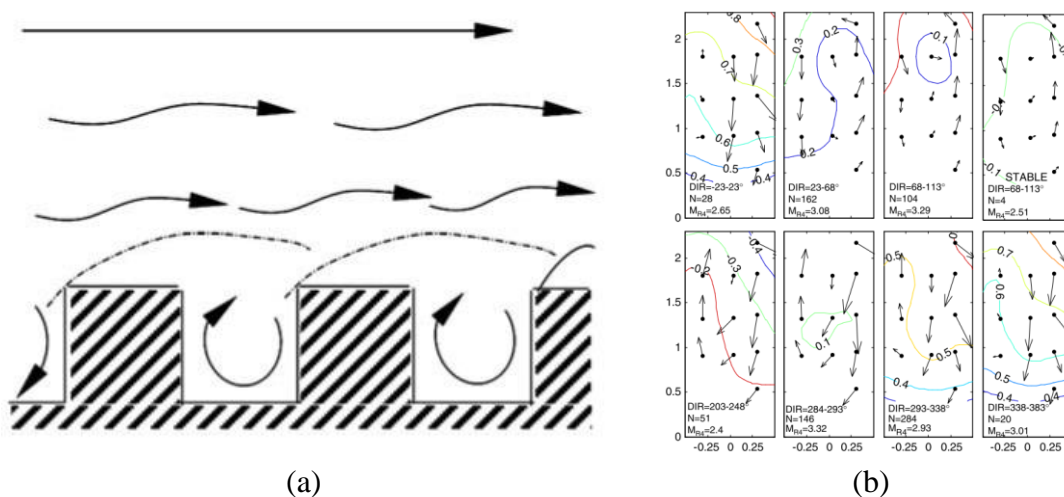


Figure 2.11 Perpendicular airflow across street canyon demonstrating (a) air skimming flow and 1 helical vortex for narrow canyon (Ahmad et al. 2005) (b) normalised air velocity and circulation in street canyon by (Eliasson et al. 2006)

Meanwhile, experimental studies within a street canyon with the canyon height to the width given the aspect ratio ~ 2.1 were observed with single helical vortex pattern with 60 °C cross-canyon orthogonal flow, see Figure 2.11(b). Additionally, the turbulent kinetic energy values closer to the ground were observed nearly constant but greater towards windward wall (Eliasson et al. 2006).

Measurements of air velocity and temperature in cross-canyon with perpendicular flows resulted to unstable vertical wind speed profile influenced by ambient wind incidence angles (Niachou et al. 2008). In addition, a clockwise circulation was observed with cross-canyon flow due to the uplifts along the downwind building, down lifts near upwind building were also influenced by the canyon flow from western and eastern directions, see Figure 2.12 below.

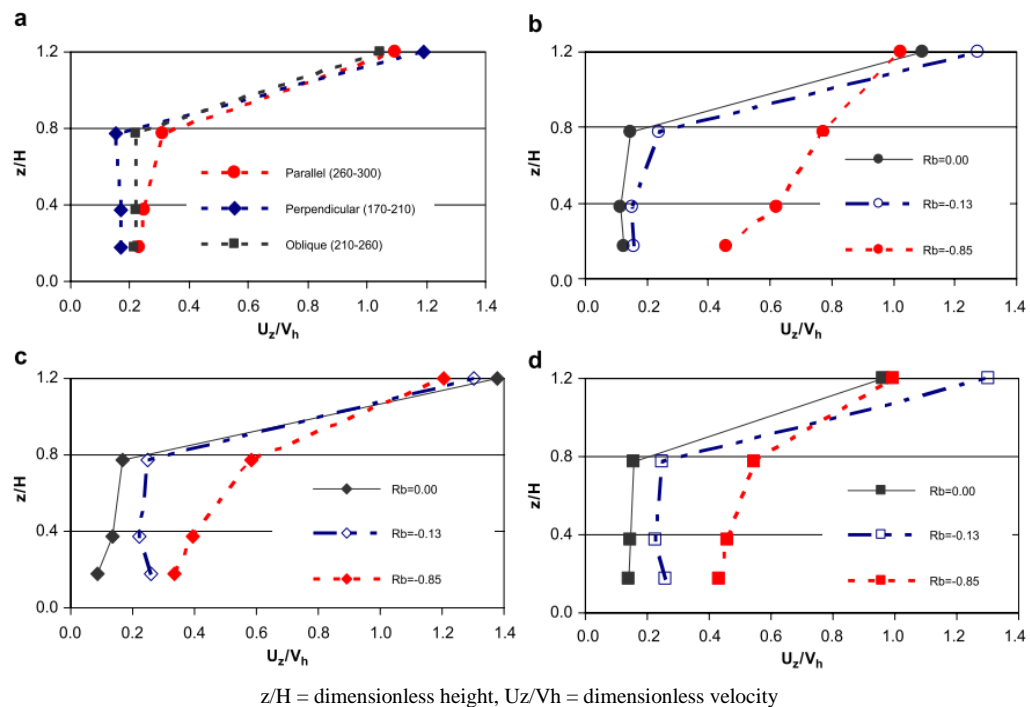


Figure 2.12 Modelling of predominant airflow cross building length from neutral to unstable Richardson bulk number comparing parallel, perpendicular and oblique flow showed highest velocity with parallel orientation (Niachou et al. 2008)

For predominant perpendicular flow, the airflow profiles within the street canyon were based on the thermal effects from ground heating. Studies of several urban block arrangements were simulated to estimate the pedestrian wind environment (Abd Razak et al. 2013), which the study concluded that the pedestrian wind speed strongly depends on the plan area ratio and building aspect ratio to define an idealised pedestrian wind speed in urban model condition, see Figure 2.13 below.

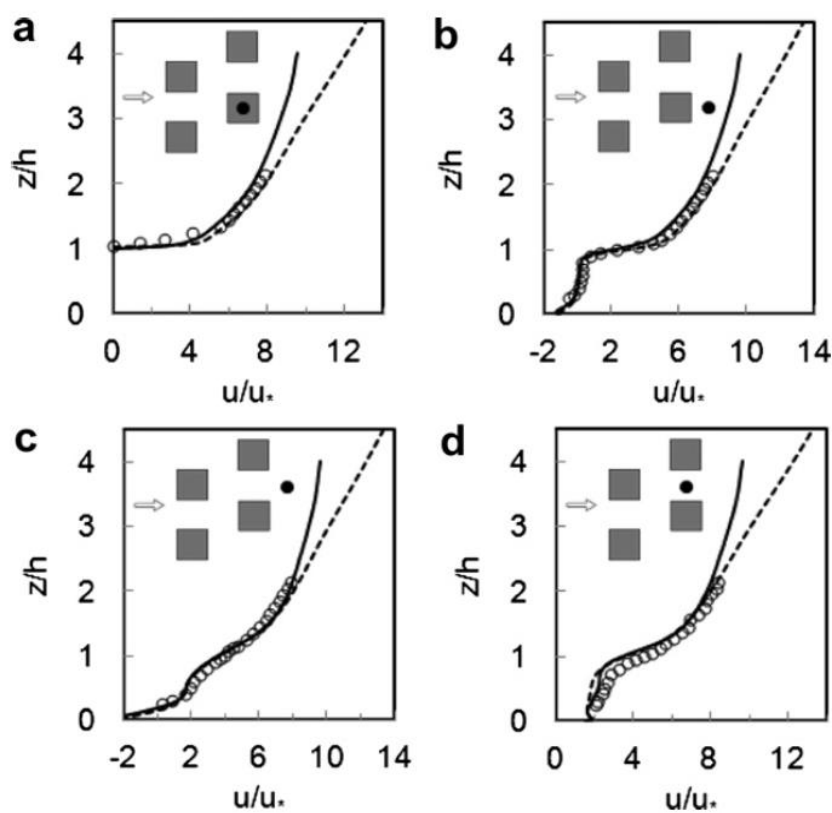


Figure 2.13 Profile of mean streamwise velocity normalised by friction velocity comparing locations: a – above cube, b – behind cube, c – in front of cube and d – in between cubes (Abd Razak et al. 2013)

A study of changing the urban canyon aspect ratios was carried out in order to compare the air temperature of each urban canyon with different heights (Memon et al. 2010). With a constant velocity value applied to the model (0.5 m/s), it was found that the highest dimensionless temperature was obtained according to the highest canyon aspect ratio, 8.

It was also noted that higher temperature was found accumulated closer to the leeward walls (shown for aspect ratio of 2 and 0.5), see Figure 2.14 below.

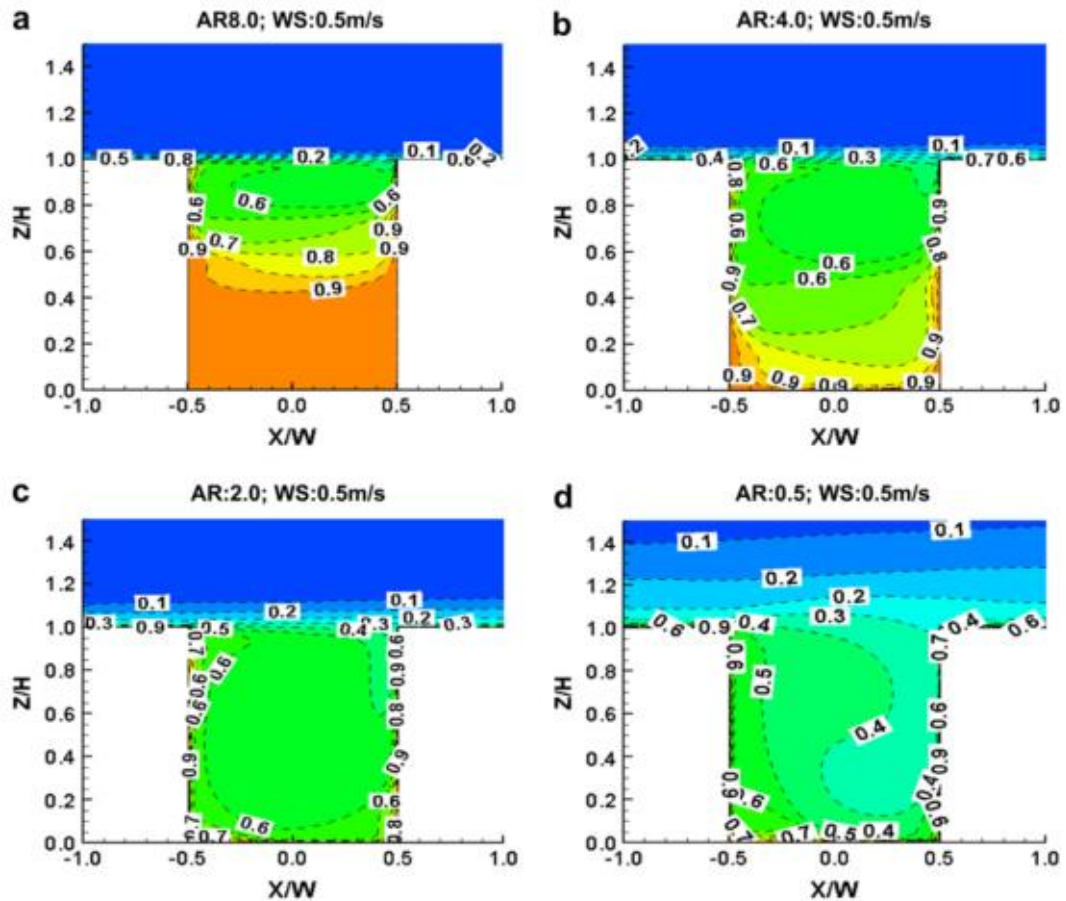


Figure 2.14 Spatial contours of normalised temperature within urban canyon comparing four aspect ratios demonstrating higher temperature was associated with higher aspect ratio with less windy condition – 0.5 m/s (Memon et al. 2010)

Simulations of urban canyon with active natural convection showed higher turbulent kinetic energy near all canyon surfaces, which affects the trends of heat transfer coefficient (Bottillo et al. 2014). It demonstrated with four times kinetic energy and double heat transfer coefficient from ground level to half height of the building. Because of the activated natural convection, air circulation increased in the canyon by the carried velocity 2 m/s as compared to the deactivated natural convection with the velocity 1.5 m/s, thus assisting in lowering several degrees in the surface temperatures. Figure 2.15

illustrates the comparison of modelling the heat flows with and without the application of natural convection.

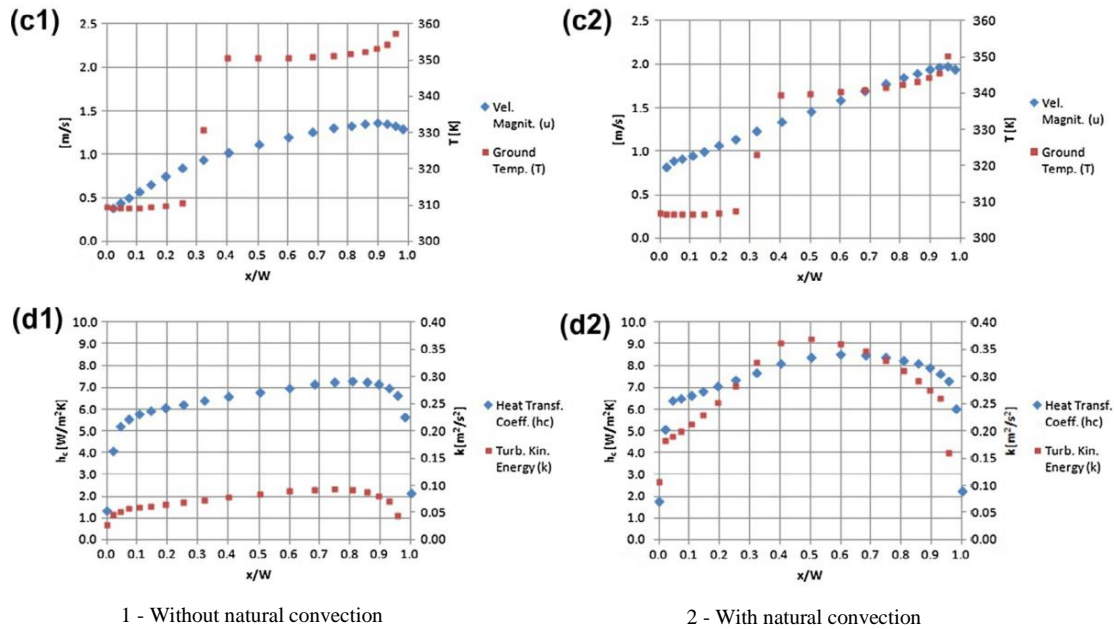


Figure 2.15 Results from the comparison suggested that positive natural convection due to the buoyancy effect from the ground surface temperature increased the velocity magnitude and low surface temperature (Bottillo et al. 2014)

The impact of heat flows on energy consumption for cooling within urban environment was highlighted more important than the rural environment (Allegrini et al. 2012), thus; by using CFD, the correlation of urban convective heat transfer coefficients (CHTC) was determined with and without natural convection for several urban geometries that included stand-alone buildings (short and long) and street canyon with different aspect ratios. Based on the comparison studies shown in Figure 2.16, it suggested that the CHTC with natural convection did not decrease to zero during low air speeds where the condition can be observed at both heated leeward and windward walls. Furthermore, it was predicted that the CHTC for leeward wall was always lower than the CHTC for windward wall due to low air velocity at leeward surfaces. To compare the analysis based on the

stand-alone buildings and street canyon, simulation results showed that the CHTC of windward wall for street canyon was lower than standalone buildings, especially the deeper canyon. It was observed that CHTC for leeward wall followed the trend of CHTC for windward wall except with higher CHTC was observed for wider street canyon as compared to infinite long stand-alone building setting.

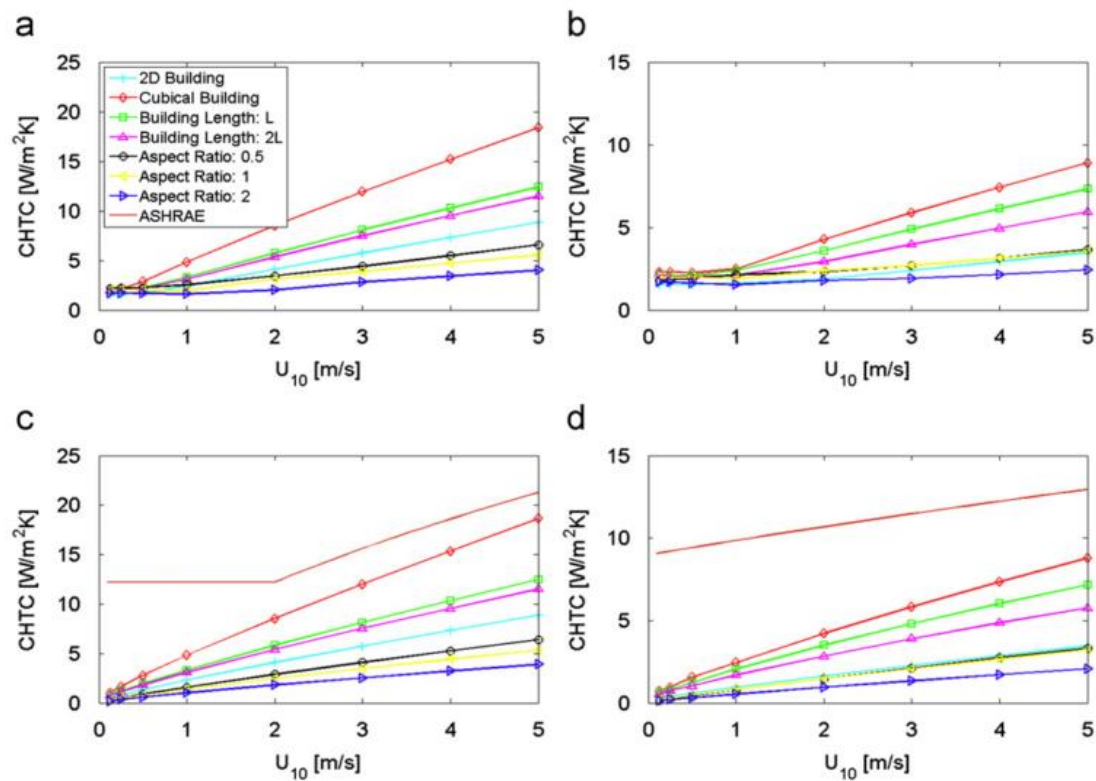


Figure 2.16 CHTC comparison between several urban configurations with and without natural convection settings (Allegrini et al. 2012)

Thermal environment in urban street canyon was investigated based on building aspect ratio, wind speed and air-surface temperature difference by using Reynolds-Averaged Navier Stokes (RANS) $k-\epsilon$ RNG turbulence model CFD simulation (Memon & Leung 2011). Results showed higher average temperature of the street canyon with higher aspect ratio, AR 2 as compared to lower aspect ratio, AR 0.5, by 0.6 K or 0.2 %. Another important finding was higher temperature found on the leeward side of the canyon as

compared to the windward side. Although it can be observed with air circulation from the windward side to the leeward airflow which can assist to reduce the temperature at the leeward side, consequently heat can still accumulate at the side. Authors stated that poor canyon configuration became the main reason of such effects during low wind speed condition. With higher aspect ratio, the penetration of direct solar radiation was expected to be reduced; however, the reduction in the convective cooling due to the configuration caused an increase in the façade temperatures. The contours of air temperature and air velocity are compared in Figure 2.17.

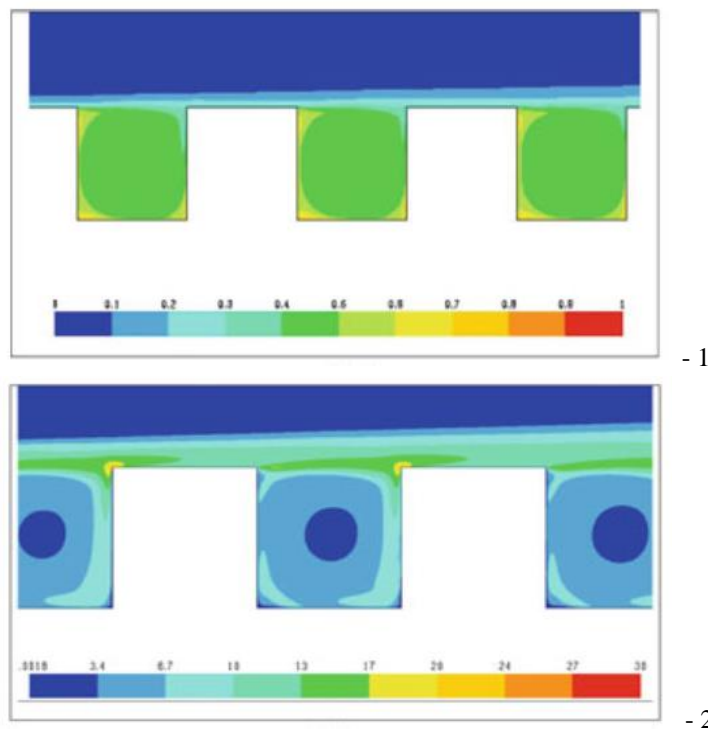
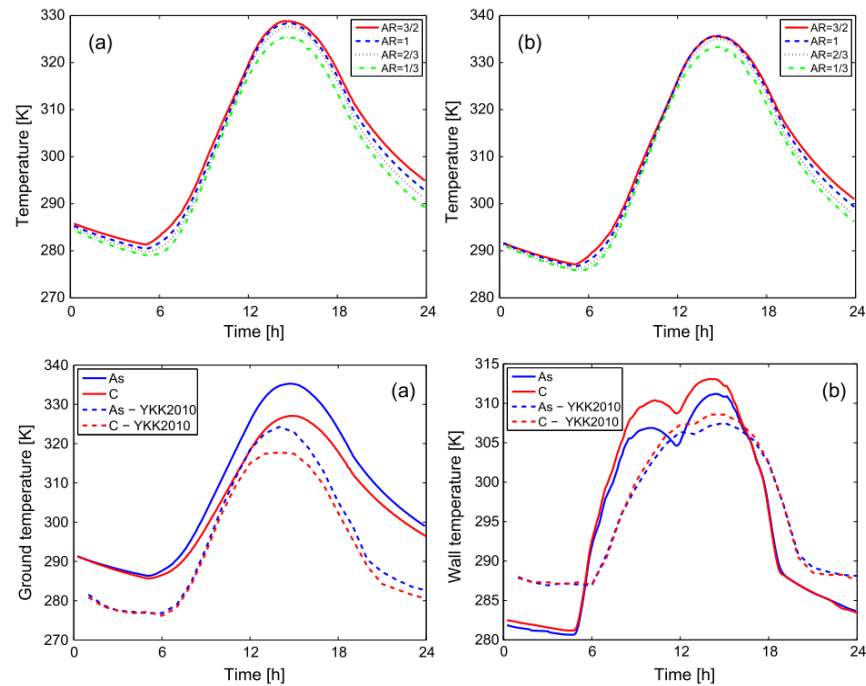


Figure 2.17 Contours inside urban canyon during even surface heating, showing higher temperature at leeward side as compared to windward side. Note that 1 - air temperature, 2 - air velocity (Memon & Leung 2011)

Four related urban parameters; urban aspect ratio, surface albedo, wind direction and wind speed were highlighted for the investigation of urban dynamic heat and flow field (Nazarian & Kleissl 2015). A matrix of 3×3 equally spaced cubes on a flat wall

boundary with a thick solid layer below the surface were used for the simulation. Additionally, the study highlighted the sensitivity of surface temperature with the variation of street canyon aspect ratio; see Figure 2.18.



As – Asphalt pavement; C – Concrete pavement, As – YKK2010 – Conductive Asphalt; C – YKK2010 – Conductive Concrete

Figure 2.18 Ground temperature comparing aspect ratio and materials (Nazarian & Kleissl 2015)

As Figure 2.18, in small aspect ratio; wall shadow was found neglected, and the canyon walls received maximum temperature in the morning and in the afternoon. In larger aspect ratio, wall shadow occurred on façade walls and asphalt ground surfaces. At this condition, both direct shortwave radiation and reflected diffuse radiation from ground have decreased, which causing maximum shortwave radiation obtained by the canyon at the time closer to solar noon. However, during the daytime, the temperature of ground surface for larger aspect ratio increased despite the shortwave radiation has reduced. Change of the asphalt ground surface to concrete ground surface reduced the temperature by 8 K, however there was an increase in the temperature of canyon façade walls up to 3.5 K.

2.2.2 Case studies of multiscale and non-generic urban canyon

For complex and multiscale urban canyon studies, research that is relevant to the investigation of urban heating commonly uses conventional measurement method for one or more measurement sites within the urban canopy layer. Typical urban geometries are not generic due to the complexity of symmetrical-asymmetrical building height, layout and form. In 2005, an investigation on outdoor thermal comfort was carried out within a Saharan old urban street canyon by conducting outdoor measurement of air temperature, air humidity, wind speed and shortwave-longwave solar radiation in several canyon aspect ratios with symmetrical and asymmetrical heights (Ali-toudert et al. 2005), see Figure 2.19.

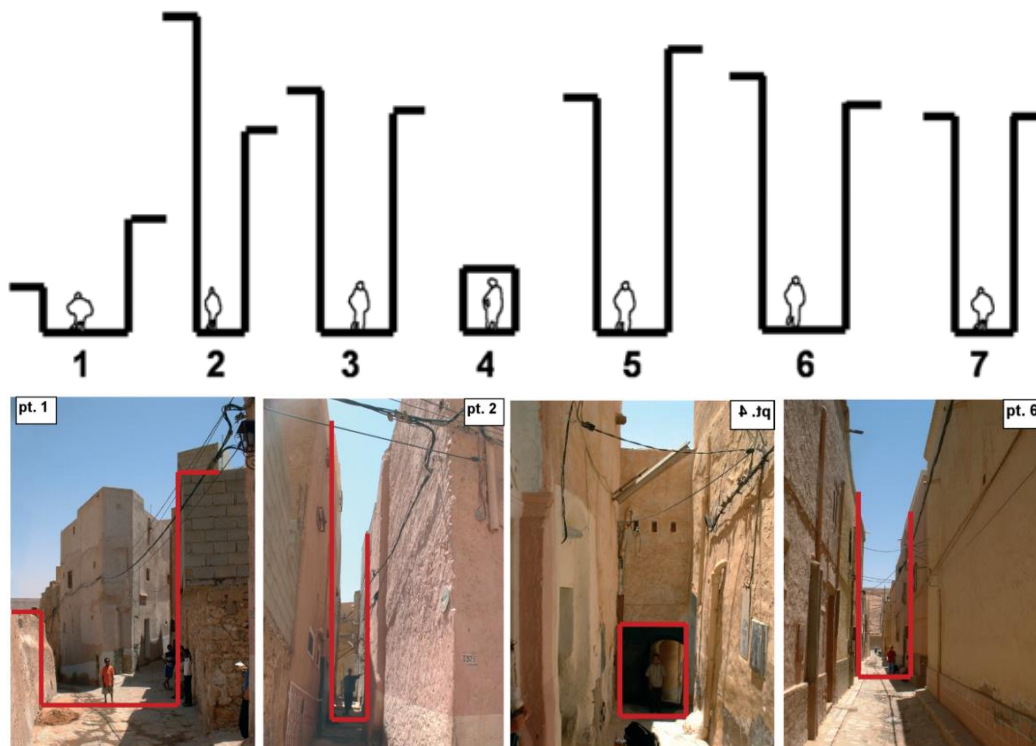


Figure 2.19 Selection of aspect ratio within the old Saharan city involved wide, narrow and enclosed types with symmetrical canyon height and asymmetrical canyon height (Ali-toudert et al. 2005)

In this work, the data collection was processed to evaluate Physiologically Equivalent Temperature (PET) index in determining pedestrian thermal comfort. Results suggested that deeper street canyon obtained more shadow effect than the shallow street canyon, resulting higher reduction in heat stress based on the explanation that less heat was absorbed by the human body within this urban configuration.

Earlier, a validated numerical model of Monte Carlo method against observational data collection was carried out to formulate the meteorological conditions of less windy night time for the case study of Granada city centre, Spain (Montávez & Jiménez 2000), resulting in a significant temperature gradient across streets by 4 °C rise in the air temperature at the canyon corners as compared to the canyon centre in the deepest canyons. Investigation on three Swiss city districts; Matthäues in Basel, Bellevaux in Lausanne and Meyrin in Geneva, were carried out by using Monte Carlo based simulation in PPF and RADIANCE to determine the correlation between urban morphology of complex urban environment and indicators of irradiation (Robinson 2006). The study concluded that full ability to model the irradiation should include latitude and reflectance to reduce error in average irradiation from 10 %.

Conversely, the Monte Carlo method for full model simulation was not suitable to be applied on environmental modelling due to nonlinearity and the complexity of the models (Ziehn & Tomlin 2008). Using high dimensional model representations (HDMR), global uncertainty and sensitivity analysis was investigated against full measurement method. Influence of meteorology and building topologies on airflow and turbulence patterns were carried out within the Gillygate street canyon in New York city, Gillygate (Ziehn & Tomlin 2008; Benson et al. 2008); see G3, G4 and Mast in Figure 2.20. The street canyon

aspect ratio in Gillygate was estimated to be 0.8. The measurement of wind speed and direction was conducted in 2003 with two anemometers which were attached to two street lamps 5.5-5.7 m above street level at ‘G3’ and ‘G4’. Additional anemometer was installed to a street lamp 19.5 m above street level at ‘Mast’ for background wind speed and direction. Using the measured data as boundary condition, a 3D simulation analysis was carried out using k- ϵ MISCAM by assuming a logarithmic and neutral stability wind at the inflow boundaries.

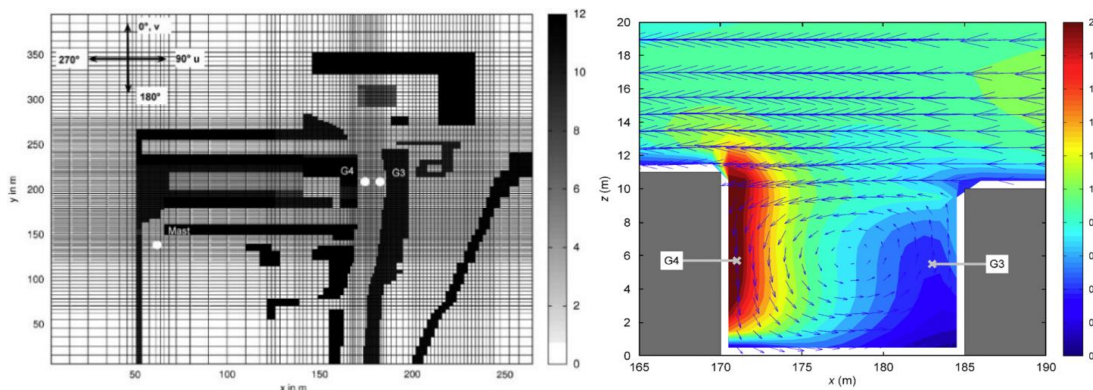


Figure 2.20 Location of wind speed and direction and the correlation between turbulent kinetic energy (TKE) at canyon surfaces (facades and ground) wind condition (Ziehn & Tomlin 2008; Benson et al. 2008)

Since 2000s, application of CFD numerical simulation to model heat flows within a complex urban environment becomes increasingly phenomenon due to its flexibility to model and to simulate various topologies and forms (Blocken, Carmeliet, et al. 2007). The best practice guideline for CFD simulation of urban flow details the method for the setup of the computational domain and boundary conditions (Franke et al. 2007). Previous work recommended that the prediction based on numerical CFD analysis requires validation with experimental data or measured data in order to assure the accuracy of the results (Toparlar et al. 2015).

The effects of local climate conditions on the façade and air temperatures within Singapore Central Business District (CBD) involving several locations of densely populated high-rise buildings and street canyon were investigated using both measurement and CFD analysis (Priyadarsini et al. 2008). Total region of 600 m × 400 m with the minimum building height of 24 m and the maximum building height of 250 m were studied and were modelled, see Figure 2.21. It was found that low wind speed within street canyon caused the increase of air temperature within the canyon as compared to higher wind speed. Also, the increased in the wind speed up to 35 % assisted to reduce the corresponding temperature by 0.7 °C. Another important factor to influence the microclimate condition within street canyon was the obtained air temperature up to 2.5 °C at the centre of narrow canyon with low albedo façade materials.

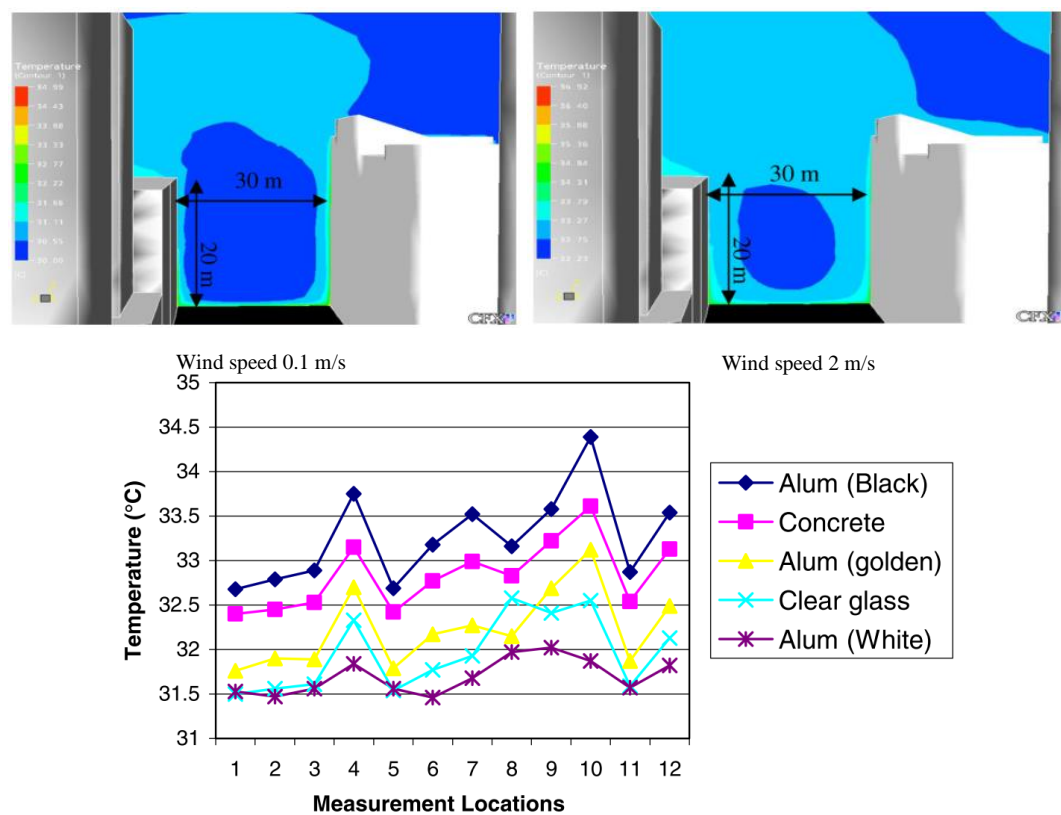


Figure 2.21 Impact of wind speed and albedo of façade materials on air temperature (Priyadarsini et al. 2008)

Approximation of air and surface temperatures was carried out using computational fluid dynamics (CFD) unsteady state RANS k- ϵ turbulent flow model (Ito et al. 2005) to determine the model precision by validating the measurement results taken on two types of urban street canyon configurations (wide and narrow) in Kyoto city, see Figure 2.22. The measurement of air and surface temperature was carried out between 10:00 hour and 16:00 hour on 24th August 2003.



1



2

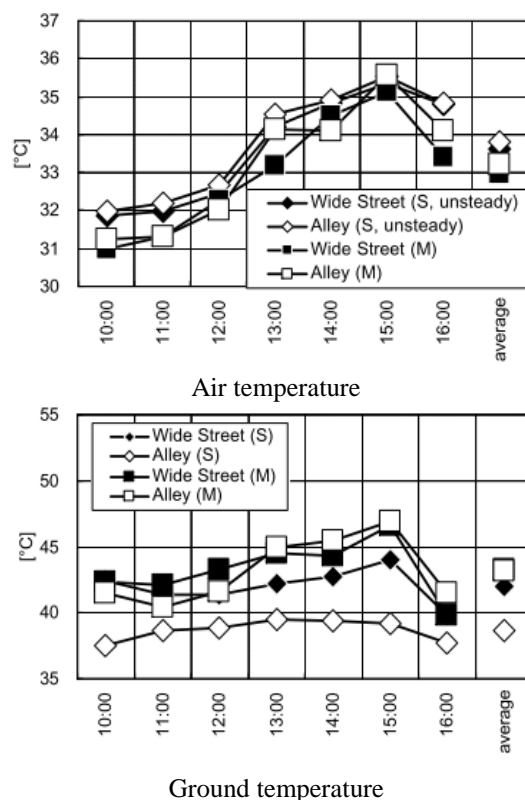


Figure 2.22 Thermal analysis of urban canyons; 1 – wide canyon, 2 – narrow canyon, demonstrating the validation of air-ground temperatures based on CFD prediction against data measurement (Ito et al. 2005)

Based on Figure 2.22, this study which most of the buildings are commercial with medium height; the measurement of the surface temperature was taken using a hand-held infrared radiation thermometer at 1.5 m above the ground level on hourly intervals. Overall, the validation results suggested that the numerical model predicted an accurate

simulation against the measured air and surface temperatures as the plotted graph of numerical model followed the plotted trend of the measured data. Additionally, it demonstrated that the predicted air temperature using numerical against measured data collection was more accurate than the predicted ground temperature. This was due to the model limitation to simulate real solar radiation and shadow.

An investigation of the Bergpolder region in Rotterdam was carried out using 3D unsteady RANS k- ϵ realizable turbulence CFD simulation with boundary condition based on hourly meteorological data provided by KNMI database including wind speed, wind direction, air temperature and solar radiation (Toparlar et al. 2015), see Figure 2.23.

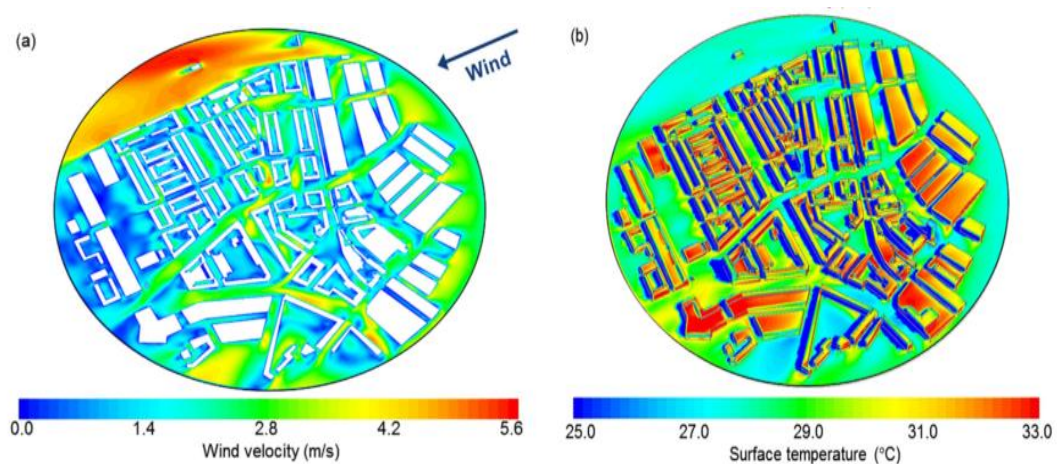


Figure 2.23 Low wind speed reduced the cooling effect from ground surfaces. This condition was found within the street canyon that was perpendicular to the predominant wind direction (Toparlar et al. 2015)

The simulations as Figure 2.23 were carried out on 15-19th July 2006 based on the specified meteorological data with on average 7.9 % difference with the experimental data (minimum difference of 0.3 % and maximum difference of 24.2 %). The simulation results highlighted the correlation between UHI effect and predominant low turbulent heat transport in the direction perpendicular to the length of a street canyon. Results also

found that the predominant cross-canyon condition reduced the ventilation cooling effect near ground surfaces which encouraged more heat to release from the surface.

Simulations of air patterns across an area of Gazi, Greece were investigated, revealing thermal discomfort issues and wind effects at some particular spots (Stavrakakis et al. 2012). Using architectural interventions such as physical and artificial shading devices and cool materials, the study reported that the reduction in mean air temperature by 1.5 °C can reduce up to 20 % thermal discomfort which was equal to 12 °C reduction in mean surface temperature. Figure 2.24 shows the comparison of surface absorbed IR radiation in top view before and after the architectural interventions. The hot colour contours represented higher radiation and the cold colour contours represented lower radiation.

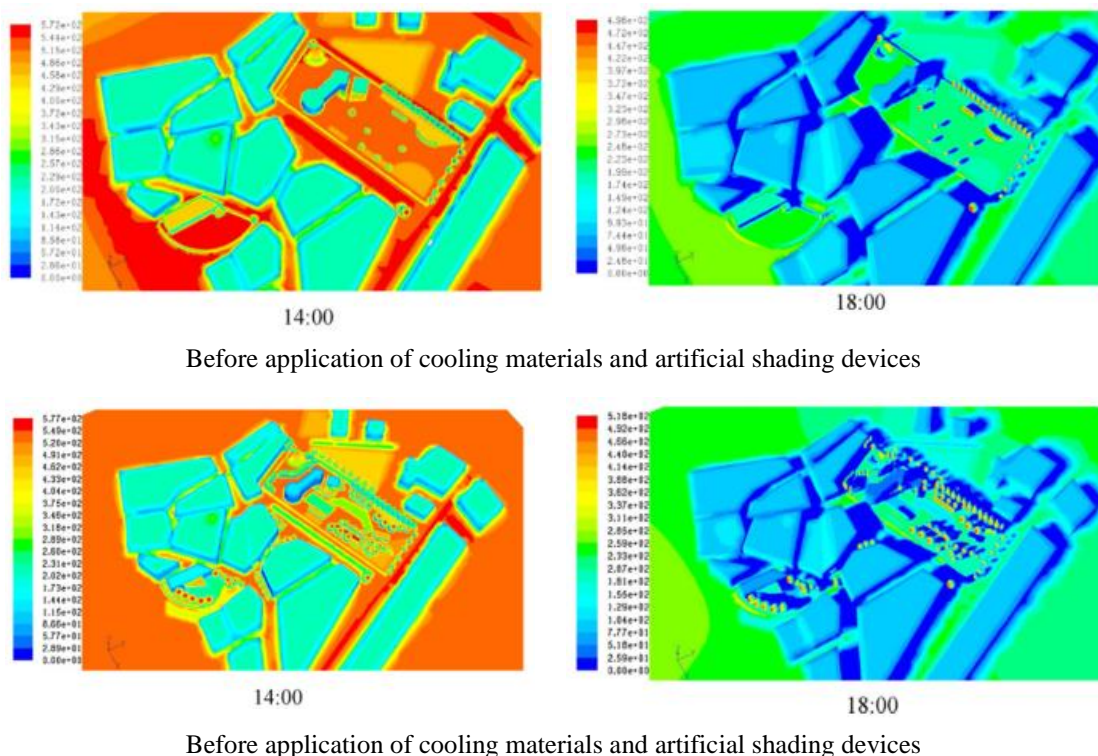


Figure 2.24 Reduction in surface IR radiation with the application of cooling materials and artificial shading devices (Stavrakakis et al. 2012)

2.3 Research and development of RPSC system for UHI mitigation

Further explanation from Chapter 1 Section 1.2 which discussed on the application of RPSC system as a UHI mitigation strategy will be detailed in this section based on the available research and development of the system. A solar collector system which utilises road pavement as the main solar absorbing element is designed to mitigate excessive road surface temperature from indirect effect to the nearby air temperature besides to prolong its lifecycle (Loomans et al. 2003). The system works by the process of heat transfer received from the surface of road pavement based on direct and indirect solar radiation. Subsequently, the absorbed temperature or heat will be transferred downward, to be received by the pavement layer(s) via conductive materials and also to be received by the embedded hydronic flow pipes in between the pavement layers (Al-Saad et al. 1994).

Examples of the system prototypes are shown in the Figure 2.25 below. Adding to the function of the system, in this thesis to be termed as ‘Road Pavement Solar Collector’ (RPSC) system, previous research also found the potential of using RPSC for its indirect application on UHI mitigation (Mallick et al. 2009) and for future energy harvesting (Wang et al. 2010; Shaopeng et al. 2011).

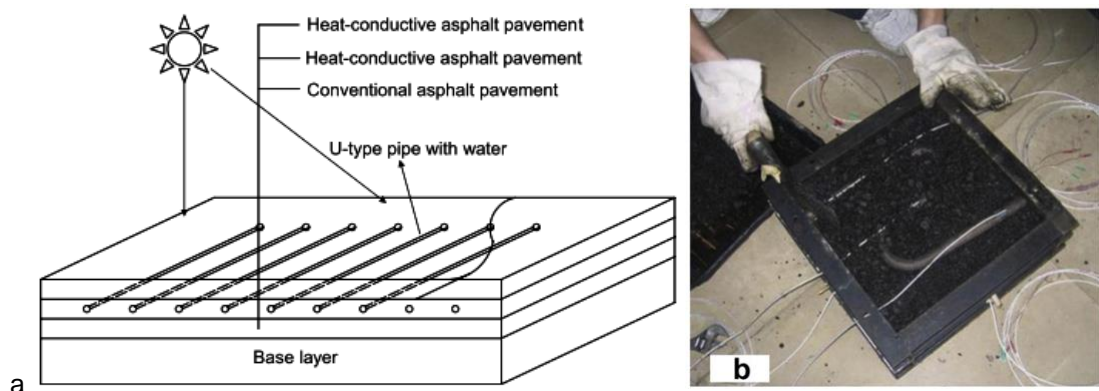


Figure 2.25 Example of hydronic pavement solar collector proposed by (a) (Wang et al. 2010; Shaopeng et al. 2011) (b) (Wang et al. 2010; Shaopeng et al. 2011)

2.3.1 Effect of high surface temperature on outdoor environment

Earlier investigations focussed on the impact of high and excessive road pavement temperature on the surrounding environment. An investigation of pavement heating on hot humid climate city, Singapore, highlighted several various impacts on its outdoor thermal environment according to pavement types (Tan & Fwa 1992), see Figure 2.26.

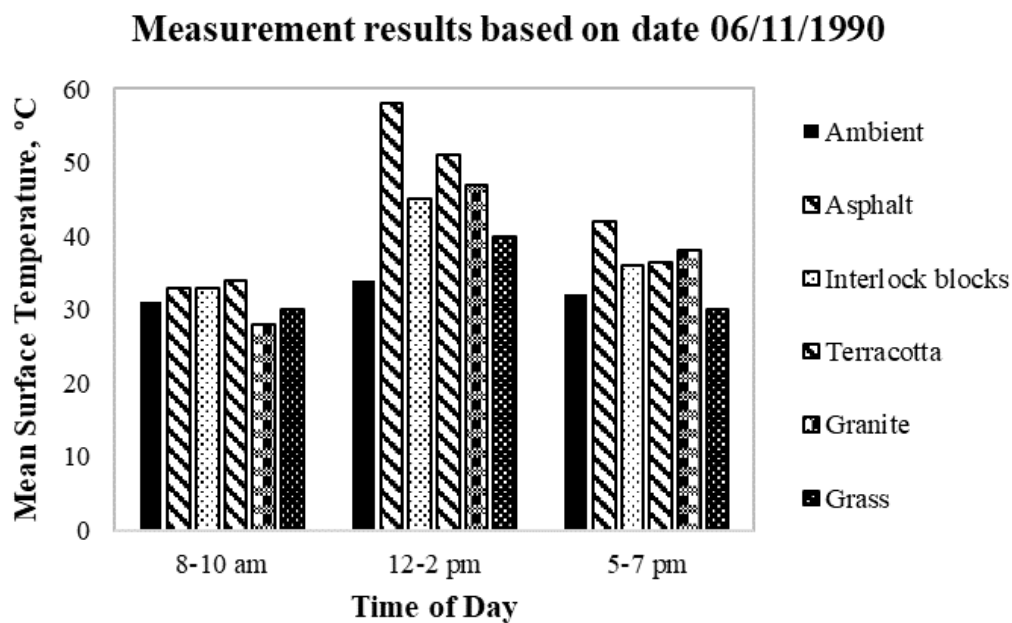


Figure 2.26 Comparison of mean surface temperature between several tested pavement surfaces showed asphalt pavement scored highest (Tan & Fwa 1992)

In Figure 2.26, mean surface temperatures were measured based on morning, noon and evening hours. Based on the measurement, results showed that asphalt pavement has the highest temperature among other pavement types during noon and evening hours and to be closely followed by terracotta and interlocki blocks. It was recommended that the dark asphalt pavement should be replaced with low absorptive and less dark pavements.

Similarly, investigation of radiant temperature was conducted on several types of surface materials (pavement and roofing) in the city of Tel Aviv, Israel (Chudnovsky et al. 2004). Based on the results, it was found that both asphalt roads and rooftops became the warmest urban elements, approximately 10 °C temperature difference during early noon hours with the least warm urban element which was tested in the study (concrete light); see Figure 2.27.

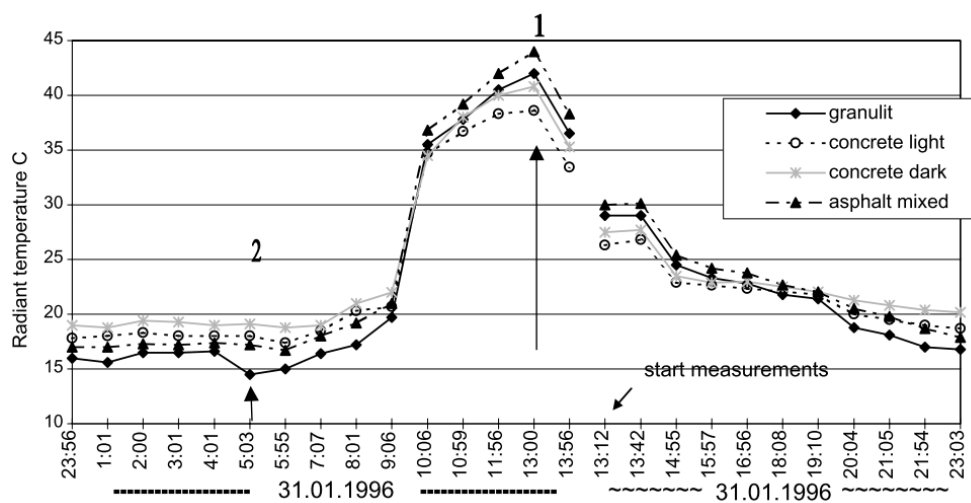


Figure 2.27 Comparative analysis between asphalt, concrete and granulate pavements have shown asphalt pavement obtained high mean surface temperature during early noon hours (Chudnovsky et al. 2004)

Another field measurement study was carried out to investigate the effects of pavements to the outdoor thermal environment, case study of winter and summer in subtropical city of Taiwan (Lin et al. 2007). The measurement focussed on a large area that far from the shadow effects of trees and buildings, see Figure 2.28. In Figure 2.28(b), results demonstrated with high correlation between the surface temperatures and air temperature, followed by globe temperature, solar radiation and wind velocity. This means higher surface temperature caused the increase in the air temperature. Results also found that

during noon hours in the summertime, asphalt and concrete pavements have affected the air temperature more than in the winter time and more than other pavement types.

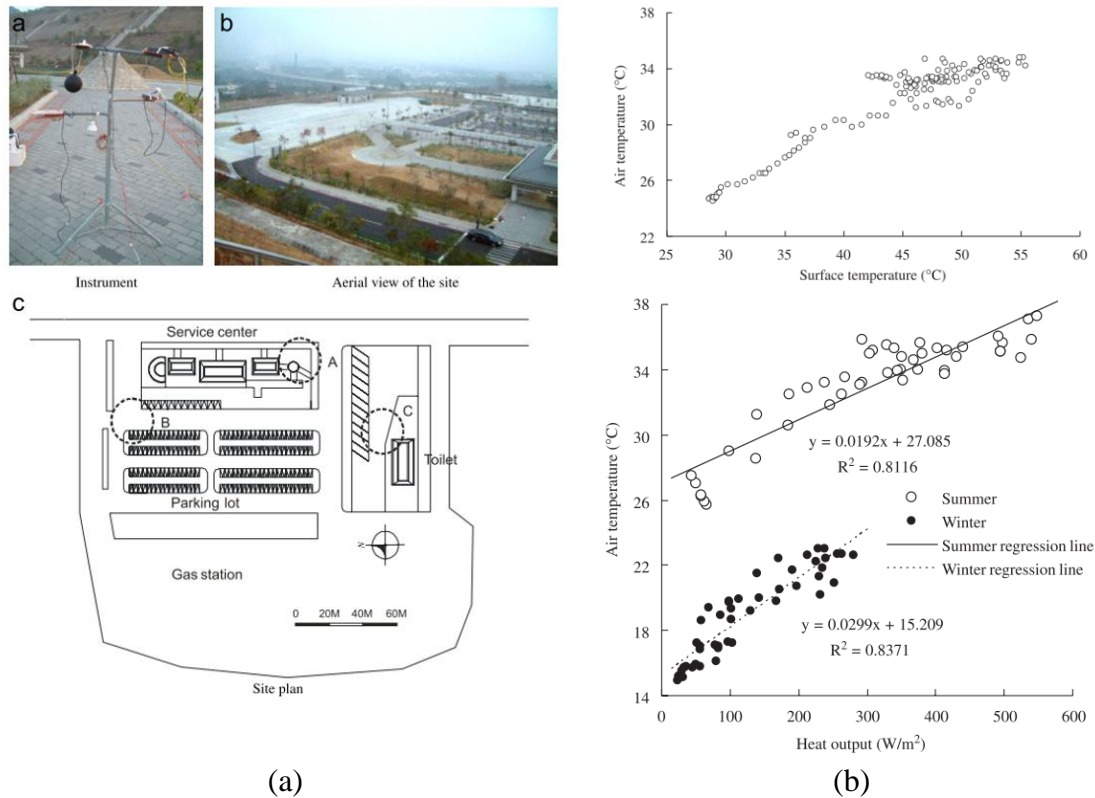


Figure 2.28 Investigation on surface temperature comparing several pavement types during summertime and winter time, with (a) shows method and site view and (b) shows the effects on air temperature and heat output (Lin et al. 2007)

It was found that slab surface temperatures are mostly higher than ambient air temperatures but the difference between the aforementioned temperatures varies according to time (Qin & Hiller 2011). Based on the comparison of the pavement temperatures in Los Angeles with the pavement temperature in Reno, it was highlighted that the maximum temperature difference between top and bottom slab during daytime was in the positive values for both cities and vice-versa for the values in the night-time; see Figure 2.29.

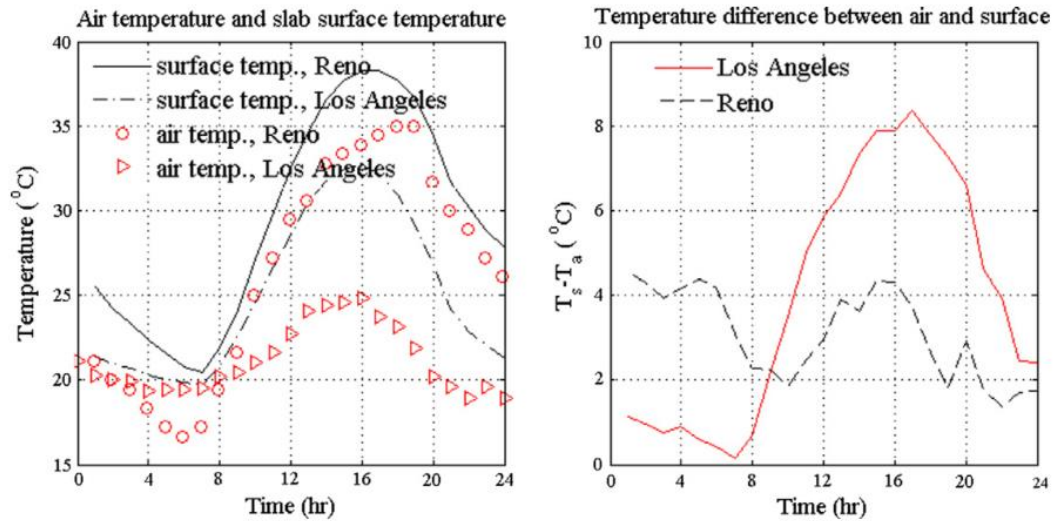


Figure 2.29 Correlation between surface temperature and air temperature of tested pavements between two cities showed the temperature difference varies according to time with positive difference during daytimes (Qin & Hiller 2011)

2.3.2 Effect of flowing pipes on pavement surface and surroundings

In 2006, a combined experimental and simulation study was carried out to investigate the effectiveness of an RPSC system based on a proposed prototype termed as ‘RTEC’ for its application in fighting against UHI effect during the summertime of Tokyo city, Japan (Hasebe, M, Yamikawa, Y and Meiarashi 2006), see Figure 2.30.

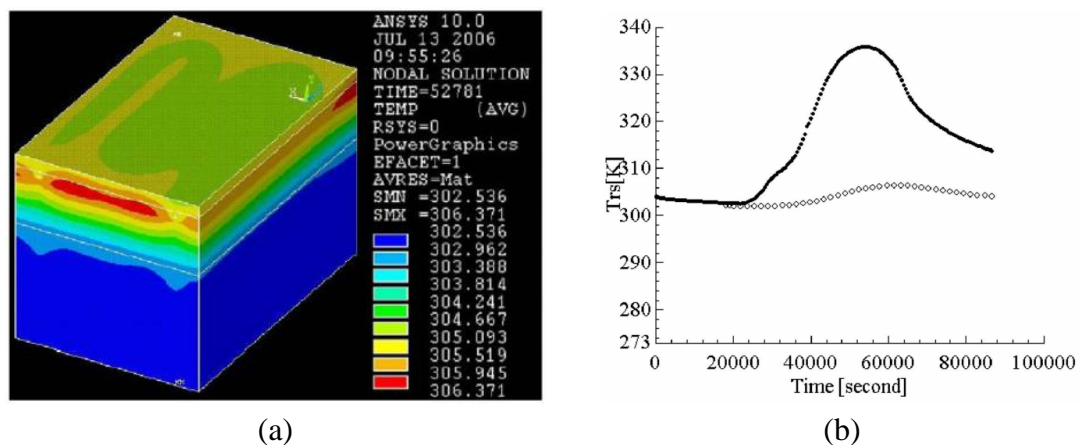


Figure 2.30 RTEC investigation for pavement excessive temperature mitigation; (a) shows distributed pavement temperature with RTEC and (b) shows temperature reduction with RTEC (Hasebe, M, Yamikawa, Y and Meiarashi 2006)

The system operated based on the circulation of water pumped from the storage into the pipe layout embedded in a heated pavement. It was expected that the final temperature of the circulating water was higher than the inlet water temperature. Based on the simulation results in see Figure 2.30, it was found that the application of RTEC system can potentially reduce the heated pavement surface by a maximum as 30 °C.

Investigation on the efficiency of tubes embedded within an asphalt pavement as a medium of heat transfer within the estimation of 365 days was carried out using simplified simulation modelling (Loomans et al. 2003), see the estimated results in yearly basis as shown in Figure 2.31. The model classified three important layers; (i) surface layer, (ii) layer where heat extraction tubes are embedded, and (iii) remaining pavement layers. Based on Figure 2.31, results highlighted that the highest potential application of using this RPSC type was during high solar radiation (summertime) which encouraged high thermal energy to be obtained by the system based on high surface temperature.

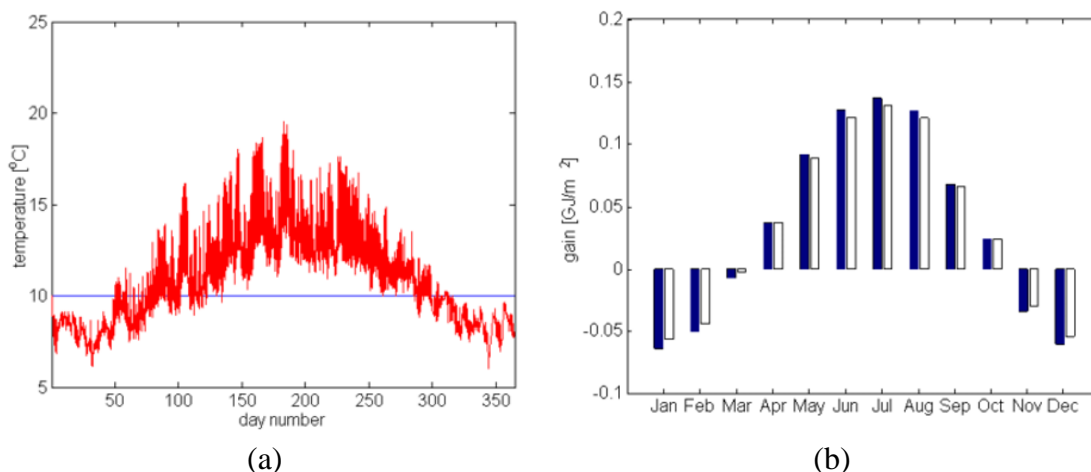


Figure 2.31 Estimated yearly thermal gain based on temperature gain showed the optimum values were during summer months (Loomans et al. 2003)

A similar RPSC concept was introduced in the study of (Mallick et al. 2009) by using laboratory and field testing. Based on the experimental results shown in Figure 2.32, it showed that the reduction in the surface temperature with the flowing water was 10.8-20.8 °C with a noticeable reduction in the near air temperature that was measured 0.1 m above the surface level.

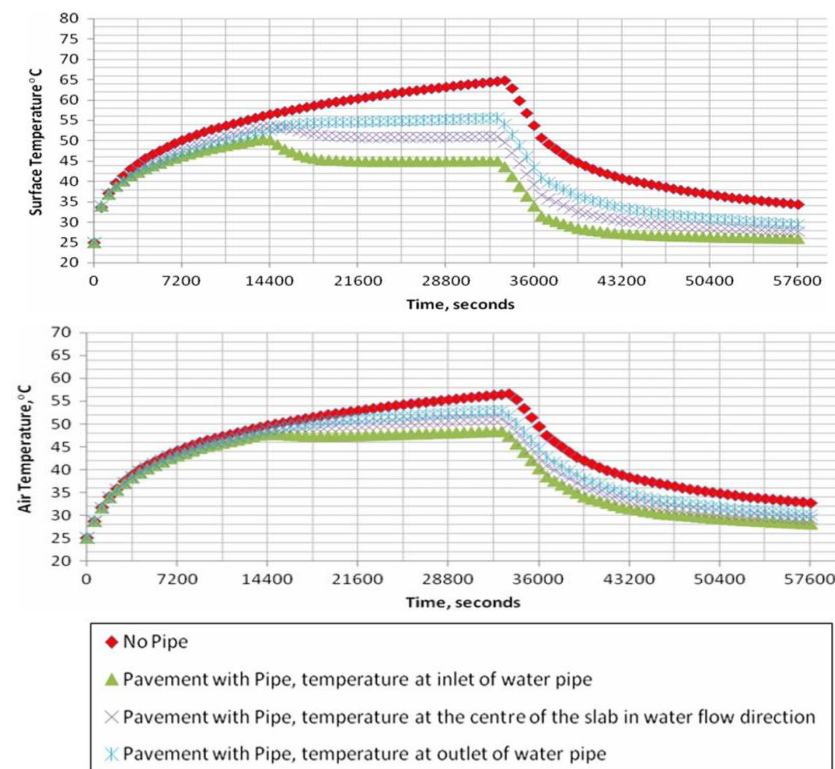


Figure 2.32 Correlation between surface temperature before-after the flowing water and air temperature showed the influence of low surface temperature to reduce air temperature above 0.1 m from the surface (Mallick et al. 2009)

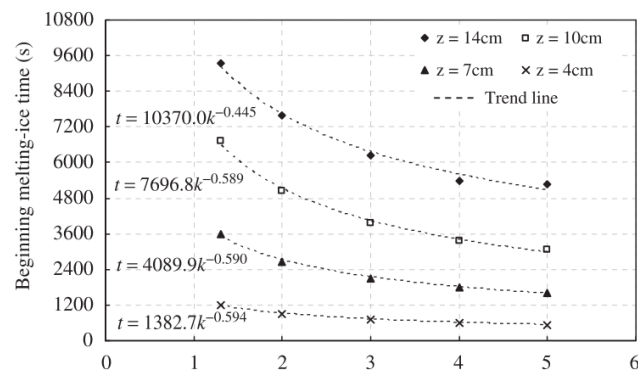
2.3.3 Effect of system adjustment on extreme weather condition

The effects of changing parameters were investigated for the system performance in reducing excessive temperature from the pavement surface during extreme weather condition to avoid the pavement from poor physical effects. In 2013; a laboratory prototype was tested to determine the system performance in terms of surface temperature reduction, showing the efficiency of the reduction approximately 75-95 % (Pascual-

Muñoz et al. 2013). Embedment of pipes was carried out at several different depths to determine the optimum impact of circulating water on determining the area of surface temperature reduction according to the depth (Chen et al. 2011), see Figure 2.33. This study was investigated during winter time, which RPSC system was also used for snow-melting. According to the results, it was found that deeper pipe embedment (in this case was embedded at bottom layer) took 0.5 hour more in terms of snow-melting despite that the conductivity of the pavement materials was maximised to 5.0 W/m °C as compared to the embedment at the middle layer. This study suggested that the optimum reduction can be achieved with the pipe embedment between 40 mm and 100 mm below the surface.



(a)



(b)

Figure 2.33 RPSC system used to fight against extreme weather during winter time. Figure (a) shows the embedment of serpentine pipe. Figure (b) shows the snow-melting time according to the embedment of pipes (Chen et al. 2011)

Apart from the adjustment of the pipe embedment, investigations on changing the gap between RPSC pipes were also highlighted. A laboratory experiment work found that the feasible gap between the pipes should be between 180 mm and 400 mm (Chen et al. 2011). Another experimental work highlighted three sizes of pipes gap; 90 mm, 120 mm and 150 mm (Gao et al. 2010). Results suggested that smaller gap between pipes caused higher

water flow rate can be obtained by the pipes, which reduced more temperature from the pavement surface; see Figure 2.34.

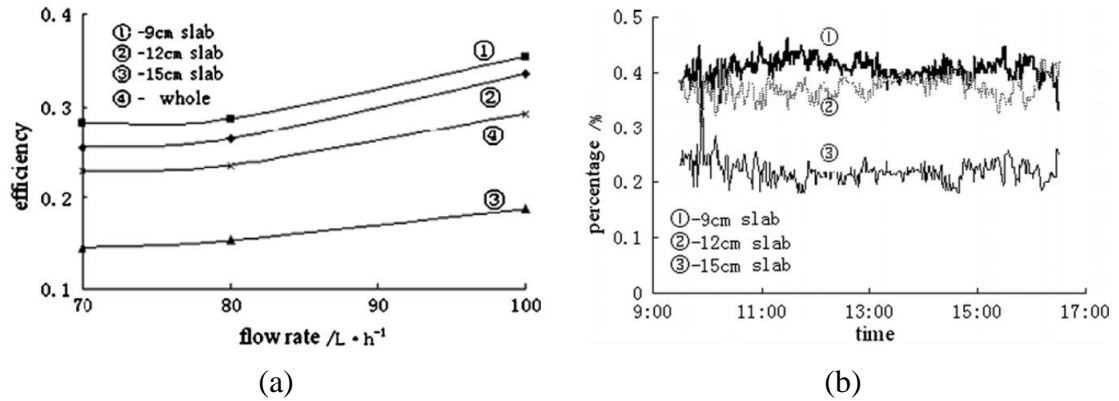


Figure 2.34 Correlation between the set gap between pipes, water flow rate and surface temperature (a) shows highest RPSC efficiency with smallest pipe gap, and (b) shows consistency in high heat collecting capacity with 90 mm (Gao et al. 2010)

Laboratory investigation of changing water flow rate in RPSC system was investigated by comparing two significant flow rate values, which is between 54mL/min and 1886mL/min with initial slab surface temperature was 38.48°C (Shaopeng et al. 2011). Based on the experiments, it was found that the surface temperature drop obtained from the changing flow rate from 54mL/min to 1886mL/min was insignificant, which was 1.87°C, see Figure 2.35.

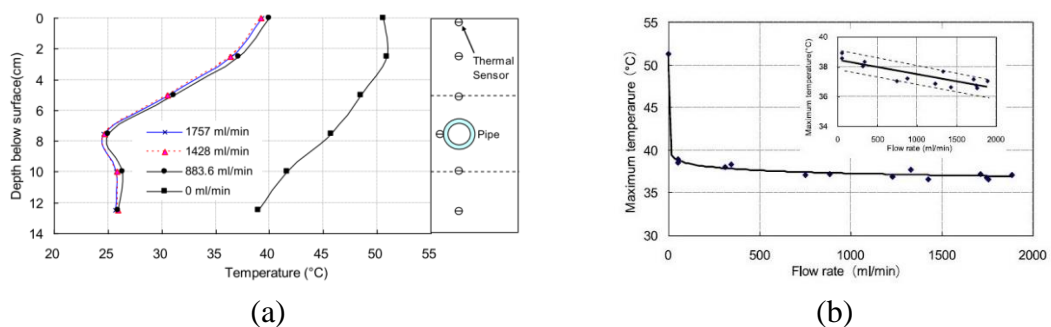


Figure 2.35 Significant effect was found in the reduction of pavement temperature when (a) comparing with and without pipe layout and vice-versa when (b) comparing two large difference flow rates (Shaopeng et al. 2011)

Another investigation based on the changes in the inlet temperature of the circulating water inside pipes was carried out to determine the rate of heat extraction from the pavement surface (Shaopeng et al. 2011). Based on the investigation, results demonstrated that high reduction in the inlet temperature set for the circulating water can potentially increase the amount of thermal collection extracted from the pavement surface, thus indirectly increases the effectiveness of the system, see Figure 2.36(a). Nevertheless, when the pipe embedment also interacted with the adjustment of the inlet temperature, it showed with larger temperature difference between the inlet water temperature and the circulating water temperature at 300 minutes, see Figure 2.36(b). At 300 minutes, equilibrium of the temperature was achieved. Overall, the use of cold water temperature is required to maximise the Delta T.

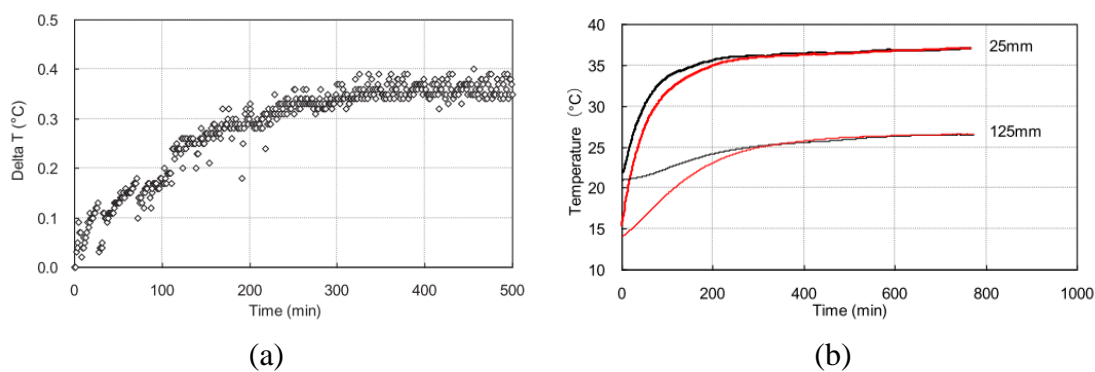


Figure 2.36 The effect of change in the inlet temperature from high to low according to transient test (a) Delta T according to time (b) surface temperature according to inlet temperature (Shaopeng et al. 2011)

Investigation on thermal collection based on the beginning of time for water circulation inside pipes was carried out at a similar initial water temperature, 20 °C (Shaopeng et al. 2011). The first experiment was conducted with an asphalt slab that was radiated for 6 hours before the water was circulated into the pipes inside the pavement. Results based on the experiment showed with 12.4 °C temperature reduction was obtained from the

heated slab after the water circulation. The second experiment was conducted with the similar type of asphalt slab that was radiated for 6 hours simultaneously with the circulating water. Results showed with 19.35 °C temperature reduction from the slab after the water circulation; suggesting the second experiment was more effective in terms of pavement temperature reduction according to time. Figure 2.37(a) and Figure 2.37(b) show the comparison between the two settings.

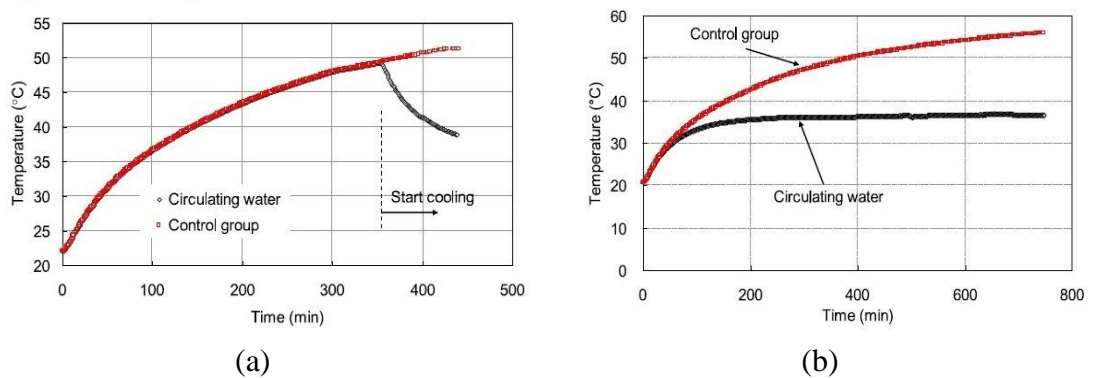


Figure 2.37 Correlation between the beginning of the time for water circulation and the obtained temperature difference, Delta T (a) after 6 hours surface radiation (b) with the beginning time for the 6 hours radiation (Shaopeng et al. 2011)

Investigation on the performance of laboratory asphalt pavements was carried out by comparing higher thermal conductivity to lower thermal conductivity based on the system application for winter time (Chen et al. 2011). In this study, graphite was used as additive material contents in the middle layer of asphalt which to increase the conductivity of an asphalt pavement, termed as 'Conductive Asphalt Concrete' (CAC). Based on the experimental results, it showed with more effective when CAC was used as compared to the low conductive asphalt in terms of snow-melting time; see Figure 2.38.

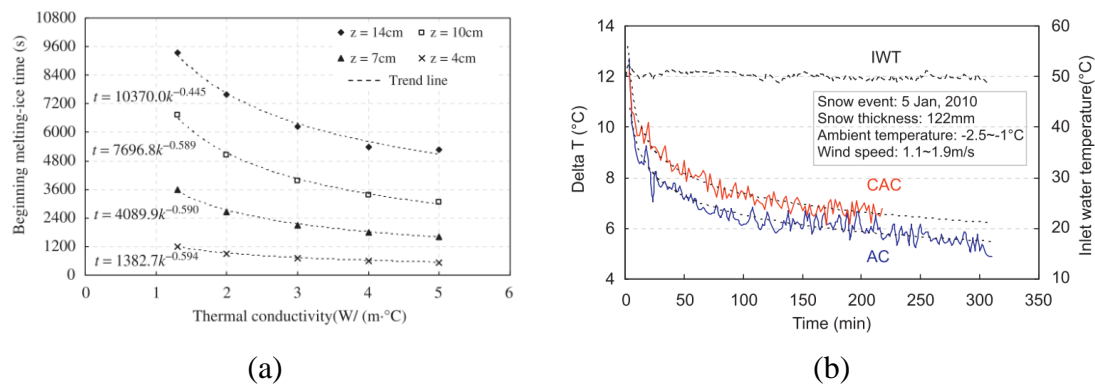


Figure 2.38 Correlation between material conductivity and the effectiveness of RPSC in terms of (a) the beginning of melting time (b) comparison of Delta T between AC and CAC (Chen et al. 2011)

In summary, enhancement in the system parameters seems promising to optimise the performance of the system against extreme weather conditions (Shaopeng et al. 2011). However, results based on the experimental setup requires further investigation which includes realistic outdoor parameters due to complex urban built form, solar heat flux and wind conditions (Tian et al. 2007).

2.3.4 Case studies of using hydronic pipes for thermal energy collection

The application of hydronic pipe systems with the embedment of pipe in the middle of road pavement layer was highlighted to be potential as an alternative system as a renewable energy system via the use of solar radiation and ground heat. Early research found the correlation of the system application for potential fuel saving (Vasiliev 1988). The system was proposed as an alternative way to support a non-nuclear energy research and development programme established by the Commission of the European Communities (Vasiliev 1988). Among important research under the commission is to encourage large commercial greenhouses to be designed with underground heating and combined use of alternative energy sources, heat recovery system and organic fuel.

One prototype was developed via the concept of Ground-Source Heat Pump (GHSP); which the system connected heat exchanger with an underground soil thermal storage (Chiasson & Spitler 2001), see Figure 2.39. The underground thermal storage was proposed to maximise the use of the system across the seasons, which to collect the solar energy during the summertime due to high solar intensity and to reduce the effect of snow on road pavement during the wintertime. The GHSP system is connected to a bridge deck that was used as a solar energy collector. The use of bridge deck is to maximise the amount of absorbed heat from the solar radiation, which was found more efficient in terms of the heat collection than the use of Ground Loop Heat Exchanger (GLHE). The research was conducted to design such system for the bridge deck of the Interstate highway in Oklahoma.

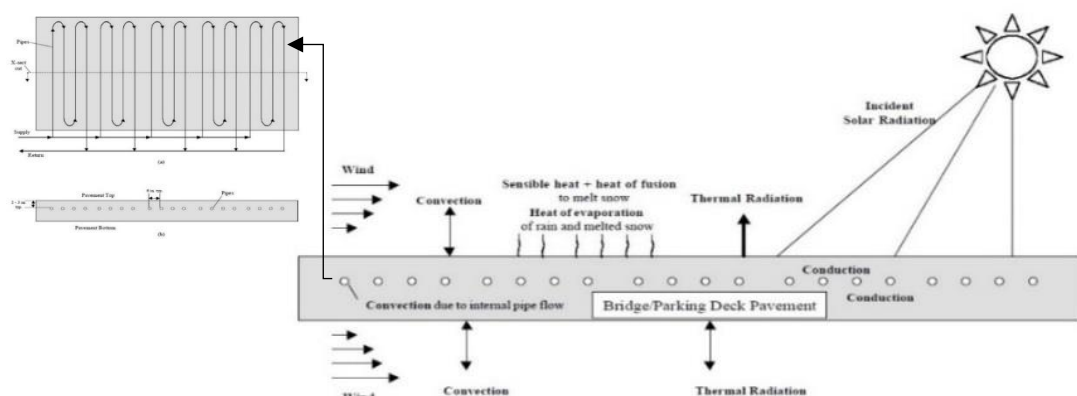


Figure 2.39 Example of the system prototype combined GHSP, bridge deck and ground soil thermal storage (a) plan view (b) cross section view (Chiasson & Spitler 2001)

In the study of (Utlut et al. 2014), Hybrid Renewable Heating System (HRES) was proposed as a comprehensive system which utilises solar radiation as the main component and has the combination of heat pump or wind turbine for generating electricity, see Figure 2.40. This study also highlighted the importance of solar radiation to assist the function of ground sourced vertical and horizontal heat pump, geothermal heat pump, combined

solar-energy sourced HRES and heat storage system. Like the previous system, the principle of the hybrid system is to provide adequate supply from high solar radiation during summer season to fulfill the demand for winter season.

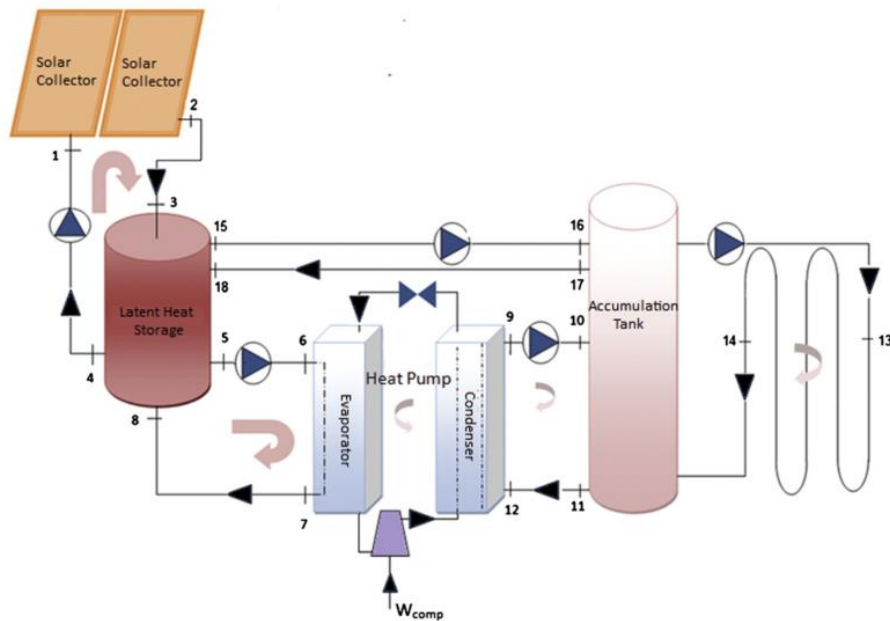


Figure 2.40 Comprehensive heating system which utilises solar radiation as the main component of the energy generation (Utlu et al. 2014)

2.4 Summary

The current literature highlighted the concern of excessive heat within urban compound, to be known as 'Urban Heat Island' (UHI) effect and how the UHI effect can be mitigated. Several points have been summarised to highlight the contribution of the literature to the theoretical background and methodology of this thesis:

1. The occurrence of UHI effect has been caused by the process of urbanisation which includes (i) modified urban environment and climate condition due to more impermeable urban materials are used with complex and dense urban built forms; and (ii) the increase in urban activities that causes more anthropogenic heat has been released, thus promoting air pollution.
2. The process of shortwave-longwave solar reflection in between vertical facades of urban canyons assists in delaying the reflection of the shortwave and longwave heat fluxes from and to the sky and the reduction in wind velocity, thus increasing the air temperature concentrated within the urban compound specifically urban canyon.
3. Extensive studies using CFD modelling to investigate the effect of urban street canyon on the air-surface temperature were used due to its capability to model huge microclimate urban scale.
4. Excessive surface temperature was found to significantly affect the near air temperature, thus indirectly causes the elevation of UHI effect.
5. Using hydronic Road Pavement Solar Collector (RPSC) system was proposed for surface temperature reduction and near air temperature reduction.
6. System optimisation based on the previous design parameters was proposed due to the benefit the potential thermal collection through outlet-inlet temperature difference, Delta T.

2.5 Research gap

Based on the review of UHI effect associated with urban configuration specifically street canyon and UHI mitigation techniques, there is insufficient information on:

1. Applying RPSC system for more realistic condition. Coupling urban street canyon configuration with the RPSC system will lead to more significant analysis, which urban built forms can cause wind-blocking, low convective cooling, shadow effect and solar refraction. Urban street canyon in a realistic condition can be configured:
 - a. Based on almost symmetrical building height facing each other
 - b. Based on shallow and deep canyon due to the increased height
 - c. Based on asymmetrical building height facing each other
2. Performance of RPSC system in reducing surface temperature based on Delta T and potential temperature collection within urban compound.
3. Performance of RPSC system in different urban canyon configuration in reducing near-air temperature
4. Parameter adjustment of the RPSC system to evaluate the system performance in maximising/minimising surface area of temperature reduction as well as maximising/minimising the system flow rate for the similar reason.

CHAPTER 3

Theoretical background

3.0 Introduction

In this chapter, the theoretical background including an energy balance of the urban environment is presented, highlighting the influence of the urban built form in determining the urban air-surface temperatures and the rise in UHI effect (see Section 3.1). In Section 3.2, the mathematical equations of heat transfer mechanism in urban surfaces involving radiation, convection and conduction effects are detailed. The process of heat transfer between the above pavement surface and the underground pavement layers is also detailed in this section. In sub-section 3.3.3, the application of hydronic RPSC system is described and correlated with the conduction and the convection process between pavement, pipes and water in the pipes.

3.1 Theoretical effects of urban landscapes on urban atmosphere

The process of urbanisation causes the changes in surface and atmospheric properties due to the transformation of thermal, moisture, radiative and aerodynamic characteristics (Oke 1987a). Within a dense urban area, heat is excessively stored, and the urban surfaces are often waterproof. The block-like geometry creates the radiation trapping and air stagnation apart from becoming rough surface. Three main consequences to be occurred with the existing urban buildings and skyscrapers are described theoretically in Section 3.1.1, 3.1.2 and 3.1.3.

3.1.1 Urban surfaces receive low solar radiation due to shadow

Solar radiation in the canyon streets are complicated by the change in horizon which affects the duration of the illumination and sunshine. Radiative interactions between building facades in the canyon streets and between buildings have possibly occurred. The interaction has to be related to the height of the buildings, H width of the canyon street, W and the street azimuth, ϵ (Landsberg 1981), see Equation 3.1 and Equation 3.2 below:

$$\text{Index of narrowness, } N = H / W \quad \text{Equation 3.1}$$

$$\text{Angle of horizon created by building line, } \tan \sigma = N \quad \text{Equation 3.2}$$

The relationship between street azimuth, angle of horizon and street narrowness is described in Table 3.1 .

Table 3.1 Relationship between street azimuth ϵ , angle of horizon σ and street of narrowness, N (Landsberg 1981)

ϵ	N				
	0.2	0.5	1.0	2.0	5.0
0	11.3	26.0	45.0	63.4	78.7
20	10.7	25.2	43.2	62.0	78.0
40	8.7	21.0	37.5	56.8	75.4
60	5.7	14.0	26.6	45.0	68.2
80	2.0	5.0	9.9	19.3	41.0

ϵ is determined based on the southerly and westerly azimuths. Thus, the horizon of the buildings influences by retarding the sunrise and advance sunset to the street dwellers and to reduce the illumination and the radiation of the sun to them. The depth below the roof line in terms of the canyon width has a major influence on determining the percentage loss of the sky radiation and illumination (Landsberg 1981). Based on the relationship in Table 3.2, the illumination loss increases when the ratio of depth below roof increases.

Table 3.2 Percentage loss in illumination by street canyon ratio (Landsberg 1981)

PERCENTAGE LOSS IN ILLUMINATION AND RADIATION CAUSED BY CANYON STREET HEIGHT AND WIDTH	
<i>Ratio of depth below roof line</i>	<i>Percentage loss in illumination, %</i>
0	50
0.25	58
0.5	65
1	75
2	85
3	90
4	92

It was highlighted that urban areas receive less sunshine as compared to the surroundings due to the turbid layer of pollutant 10-20 % (Landsberg 1981). The amount of energy flux in an urban canyon is determined based on the solar elevation from the ground. With lower solar elevation, especially in winter and autumn, the loss in the urban energy at the

ground was found greater, especially in the early morning and in the late afternoon hours. In summer and spring, the dispersal of the pollutants increases with high contribution of convection, thus radiation loss is reduced.

3.1.2 Heat reflection from sunny walls

Under cloudless sky and almost no wind conditions, advection effect Q_A (by forced convection) is neglected and anthropogenic heat release Q_F is assumed to be included within surface heat storage, ΔQ_S . During this condition, it is obvious that the energy flux of the canyon surfaces increases according to the zenith angle of the solar radiation. The peak irradiation was observed at the middle of the day meanwhile shadow takes place at east-facing walls after midday. At night, net long-wave radiation from all canyon surfaces was observed to be relatively small. However, some portion of cold sky radiative will be replaced by canyon surfaces that are much warmer (Oke 1987a). The characteristics of an urban canyon and weather conditions within play important roles to influence the energy budget within the canyon, thus has complicated its energy balance. For example, higher canyon aspect ratio causes the changes in the solar radiation either in penetrating into or in escaping out of the canyon. Meanwhile, higher albedo materials help in increasing the reflection of the flux out of the canyon.

As mentioned in Section 2.2, the total unit of simplified canyon surfaces is calculated based on three sides with active surfaces which contain walls and floor, and three open sides which includes an imaginary lid near roof level and two imaginary enclosed walls at both ends of the canyon. The energy exchanges inside a canyon are based on the energy balance calculated for walls and floor, respectively as stated in Equation 3.3 and Equation 3.4 (Landsberg 1981; Oke 1987a).

$$\text{For walls, } Q^* = Q_H + \Delta Q_S \quad \text{Equation 3.3}$$

$$\text{For floor, } Q^* = Q_H + Q_E \Delta Q_S \quad \text{Equation 3.4}$$

Where Q^* is total all-wave radiation, Q_H is turbulent sensible heat, Q_E is turbulent latent heat and ΔQ_S is total energy storage, rate per volume. Turbulent sensible heat, Q_H is absorbed or transmitted by the Earth or the air during the temperature exchange. Turbulent latent heat, Q_E is absorbed or released when there is a change in the state of water i.e. evaporation. ΔQ_S becomes the heat storage of ground, streets and walls (also known as urban surfaces) based on the heat exchange by conduction. Additional component of soil heat flux, Q_G was also introduced to the floor surface energy formulation (Oke 1987a); see Equation 3.5.

$$\text{For floor, } Q^* = Q_H + Q_E + \Delta Q_S + Q_G \quad \text{Equation 3.5}$$

Studies have determined that ΔQ_S is the fluxes of energy into (Q_{in}) and out (Q_{out}) of a system volume (Oke 1987a). Three possibilities can be occurred: (i) Q_{in} exceeds Q_{out} causes warming condition, (ii) Q_{in} is less than Q_{out} causes cooling condition, and (iii) Q_{in} is equal to Q_{out} . Figure 3.1 illustrates the concept indicated based on direction arrow either in vertical flow or in horizontal flow. In Figure 3.1, positive ΔQ_S depicts that there is gain in the net energy storage of the surface thus warming effect will occur in the volume meanwhile the negative ΔQ_S depicts that the energy storage gain is depleted thus cooling effect will take place. For $Q_{in} = Q_{out}$, no net change in the energy of the system, so thus the temperature.

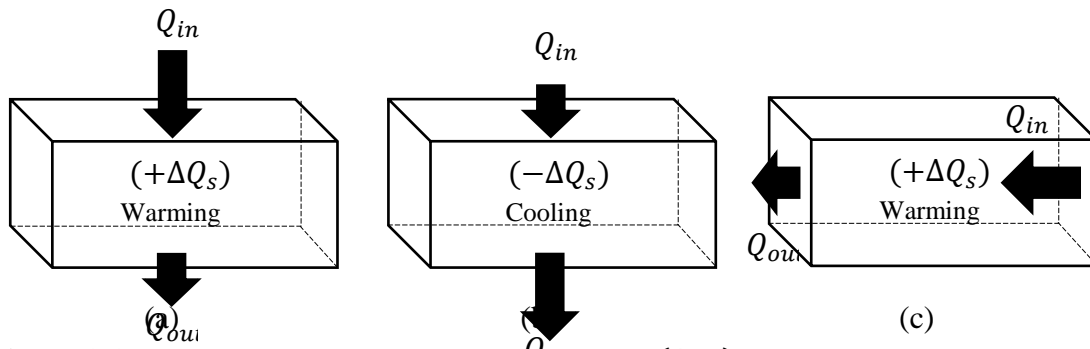


Figure 3.1 Illustration depicting the energy flux for (ΔQ_s) (a) warming condition with vertical flux convergence - Q_{in} exceeds Q_{out} , (b) cooling condition with vertical flux divergence - Q_{in} is less than Q_{out} , and (c) warming condition with horizontal flux divergence - Q_{in} exceeds Q_{out} (Oke 1987a)

3.1.2.1 Comparing energy balance between urban rural surface and urban surface

Energy balance of a specific area or plane can be determined based on its surface landscape. For a simplified surface, the net radiation (Q^*) can be calculated based on the total of sensible heat flux (Q_H), latent heat flux (Q_E) and conductive heat flux (ΔQ_s) in to and out from the surface materials (Arnfield 2003); see Equation 3.6 below:

$$Q^* = Q_H + Q_E + \Delta Q_s \quad \text{Equation 3.6}$$

For a complicated urban landscape, the evaluation of the energy fluxes has to consider the imaginary volume extended above the ground surface until the roof level within the margin of a UCL with the condition that the energy exchanges are negligible with respect to time (Arnfield 2003). The energy balance of the volume is calculated based on Equation 3.7:

$$Q^* + Q_F = Q_H + Q_E + \Delta Q_s + \Delta Q_A \quad \text{Equation 3.7}$$

Where Q_F is heat and water sources in the city associated with combustion or to be known as anthropogenic heat, ΔQ_S is the storage heat flux of all energy storage mechanism (buildings, soil, air, vegetation etc.) and Q_A is net advection through the sides of the volume based on horizontal transfer of sensible and latent heat. Within an urban street canyon (Mirzaei & Haghighat 2012), the net radiation budget, Q^* to the surfaces can be simplified based on the upward and downward of shortwave radiation ($S_r \uparrow, S_r \downarrow$) and longwave radiation ($L_r \uparrow, L_r \downarrow$); see Equation 3.8:

$$Q^* = S_r \uparrow - S_r \downarrow + L_r \uparrow - L_r \downarrow \quad \text{Equation 3.8}$$

The net thermal radiation, $L_r \uparrow$ and $L_r \downarrow$ were defined as atmospheric counter radiation and ground emitting longwave radiation, respectively (Feng & Feng 2012); shown in Equation 3.9 and Equation 3.10:

$$L_r \uparrow = \sigma T_s^4 \quad \text{Equation 3.9}$$

$$L_r \downarrow = \sigma T_a^4 \quad \text{Equation 3.10}$$

Where σ is the Stefan-Boltzmann constant ($5.670367 \times 10^{-8} \text{ kg s}^{-3} \text{ K}^{-3}$), T_s is road surface temperature and T_a is air temperature. The net shortwave solar radiation accounts for the beam or direct solar radiation ($S_r \uparrow$) and diffuse solar radiation ($S_r \downarrow$) which include the geographic latitude, time angle, solar declination angle, precipitation and dust particle (Feng & Feng 2012).

An example given by Landsberg (1981) showed a significant difference in terms of the ΔQ_S value comparing urban and rural areas, which the obtained ΔQ_S in urban area was 50 % and the obtained ΔQ_S in rural area was 19 %. As the illustration showed in Figure 3.2(a) and Figure 3.2(b), warmer air temperature under the canyon layer within urban area was detected as compared to the air temperature under the same layer within rural area.

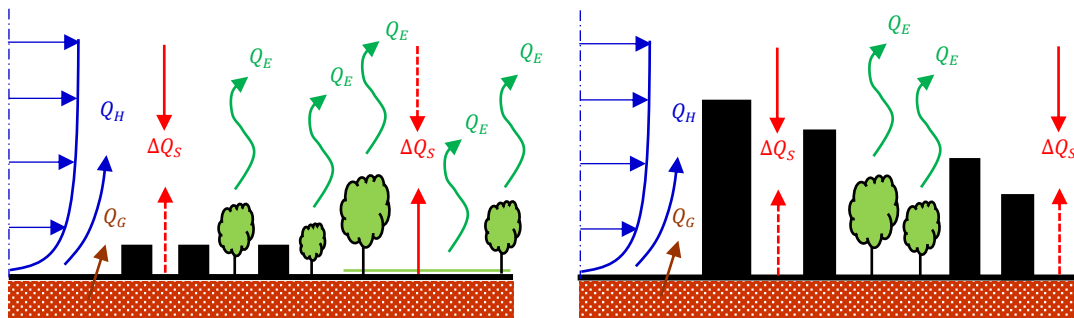


Figure 3.2 Illustration of energy balance comparing (a) rural area, and (b) urban area

Additionally, Landsberg (1981) gave another example regarding a rural case study in Columbia, Maryland which showed diurnal Q_E as the main component to the energy balance due to the increased reflected short-wave radiation due to high albedo in growing vegetation. Meanwhile, diurnal Q_H is the principal element to carry the heat from the canyon upward, about 64 % out of the net radiation was measured for the case study of Montreal urban area. Strong Q_A causes Q_H to become weak and vice-versa to weak Q_A (Landsberg 1981).

3.1.3 Reduction in cooling due to buildings act as obstacle to airflow

Buildings act as an obstacle to the wind, thus change the characteristic of the airflow either in gradual motion or in drastic motion. Figure 3.3 shows the wind velocity profile before and after it flows over an obstacle block-like building.

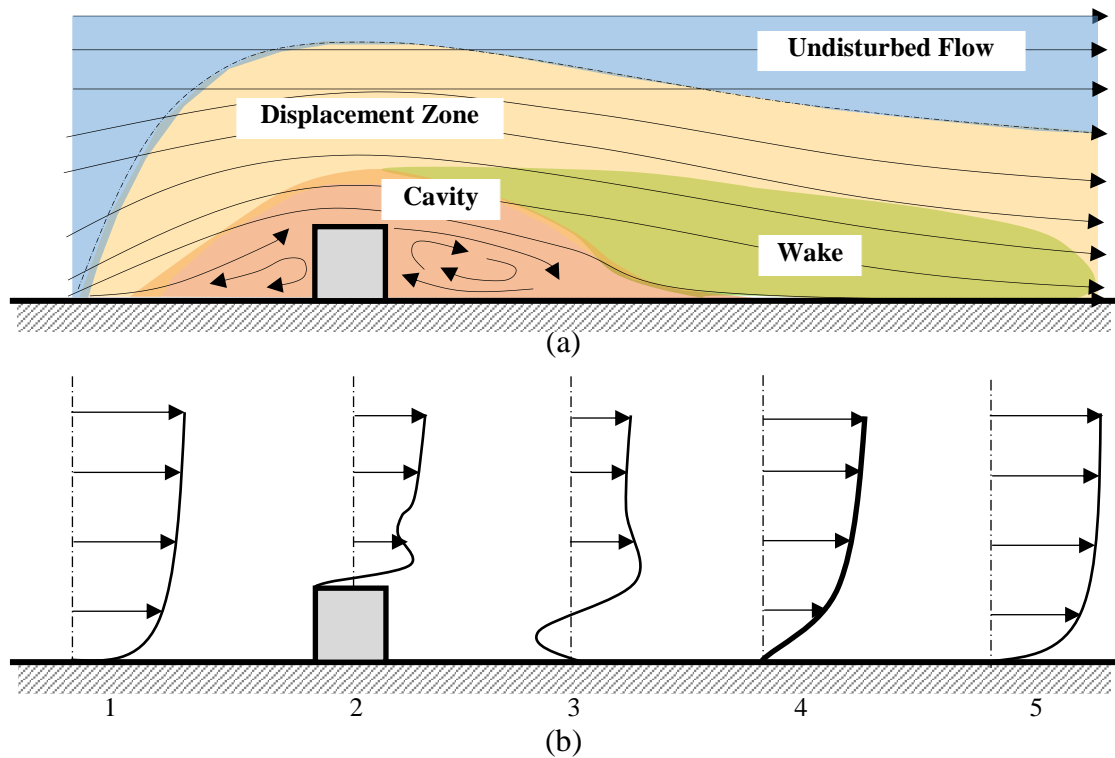


Figure 3.3 Illustration demonstrating (a) streamlines and flow zone (b) wind velocity profiles with a building acts as an obstacle (Oke 1987a)

The logarithmic air profile 1 was observed to be sharply distorted over the building (profile 2) due to the sharp decrease in the wind velocity between the building roof level and the ground level (Oke 1987a). At profile 3 after the airflow has passed the building block, the streamlines begin to diverge, and a return flow eddy seems to be observed before it turns into an undisturbed form (profile 4). Farther than the building block (profile 5), it can be observed that the velocity profile is not as steep as profile 1 due to the remaining turbulence in the wake continues to facilitate the momentum transport at greater rate for the terrain.

An airflow pattern also depends on the geometry of urban array, specifically the ratio of height to width (H/W). For widely spaced building array, $H/W < 0.4$ for cubic and < 0.3 for rows, the airflow patterns seem not majorly changed and isolated. For closer spacing,

$H/W = 0.7$ for cubic and $H/W = 0.65$ for rows, the interference of wake from any building which leads to a complicated pattern seems to happen. Skimming with lee vortex airflow can be observed when the building spacing becomes much closer. Figure 3.4 shows the comparison between isolated roughness flow, wake interference flow and skimming flow within a building spacing with difference width (Oke 1987a).

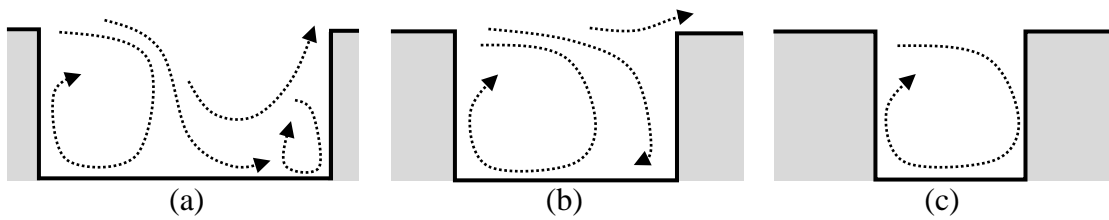


Figure 3.4 Illustration of airflow patterns of (a) isolated roughness flow with $H/W < 0.4$ for cubic and < 0.3 for rows, (b) wake interference flow with $H/W = 0.7$ for cubic and $= 0.65$ for rows, and (c) skimming flow with $H/W \geq 1$ (Oke 1987a)

Theory of atmosphere (Landsberg 1981), which firstly developed as the theory of flow in 1905 explains that surface influence causes vectors of motion in successive layer up to the layer where the friction stops, demonstrating the formation of logarithmic wind profile. An unobstructed parallel wind by friction towards isobars or geostrophic wind, \bar{V}_G is represented as shown in Equation 3.11 and Equation 3.12 below:

$$\bar{V}_G = - \frac{1}{\rho f} \frac{\partial p}{\partial x} \quad \text{Equation 3.11}$$

$$f = 2 \Omega \sin \phi \quad \text{Equation 3.12}$$

Where ρ is atmospheric density, f is Coriolis parameter, Ω is angular velocity, ϕ is latitude and $\frac{\partial p}{\partial x}$ is horizontal pressure gradient from higher to lower pressure. For the ideal case, Nongeostrophic wind components closer to the surface or horizontal plane makes

45 ° angle with tangents to the spiral. The relationship between geostrophic wind and nongeostrophic wind is expressed in Equation 3.13:

$$\bar{v}_z - \bar{V}_G = \frac{1}{f} \frac{d}{dx} \left(\frac{\tau_z}{\rho} \right) \quad \text{Equation 3.13}$$

Where \bar{v}_z is average wind vector at level z below geostrophic wind level and τ_z is shear stress. Shear stress which also means Reynold stress is determined based on the turbulent components of wind speed, u' , v' and w' .

3.2 Mechanism of heat transfer within urban area

The energy balance of an urban area combines three processes of heat transfer, which are: (i) radiation, (ii) conduction and (iii) convection. The mode of heat transfer must be in the condition from a higher temperature medium to a lower temperature medium (Cengel & Boles 2015). In general, during the daylight, the urban surfaces are radiated by the sun, which partly is absorbed, partly is reflected and the remaining is transmitted. Thus, the conservation of energy principle is based on the equal of incident solar radiation (to be named as '1') to the sum of the absorbed, reflected, and transmitted solar radiation as Equation 3.14 (Cengel & Boles 2015):

$$\alpha + r + t = 1 \quad \text{Equation 3.14}$$

The three components in **Error! Reference source not found.** symbolise the fraction of incident radiation to be absorbed, reflected and transmitted; thus α is the absorptivity, r is the reflectivity and t is the transmissivity of the surface for solar energy.

3.2.1 Radiation heat transfer

The maximum radiation emitted by an idealised surface or blackbody (Cengel & Ghajar 2015) is written as:

$$Q_{emit,max} = \sigma A_s T_s^4 \quad \text{Equation 3.15}$$

σ is Stefan-Boltzmann constant, $5.670 \times 10^{-8} \text{ W/m}^2 \cdot \text{K}^4$ and T_s is the temperature of the surface in Kelvin. With a surface with less than the radiation emitted by a blackbody (Cengel & Ghajar 2015), the equation is written as:

$$Q_{emit} = \varepsilon \sigma A_s T_s^4 \quad \text{Equation 3.16}$$

Where surface emissivity, ε is varied based on the range $0 < \varepsilon < 1$, indicating that 1 is full radiation to be emitted by an idealised surface such as blackbody and 0 is no radiation to be emitted by a surface. Contrarily for absorptivity, α within the range $0 < \alpha < 1$, a blackbody becomes a perfect absorber 1 as well as a perfect emitter. According to Kirchhoff's law of radiation, the emissivity and the absorptivity of a surface are equal when the temperature and the wavelength are the same, however, the temperature and the wavelength values are ignored for practicality. This has given the average absorptivity is equal to the average emissivity, shown in Equation 3.17:

$$Q_{absorption} = \alpha \cdot Q_{incident} \quad \text{Equation 3.17}$$

Where $Q_{Incident}$ is the incident radiation on a surface. When the rate of radiation absorption is higher than the rate of the radiation emission, the surface is gaining the

energy by radiation and vice-versa. Thus, net rate of radiation heat transfer between two surfaces is based on the surface emissivity ε and surface area, A_s at a thermodynamic temperature T_s , which is enclosed by a larger surface at thermodynamic T_{surr} (separated by gas or air) that does not intrude with radiation, shown in Equation 3.18:

$$Q_{radiation} = \varepsilon \sigma A_s (T_s^4 - T_{surr}^4) \quad \text{Equation 3.18}$$

3.2.2 Conduction heat transfer

The rate of conduction, $Q_{conduction}$ depends on the geometry of the medium, the medium thickness, the material of the medium and the temperature difference across the medium (Cengel & Ghajar 2015). In a steady state conduction, the rate of heat conduction through a plane layer is proportional to the temperature difference across the layer and the heat transfer area, but is inversely proportional to the thickness of the layer, see Equation 3.19.

$$\text{Rate of heat conduction} \propto \text{Area} \times \frac{\text{Temperature difference}}{\text{Thickness}}$$

$$Q_{conduction} = -kA \frac{\Delta T}{\Delta x} \quad \text{Equation 3.19}$$

Where k is thermal conductivity of the material ($\text{W/m} \cdot \text{K}$), A is the total area of the material, ΔT is the temperature difference and Δx is the thickness of the material, $x \rightarrow 0$.

According to Fourier's law of heat conduction, $\frac{\Delta T}{\Delta x}$ is expressed as $\frac{dT}{dx}$ which means the rate of the change in the temperature at location x . The negative sign before k ensures the heat transfer in the positive x direction is a positive quantity.

3.2.2.1 Thermal conductivity and diffusivity

Thermal conductivity of a material is described as the rate of heat transfer through a unit thickness of the material per unit area per unit temperature difference (Cengel & Ghajar 2015). Higher conductive material will have large thermal diffusivity and low heat capacity. This means thermal diffusivity of a material can be meant as the ratio of the heat conducted through the material to the heat stored per unit volume. Thus, the relationship between the thermal conductivity and the thermal diffusivity of a material can be found in Equation 3.20:

$$\begin{aligned}\text{Thermal diffusivity, } \alpha &= \frac{\text{Heat conduction}}{\text{Heat storage}} \\ &= \frac{k}{\rho c_p}\end{aligned}\quad \text{Equation 3.20}$$

Where ρc_p is the specific heat capacity which represents the energy a material stores per unit volume.

3.2.3 Convection heat transfer

Convection heat transfer is the energy transfer between a solid surface and the adjacent gas or liquid either with the effects of conduction or fluid motion (Cengel & Ghajar 2015). Higher convection heat transfer is caused by faster fluid motion; meanwhile without the presence of the bulk motion of the fluid, the heat transfer between a solid surface and the adjacent fluid is by means of conduction. Two types of convection can be observed: (i) the forced convection where there is a force in the fluid flow over a surface to flow over a surface, or (ii) natural convection where the fluid motion is based on the natural

buoyancy force that is driven by the density differences due to the variation in the temperature from the solid surface to the hot block shown in Figure 3.5.

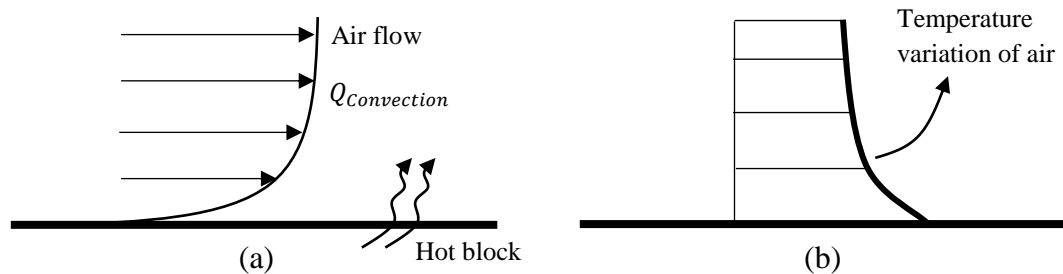


Figure 3.5 Illustration following (Cengel & Ghajar 2015) showing (a) velocity variation of air (b) temperature variation of air

According to Newton's law of cooling (Cengel & Ghajar 2015), the rate of convection heat transfer, $Q_{convection}$ is proportional to the difference in the temperature, shown in Equation 3.21:

$$Q_{convection} = h_{cv} A_s (T_s - T_{\infty}) \quad \text{Equation 3.21}$$

Where h_{cv} is the convection heat transfer, A_s is the surface area of the heat transfer and T_{∞} is the temperature of the fluid. In calculating h_{cv} , several variables are important to be considered: (i) surface geometry, (ii) nature of fluid motion, (iii) properties of the fluids, and (iv) the bulk fluid velocity.

3.2.4 Heat transfer between pavement surface and air layer

According to the first law of thermodynamics, the total energy of an isolated system is constant whereby the energy can be transferred from one form to another but can never be destroyed and created. Meanwhile Fourier's law stated that the first law of

thermodynamics, conjugated with Fourier's law is an empirical relationship integrating the conduction rate of a material and its temperature gradient following the direction of the energy flow. Based on the energy balance approach, the heat flux obtained by the urban surfaces ($Q_{s-conduction}$) from the total calculation of the solar radiation heat flux Q_{solar} can be obtained with thermal radiation heat flux ($Q_{thermal}$) and convection heat flux ($Q_{convection}$); shown in Equation 3.22 and Equation 3.23:

$$Q_{s-conduction} = Q_{solar} + Q_{thermal} + Q_{convection} \quad \text{Equation 3.22}$$

$$Q_{s-conduction} = \alpha_s I_t + \beta (T_a - T_s) \quad \text{Equation 3.23}$$

α_s is the absorption coefficient of asphalt mixtures¹, I_t solar radiation incident on the pavement surface, β the multiplex coefficient of heat transfer² and $(T_a - T_s)$ is the value of atmosphere temperature deducts the value of the pavement surface temperature (Wang et al. 2010). The amount of shortwave radiation absorbed by a surface is determined with solar absorptivity of the surface ($\gamma_{absorption}$), intensity factor of the sun according to the sun angle during a 24-hour day (I_f) and daily peak value of solar radiation Q_{solar} (Qin & Hiller 2011), shown in Equation 3.24 and Equation 3.25:

$$Q_{s-absorption} = \gamma_{absorption} \times I_f \times Q_{solar} \quad \text{Equation 3.24}$$

$$\text{Thus, } Q_{solar} = \frac{Q_{s-absorption}}{\gamma_{absorption} \times I_f} \quad \text{Equation 3.25}$$

Calculation of longwave heat flux between natural ground surfaces and sky, $Q_{thermal}$ follows Stefan-Boltzmann law (Qin & Hiller 2011), see Equation 3.26:

¹ According to (Wang et al. 2010), α_s is referred to the value of 0.9

² According to (Wang et al. 2010), β is referred to the value of 0.94

$$Q_{Thermal} = \sigma \varepsilon (T_{sky}^4 - T_s^4) \quad \text{Equation 3.26}$$

Where ε is emissivity of the ground surface and T_{sky} is the effective sky temperature. Effective sky temperature, T_{sky} means the temperature of blackbody radiation that is having the same flux as the downward atmospheric radiation does not equal to air temperature, shown in Equation 3.27:

$$T_{sky} = \varepsilon_{sky}^{0.25} T_a \quad \text{Equation 3.27}$$

Where ε_{sky} is sky emissivity with the value of $\varepsilon_{sky} = 0.754 + 0.0044T_{dp}$ and T_{dp} is the dew point temperature.

$Q_{convection}$ is calculated based on the convective heat transfer coefficient (h_c) and the temperature difference between temperature of pavement surface and air temperature ($T_s - T_a$), to be adapted based on Equation 3.10 which highlighting the temperature difference between the surface and the adjacent liquid (Bilgen & Richard 2002), shown in Equation 3.28:

$$Q_{convection} = h_{cv} (T_s - T_a) \quad \text{Equation 3.28}$$

It was observed that the air motion is zero at the pavement surface due to zero velocity relative to the surface, to be known as no-slip condition. This condition determines the development of air velocity profiles, creating ‘boundary layer’ which is a flow region adjacent to the pavement surface which the viscous effects and velocity gradients are

significant. Consequently, the air force applies on the pavement surface in the flow direction, to be known as ‘surface drag’ also exists due to no-slip condition.

With no-slip condition, the heat transfer between the air layer and the pavement surface is similar to the conduction heat transfer since the fluid layer is motionless (Cengel & Ghajar 2015); see Equation 3.29:

$$\begin{aligned}
 Q_{convection} &= Q_{conduction} = -kA \frac{\partial T}{\partial y}; y = 0 \\
 &= h_{cv} (T_s - T_a) = -kA \frac{\partial T}{\partial y} \\
 \therefore h_{cv} &= \frac{k_{air}(\partial T / \partial y)}{T_s - T_a} \quad \text{Equation 3.29}
 \end{aligned}$$

Where $\frac{\partial T}{\partial y}$ is the temperature gradient at the surface and h_{cv} has the range between 10^6 and 5×10^6 (Bilgen & Richard 2002). Realistically, the convection heat transfer varies along the flow direction, x . Thus, the average or mean convection heat transfer coefficient is determined based on the average location convection heat transfer coefficient over the entire surface (Cengel & Ghajar 2015). It is a common practice to use dimensionless number to simplify the number of total variables, thus Nu number is used to represent the dimensionless heat transfer coefficient h_{cv} ; see Equation 3.30:

$$\begin{aligned}
 Nu &= \frac{\text{Convective heat transfer}}{\text{Conductive heat transfer}} \\
 &= \frac{h_{cv} \Delta T}{k_{air} \Delta T / L_{BL}} \\
 &= \frac{h_{cv} \cdot L_{BL}}{k_{air}} \quad \text{Equation 3.30}
 \end{aligned}$$

Where Nu is the dimensionless convection heat transfer coefficient (Cengel & Ghajar 2015) or the dimensionless number that becomes the ratio of convective to conductive heat transfer across to the boundary, L_{BL} is characteristic length and k_{air} is the thermal conductivity of air. Larger Nu represents the more effective convection heat transfer. Nu = 1 means the heat transfer across the layer is by pure conduction.

3.2.4.1 Urban airflow

h_{cv} becomes the function of the local Reynolds number (Re), k_{air} , the Prandtl number of air (Pr) and the characteristic length of the medium the air acts on to (Qin & Hiller 2011), see Equation 3.31:

$$h_{cv} = 5.6 + 0.332 \text{ Re}^{0.5} \text{Pr} \frac{k_{air}}{L} \quad \text{Equation 3.31}$$

Reynolds number is the dimensionless ratio of inertia forces to viscous forces in fluid, see Equation 3.32 below:

$$\begin{aligned} \text{Re} &= \frac{\text{inertia forces}}{\text{viscous forces}} = \frac{UL_{BL}}{v} \\ &= \frac{\rho UL_{BL}}{\mu} \end{aligned} \quad \text{Equation 3.32}$$

Where U is local wind velocity in m/s, v is air kinematic viscosity³ in $\text{m}^2 \text{ s}^{-1}$, ρ is air density and μ is dynamic viscosity of the air. Large Re is caused by large inertia forces

³ Air kinematic viscosity v is recommended as 16.01×10^{-6} (Qin & Hiller 2011)

and large viscous forces which are proportional to inertia forces; a type of flow known as ‘turbulent flow’. It should be noted that Pr is a dimensionless parameter that is used to calculate the heat transfer between a moving fluid and a solid body, see Equation 3.33.

$$\begin{aligned} Pr &= \frac{\text{Molecular diffusivity of momentum}}{\text{Molecular diffusivity of heat}} \\ &= \frac{C_p \nu}{k} \end{aligned} \quad \text{Equation 3.33}$$

Where C_p is fluid heat capacity per unit volume and k is thermal conductivity.

3.2.5 Heat transfer between pavement and RPSC system

The application of RPSC system for energy harvesting and snow melting was reviewed (Pan et al. 2015) and the summary of the process of heat transfer between the system and the pavement are shown in Equation 3.34, Equation 3.35 and Equation 3.36 below:

For heat conduction through pavement (from surface to pavement layer):

$$Q_{\text{Conduction-pavement}} = -k_{\text{pavement}} \left(\frac{\partial T}{\partial y} \right) \quad \text{Equation 3.34}$$

Where $-k_{\text{pavement}}$ is thermal conductivity of the pavement used for the system and $\frac{\partial T}{\partial y}$ is the temperature gradient T in a direction, y .

For conduction through pipes:

$$Q_{\text{Conduction-pipe}} = -k_{\text{pipe}} \left(\frac{\partial T}{\partial y} \right) \quad \text{Equation 3.35}$$

Where $-k_{pipe}$ is thermal conductivity of the pavement used for the system and $\frac{\partial T}{\partial y}$ is the temperature gradient T in a direction, y .

For heat convection between water and pipes:

$$Q_{Convection-w_p} = h_{water-pipe} A_s (T_{pipe} - T_{water}) \quad \text{Equation 3.36}$$

Where $h_{water-pipe}$ is the convection coefficient between the water and pipes and A_s is the surface area of the pipes.

3.3 Summary

In this chapter, the theoretical background of the study consisting the correlation between urban built form and the elevation of UHI effect was fully detailed as well as the correlation between urban surfaces above the ground level and underground pavement layers. To understand the climate condition of a complex urban surface, this study focussed on the equations which were simplified for the case of urban canyon that is commonly found within the urban environment. The effect of the microclimate setting within the urban street canyon will determine the temperature and the heat flux obtained by the pavement surface within. Application of the hydronic RPSC system within this type of pavement condition and the system performance in reducing surface and near-air temperatures will be investigated. Based on this theoretical background, the thesis methodology of coupling hydronic RPSC system with urban street canyon is fully described in Chapter 4.

CHAPTER 4

Computational method

4.0 Introduction

Chapter 4 describes the computational method of investigating the performance of hydronic RPSC system in mitigating the UHI effect within an urban environment, which in this study will be configured as urban street canyon. Section 4.1 introduces the methodology of de-coupled CFD modelling combining urban environment and hydronic RPSC system by the application of CFD based on Finite-Volume Method (FVM) of ANSYS Fluent. Section 4.2 and 4.3 details the geometry of the computational domains and the type of mesh set for the computational domains. The boundary condition set for the computational domain representing an urban environment is described in Section 4.4 meanwhile the solution convergence is detailed in Section 4.5. Section 4.6 explains on the calculation of RPSC performance in surface temperature reduction (STR) and potential temperature collection (PTC) meanwhile Section 4.7 describes the validation results of the computational models with the previous published works which were done by experimental setup.

4.1 Introduction to the computational method

In this study, an embedded hydronic pavement solar collector (RPSC) system is proposed as a mitigation system within a simplified urban canyon model, which urban canyon model is commonly used to investigate the thermal UHI effect from the aspect ratio of the canyon buildings. This combination is to provide additional parameter in comparison to previous studies by including the effect of building canyon to the performance of the RPSC system.

A ‘de-coupled’ CFD model, which combines the results of two separated domains was carried out as the main investigative technique. The first domain, to be called as ‘macro domain’, consists of an urban canyon that was configured as two rows of buildings with medium length. Macro domain is classified as the domain where heat fluxes emit, absorb, radiate and reflect between ground surface level and above ground level that includes surrounding environment i.e. buildings, sunshine, wind flow and ambient air temperature. The second domain, to be called as ‘micro domain’, consists of hydronic pipe(s) as RPSC system embedded within a specific depth underneath the ground surface. ‘De-coupled’ simulation means the simulation of macro domain and micro domain was carried out separately but to be connected based on area-weighted average temperature values.

The reason of choosing ‘de-coupled’ method was to avoid excessive number of cell generated from the combined RPSC system within one domain and to reduce bad quality of mesh when too large size of cells is combined with too small size of cells. To connect both domains, an average temperature output of the ground surface that was obtained from the macro domain was applied as the boundary temperature or an input temperature for the micro domain in the purpose of calculating the heat output with flowing RPSC

system and vice-versa. Figure 4.1 describes the flow chart of the research methodology. In this figure, the pre-processing stage which consists of the geometry description, mesh setting, selection of solver setting, details of boundary condition, and validation of mesh settings with previous publications was the main content of this chapter.

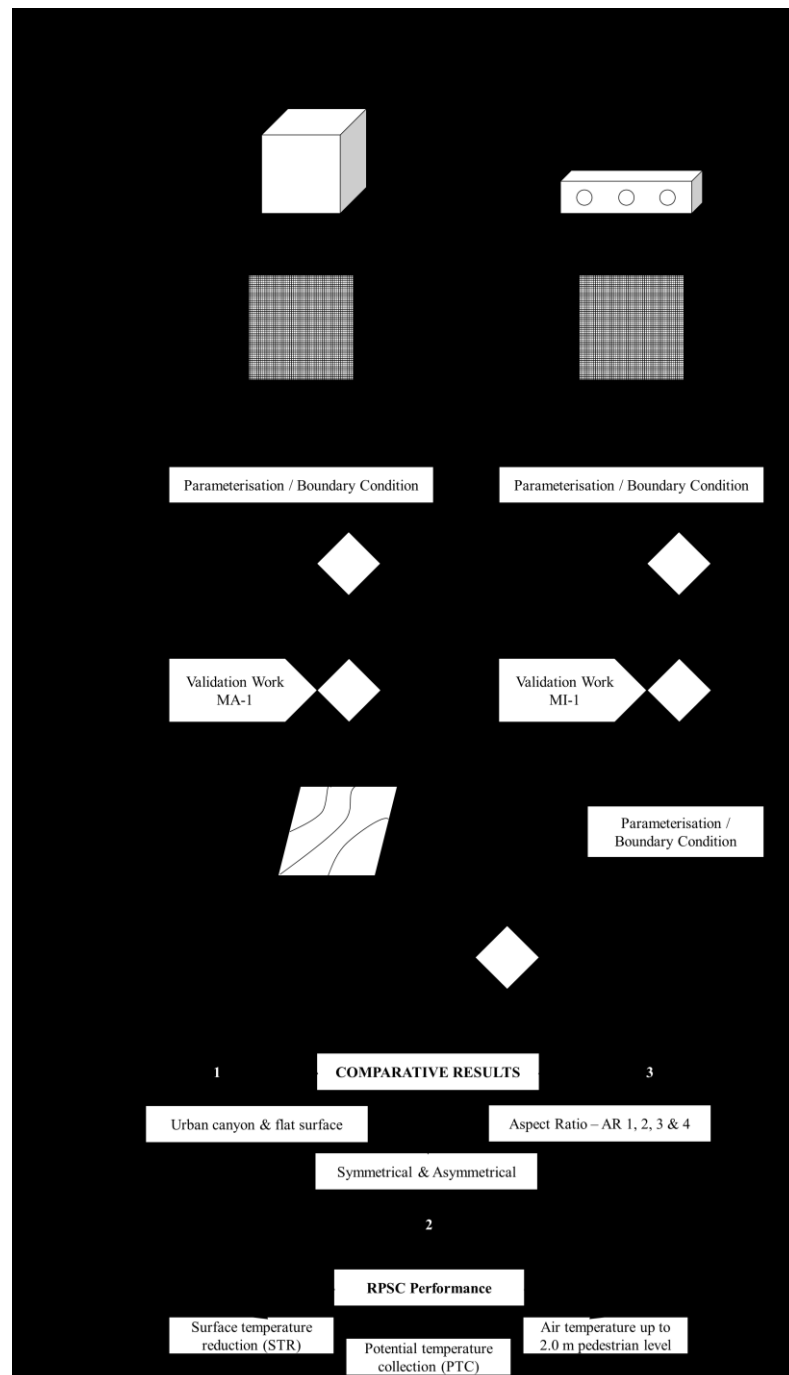


Figure 4.1 Flow chart of de-coupled CFD based on finite-volume method (FVM)

Details of applying CFD based Finite-Volume Method (FVM) as the solver setting of both domains are described in Section 4.1.1, 4.1.2 and 4.1.3.

4.1.1 Solver setting: CFD based on Finite-Volume Method (FVM)

In this study, ANSYS Fluent pressure-based solver of finite-volume method (FVM) was applied for solving the dynamics of low-speed incompressible flows in urban microclimate; to be specified as macro domain in this study. Incompressible flow in the macro domain means the density of the air will not change with motion. FVM is a technique based on discretisation equation which the resulting solution satisfies the conservation of quantities (i.e. energy, species, momentum and mass) either in one of the control volumes or in the whole computational domains due to the division of the domain into several control volumes, to be specified as elements or cells. Additionally, the location of the variable of interest is at the centroid of the control volume (Rübenkönig n.d.). Figure 4.2 shows two examples of control volumes, cell-centred and four faces.

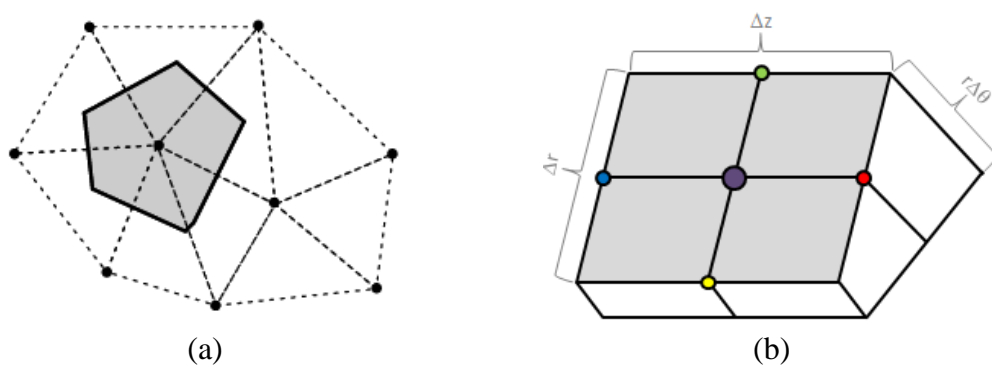


Figure 4.2 Representation of control volume in the form of (a) cell-centred (b) tri-dimensional four faces where the central node is in purple. 1st April 2017. Retrieved from: <http://www.iue.tuwien.ac.at/phd/heinzl/node25.html>

As referred to Figure 4.2, the 3D cells and grid points or nodes are usually in the form of hexahedral, tetrahedral or prism. Finite volume method (FVM) is an integral form of the

conservation equations to control the volume defined by a cell to obtain the discrete equations for the cell. A reduced equation for steady and incompressible flow is as below:

$$\int_S \vec{V} \cdot \hat{n} dS = 0 \quad \text{Equation 4.1}$$

Where it means the integration is on the surface S of the control volume and \hat{n} is the external normal at the surface. The net volume flow into the control volume is 0. An example of a rectangular cell with velocity at face i is taken to be $\vec{V}_i = u_i \hat{i} + v_i \hat{j}$ and when the Equation 4.2 was applied to the control volume defined by the cell, it gives the discrete form of the continuity equation for the cell.

$$-u_1 \Delta y - v_2 \Delta x + u_3 \Delta y + v_4 \Delta x = 0 \quad \text{Equation 4.2}$$

The discrete form of to the sum of the net mass flow into the cell is equivalent to 0 which means the mass is conserved for the cell usually at the cell centres.

4.1.2 CFD governing equation

The governing equation for the simulated model is based on the principle of momentum, continuity and energy conservation which used pressure and steady RANS equations in the combination with the turbulence model of Standard $k - \varepsilon$ model, which has been widely used for urban simulation (Fluent 2009; Bottillo et al. 2014) as details below:

Momentum equation:

$$\bar{u}_j \frac{\partial \bar{u}_i}{\partial x_j} = -\frac{1}{\rho} \frac{\partial \bar{p}}{\partial x_i} + \frac{\mu}{\rho} \frac{\partial^2 \bar{u}_i}{\partial x_i \partial x_j} - \frac{\partial}{\partial x_j} (\overline{u'_i u'_j}) + f_i \quad \text{Equation 4.3}$$

Continuity equation:

$$\frac{\partial \bar{u}_i}{\partial x_i} = 0 \quad \text{Equation 4.4}$$

Heat conservation equation:

$$\bar{u}_i \frac{\partial \bar{T}}{\partial x_i} + \frac{\partial}{\partial x_i} \left(K_T \frac{\partial \bar{T}}{\partial x_i} \right) = 0 \quad \text{Equation 4.5}$$

\bar{u}_i is the average speed of air flow, $\overline{u'_i u'_j}$ is Reynolds stress, ρ is the air density and μ is the molecular viscosity. f_i is thermal-induced buoyant force. \bar{T} is potential temperature and K_T is the heat diffusivity. The turbulence kinetic energy k and the rate of dissipation ε are obtained from transport equations as below:

$$\frac{\partial}{\partial t} (\rho k) + \frac{\partial}{\partial x_i} (\rho k u_i) = \frac{\partial}{\partial x_j} \left[\left(\mu + \frac{\mu_t}{\sigma_k} \right) \frac{\partial k}{\partial x_j} \right] + G_k + G_b - \rho \varepsilon \quad \text{Equation 4.6}$$

$$\frac{\partial}{\partial t} (\rho \varepsilon) + \frac{\partial}{\partial x_i} (\rho \varepsilon u_i) = \frac{\partial}{\partial x_j} \left[\left(\mu + \frac{\mu_t}{\sigma_\varepsilon} \right) \frac{\partial \varepsilon}{\partial x_j} \right] + C_{1\varepsilon} \frac{\varepsilon}{k} (G_k + C_{3\varepsilon} G_b) - C_{2\varepsilon} \rho \frac{\varepsilon^2}{k} \quad \text{Equation 4.7}$$

G_k is the generation of turbulence kinetic energy because of the mean velocity gradient (MVG) and G_b is the generation of turbulence kinetic energy because of buoyancy. In ANSYS Fluent, $C_{1\varepsilon}$, $C_{2\varepsilon}$ and $C_{3\varepsilon}$ constant and the K_T and μ_t are reported as Standard $k - \varepsilon$ model. σ_k and σ_ε is the turbulent Prandtl numbers for k and ε , respectively.

4.1.2.1 Radiation model

The Discrete Ordinate (DO) radiation model was used in solving the radiative transfer equation (RTE) for a finite number associated with a vector direction \vec{s} which is fixed in

the global Cartesian system (x , y and z). DO model solves many transport equations within the directions \vec{s} and the solution method is equal to that used for fluid flow and energy equations (Ansys 2009). RTE for absorbing, emitting and scattering medium at position \vec{r} in the direction \vec{s} is written as:

$$\frac{dI(\vec{r}, \vec{s})}{ds} + (a + \sigma_s)I(\vec{r}, \vec{s}) = an^2 \frac{\sigma T^4}{\pi} + \frac{\sigma_s}{4\pi} \int_0^{4\pi} I(\vec{r}, \vec{s}') \phi(\vec{s} \cdot \vec{s}') d\Omega' \quad \text{Equation 4.8}$$

Where \vec{r} is position vector, \vec{s} is direction vector, \vec{s}' is scattering direction vector, s is path length, a is absorption coefficient, n is refractive index, σ_s is scattering coefficient, σ is Stefan-Boltzmann constant ($5.672 \times 10^{-8} \text{ W/m}^2\text{-K}^4$), I is radiation intensity which depends on position \vec{r} and direction \vec{s} , T is location temperature and ϕ is phase function.

Solar Ray Tracing of the Solar Load Model was coupled with DO model which is a highly efficient and practical for applying 3D solar loads as heat sources (sun's rays entering computational domain) in the energy equations. Using solar calculator tool, the sun's location in the sky for a given day, time, date and position. Solar Load Model has the utility to supply outside beam direction and intensity parameters directly to the DO model if DO model is used to calculate radiation effects within the domain (Fluent 2009). Solar Calculator requires several inputs: (i) global position – latitude, longitude, time zone (relative to GMT) (ii) starting date and time (iii) mesh orientation (iv) solar irradiation method (v) sunshine factor. For mesh orientation, North and East direction vector were required to be specified in the CFD mesh meanwhile the default solar irradiation method is Fair Weather Conditions. The equation for normal direct irradiation applying the Fair Weather Conditions Method was referred to ASHRAE Handbook, see Equation 4.9:

$$Edn \frac{A}{\frac{B}{e^{\sin(\beta)}}} \quad \text{Equation 4.9}$$

A and B are apparent solar irradiation at air mass $m = 0$ and atmospheric extinction coefficient, respectively. These values are based on the earth's surface on a clear day. β is the solar altitude (in degrees) above the horizontal.

4.1.2.2 Conduction and convection heat transfer

In modelling of heat transfer involving conduction and convection effects, the relevant physical models, thermal boundary conditions, input material properties which govern heat transfer should be activated. Fluent solves the energy equation as the following form:

$$\frac{\partial}{\partial t}(\rho E) + \nabla \cdot (\vec{v}(\rho E + p)) = \nabla \cdot \left(k_{\text{eff}} \nabla T - \sum_j h_j \vec{J}_j + (\vec{\tau} \cdot \vec{v}) \right) + S_h \quad \text{Equation 4.10}$$

k_{eff} is the effective conductivity ($k + k_t$). k_t is the turbulent thermal conductivity, was defined according to the turbulence model being used and \vec{J}_j is the diffusion flux of species j . The first three terms on the right-hand side of Equation 4.10 represent energy transfer due to conduction, species diffusion, and viscous dissipation, respectively. S_h includes the heat of chemical reaction, and any other volumetric heat sources you have defined. E is defined as:

$$E = h - \frac{p}{\rho} + \frac{v^2}{2} \quad \text{Equation 4.11}$$

h for incompressible flow can be determined as below:

Equation 4.12

In 2014, a simplified urban canyon was modelled in ANSYS Fluent with two building rows consisting of 100 m length (L) \times 20 m width (W) \times 20 m height (H) (Bottillo et al. 2014). In determining the total size of airflow domain, the height of the urban canyon, H becomes the main reference. The gap between inlet plane and first windward wall was determined 5H (Bottillo et al. 2014). Windward wall means the wall is positioned to be facing with the direction of the airflow from the inlet plane. Conversely, the gap between second leeward wall and outlet plane was determined 15H. The other walls of the domain (at sides and top wall) were set to be in symmetrical condition and were determined with the gap of 5H from the building walls. A 3D perspective of urban domain is presented (Bottillo et al. 2014), see Figure 4.3.

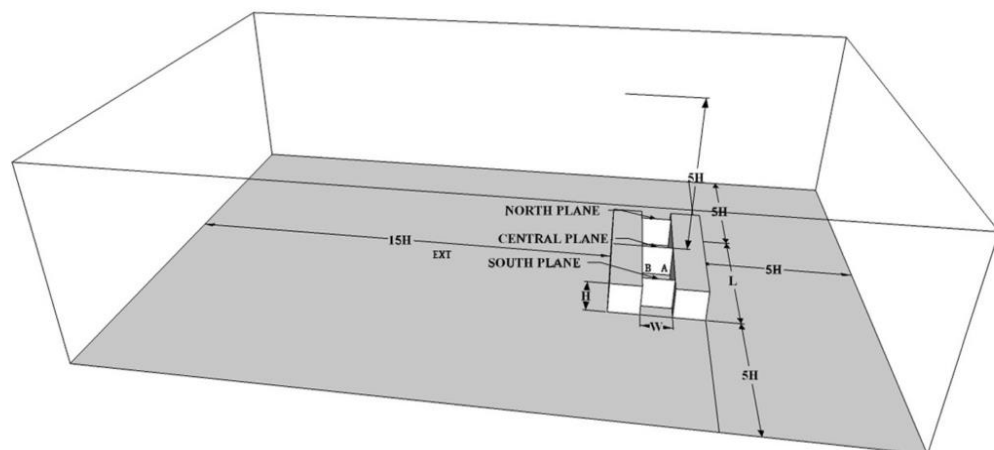


Figure 4.3 A benchmark urban canyon domain configuration (Bottillo et al. 2014)

The 3D urban domain is the simulation model imitating an elongated urban canyon in the city of Milan, Italy for investigating the fluid dynamics of heat transfer at the specified

urban canyon. Validation of the airflow profile at certain points outside and inside the canyon were compared for both simulation and case studies with satisfactory results. Due to this reason, the urban domain by Bottillo (2014) was used as the benchmark geometry of the macro domain presented in this research, where five variables were set as the boundary of the macro domain, which are (i) solar radiation, (ii) air flow, (iii) canyon geometry, (iv) building wall temperature, and (v) underground pavement temperature; see Figure 4.4.

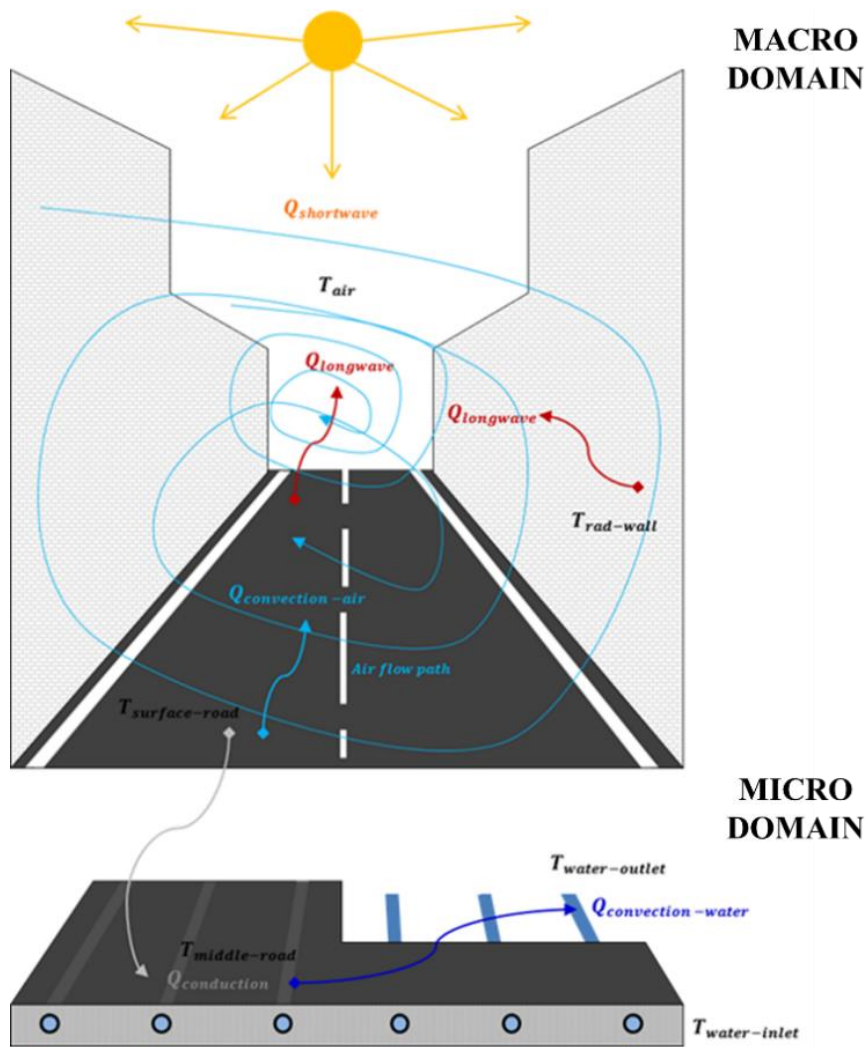


Figure 4.4 Proposed diagram of de-coupled macro domain and micro domain

4.2.1 Description of macro domain of the study

As refer to the benchmark study (Bottillo et al. 2014), a canyon street with width, $W = 20$ m was sandwiched in between two buildings with the length, $L = 100$ m and the height, $H = 20$ m. This has made the aspect ratio, AR of the street canyon is equivalent to 1 based on height over width ratio, H/W and to 5 based on length over width ratio, L/W . Based on the best practice guidelines of CFD simulation associated with urban flow (Franke et al. 2007), the outflow distance to the building region requires three times longer than the inflow distance to the building region in order to allow the airflow to re-develop after it passes the building region, where the air recirculation has taken place. A sufficient gap should be allowed between the sides of building openings and the walls with symmetrical condition (lateral and top). In this study, the gap was set to $5H$. Figure 4.5 shows the domain description based on elevation view, 3D view and plan view.

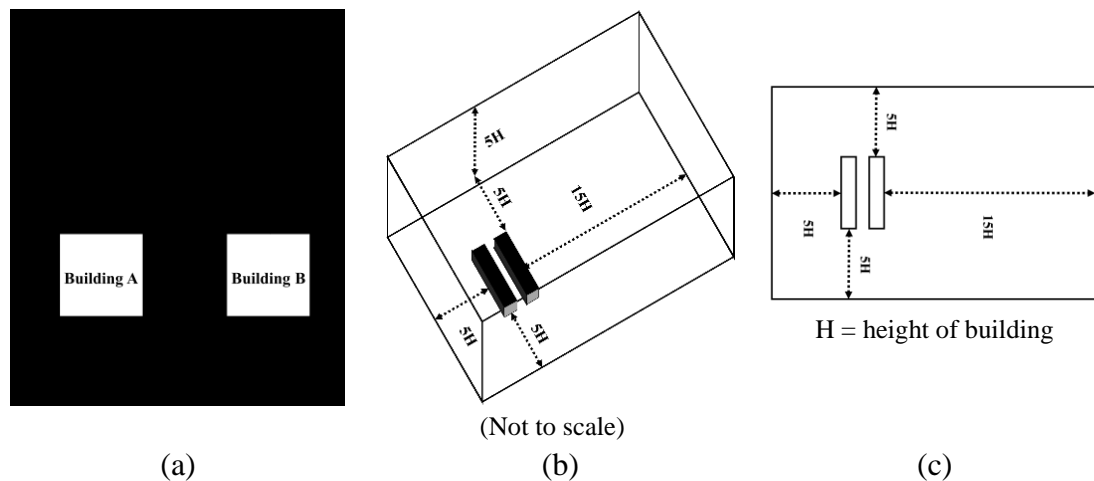


Figure 4.5 Details of domain size (a) elevation view (b) 3D perspective (c) plan view

Details on the geometry construction of the domain using Google Sketchup Pro, AutoCAD and ANSYS DesignModeler before full simulation was conducted in ANSYS Fluent are fully described in Appendix A.1.

4.2.1.1 Control volume - aspect ratio = 0

It should be noted that a flat surface without urban canyon is equivalent to $H/W = 0$ due to zero height and zero canyon width. Previous investigation (Levermore & Cheung 2012) highlighted the calculation of air temperature based on empirical models built for a surface with building canyon and for a surface without building canyon (rural or flat surface). Models suggested that with building canyon, the air temperature was observed higher than the setting with flat surface, see Figure 4.6.

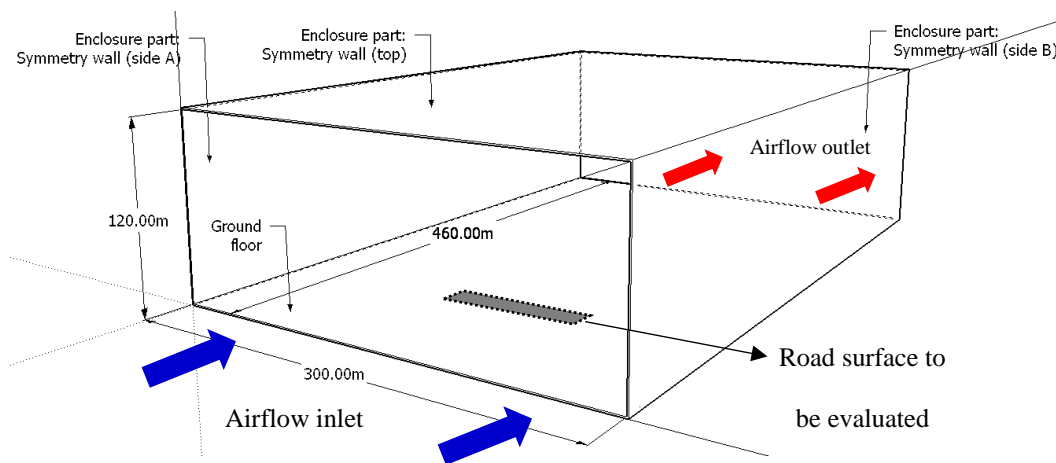


Figure 4.6 Empty domain consisting fluid flow and flat ground (no buildings)

In this study, a macro domain consisting of urban canyon was compared to a macro domain consisting of flat ground surface (no buildings). To simplify the comparison between the two domains, the dimension of both domains had to be similar, with 460 m $L \times 300$ m $W \times 120$ m H . It should be noted that the geometry location, distance and direction in x , y and z for both domain had to be similar, ensuring the ground road surface within street canyon and without street canyon can be correspondingly compared. This road surface area is where RPSC system was installed and evaluated in Chapter 6.

4.2.1.2 Control volume - aspect ratio > 1

The influence of canyon aspect ratios (AR) on UHI effect was highlighted to be the reason of RPSC application within the urban environment. This study extended the setting of urban aspect ratio based on $H/W = 1$ to $H/W = 2, 3$ and 4 , representing the potential ratio of tall buildings to canyon width applied for large metropolitan; see Figure 4.7.

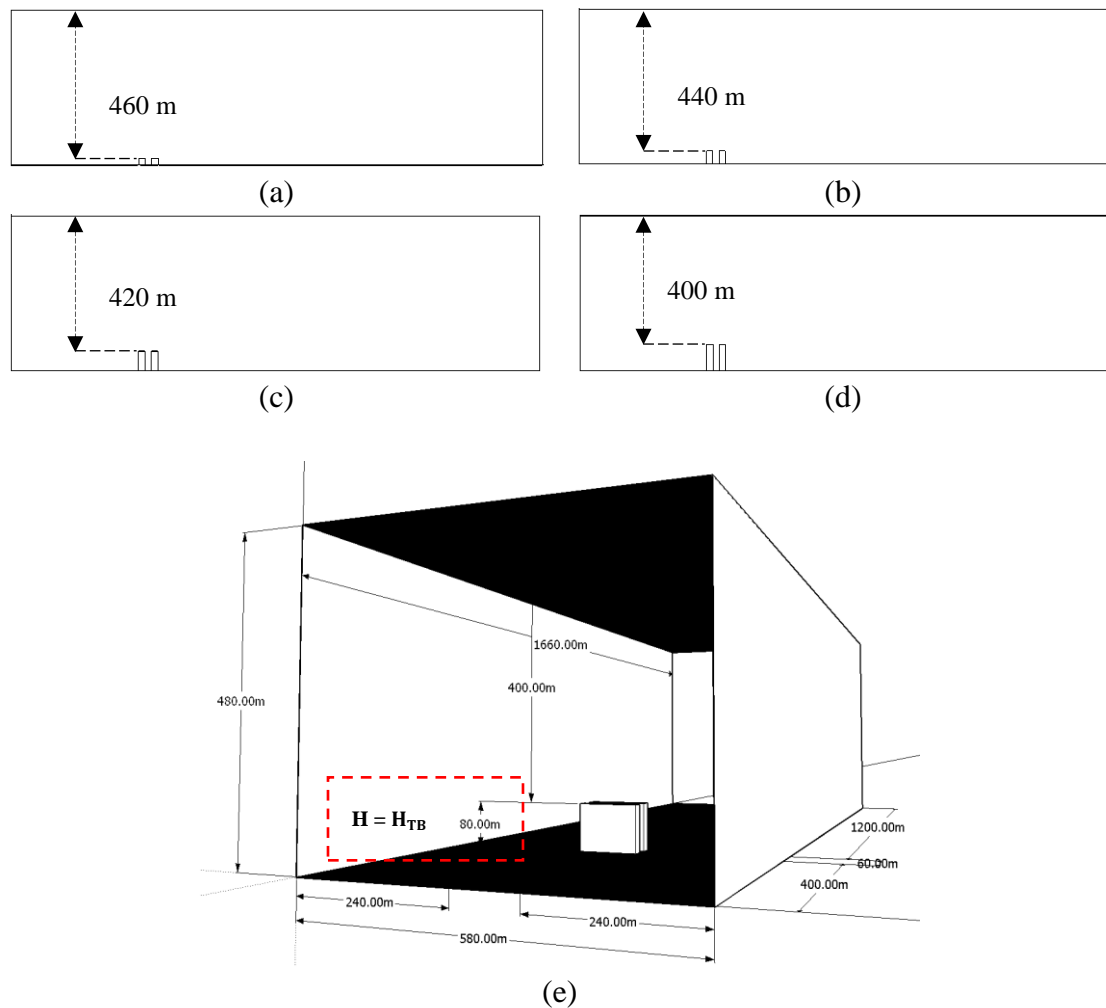


Figure 4.7 Sectional elevation showing (a) AR 1 (b) AR 2 (c) AR 3 (d) AR 4. Figure (e) shows full dimension of the domain based on the tallest building height, AR 4 among the compared aspect ratios.

Section 4.2.1 has stated that the aspect ratio of 1, $AR\ 1 = 20\ m$ when $H = 20\ m$ and $W = 20\ m$. Thus, $AR\ 2, 3$ and 4 were $40\ m, 60\ m$ and $80\ m$, respectively. To configure the size of the domain for $AR\ 2, 3$ and 4 , the tallest height (H_{TB}) among the compared aspect ratio

was used as the reference 'H' as per Figure 4.7(e). This means the tallest height evaluated for this study is AR 4, 80 m. This was to standardise the size of all domains in one controlled size.

4.2.1.3 Control volume - different building height

In a realistic urban environment, it should be noted that buildings are designed with different heights, causing variety in the canyon aspect ratio at the microclimate setting. A CFD airflow domain is recommended to be built with the domain blockage ratio should not be more than 3 % to (Franke et al. 2007). Following this recommendation, a macro domain with two buildings in symmetrical height was compared to two macro domains with the canyon buildings were set in asymmetrical height, see the asymmetrical canyon height setup in two configurations as Figure 4.8.

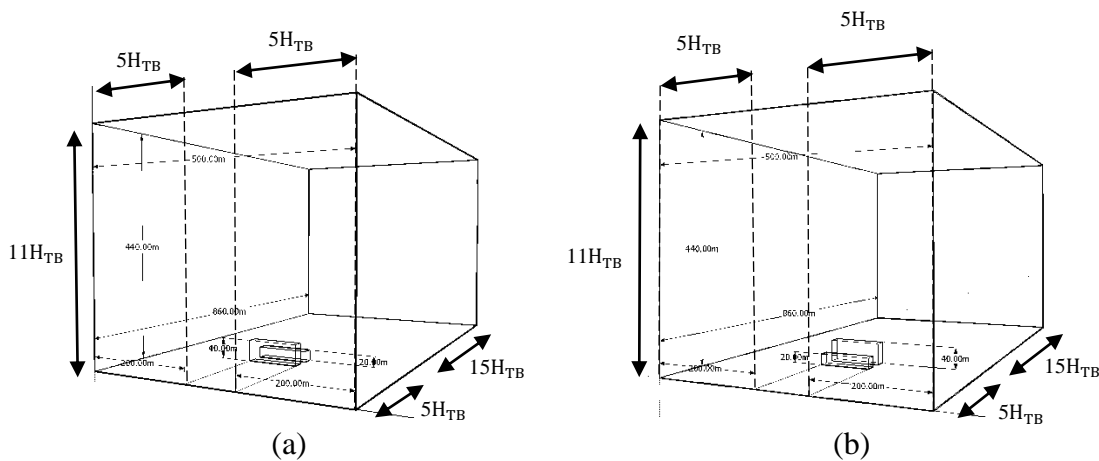


Figure 4.8 Comparison of (a) Building A is higher than Building B (b) vice-versa

As refer to Figure 4.8, the building length and width for the domains with asymmetrical urban canyon height were retained to the previous setting (100 m L \times 20 m W) to ensure the comparison between symmetrical and asymmetrical canyons was not influenced by the size of the domain, thus the changes in the Reynolds number for the comparative

domains were insignificant. This setting was ideal to resemble the condition of large and wide urban environment. The macro domain with asymmetrical canyon height was changed into two physical conditions: (i) first approaching building row, Building A has the height which was half the second approaching row, Building B – Type 1 (ii) Building A has the height which was double the Building B – Type 2. The tallest building height was set 40 m meanwhile the shortest building height was set at default, 20 m. To determine the size of the domain, the tallest height among the building, $H = H_{TB} = 40$ m became the reference.

4.2.2 Description of micro domain of the study

In this study, the 3D geometry of RPSC system was designed by embedding a 0.02 m (20 mm) diameter with 10 m length circular hollow copper pipe 0.15 m (150 mm) beneath a pavement surface. The pavement dimension was: 10 m L \times 1 m W \times 0.3 m thickness. Figure 4.9 describes the 3D model of 1 pipe RPSC system.

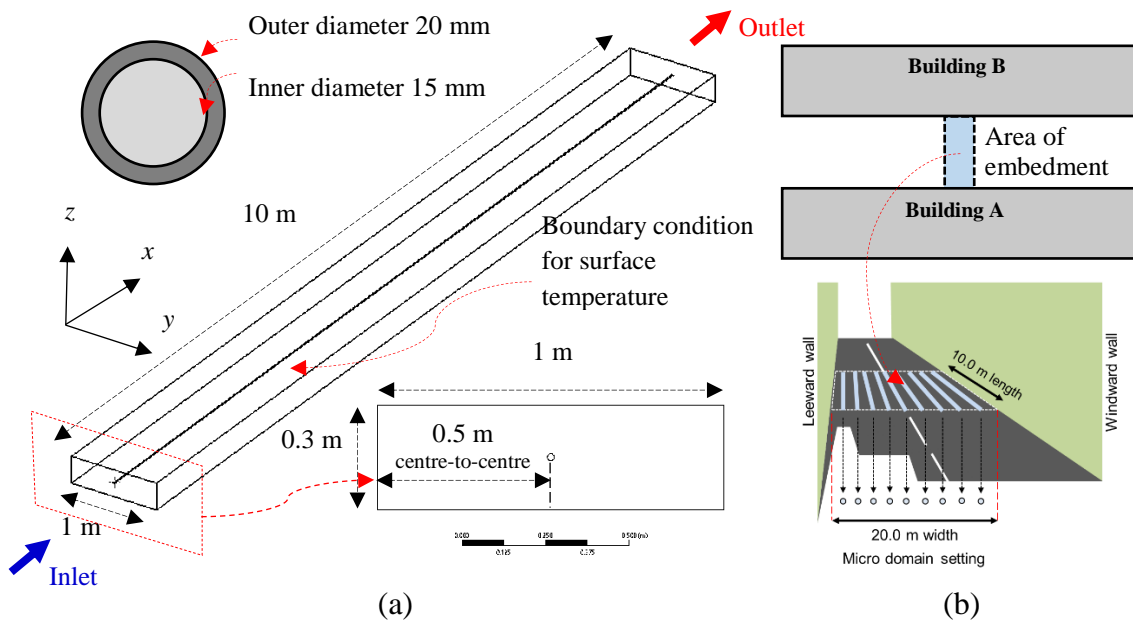


Figure 4.9 Description of 3D RPSC model with 1 pipe (a) size of domain, pipe and pavement body (b) pipe embedment within street canyon of urban domain

As Figure 4.9(a), the embedment of the pipe was set to be half of the pavement depth due to the assumption that there was a temperature influence from underground soil to the pavement layers apart from the influence from the surface temperature. The embedment of the pipe was located at the centre of the pavement width. Based on Figure 4.9(b), the location of the pipe embedment was shown to be approximately 10 % out of the pavement surface area of the macro domain. This was considered to avoid excessive number of mesh cell and high computational time if the pipe length was in full length following the length of the street canyon. The first pipe model was designed to be layered at the centre of the canyon with 1 m distance to the next pipe layer. With this technique, the similar pipe model can be used repeatedly for another surface location by applying an average temperature value on the pavement ground surface.

4.2.2.1 Adjustment in RPSC body with additional embedded pipes

4 RPSC pipes with the similar diameter were designed to be embedded 0.15 m (150 mm) beneath road surface of a pavement with the previous default dimension. Using 4 pipes in one pavement, the gap between the pipes was determined 0.25 m (250 mm). The previous work recommended that a feasible gap between hydronic RPSC pipes should be between 0.18 m (180 mm) and 0.4 m (400 mm) (Chen et al. 2011), thus the gap of 0.25 m becomes sufficient for this study. Figure 4.10 describes full specification of RPSC micro domain with 4 straight pipes that were layered 0.15 m beneath the pavement surface.

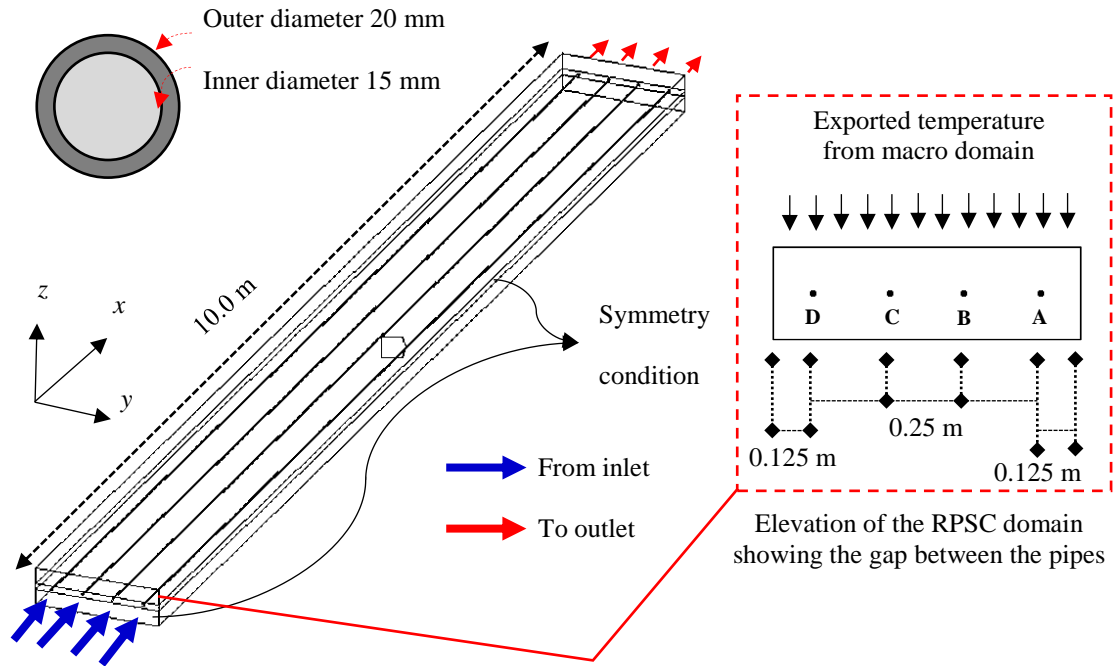


Figure 4.10 Configuration of RPSC domain with additional pipes (Pipe A - D) embedded beneath the surface layer

4.2.2.2 Comparison between straight pipe layout and serpentine pipe layout

Previous researches in optimising the RPSC performance have not included the comparison between the straight pipe layout (Type STP) and the serpentine pipe layout (Type SPP). In this study, the configuration of RPSC Type STP and Type SPP was determined with similar pavement body and its dimension except for the physic of the pipes. For Type STP, 4 straight pipes were layered 0.15 m (150 mm) beneath the pavement surface with 10.0 m length each meanwhile for Type SPP, 40.0 m full length serpentine pipe was coiled beneath the same depth, becoming 4 connected pipes layout at the similar pipe embedment as Type STP. Based on Figure 4.11, the similarity and the differences between RPSC Type STP and Type SPP are detailed with specification.

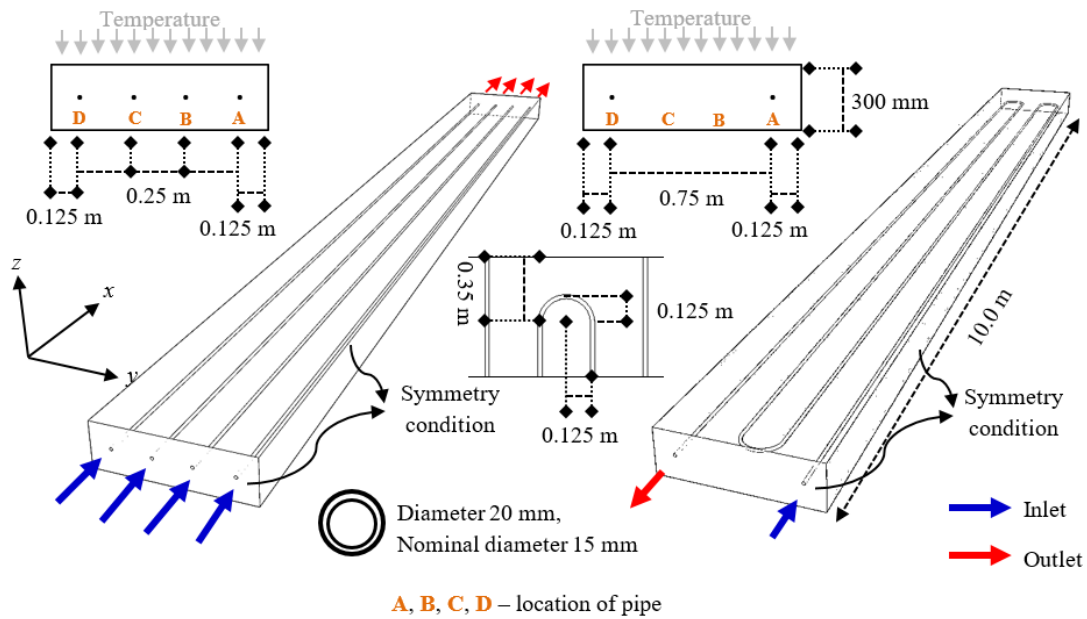


Figure 4.11 Configuration of RPSC domain with additional pipes (Pipe A - D) embedded beneath the surface layer

Type STP was designed with four inlets and with four outlets meanwhile Type SPP had only inlet and one outlet. The comparison between the two RPSC layouts leads to the analysis of the system application and performance on urban environment in reducing the surface temperature and in collecting potential temperature from an exposed pavement surface to the abundant solar radiation.

4.3 Mesh: type and setting

In this study, 3D urban domain with dynamic heat transfer and airflow consists of two building rows with similar and dissimilar aspect ratio and the main concern of the simulation is within microclimate zone; between surface level and roof level. The mesh selection for the domain should be compatible with its generic geometry form. Two types of mesh settings were used: unstructured mesh and structured mesh, see Section 4.3.1 and 4.3.2.

4.3.1 Macro domain - unstructured mesh

The first attempt of using Patch Independent Mesh Algorithm has generated hybrid cells (tetrahedron-hexahedral) for the macro domain. This method is a top-down approach where volumes were meshed first before faces and edges were meshed. Although with controlled cell sizing, all faces and edges were not necessarily conformed, thus consuming less computational time to generate unnecessary fine cells at non-essential areas. This type of method also good to be applied for poor quality CAD geometries. Figure 4.12 shows the top view of the 3D macro domain after mesh generation and the closed-up image of the generated cells for the building walls and street canyon ground surface.

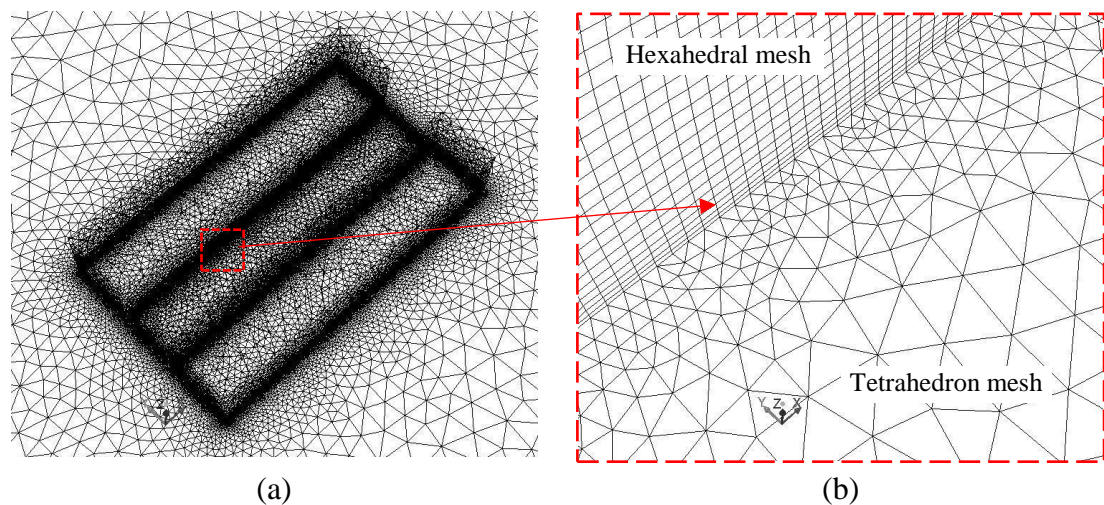


Figure 4.12 Mesh images by using Patch Independent Algorithm; showing (a) top view of generated mesh with finer mesh nearby street canyon and buildings (b) closed-up image of hybrid mesh (tetrahedron-hexahedral) within street canyon

As refer to Figure 4.12, the macro domain which consists of street canyon of AR 1 was initially set up with uniform edge for the cells at the building's length and width in x-axis and y-axis, respectively. For the cell edge at z-axis (building height), Inflation of 'First Layer Thickness' option was used to ensure the sizing of the cell edge was in bias

condition; which means smallest edge size was set closer to the ground and to the street canyon surface area and the cell edge afterward became larger. First Layer Thickness was the core influence of the generated cells for the macro domain. The first cell thickness was set 0.1 m with the maximum number of cell layer was 20 and the growth rate was set 1.2 as suggested in ANSYS Meshing.

4.3.1.1 Mesh independence test

Verification of the mesh accuracy was carried out to ensure the results generated based on the mesh setting are independent from the size of the cell. The concept of mesh independence study is based on mesh refinement which deals with the evaluation and refinement of elements where the subsequent error indicator is larger than the present criterion. With mesh improvement, higher order polynomials will keep running until the solution is expected to improve with a fixed mesh (Fluent 2009). Table 4.1 describes the comparison of mesh setting for mesh independence study of the model.

Table 4.1 Comparison of mesh setting for independence study

SIZE FOR BUILDING EDGES (LENGTH & WIDTH, m)	MESH DESCRIPTION	NO OF ELEMENT	NO OF NODE
1.00	Coarse, hybrid	609,332	213,514
0.50	Medium, hybrid	1,125,457	373,925
0.25	Fine, hybrid	2,063,739	659,968

This study used mesh refinement of h-method to optimise the distribution of mesh size, h over a finite element (Fluent 2009). Based on Table 4.1, three sizes set up for the building edges (length and width only) were determined. The comparison between coarse mesh, medium mesh and fine mesh was carried out based on three points (Point 1, 2 and 3) located within the street canyon; see Figure 4.13.

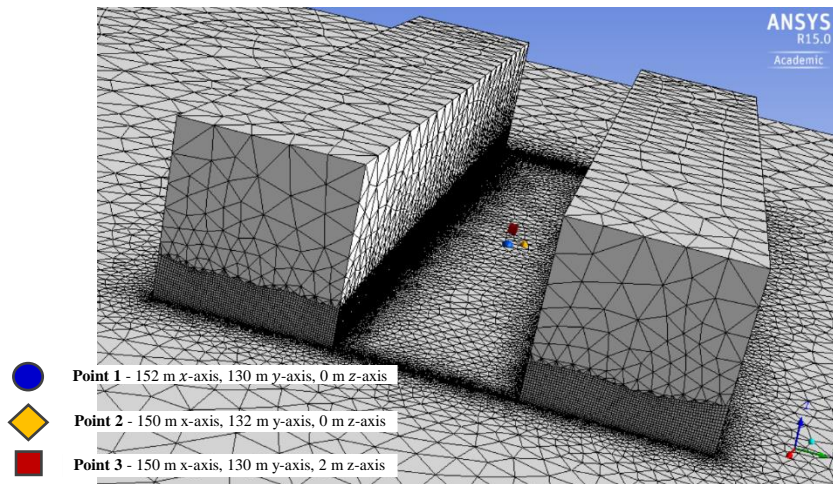


Figure 4.13 Mesh independence study based on the three location, Point 1, 2 and 3 within street canyon zone

Based on Figure 4.13, those three temperature points (surface temperature for Point 1 and 2; and air temperature for Point 3) were distanced 2 m away from the centre coordinate according to the axis; which the centre coordinate for the domain was given 150 m, 130 m and 0 m at x -axis, y -axis and z -axis, respectively. Temperature values plotted at the points were compared from coarse to medium and from medium to fine in Figure 4.14 and the increased rate in percentage (%) from Figure 4.14 was then calculated.

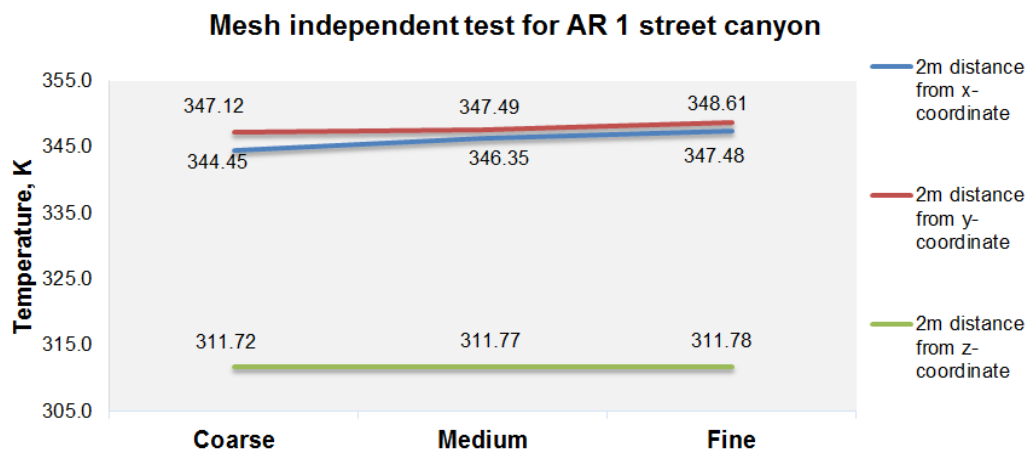


Figure 4.14 Temperature values plotted at Point 1, 2 and 3 according to Figure 4.13

Based on Figure 4.14, the increased rate in the temperature value for Point 1 was 0.55 % from coarse to medium and 0.33 % from medium to fine. Similar trend was found for Point 3 where the increased rate was 0.016 % from coarse to medium and 0.003 % from medium to fine. Based on this trend, refinement in the mesh setting helped to reduce the percentage difference of the compared temperature values. For Point 2, higher increased rate was observed between medium mesh and fine mesh (0.32 %) as compared to the value between coarse mesh and fine mesh (0.11 %), however the percentage difference seems nominal.

Overall, it was found that the average temperature dependency on mesh sizing was insignificant, thus the finest mesh model (fine mesh) with total element of 2,063,739 and total node of 659,968 was selected for the validation analysis in comparing the model with the benchmark case studies. The same setting for AR 1 was applied for empty domain (AR = 0) with the total element of 2,010,784 and total node of 731,198 which was used for the comparative analysis between urban domain (AR 1) and flat/rural domain (AR 0).

4.3.2 Macro domain - structured mesh

To ensure a structured mesh can be fully generated for macro domain, the domain volume was sliced into numbers of volume body before edge sizing was determined. The slicing technique can be done when one plane or surface becomes one reference for slicing, see the sliced macro domain with Automatic Meshing Method shown in Figure 4.15. Details on the structured mesh for the macro domain with higher aspect ratios and with different building height are described in Appendix A.2.

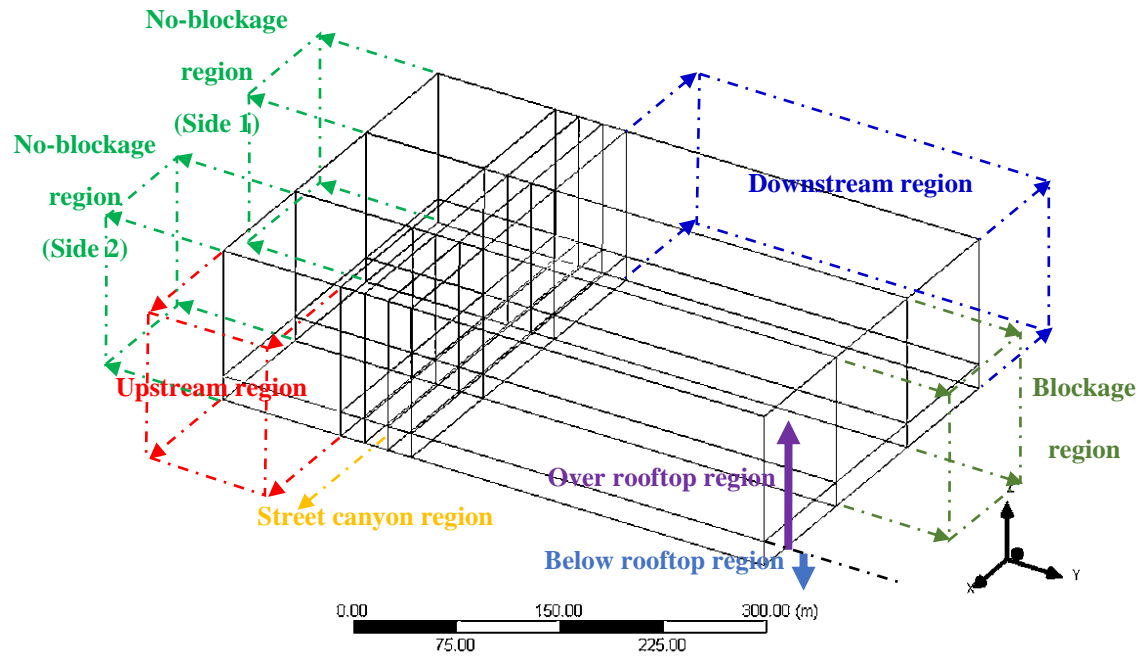


Figure 4.15 Mesh generation using Automatic Meshing Method with sliced volumes

Table 4.2 describes the edge sizing and bias values set for the macro domain with the aspect ratio more than 1.

Table 4.2 Mesh setting for macro domain with aspect ratio (AR) of 1, 2, 3 and 4

SOLUTION		COARSE MESH	MEDIUM MESH	FINE MESH
Cell information				
Total number of cell		1.2 millions	2.2 millions	4.9 millions
Edge sizing on macro domain				
(i)	Length between inlet and Windward Wall 1 Building A ($5H_{TB}$) on x axis (m)	8.0 with bias factor 10	6.0 with bias factor 10	4.0 with bias factor 10
(ii)	Length between inlet and Leeward Wall 2 Building B ($15H_{TB}$) on x axis (m)			
(iii)	Width between symmetrical wall and building edge walls ($3H_{TB}$) on y axis (m)			
Up to 20.0 m above ground surface (H_{0-20}) (m)		1.0 with bias factor 10		
Between 20.0 m and 40.0 m above ground surface (H_{20-40}) (m)		4.0 with bias factor 2		
Between 40.0 m and 60.0 m above ground surface (H_{60-80}) (m)		8.0 with bias factor 1.2		

Between 60.0 m and 80.0 m above ground surface ($H_{>80}$) (m)	10.0 with bias factor 1.5		
Above 80.0 m ground level to symmetry boundary wall ($5H_{TB}$) (m)	20.0 with bias factor 2.5		
<i>Edge sizing on building rows</i>			
(i) Length on x axis (m)	2.0	1.6	1.0
(ii) Width on y axis (m)			
(iii) Building height (H) on z axis (m)	1.0 with bias factor 10		

It should be noted that all edge sizing set for the macro domain were employed with hard behaviour, ensuring all generated cells were fully structured with symmetrical cell height. With bias factor, number of cell generated for large domain can be optimised by ensuring cell refinement at the necessary domain region, leaving other cell sizing to grow accordingly. Table 4.3 describes the mesh setting for the study which compared symmetrical and asymmetrical canyon heights.

Table 4.3 Mesh setting for macro domain with asymmetrical canyon height

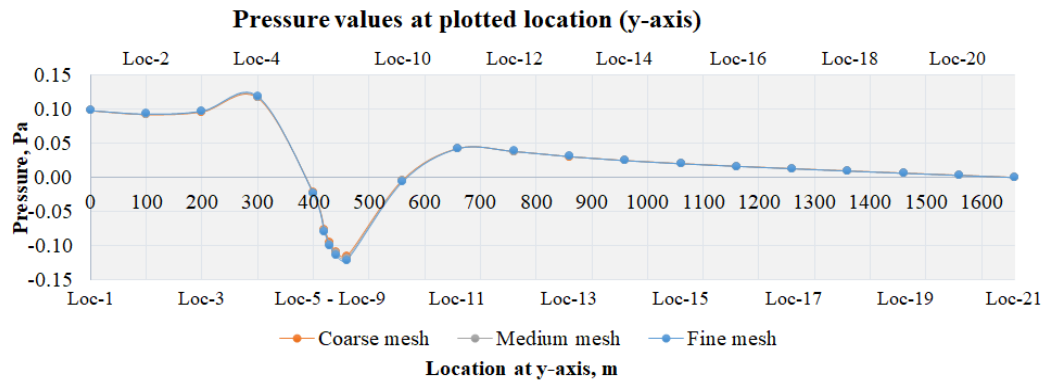
SOLUTION		COARSE MESH	MEDIUM MESH	FINE MESH
Cell information				
Total number of cell		2.2 millions	3.0 millions	4.8 millions
Edge sizing on macro domain				
(i) Length between inlet and Windward Wall 1 Building A ($5H_{TB}$) on x axis (m)		4.5 with bias factor 10	4.0 with bias factor 10	3.5 with bias factor 10
(ii) Length between inlet and Leeward Wall 2 Building B ($15H_{TB}$) on x axis (m)				
(iii) Width between symmetrical wall and building edge walls ($5H_{TB}$) on y axis (m)				
Up to 20.0 m above building height (H_{TB}) (m)		4.5 with bias factor 2	4.0 with bias factor 2	3.5 with bias factor 2
40.0 m above ground level to symmetry boundary wall ($10H_{TB}$) (m)		13.0 with bias factor 4	12.0 with bias factor 4	10.0 with bias factor 4
Edge sizing on building rows				
(i) Length on x axis (m)		1.15	1.0	0.85
(ii) Width on y axis (m)				
(iii) Building height (H_{TB}) on z axis (m)		1.15 with bias factor 10	1.0 with bias factor 10	0.85 with bias factor 10

The mesh independence test for all domains were carried out by using Reynolds Averaged Navier-Stoke (RANS) equations with the Standard $k-\varepsilon$ turbulent model with 2.0 m/s constant velocity at inlet plane coupled with turbulent intensity of 10.0 % and sand-grain roughness height k_s 1.0 m.

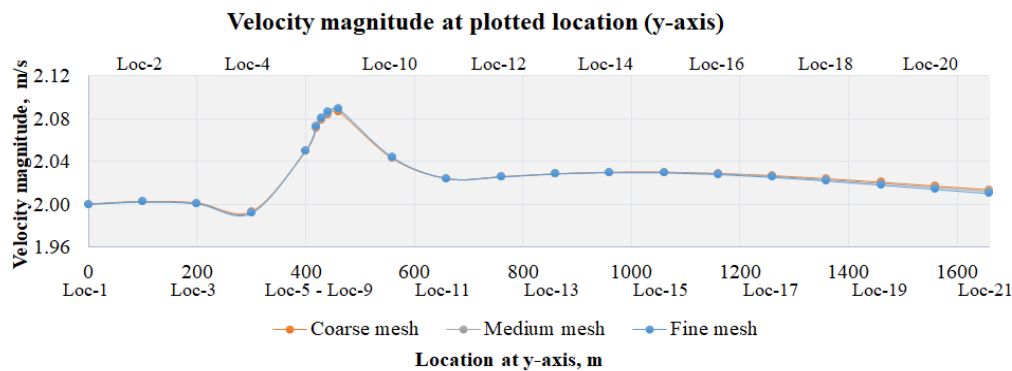
4.3.2.1 Mesh independence test

In Table 4.2 and Table 4.3, adjustment in the values of edge sizing was done to compare the generated number of cell for coarse mesh, medium mesh and fine mesh and to verify the independency of the simulation results from the influence of grid sizing and number of cell. Based on Table 4.2 which compares the mesh settings for different aspect ratio, AR (from AR 1 to AR 4), it should be noted that the additional number of cell generated for medium mesh was approximately 55 % more than the coarse mesh and approximately with 45 % additional cell generated for fine mesh as compared to the medium mesh. The result verification of the macro domain according to the mesh settings (coarse, medium, fine) was carried out only for the domain with default aspect ratio, AR 1. As the size of the domain with AR 1, 2, 3 and 4 was standardised from the beginning, there is no need to repeat the mesh independence study for all domains.

For the study that compared the setting of macro domain with different canyon aspect ratios, 21 points (Loc-1 – Loc-21) were plotted 20 m above the canyon rooftop or 100 m above the ground level (0 m) in z-axis across the length of the macro domain (in y-axis) and the distance was determined based on the length to be divided with the total number of plotted point, see the plotted pressure and velocity values in Figure 4.16(a) and Figure 4.16(b), respectively.



(a)



(b)

Figure 4.16 Mesh verification test based on 21 plotted points comparing (a) air pressure, Pa (b) air velocity magnitude, m/s

As refer to Figure 4.16, the blockage to the airflow (due to the existing urban canyon) has reduced the air pressure approximately 5 % while the air velocity at the height (100 m above ground level) was conversely increased with similar rate, see the values plotted between Loc-5 and Loc-9. Before reaching Building A, a steady wind velocity was observed in trend, however a slight drop in the velocity due to the blockage wall from Building A has caused air movement in spatial direction (x -axis, y -axis and z -axis) and reverse swirling to z -axis. After the airflow has passed over the street canyon region (Loc-9), the air velocity was reduced approximately 2.4 % due to the collision of high pressurised airflow behind Building B and the steady incline and drop in the velocity can be observed when the air reached the outlet plane, between 2.02 m/s and 2.04 % velocity.

Equation 4.13 explains the calculation of the percentage error comparing the mesh settings.

$$\text{Percentage error, \%} = \frac{[\text{Highest value} - \text{Lowest value}]}{\text{Value based on mesh type}} \times 100.0 \% \quad \text{Equation 4.13}$$

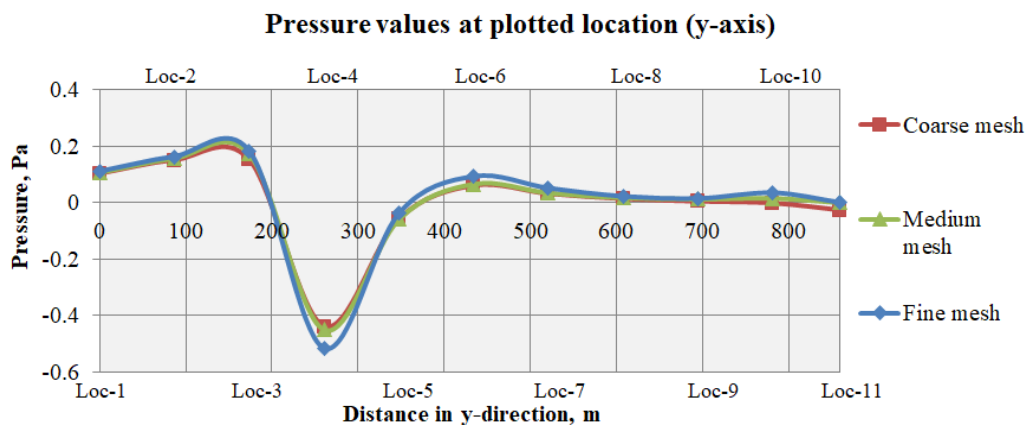
Where ‘Value based on mesh type’ should be rotated based on coarse, medium and fine values and the average value calculated from the sum value of 21 points were obtained. Based on the results, it showed that the average percentage error in % comparing the values of pressure and velocity magnitude that were plotted at all points of coarse, medium and fine mesh was nominal and insignificant (on average 0.4-1 % for pressure values and 0.0013-0.0028 % for velocity magnitude). Thus, based on the three mesh settings; medium mesh was selected as the optimum mesh for its optimum number of cell (not too low and not too high) according to computational time as compared to the other two mesh settings. Table 4.4 describes the information of mesh setting applied for the macro domain of aspect ratio (AR) 1, 2, 3 and 4.

Table 4.4 Cell information based on medium mesh setting for different aspect ratios

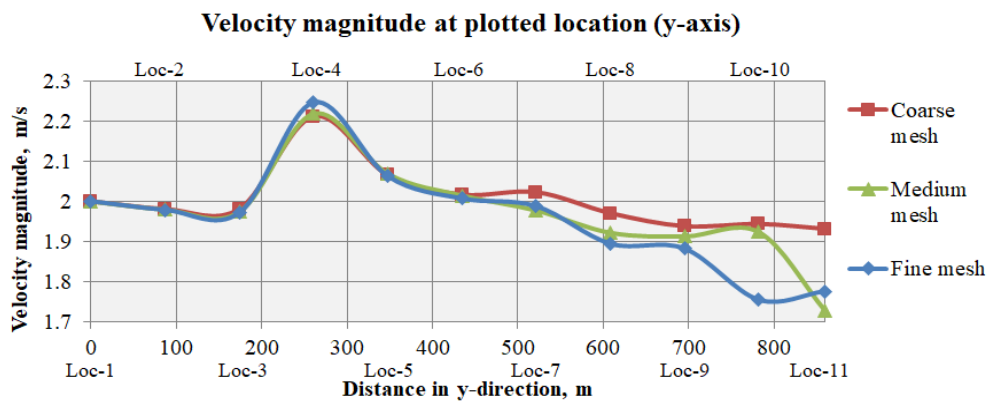
Cell information for medium mesh according to aspect ratio (AR)	AR 1	AR 2	AR 3	AR 4
Height, H	20.0 m	40.0 m	60.0 m	80.0 m
Canyon width, W	20.0 m	20.0 m	20.0 m	20.0 m
Height over width, H/W	1	2	3	4
No of node	2,224,848	2,217,408	2,212,944	2,209,968
No of Element/Cell	2,155,140	2,146,950	2,142,036	2,138,760
Percentage of reduction in number of cell against AR 1	NA	0.38 %	0.61 %	0.76 %

Based on Table 4.4, it was observed that the reduction in the number of cell from AR 1 to AR 2, to AR 3 and to AR 4 was nominal, on average 0.38-0.76 %, reaffirming the

unnecessary reason to repeat the mesh independence test for the domains with the canyon aspect ratio more than 1. Based on Table 4.3, the measurement of air pressure and air velocity magnitude based on 11 points plotted across the macro domain in y-axis was compared between the mesh settings (coarse, medium, fine) for the study of macro domain with asymmetrical canyon height, see Figure 4.17.



(a)



(b)

Figure 4.17 Mesh verification test based on 11 plotted points comparing (a) air pressure, Pa (b) air velocity magnitude, m/s

Those 11 points (Loc-1 - Loc-11) were located above 20 m from the height of the canyon rooftop or 60 m from the ground level (0 m) in z-axis and the distance between the points was based on equal division of the total domain length in y-axis to 11 points. Based on

Figure 4.17(a), it can be observed that the plotted trend of the pressure values for all mesh settings were comparable with nominal variation between fine mesh and the other two mesh settings from Loc-3 to Loc-7. It should be noted that the street canyon was located in between these plotted points. Although there was nominal variation observed at Loc-10 and Loc-11, it became unnecessarily important as compared to the points plotted closer to the region where street canyon was located.

The graph trend of air velocity magnitude plotted in Figure 4.17(b) was observed comparable only between Loc-1 and Loc-6 but the difference in the air velocity values seemed significant, between 0.5 m/s and 2 m/s for the plotted points after Loc-6. It was agreed that there was reduction in the velocity values for all mesh settings when the air reached the outlet plane thus the significant changes after passing the buildings were not significant for the study. The verification results have shown that too high cell number was not optimum to be used for the macro domain with asymmetrical canyon height. Medium mesh, which the results were observed not much different with coarse mesh was selected as the optimum mesh for further analysis.

4.3.3 Micro domain

For the micro domain which consists of 1 RPSC pipe, similar Automatic Meshing Method with pipe body sizing technique was used to determine the cells were in major hexahedral. It should be highlighted that the dimension of RPSC pavement was 10 m L \times 1 m W \times 300 mm thickness. The pipe body sizing means the size of the cell was determined based on the selection of pipe body to influence the size of the cells located afar from the pipe body, see the mesh generated for RPSC pavement and pipe in Figure 4.18.

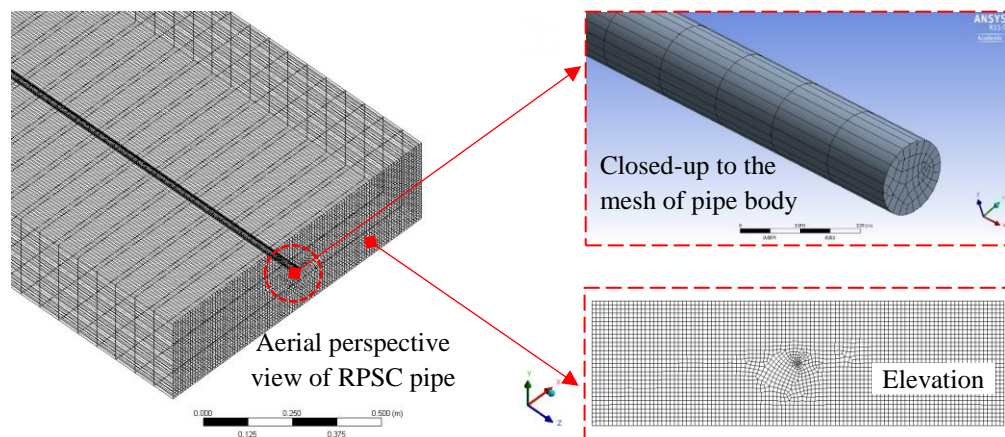


Figure 4.18 Mesh setting for RPSC pipe with Automatic Meshing Method

The same setup was applied for the comparison of straight pipes (STP) and serpentine pipes (SPP), see Appendix A.3 and Figure 4.19. Table 4.5 below shows the generated cells for Type STP and Type SPP in coarse, medium and fine.

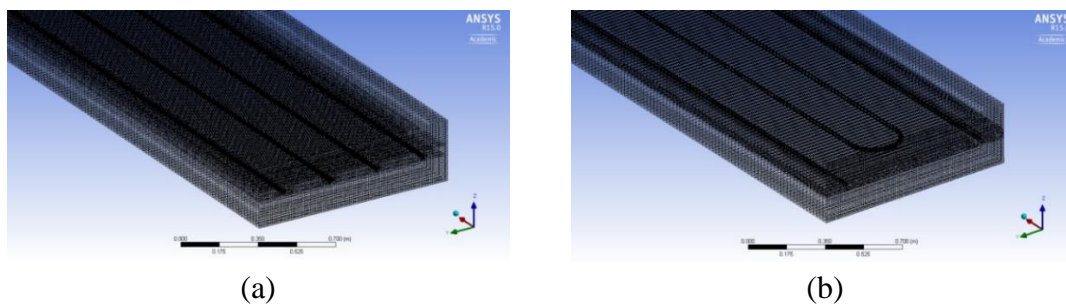


Figure 4.19 Mesh setting for RPSC pipe with Automatic Meshing Method

Table 4.5 Mesh independence study for STP and SPP

DESCRIPTION	COARSE MESH	MEDIUM MESH	FINE MESH
Length, m	0.0250	0.02250	0.0200
Width, m	0.0010	0.00975	0.0095
Thickness, m	0.0010	0.00975	0.0095
Pipe length, m	0.0250	0.02250	0.0200
No of cell - Type STP	1,414,800	1,625,140	1,979,000
No of cell - Type SPP	4,476,319	4,699,219	4,922,119

4.4 Boundary conditions

The simulation analysis was set following the experimental data in the city of Milan at the longitude of 9.18 °E, latitude of 45.47°N and the UTC of +1 during summer month (Bottillo et al. 2014). During this month, summer days in Milan are in the combination of hot temperature with less windy. This study imitated similar boundary condition set for the weather of the simulation due to the reason the previous published work (Bottillo et al. 2014) was validated with the experimental data set in several days of summer June. Thus, this study simulated the domain during 21st June at 13:00 noon.

4.4.1 Macro domain

During 21st June at 13:00 noon, the unobstructed air temperature was determined 303 K (30 °C) and the air velocity was 2 m/s. With air velocity 2 m/s, the turbulence intensity set for the inlet condition was 10 %. It should be highlighted this research applied the aerodynamic roughness $z_0 = 0.05$ set for ground surface was determined based on sand-grain roughness height k_s and roughness constant C_s (Bottillo et al. 2014; Blocken, Stathopoulos, et al. 2007). k_s was determined 1 m and C_s was determined 0.5 m; see Equation 4.14.

$$k_s = \frac{9.793z_0}{C_s} \quad \text{Equation 4.14}$$

Table 4.6 describes the boundary condition applied for ground road surface, soil and building walls.

Table 4.6 Boundary condition applied on ground surface, soil and building walls

DESCRIPTION	ROAD SURFACE	BUILDING WALLS
Temperature, K	288 (soil)	299
Density, kg/m ³	1000	1000
Specific heat, J/kg K	1000	1000
Emissivity	0.9	0.9
Thermal conductivity, W/m K	2	2
Surface thickness, m	5	0.3

4.4.2 Micro domain

Simulation of RPSC was carried out with the assumption number of pipes were embedded 0.15 m (150 mm) below the ground surface. Figure 4.20 compares the RPSC embedment beneath the ground surface with buildings and beneath a flat surface.

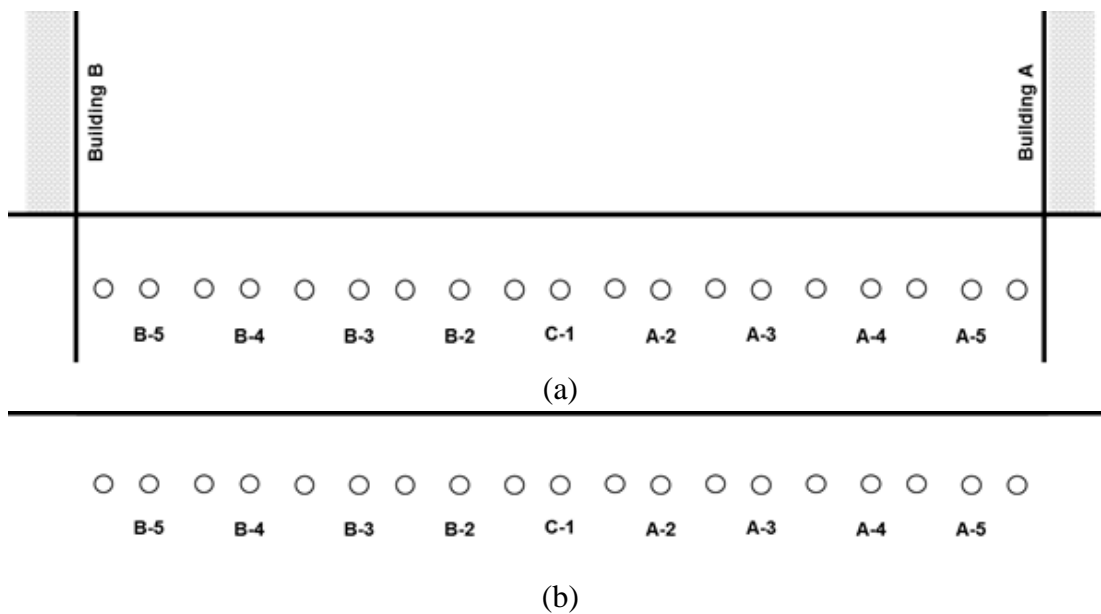


Figure 4.20 Location of pipes beneath ground surface (a) with buildings – urban macro domain (b) flat surface – flat/rural macro domain

As refer to Figure 4.20, 9 locations of pipe embedment were selected and renamed based on every two-location gap (2 m distance centre-to-centre between the first selected pipe location and the second selected pipe location). The pipe that was located at the centre of

the canyon was selected as the benchmark pipe location to determine the next pipe location. Based on this figure, pipe location C-1 became the centre pipe location and additional 4 pipe locations were selected towards Building A (pipe A-2, A-3, A-4 and A-5) and another 4 pipe locations were selected towards Building B (pipe B-2, B-3, B-4 and B-5). Similar pipe locations were selected for flat/rural macro domain.

For RPSC system, the default water velocity set at inlet plane was 0.1 m/s, assuming the speed of water was very low. The water temperature set for the domain was within an acceptable range, 293 K (20 °C) (Bobes-Jesus et al. 2013). Other details on boundary condition applied for RPSC domain including pavement surface, copper pipe wall and water flow are described in Table 4.7.

Table 4.7 Boundary condition applied on RPSC domain

DESCRIPTION	PAVEMENT SURFACE	COPPER PIPE WALL	WATER FLOW
Temperature, K	Not applied	Not applied	293
Density, kg/m ³	1000	8978	998.2
Specific heat, J/kg K	1000	381	4182
Emissivity	0.9	0.8	Not applied
Thermal conductivity, W/m K	2	387.6	0.6
Surface thickness, m	Not applied	0.005	Not applied
Internal temperature, K	288	Not applied	Not applied

Optimisation of RPSC system was studied based on four parameters involved with the system. Full description on the four parameters used for this study for 1 pipe simulation and 4 pipes simulation is summarised in Table 4.8.

Table 4.8 Summary of parameter values used for RPSC system

DESCRIPTION	PIPE DIAMETER	PIPE DEPTH	WATER VELOCITY	INLET WATER TEMPERATURE
1 pipe simulation Default value Range	0.02 m 0.015 m, 0.02 m, 0.025 m, 0.035 m, 0.05 m, 0.065 m, 0.075 m	0.15 m 0.025 m, 0.05 m, 0.075 m, 0.1 m, 0.125 m, 0.15 m	0.1 m/s 0.1 m/s, 0.25 m/s, 0.5 m/s, 0.75 m/s, 1 m/s, 1.25 m/s, 1.5 m/s, 2 m/s	293 K 278 K, 288 K, 293 K, 298 K
4 pipes STP Default value Range	0.02 m -	0.15 m -	0.1 m/s 0.1 m/s, 0.25 m/s	293 K -
4 pipes SPP Default value Range	0.02 m -	0.15 m -	0.1 m/s 0.1 m/s, 0.25 m/s	293 K -

4.5 Solution convergence criterion

For most CFD problems, default convergence criterion suggested in ANSYS Fluent is sufficient, which it requires the scaled residuals decrease to 10^{-3} for all equations except the energy and P-1 equations, which requires the scaled residuals to decrease to 10^{-6} . This criterion might not be appropriate to be used exclusively for certain situations. Thus, additional judgments or monitoring are required (Fluent 2009), such as:

- (i) To examine the unscaled residual and compare it with an appropriate scale.
- (ii) To examine the behaviour of the residual. This is to ensure that the residual continues to remain low for several iterations before concluding the solution has converged.
- (iii) To monitor integrated quantities, before concluding the converged solution.
- (iv) To examine the un-normalized unscaled residual and to determine if the residual is small compared to some appropriate scale.

4.6 Post-computer solution: performance calculation

In this study, the calculation of RPSC performance is quantified based on *Delta T*, Potential Temperature Collection, PTC (%) and Surface Temperature Reduction, STR (%) as per Equation 4.15, Equation 4.16 and Equation 4.17, respectively.

$$\Delta T \text{ (K)} = T_{w,o} - T_{w,i} \quad \text{Equation 4.15}$$

Where *Delta T* is based on the difference between the inlet water temperature, $T_{w,i}$ (K) and the outlet water temperature, $T_{w,o}$ (K). To calculate PTC, the derived value is obtained by percentage of *Delta T* per inlet water temperature value, $T_{w,i}$.

$$\text{Potential Temperature Collection, PTC (\%)} = \left(\frac{\Delta T}{T_{w,i}} \right) \times 100\% \quad \text{Equation 4.16}$$

The STR value is the percentage based on the deduction value of the surface temperature, $T_{1,s}$ (K) to the outlet water temperature, $T_{w,o}$ is required per surface temperature, $T_{1,s}$.

$$\text{Surface Temperature Reduction, STR (\%)} = \left(\frac{T_{1,s} - T_{w,o}}{T_{1,s}} \right) \times 100\% \quad \text{Equation 4.17}$$

In this study, the percentage of the system efficiency was calculated based on the deduction of the value of higher PTC/STR per the lower PTC/STR. For the efficiency and deficiency of the system, the calculation is as per Equation 4.18 and Equation 4.19.

$$\text{System efficiency (\%)} \text{ in PTC or STR} = \frac{\text{High value} - \text{Low value}}{\text{Low value}} \times 100\% \quad \text{Equation 4.18}$$

$$\text{System deficiency (\%)} \text{ in PTC or STR} = \frac{\text{High value} - \text{Low value}}{\text{High value}} \times 100\%$$

Equation 4.19

4.7 Method validation

The simulation work required validation (Bottillo et al. 2014; Shaopeng et al. 2011). However, it should be highlighted that this study has validated each domain based on an individual analysis due to no integrated study has been carried out before; thus, several published works were referred (Bottillo et al. 2014; Shaopeng et al. 2011; Uehara et al. 2000).

4.7.1 Validation for macro domain

For the validation of macro domain, the results were compared against the published work (Bottillo et al. 2014) in four analysis: (i) wind profile approaching the first building wall from the inlet plane, (ii) dimensionless air velocity profile in the canyon, (iii) dimensionless air temperature profile in the canyon, and (iv) ground surface temperature measured from selected points. Figure 4.21 shows the comparative air velocity profiles with the difference in the values between current model and the previous published work (Bottillo et al. 2014) were less than 1 % on average at all locations. The results from this figure were based on the unstructured mesh setting of macro domain with AR 1.

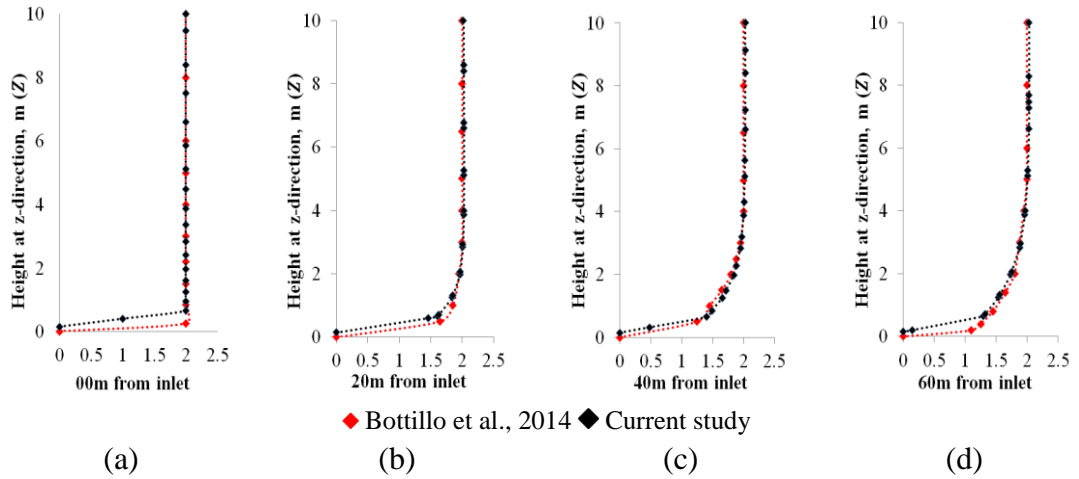


Figure 4.21 Validation of air velocity at four locations in y-axis (a) 0 m – inlet plane (b) 20 m away from inlet (c) 40 m away from inlet (d) 60 m away from inlet

Figure 4.22 displays the plot of the air velocity and air temperature profiles in between the canyon buildings against a wind tunnel experimental work (Uehara et al. 2000).

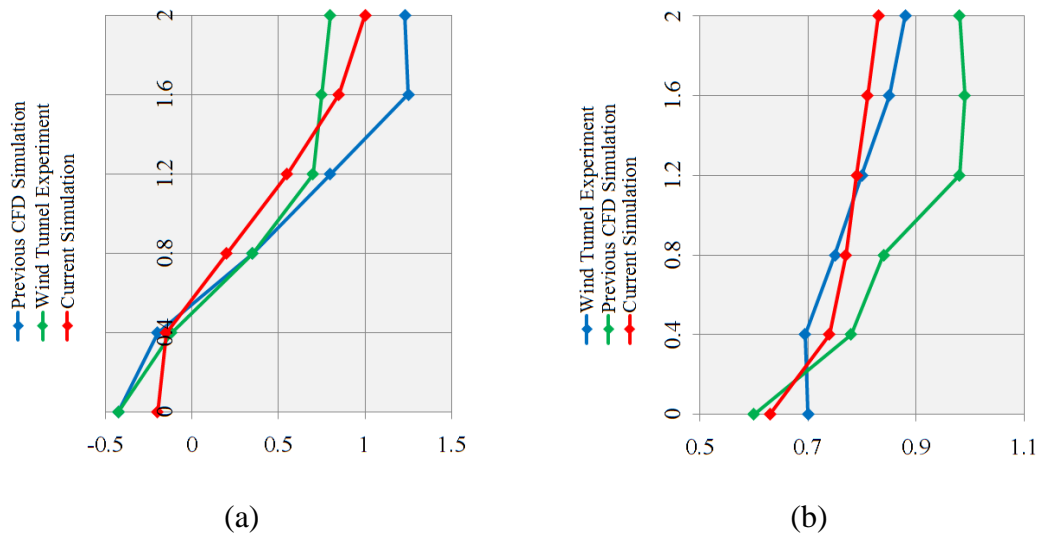


Figure 4.22 Macro domain validation of unstructured mesh, plotting (a) canyon wind velocity profile (b) canyon air temperature profile

It should be noted that the current model geometry was based on two building rows which created a long and narrow width canyon street (0.5 m length \times 0.1 m width \times 0.1 m height) meanwhile the experimental geometry was based on several blocks of Styrofoam cube

with dimension $0.1 \text{ m L} \times 0.1 \text{ m W} \times 0.1 \text{ m H}$ with the measurement carried out between the 5th block and the 6th block. The z -height profiles of $0.002 \text{ m} - 0.2 \text{ m}$ above ground surface were plotted in the very centre of the long canyon (290.0 m in x -axis). Overall, it can be observed that the current simulation satisfied trend of dimensionless air velocity and temperature profiles against a wind tunnel experiment as compared to the previously CFD simulation (Bottillo et al. 2014). Results showed that the error between the current simulation and wind tunnel was 4.57% on average and the average difference with the previous CFD simulation was 10.61% on average.

In Section 4.3.2, the unstructured mesh of macro domain was replaced with structured mesh of macro domain due to the assimilation of the generic canyon shape with the shape of rectangular macro domain. Based on Figure 4.23, it can be observed that the plotted trend of air velocity profile was in a better correlation with the experimental result as compared to the results generated for unstructured mesh.

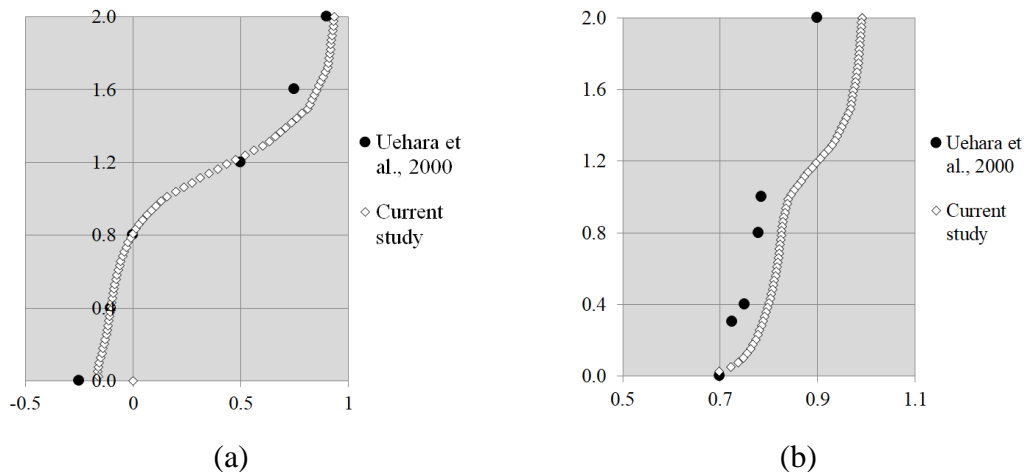


Figure 4.23 Macro domain validation of structured mesh, plotting (a) dimensionless canyon wind velocity profile (b) dimensionless canyon air temperature profile

In Figure 4.23, there was slightly overestimated values for the plotted points at 1.60 m above ground level. For the air temperature profile as per Figure 4.23(b), it was demonstrated that the plotted values for the profile at the centre canyon location had good validation against the experimental results specifically near to the ground as compared to the above roof top level.

For the analysis of (iv), the temperature at Point 1 gave minimal error, on average 5.33 % and for the Point 3, the percentage error was on average 13.8 %; see Figure 4.24. Point 2 obtained the largest variance although the graph trend was comparable with the reference work. It should be noted that the implemented DO model has dominant values for radiation intensities, causing slightly higher temperature was obtained by the shadowed surface area nearby Building B. Further details can be found in Chapter 5, which describes the analysis based on field measurement studies carried out in two urban canyons for Kuala Lumpur city centre including the shadow effects from buildings, trees and vehicles.

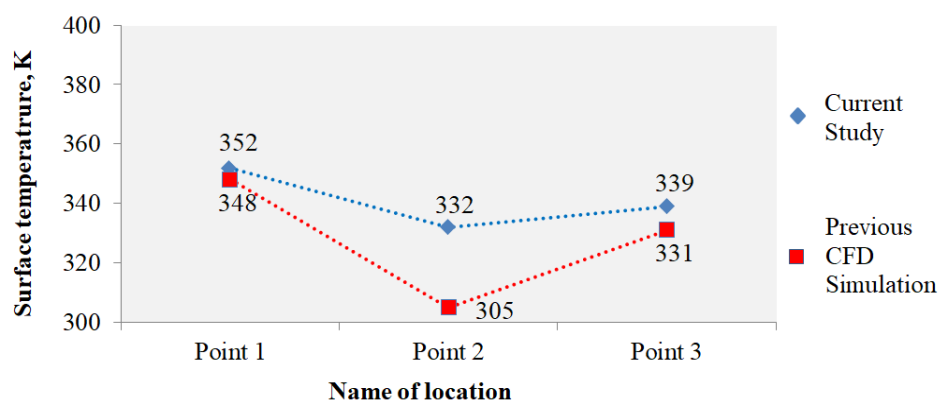


Figure 4.24 Validation of three temperature points at Point 1, 2 and 3 of ground surface

4.7.2 Micro domain method

The model method of the micro domain was validated against an experimental setup (Shaopeng et al. 2011) which controlled the surrounding temperature at $25 \pm 1^\circ\text{C}$. The pipe was modelled as per the experimental setup as shown in Figure 4.25.

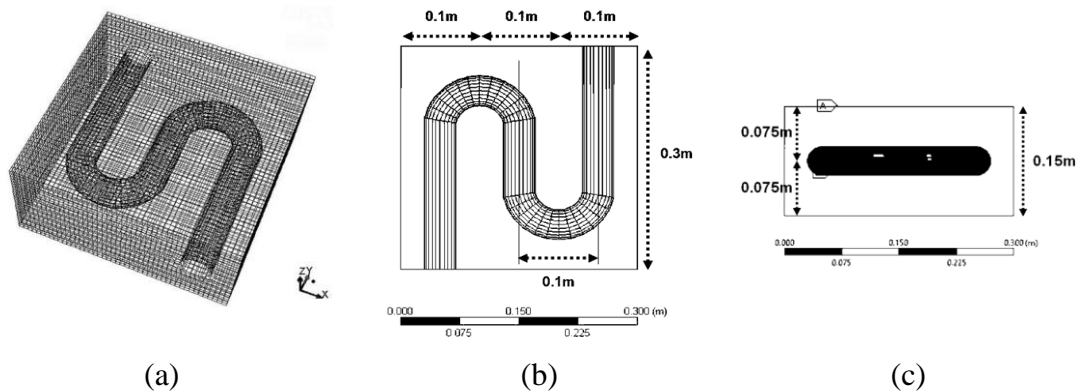


Figure 4.25 Method validation following the experimental work of (Shaopeng et al. 2011) (a) current meshing technique (b) plan dimension (c) depth dimension

To simplify the validation of the model, the surface heat flux of the micro model was set between 25 W/m^2 and 100 W/m^2 and the selection was based on the lowest percentage error when compared with the results of the laboratory test; see Figure 4.26.

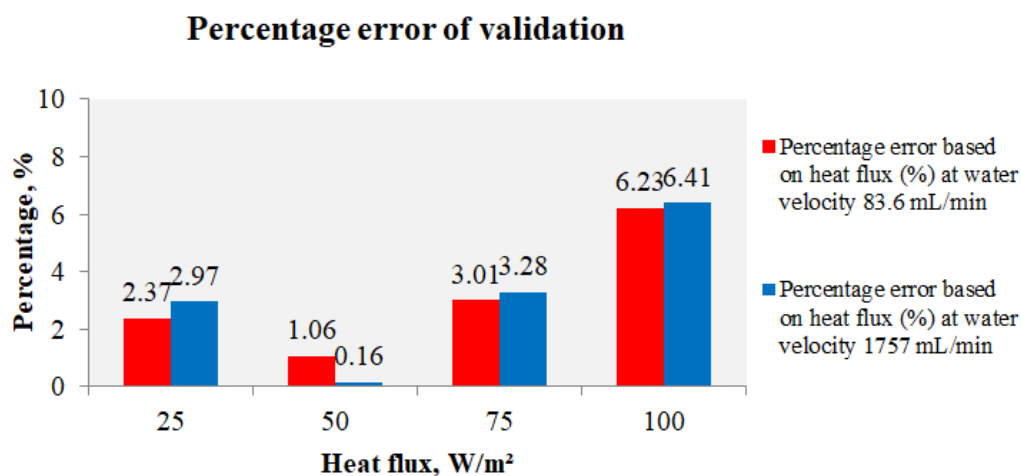


Figure 4.26 Selection of surface heat flux based on experimental validation error, %

Based on Figure 4.26, 50 W/m² surface heat flux provided the lowest percentage error for both water inlet velocities and was assumed to be the heat flux values in the experiment (Shaopeng et al. 2011). To further analyse and compare the current model with the laboratory work, the temperature distribution within the pavement depth was plotted (0.0 mm to 140.0 mm) and compared as displayed in Figure 4.27. Based on Figure 4.27, two flow rates were tested (Shaopeng et al. 2011) to evaluate the effect on the pavement's temperature distribution. The result demonstrated the heat transfer in top down direction; from the top surface to the bottom layers of the pavement. Based on Figure 4.27, it can be noticed that the simulation of the RPSC has slightly underestimated the experimental results (Shaopeng et al. 2011).

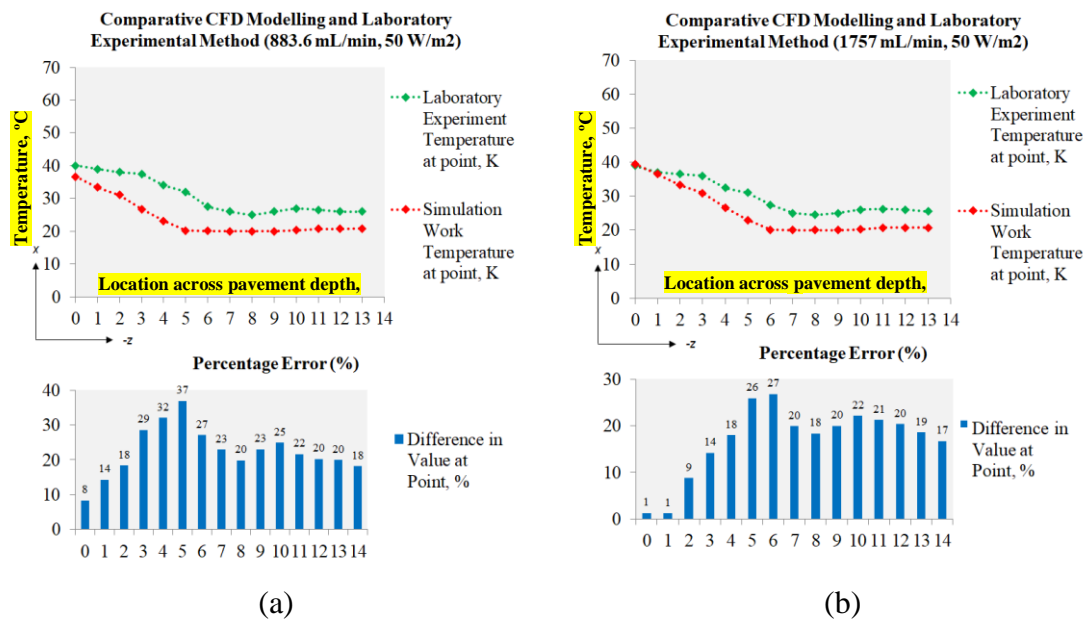


Figure 4.27 Trend comparison between the simulation and experimental results according to the depth from the surface of (a) 883.6 mL/min (b) 1757 mL/min

In the laboratory experiment, the surface of the RPSC specimen was exposed to the ambient of the room, causing the dynamic heat transfer in the bottom-up and the top-down directions while the circulating water in the pipe was reducing the pavement

temperature. It was mentioned earlier that the surface heat flux had to be assumed 50 W/m²; thus, there was no heat exchange occurring between the pavement surface and the external environment. However, it can be observed that the trend was similar as compared to the experimental results (Shaopeng et al. 2011) and the percentage error ranged 1-37 % depending on the plotted locations. It was observed with 1-27 % reduction the percentage error when smaller flow rate was changed to larger flow.

For the validation of micro domain with 4 pipes, the temperature trend plotted across pavement depth based on the medium mesh setting was compared with the previous experimental work of (Shaopeng et al. 2011) with the water flow rate 1757 mL/min with surface heat flux 50 W/m², see Figure 4.28. Results are presented as Figure 4.28 demonstrated with nominal error calculated for the medium mesh against the experimental temperature values, on overall with average 1.874 % which improved much on the previous micro domain validation. Out of 15 points, Point 3 has obtained the highest error value, not more than 5.0 %.

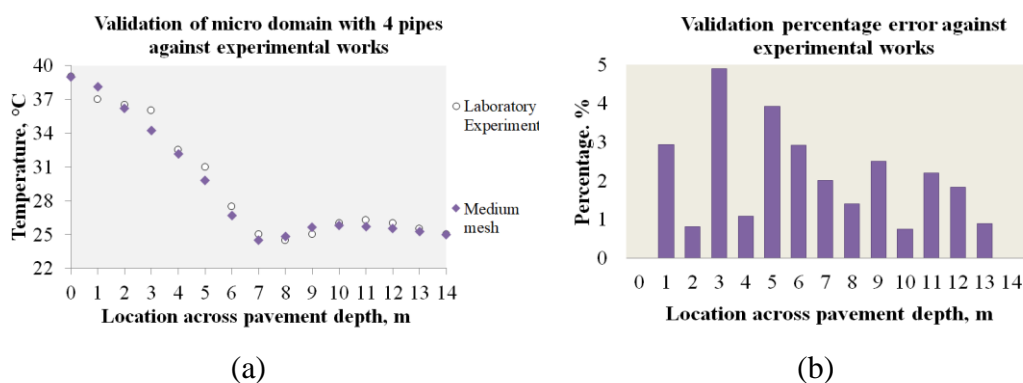


Figure 4.28 Validation of micro domain with 4 pipes against experimental results according to the depth from the surface with 1757 mL/min flow rate

4.8 Summary

In summary, Chapter 4 presented the computational method combining the modelling of macro domain which represents a simplified urban environment above ground surface with the modelling of micro domain which represents the below pavement condition with hydronic RPSC system. The ‘de-coupled’ ANSYS CFD codes with Standard $k - \varepsilon$ viscosity model combined Discrete Ordinate (DO) radiation model and Solar Load Model was initially verified based on mesh independent test in three mesh settings, coarse, medium and fine. Subsequently, the selected mesh setting was validated against published experimental data. Based on the comparison of the current simulation model with the published works, the simulation model was validated and used to investigate and achieve the aim and objectives of this study.

CHAPTER 5

Experimental methods

5.0 Introduction

This chapter presents the experimental work carried out to investigate thermal effect of building facades and road surfaces from two selected urban street canyons, named ROAD 1 and ROAD 2 during the month of August 2015 and month of March 2016. Section 5.1 details the rationale for using case studies in the investigation of thermal effect i.e. UHI effect within urban setting. Introduction to the background of the case studies with the description of the local weather conditions and street canyon configuration is available in Section 5.2. In Section 5.3, details of the methodology of the conducted experimental works including mobile measuring technique is fully explained together with indoor and outdoor calibrations tests. Section 5.4 demonstrated the analysis based on the data collection and the validation of the road and facade temperatures comparing the CFD modelling of the case studies and the data collection.

5.1 Rationale for experimental case studies

Previous work investigated UHI and urban heating by carrying out outdoor measurement work on case studies within the urban environment and topology (Voogt & Oke 2003; Kantzioura et al. 2012; Radhi et al. 2014; Taleghani 2017; Gülten et al. 2016; Karachaliou et al. 2016; Kleerekoper et al. 2015; Coutts et al. 2016). This established that temperature sensory devices assist in establishing the relationship between the impact of high surface temperatures with the surrounding environment. For example, the measurement of surface temperature showed higher indication of UHI effect with urban canyon configuration (Voogt & Oke 2003) meanwhile high absorptive surface materials were found to significantly increase the local ambient temperature which led to the increase in urban heating (Kantzioura et al. 2012).

Measuring surface temperatures were studied using detecting thermal infrared devices. The device with large area capacity such as airborne thermal infrared (TIR) remote sensing was used under an investigation of using small aircraft equipped with wide angle lenses (Voogt & Oke 2003). It was found that airborne thermal infrared remote sensing is an appropriate tool for larger monitoring due to its capacity of very high resolution (Coutts et al. 2016), however it showed weak correlation between land surface temperature and high air temperature.

Using a thermal infrared camera was found significant to correlate the interaction between human-physical factors and microclimatic conditions such as air-surface temperatures, airflow, solar radiation and humidity (Kantzioura et al. 2012). In this work, average surface temperature and temperature emitted from the surface for each building floor and facades was measured and calculated within 3-summer days in Thessaloniki, Greece for

12 hours. In the work of (Radhi et al. 2014), two types of UHI was highlighted to be surface temperature and air temperature. Higher surface temperature led to the increase of air temperature closer to the surface, thus the measurements included surface temperature, wind temperature, wind speed and direction were carried out.

Comparative analysis was found increasingly important to evaluate and validate the temperature measurement from urban surfaces. In the work of (Kleerekoper et al. 2015), results from the thermal infrared camera were validated with thermocouples in two settings (laboratory-scale urban canyon and full-scale outdoor urban canyon), showing the reduction in the temperature errors with the full-scale measurement setting. According to (Karachaliou et al. 2016), thermal infrared camera was used to capture the comparison between conventional roofing system and green roofing system. The after effect of installing trees along the street canyon was emphasised by using simulation model (Gülten et al. 2016), furthermore it was emphasised that the simulation model was initially validated from previous outdoor measurements using thermal infrared camera device.

5.2 Background of study: Kuala Lumpur conurbation centre

This study conducted data collection based on case studies of urban canyon selected within Kuala Lumpur conurbation centre on several days between 04th August and 15th August 2015 and on several days between 07th March and 18th March 2016. Kuala Lumpur is the capital city of Malaysia which has been recognised to be the main conurbation centre of the country (Elsayed 2012b). The city, where it becomes the major hub for commercial and industrial activities; is located in between the north and east of the mount of Titiwangsa, the Strait of Malacca to the west and the Port Dickson to the south (Yusuf et al. 2014). The city has huge impact on the surroundings development not

only to the east-west parts of between Gombak and Port Klang, respectively; but also towards the north-south parts of Negeri Sembilan and Rawang, respectively (Yusuf et al. 2014).

Since 2004, the city was populated with multi-storey buildings with activities circulated within the centre. In the same year, it was reported that the intensity in the air temperature was increased 1.5°C from the measurement taken in 1985, demonstrating the existence of UHI effect based on the growth in the city population and land use (Elsayed 2012a). The climate of Kuala Lumpur was evidenced with insignificant variation on the temperature itself; where the hottest monthly temperature is between 32 and 33°C meanwhile the coolest monthly temperature is 31°C (Elsayed 2012b).

According to the Malaysia Meteorology Department (MMD), Kuala Lumpur is a capital city with a hot humid climate where it is sunny and rainy throughout the year. Malaysia climate is characterised by two types of monsoon: (i) southwest monsoon; relatively drier weather which occurs between late May and September, and (ii) northeast monsoon; relatively heavy rainfall to the east coast states which occurs between November and March. Due to this, events such as flooding occurs annually to the lower ground and nearby river areas of several Malaysia states. From March 2016 to April 2016, a heat wave effect caused by El Nino had occurred in Kuala Lumpur, which happened during the investigation was carried out; causing difficulty in the data collection due to excessive hot weather condition with less windy and rainy as compared to the investigation days in August 2015.

5.2.1 Weather condition of Kuala Lumpur conurbation centre

The nearby weather station data collection for humidity and air temperature was taken from Sultan Abdul Aziz Airport, Subang where the location was 17.29 km distanced from Raja Chulan road, Kuala Lumpur. The station was referred for its almost completed information on local microclimatic condition. Figure 5.1 shows the map view of the distance between Sultan Abdul Aziz Shah Airport, Subang and Raja Chulan road, Kuala Lumpur.



Figure 5.1 Distance between the location of Sultan Aziz Shah Airport, Subang and the location of Raja Chulan road, Kuala Lumpur

In this study, all data was assumed to be measured at the similar elevation height, 58.6 m based on Weather Underground, see Appendix A.4. For the month of August 2015, average relative humidity, RH during the date of data collection was 77 – 85 % meanwhile mean air temperature was 302 K (29 °C). For the month of March 2016, average RH was 74 – 85 % meanwhile the mean air temperature was 303 K (30 °C); see Table 5.1.

Table 5.1 Parameter description and value based on local weather station

PARAMETER	VALUE
04th – 15th August 2015	
Weather station point and location	3.13 °N 101.55 °E, Sultan Abdul Aziz Shah-Subang, Malaysia
Elevation height of measurement	27 m
Average relative humidity, RH	77 - 85%
Mean air temperature	302 K (29 °C)
07th – 18th March 2016	
Weather station point and location	3.13 °N 101.55 °E, Sultan Abdul Aziz Shah-Subang, Malaysia
Measured height of measurement	21.95 m
Average relative humidity, RH	74 - 85%
Mean air temperature	303 K (30 °C)

Details on the wind speed, wind direction and cloud cover condition for the case studies according to date and time were described in Appendix A.5, retrieved from enclosed weather information provided by Malaysia Meteorological Department (MMD) based on Petaling Jaya weather station for month of August 2015 and by the data derived from Sultan Abdul Aziz Airport for month of March 2016.

5.2.2 Description of street canyon

The data collection on the climate of Kuala Lumpur was carried out based on the temperature images captured for the horizontal and vertical street canyon surfaces (road surface and building facades). The first data collection was carried out on the month of August which involved with two street canyon configurations. The first canyon configuration, Raja Chulan road was selected based on its regular straightforward street canyon layout, to be named ROAD 1. The second canyon configuration, Sultan Ismail road was selected based on its irregular rounded street canyon, to be named ROAD 2. Both street canyons were built in asymmetrical building height adjacent to one another. The data collection for both street canyons was carried out over 3 alternate days

experiencing real peak hour traffic condition. For ROAD 1, the date of measurement was taken on 4th, 6th and 8th of August 2015 and on 7th, 9th and 11th of March 2016. Meanwhile for ROAD 2, the date of measurement was taken on 11th, 13th and 15th of August 2015 and on 14th, 16th and 18th of March 2016. All data were measured during the working-day traffic intense; where both roadways are kept busy with vehicles from the early morning (before 09:00) until the late evening (17:00 – 20:00), see Figure 5.2.



Figure 5.2 Traffic intensity of ROAD 1 on 5th August 2015 (a) at 9 am (b) at 3 pm

Both roads consist of two-way lanes that provided public accessibility with traffic control. Table 5.2 details the comparative study of the number of vehicles passed by for the first 20 minutes for every two hours between 09:00 and 15:40 on 06th and 14th August 2015.

Table 5.2 Number of vehicle passed by ROAD 1 and ROAD 2

TIME	ROAD 1		ROAD 2	
	(a)	(b)	(a)	(b)
09:00 – 09:20	380	283	502	398
	663		900	
11:00 – 11:20	770	271	874	329
	1041		1203	
13:00 – 13:20	562	314	407	587
	876		994	
15:00 – 15:20	428	325	384	379
	753		763	
*** (a) Indicated as first lane (b) Indicated as the opposite lane				

For ROAD 1, surface temperature measurement was determined between the location points of 3.15 N 101.70 E and 3.15 N 101.71 E, calculated the total road length of 375.56 m. The configuration of the building row alongside the road is virtually in straight direction while the building entrances are virtually facing the road in the similar order. For ROAD 2, the measurement was determined between the location point of 3.15 N 101.70 E and 3.15 N 101.71 E. The road configuration was observed different than ROAD 1 where the road was designed in the combination of straight-curve shape until the road meets ROAD 1 at the three junctions of location point 3.15 N 101.71 E. The road configurations were generated from online Google Map in aerial perspective view as in Figure 5.3.

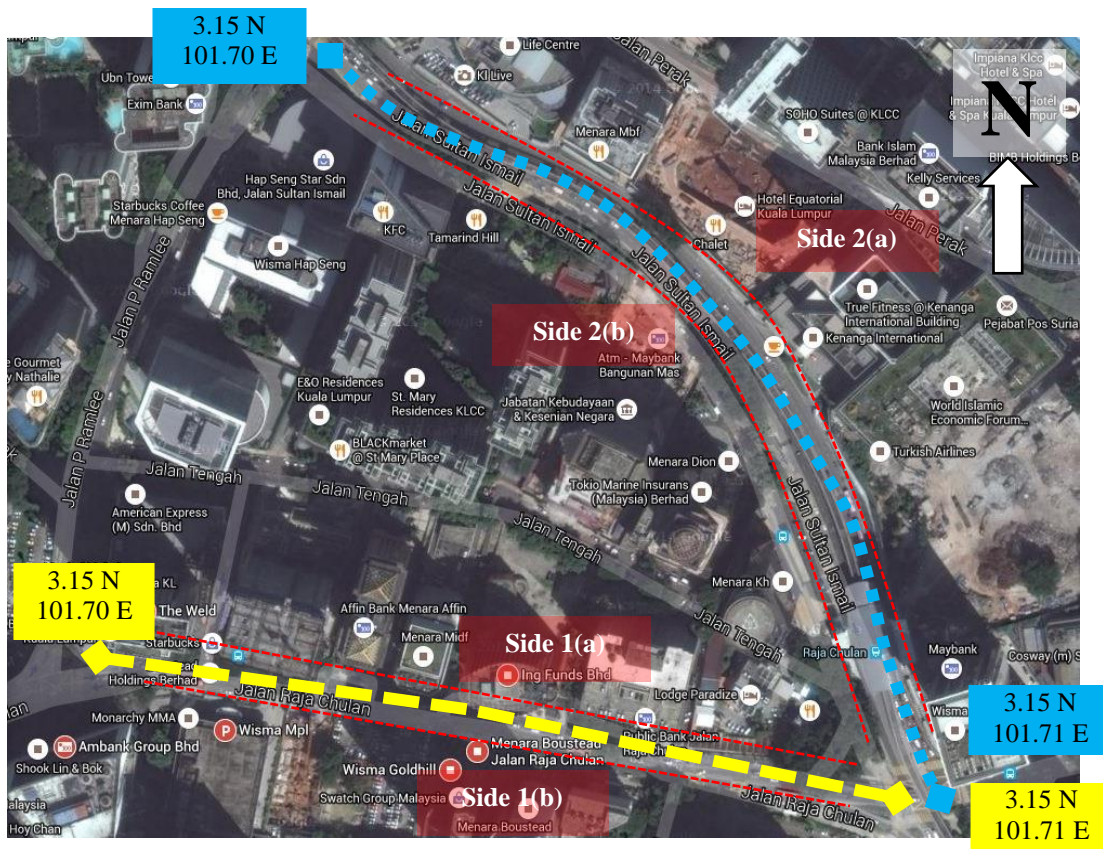
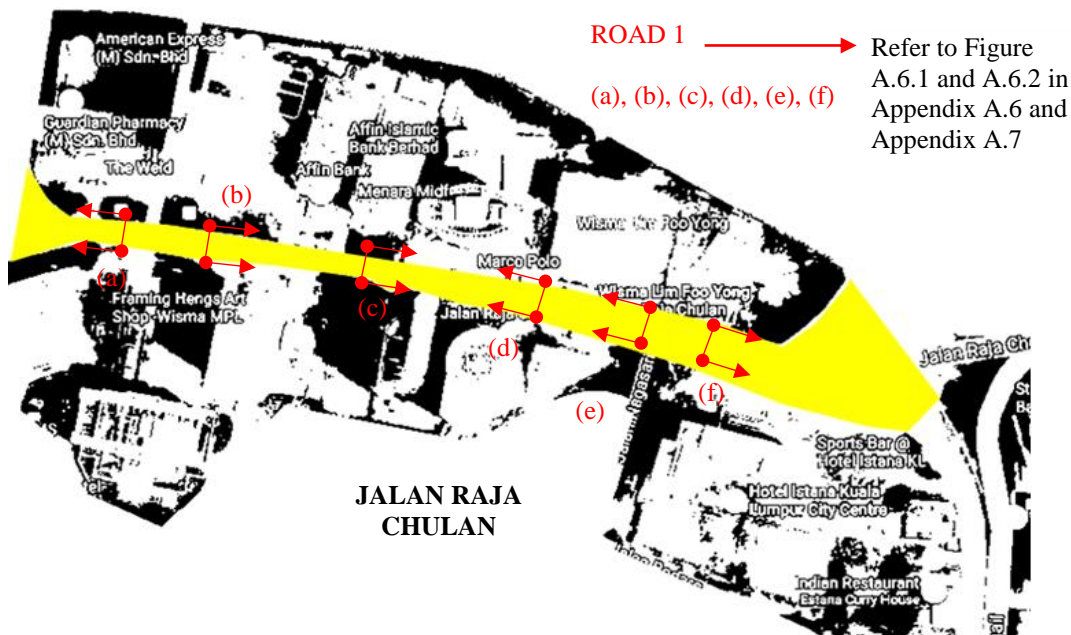


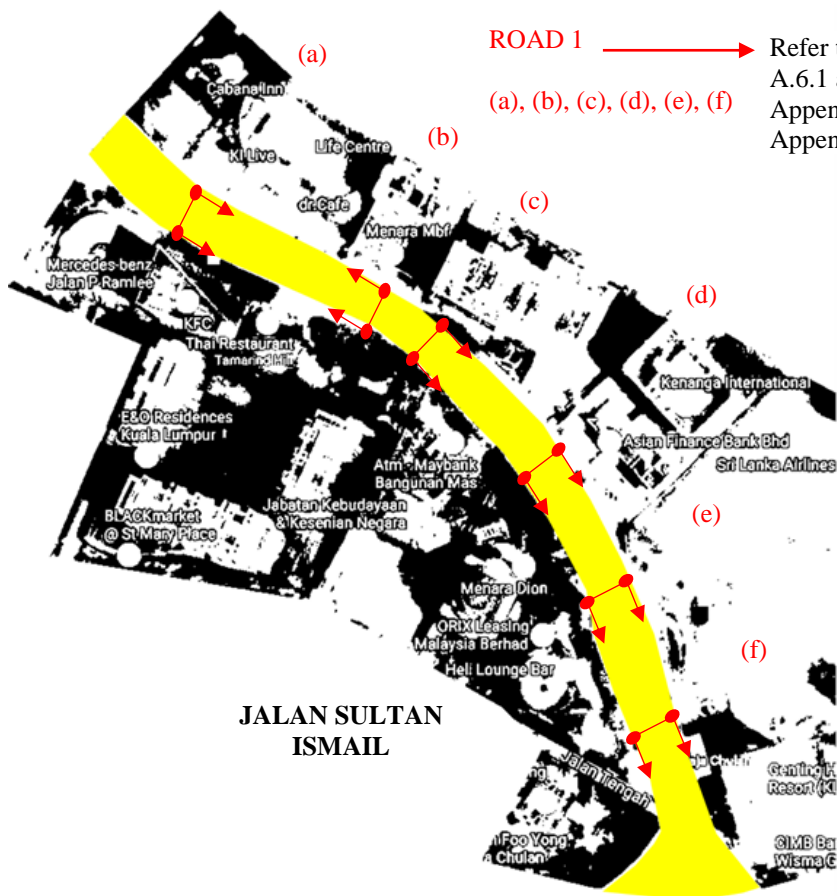
Figure 5.3 Roadways configuration (a) ROAD 1 - yellow (b) ROAD 2 – blue. Side (a) means the left side of the canyon meanwhile Side (b) means the right side of the canyon.

In Chapter 4 under Section 4.2, the aspect ratio of generic urban canyon was categorised in symmetrical and asymmetrical types. For symmetrical canyon aspect ratio was categorised into four ratios; AR 1, AR 2, AR 3 and AR 4. Meanwhile, for asymmetrical type; two settings were categorised into Asymmetrical canyon height Type 1 (AC1) and Asymmetrical canyon height Type 2 (AC2). The compatibility of the computational urban canyon in both types (symmetrical and asymmetrical) with the experimental case studies of ROAD 1 and ROAD 2 was carried out by determining the aspect ratio of both roads. The realistic configuration of urban canyons in Kuala Lumpur conurbation centre was observed to be built with complex building shapes and height, resulting with different aspect ratio of H/W of the canyon's left side to the aspect ratio of H/W of the canyon's right side. Thus, several individual aspect ratios from ROAD 1 and ROAD 2 was determined to evaluate the compatibility of the computational urban canyon with the urban canyon from the case studies.

As refer to Figure 5.3; to determine the aspect ratio of ROAD 1 and ROAD 2, the total height of one building from Side (a) and the total height from the adjacent building from Side (b) were determined. The calculation of the aspect ratio, H/W of the canyon street for ROAD 1 and ROAD 2 was modified from the 'height of building H' to the 'average height of building from Side (a) and Side (b) over width of the road W due to dissimilar height of the buildings facing one another alongside the concentrated roads. Thus, 6 cross-sectional elevations were determined to evaluate the aspect ratio, see Figure 5.4. Description on the reference building height within ROAD 1 and ROAD 2 which determined the aspect ratio of the sectional elevations of Section (a)-(f) is detailed in Appendix A.6.



(a)



(b)

Figure 5.4 Plan view showing 6 cross-sectional elevations; Section (a)-(f) for the street canyon studies of (a) ROAD 1 (b) ROAD 2

Based on Figure 5.4 and Appendix A.7, individual aspect ratio and average aspect ratio of ROAD 1 and ROAD 2 combining the aspect ratio of Side (a) and Side (b) was calculated and to be summarised Table 5.3 below. Additionally, Table 5.3 also describes its compatibility with the computational canyons as described in Chapter 4 Section 4.2.

Table 5.3 Canyon aspect ratio of 6 cross-sectional elevations in ROAD 1 and ROAD 2


DESCRIPTION	ASPECT RATIO, AR					
	Section (a)	Section (b)	Section (c)	Section (d)	Section (e)	Section (f)
ROAD 1	5.96	1.00	2.45	5.42	0.50	0.69
Side (a)	6.65	1.69	4.89	4.85	0.32	0.12
Side (b)	5.28	0.31	0.00	5.98	0.68	1.26
Configuration	S	AC1	NFBR	S	S	AC2
Compatibility to generic urban canyon in Chapter 4	AR 4	AC1	Not applied	AR 4	AR 1	AC2
Average canyon aspect ratio				2.67 ≈ 3.00		
ROAD 2	1.00	0.71	0.74	0.98	1.47	1.76
Side (a)	0.18	0.58	0.00	0.22	0.00	3.52
Side (b)	1.81	0.83	1.47	1.74	2.95	0.00
Configuration	AC1	AC2	NSBR	AC2	NSBR	NFBR
Compatibility to generic urban canyon in Chapter 4	AC1	AC2	Not applied	AC2	Not applied	Not applied
Average canyon aspect ratio				1.11 ≈ 1.00		

Example of measuring aspect ratio (AR) of Canyon ROAD 1 Section (d)

Aspect Ratio of Side (a) =

Total height (H) of building in **Yellow Line**

Total width (W) of ROAD 1 in **Blue Line**



Aspect Ratio of Side (b) =

Total height (H) of building in **Green Line**

Total width (W) of ROAD 1 in **Blue Line**

Average Aspect Ratio of Side (a) and Side (b) =

$$\frac{(\text{Aspect Ratio (H/W) of Side (a)} + \text{Aspect Ratio (H/W) of Side (b)})}{2}$$

*** H = Height of one sided building, W = width between two adjacent buildings

*** Average canyon aspect ratio for each section was calculated based on

= ((H/W Side a) + (H/W Side b) / 2

*** Average canyon aspect ratio alongside ROAD 1 and ROAD 2 was calculated based on

= (sum of H/W for all sections) / 6

*** S = Symmetrical canyon height, AC1 = Asymmetrical canyon height Type 1, AC2 = Asymmetrical canyon height Type 2, NFBR = No first building row, NSBR = No second building row,

5.3 Temperature measurement using infrared thermal camera

In this study, evaluation of outdoor temperature of building facades and ground surfaces was carried out using a series of infrared thermal imaging device FLIR T650sc. Figure 5.5(a) shows the complete set of FLIR T650sc consisting the infrared thermal imaging camera, additional battery pack with standby mode, battery charger and memory card with the capacity of 32 GB. Figure 5.5(b) displays the camera monitoring screen during the first trial of capturing thermal image.

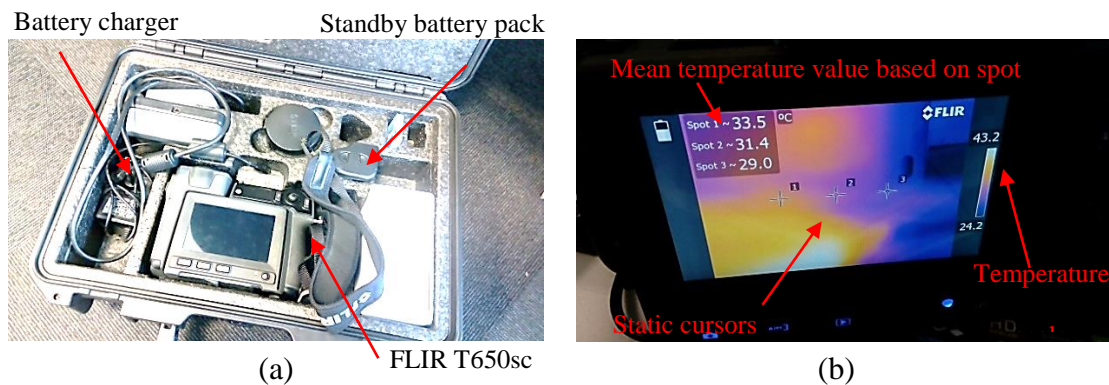


Figure 5.5 Product display of (a) one whole package of FLIR T650sc (b) infrared contours and static cursors detected temperatures on three spots

This camera is built up with the resolution of 640×480 pixels within the temperature range of -40°C and 2000°C and with the thermal sensitivity as low as 0.02°C at 30°C . The sensitivity of the camera lenses is $\pm 1^{\circ}\text{C}$ with higher range for the measurement of ambient temperature. FLIR T650sc has the image frequency of 30 Hz with the spectral range between 7.5 and $14\text{ }\mu\text{m}$. Two packs of batteries which were completed with battery charger were brought during the data collection and one of the battery packs was on a standby mode. The camera is built up with external memory card slot; thus, for this study, a memory card with the capacity of 32 GB was used during the data collection. The camera is built with the setting of automatic temperature scale on the right side of the camera monitoring screen and mean temperature values appeared on the upper left side,

which was derived based on static cursors built on the screen. For accurate measurements, object parameters such as emissivity, reflected apparent temperature, object distance, atmospheric temperature and relative humidity are recommended to be set. Measuring temperature of urban surfaces can be complicated due to various types of building materials and emissivity. To avoid the complexity in determining each of the surface parameter values, parameter values recommended by the FLIR T650sc user manual was referred except for object distance that was changed from 1 m to 100 m (due to the maximum distance of the camera with surfaces) and relative humidity from 50 % to 80 % (as following local weather station), see Table 5.4.

Table 5.4 Object parameter using FLIR T650sc user manual

OBJECT PARAMETER	VALUE
Atmospheric temperature	+ 20 °C
Emissivity	0.95
Object distance	100 m
Reflected apparent temperature	+ 20 °C
Relative humidity	80 %

5.3.1 Experimental setup: mobile measuring technique

The process of thermal imaging at ROAD 1 and ROAD 2 using FLIR T650sc was carried out based on hourly interval between 09:00 and 16:00 am. Mobile measuring technique was introduced in this study by walk and stop alongside the street canyon of ROAD 1 and ROAD 2 for capturing the temperature of building facades and road surfaces. For large and tall buildings, FLIR T650sc is provided with the ability to adjust the angle of the camera lens to fit in the building facades in the monitoring screen from 0 ° to 90 °. Further explanation on the technique can be found in Figure 5.6 and Figure 5.7.

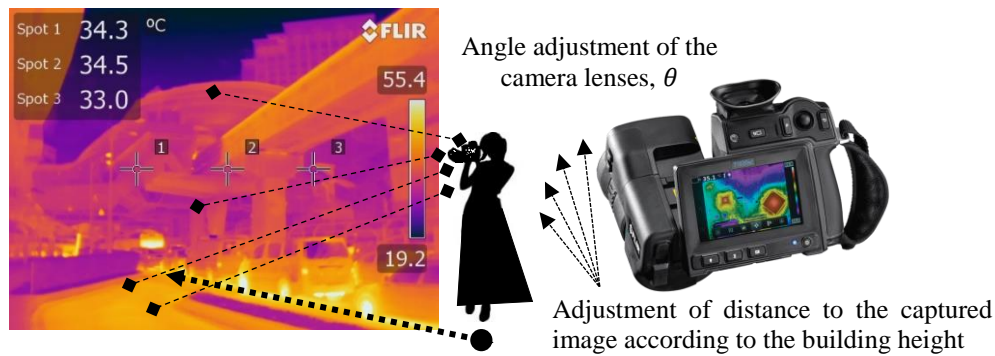


Figure 5.6 Mobile measuring technique of thermal imaging process for ROAD 1 and ROAD 2 based on walk and stop at both road lanes

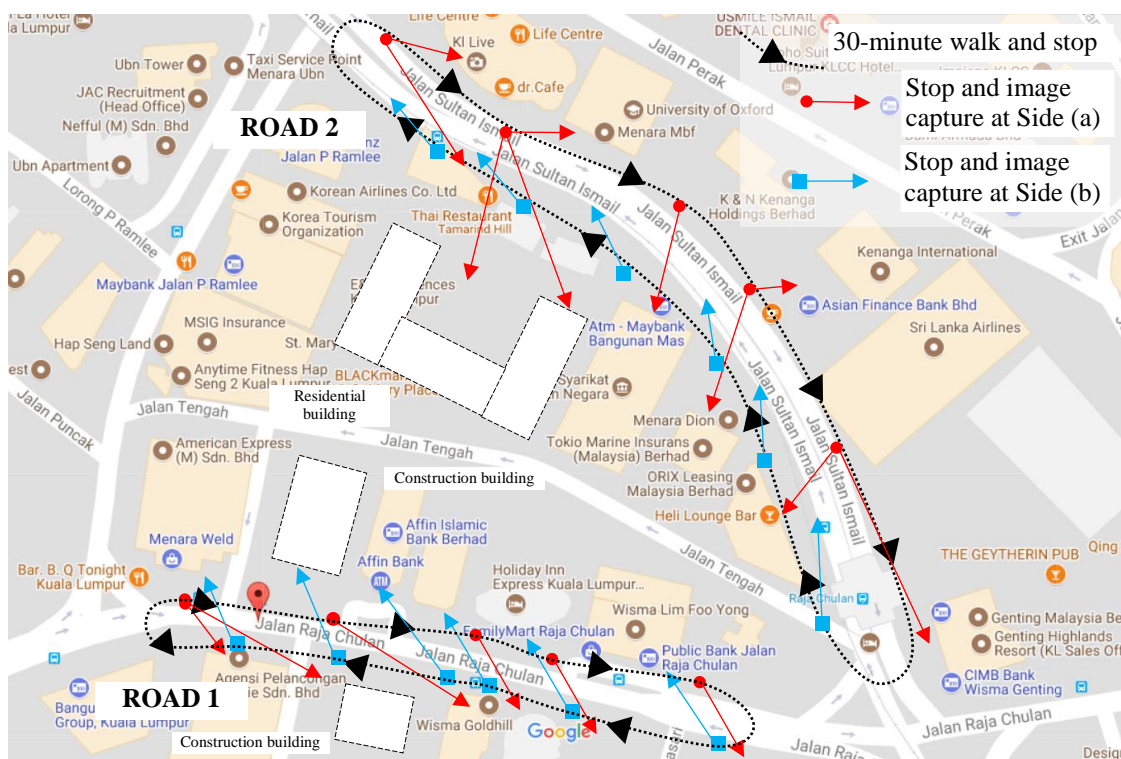


Figure 5.7 Cycle of thermal imaging process in 30 minutes for every 1-hour interval between 09:00 hour and 16:00 hour for ROAD 1 and ROAD 2

As per Figure 5.7, one-way walk and stop required 15 minutes' time, thus for two-way walk and stop, time consumed up to 30 minutes. There are two reasons of doing a U-turn walking and stop technique: (i) difficulty to capture the image of buildings from one-sided road due to size, and (ii) average surface temperature from both sideways can be obtained due to unknown material parameters set for the captured surface images. It was

also estimated between 80 and 100 snapshots were taken on overall surface per canyon road; resulting 240-300 surface spots were measured for a complete cycle. For ROAD 1 and ROAD 2, the first measurement point was located on the coordinate of 3.15 °N 101.70 °E and 3.15 °N 101.70 °E, respectively before one complete cycle was completed at the same point and before the next hour time step began. Example of data collection using FLIR T650sc is shown in Figure 5.8, representing the infrared thermal images of ROAD 1 at Section (A), which consist of building facades from Side 1 and Side 2 and road surface. Full thermal data collection can be referred to Appendix A.8.

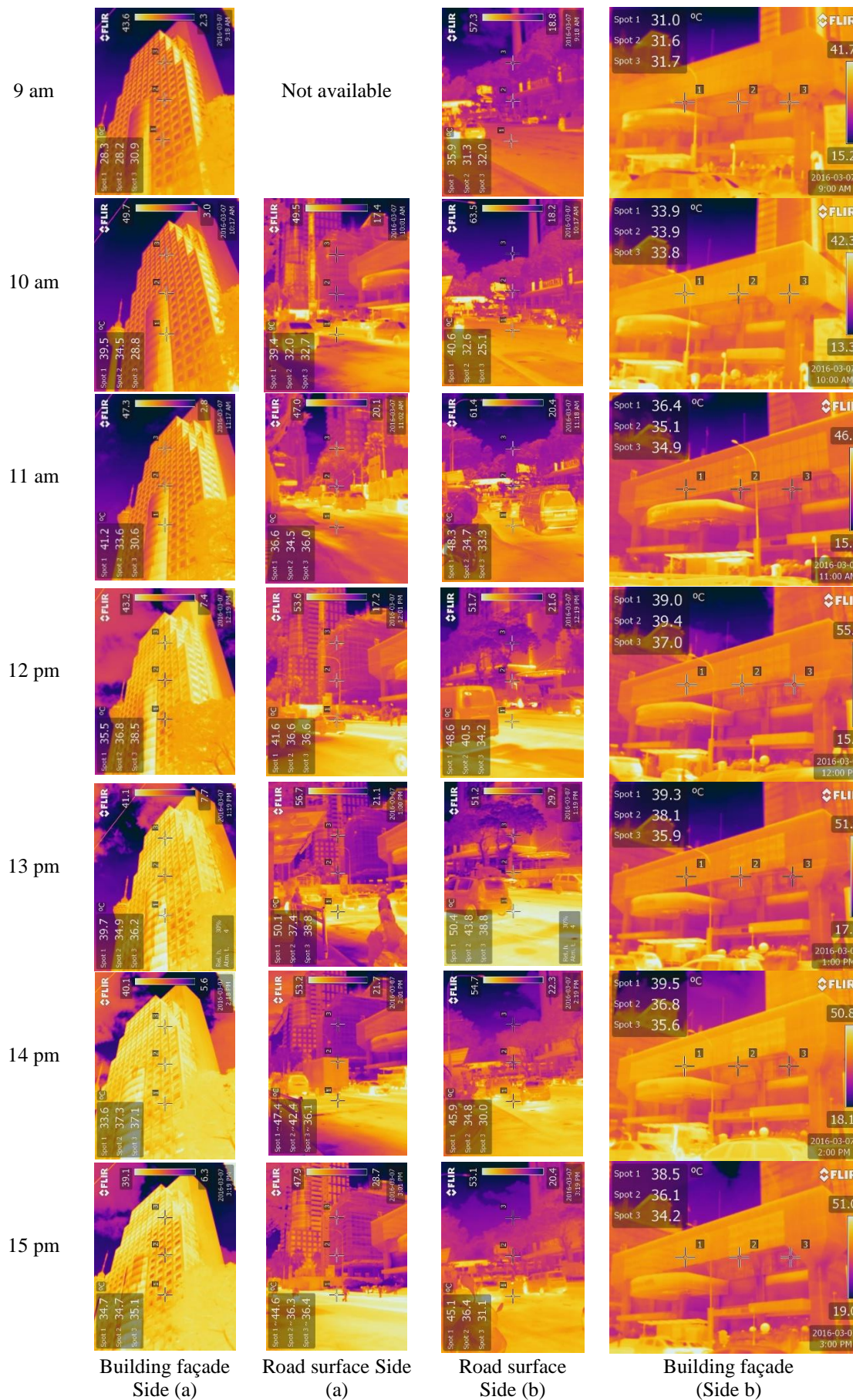


Figure 5.8 Arrangement of thermal image according to time for ROAD 1 Section (A)

5.3.2 Equipment calibration based on distance

To evaluate the sensitivity of FLIR T650sc in thermal sensor with various distance, calibration of the camera was carried out comparing the results from the camera with the thermal measurement of thermocouples Type K and data logger. Figure 5.9 describes how the calibration was evaluated.

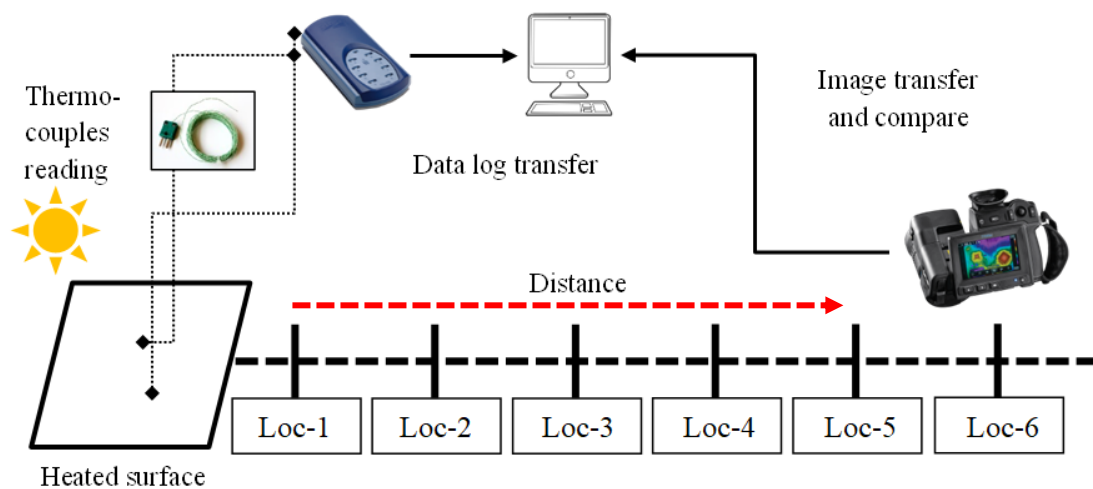


Figure 5.9 Process of calibration based on various distance comparing thermocouples Type K and FLIR T650sc

A heated surface or plane became an object of study where thermocouples Type K were installed and connected to a temperature data logging device type Pico TC-08, see details in Appendix A.9. The thermocouples were expected to read the temperature of the surface in seconds. With the recorded time after thermocouples began to provide the temperature reading, FLIR T650sc was used to capture the thermal image of the heated surface beginning at the first location, Loc-1 and move to the next location, Loc-2 in 3-5 second gap. The process was continuous until the final location where the farthest distance tested from the heated surface was reached. The same practice was repeated for several times after succeeded the first cycle.

To process the thermal images, FLIR R&D software, ResearchIR MAX was used to check, move, add and remove the cursors used to spot the temperature value from the heated surface. Calibration of the camera was conducted comparing the obtained results based on the previous practice.

5.3.2.1 Indoor calibration: University of Sheffield, United Kingdom

The first calibration was conducted on 8th January 2015 to evaluate the temperature of a flat surface with sand papers stitched to a cardboard box within a room with the area of 10 m length \times 3 m width \times 3 m height and with the ambience temperature was maintained to $\pm 20^{\circ}\text{C}$ using centralised air-conditioning unit. A clear halogen light bulb with 30 W was used as the heat source located behind the sand paper surface. The distance from the heated surface was set at every 1 m gap until the final location, 10 m from the heated surface was reached.

Figure 5.10 below shows the calibration setup and thermal images of the heated surface at difference distances. 4 thermocouples Type K were stitched to the sand paper and connected to the data logging. After obtaining the results from thermal images according to the distance, FLIR ResearchIR MAX was used to ensure the temperature spots captured earlier were at the right location of thermocouples specifically Point A. Additional information on the results based on the calibration is described in Appendix A.10. In this study, only three locations were compared to the results of thermocouple reading: (i) 3 m distance, (ii) 6 m distance, and (iii) 9 m distance from the heated surface. This means, the comparison for 3 m distance was 9 seconds after the measurement began meanwhile for 6 m and 9 m, the temperature values should be obtained at 18th second and 27th second, respectively.

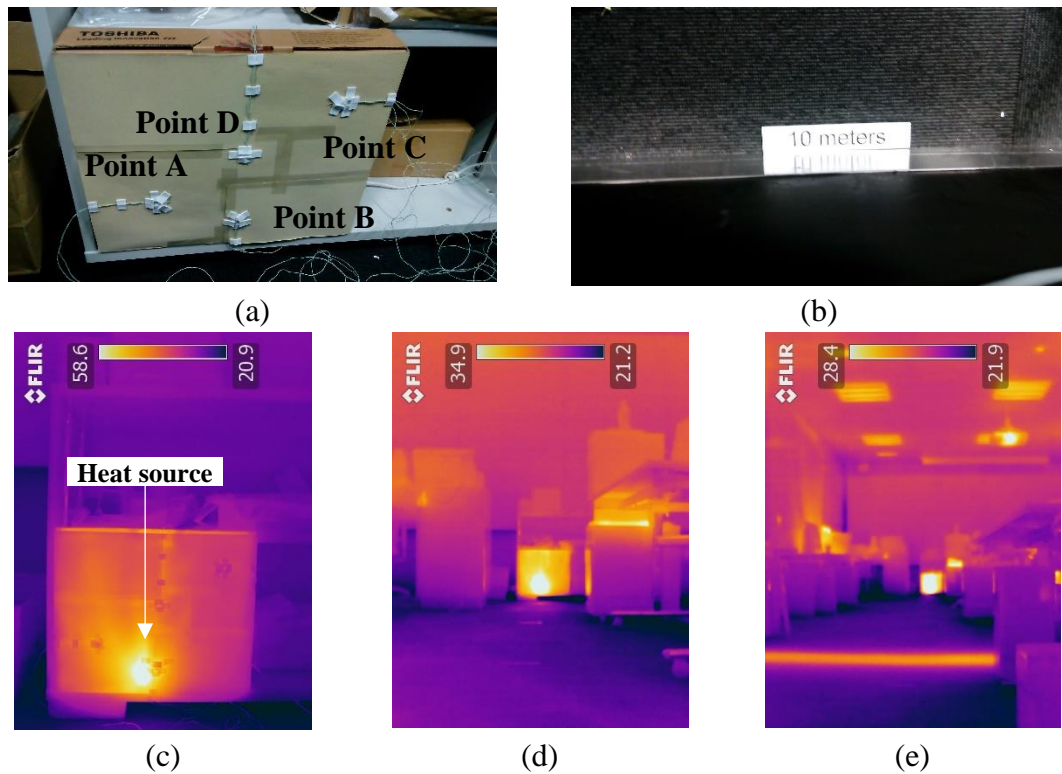


Figure 5.10 Calibration setup showing (a) heated sand paper surface with 4 thermocouples Type K stitched on surface (b) final location of where thermal image was captured. Also, thermal image at (c) 1 m distance (d) 5 m (e) 10 m

Point A was indicated as the two spots that were used for the comparison of the obtained values with the thermal camera. For Point A, it was observed that within an hour measurement, the surface temperature did not fluctuate above and below the range between 29.7 °C and 31 °C, showing that the stability of the temperature was achieved before 20:09 pm. The comparative temperature results between thermocouples and FLIR T650sc infrared thermal camera are displayed in Figure 5.11 together with the percentage of error comparing both measurement tools.

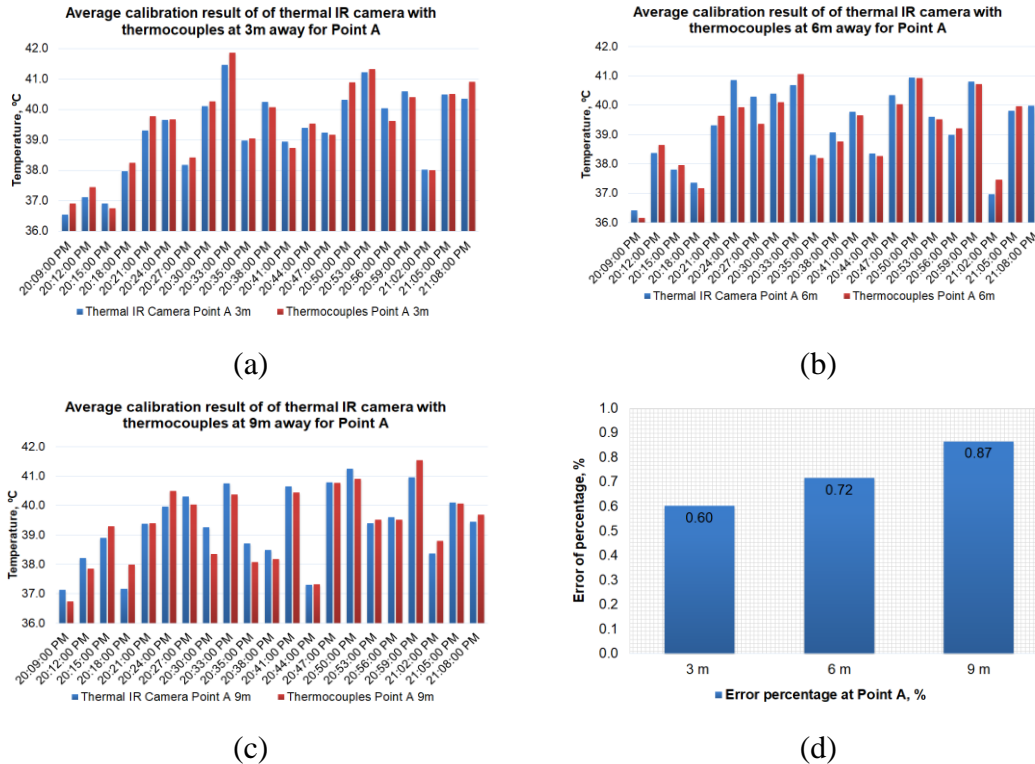


Figure 5.11 Comparative temperature results obtained by thermocouples and FLIR T650sc infrared thermal camera at (a) 3 m, (b) 6 m and (c) 9 m distance (d) average percentage of error, % according to the distance from the heat source

Based on Figure 5.11, it was observed that the temperature values obtained from the camera for Point A have carefully followed the trend obtained from the thermocouple, resulting the temperature values of all measured period and location (3 m, 6 m and 9 m) were comparable to one another. Based on Figure 5.11(d), it shows that the percentage of error for the location afar from the heated surface was still below 1.0 %.

The limitation of this calibration study was the maximum length of the tested room was 10 m. Additionally, the room temperature was controlled from the beginning of the test. For outdoor measurement, it should be highlighted that various parameters will influence the temperature results. Thus, another calibration for the outdoor setting was carried out during hot tropical day on 28th March 2016 in Malaysia.

5.3.2.2 Outdoor calibration study with hot humid weather, Malaysia

An outdoor calibration test was setup within a residential area named Taman Melawati, Kuala Lumpur, Malaysia in the afternoon dated 18th March 2016. The measurement of road surface temperature comparing thermocouple measurement and FLIR T650sc was carried out beginning at 13:00 hour, see additional information in Appendix A.11. In this study, the distance of standing was made 3 times longer than the previous indoor calibration study; which means the minimum gap from the temperature reading points was 5 m and with 5 m interval, the maximum gap towards the temperature reading points was 30 m. Results are displayed in Figure 5.12 as below.

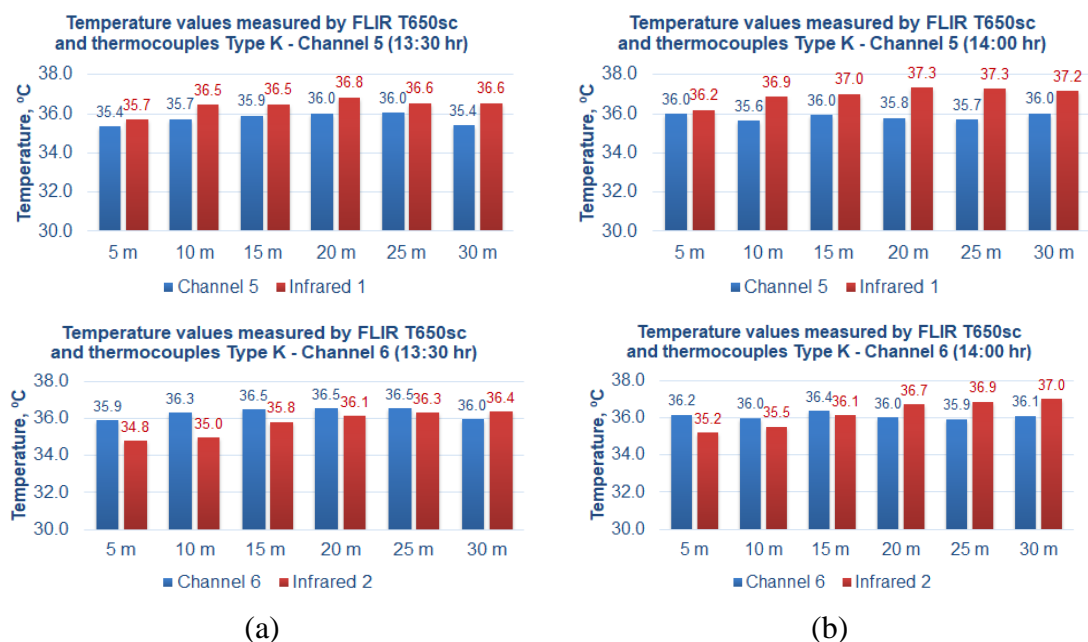


Figure 5.12 Average temperature values obtained against distance from the measuring points (a) at 13:30 hour (b) at 14:00 hour

It should be noted that only two thermocouples, Channel 5 and Channel 6 were used for the comparison due to the nearly compatible temperature values plotted during the measurement. The best compatible results of calibrating FLIR T650sc and thermocouples against distance (from 5 m to 30 m) were obtained during 13:30 pm, where the percentage

of error was 0.61-3.67 %, followed by the measurement during 14:00 pm, with its highest percentage of error, 4.44 %. Overall, the temperature difference for outdoor test can be ranged between 0.3 °C and 3 °C, given the percentage range between 0.05 % and 7 %.

5.4 Data collection: input, observation and analysis

In this section, results and discussion are presented in three sub-sections: (i) Section 5.4.1 represents the observation and analysis of street canyon surface temperature (building facades and road surface) to be based on hourly solar intensity including dates, month and year, (ii) Section 5.4.2 represents the result and analysis to be based on urban canyon aspect ratio. Section 5.4.3 represents the CFD modelling investigation based on the case study of ROAD 1 and ROAD 2 and the validation results of the model against the data collection.

As mentioned earlier in Section 5.3.1 that mobile measuring technique was carried out to capture the infrared thermal images of building facades from Side 1 and Side 2 together with road surface. Using FLIR ResearchIR MAX, additional 30 measurement spots were added together with measurement polylines to ensure average surface temperature was properly obtained while minimising the temperature error. Example of processing infrared thermal image using FLIR ResearchIR MAX is shown in Figure 5.13 below.

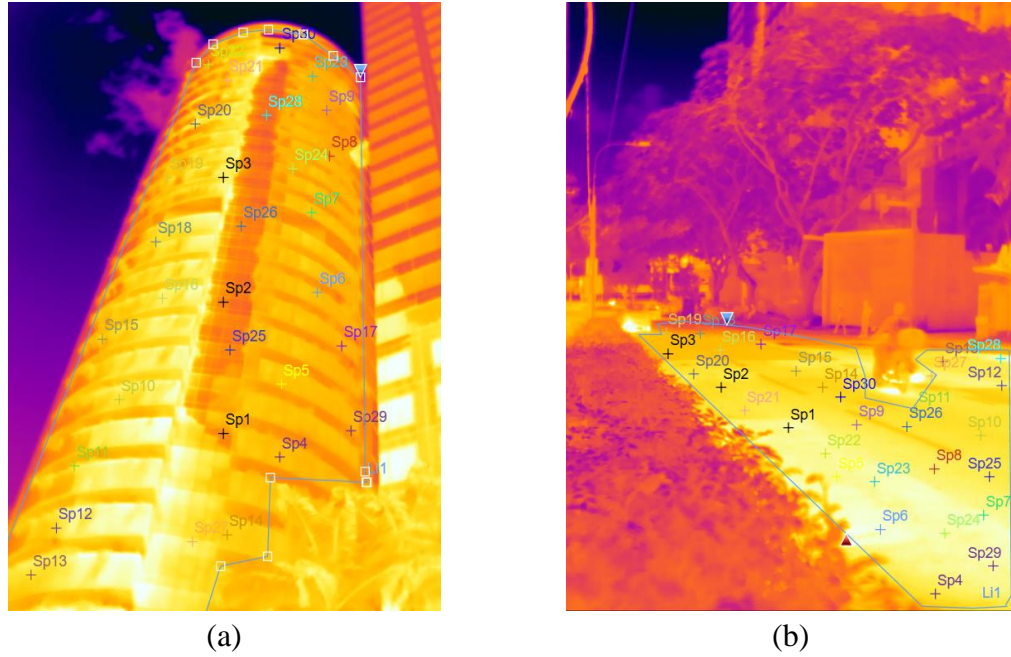


Figure 5.13 Additional measurement spots and polylines to obtain the average of (a) façade temperature (b) road surface temperature

5.4.1 Observation of surface temperatures based on time and date

Figure 5.14 and Figure 5.15 show the temperature of building façade with local wind speed and ambient temperature (as referred to Appendix A.5), respectively for ROAD 1 and ROAD 2 in three interval days of August 2015 and of March 2016 based on hourly intensity. For ROAD 1; During the first set of data collection, which is on 4th, 6th and 8th August 2015 (refer to Figure 5.14(a)), it was observed that the façade temperature of the buildings had the increasing trend from the early morning hours until the temperature peak was observed during 14:00 hour. It was observed that on 4th August 2015, the façade temperature had reduced from 14:00 hour to 15:00 hour by $\pm 4-5$ °C, meanwhile the façade temperature on 6th and 8th August 2015 did not change significantly. Similar trend as the first set of data collection was observed for the second set of data collection, which is on 7th, 9th and 11th March 2015 (refer Figure 5.14(b)); however, it was also observed with the temperature gain $\pm 3-5$ °C during almost all hours from the measurement of August 2015 to the measurement of March 2016.

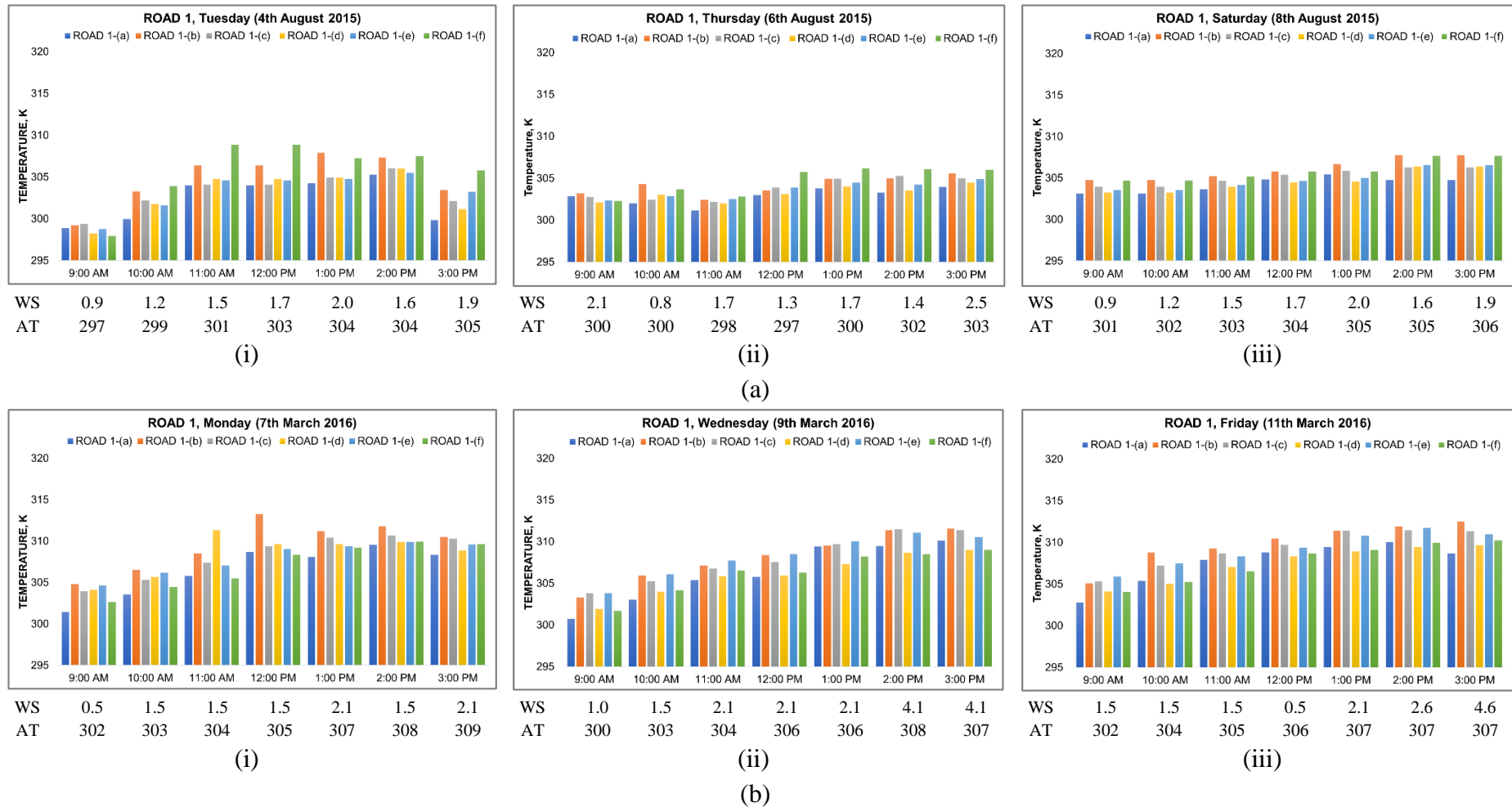


Figure 5.14 Average values calculated from thermal images of ROAD 1 consisting (a) façade temperature combining Side 1 and Side 2 during August 2015 (b) façade temperature combining Side 1 and Side 2 during March 2016. It should be noted that WS was indicated as wind speed in m/s and AT was indicated as ambient temperature in K.

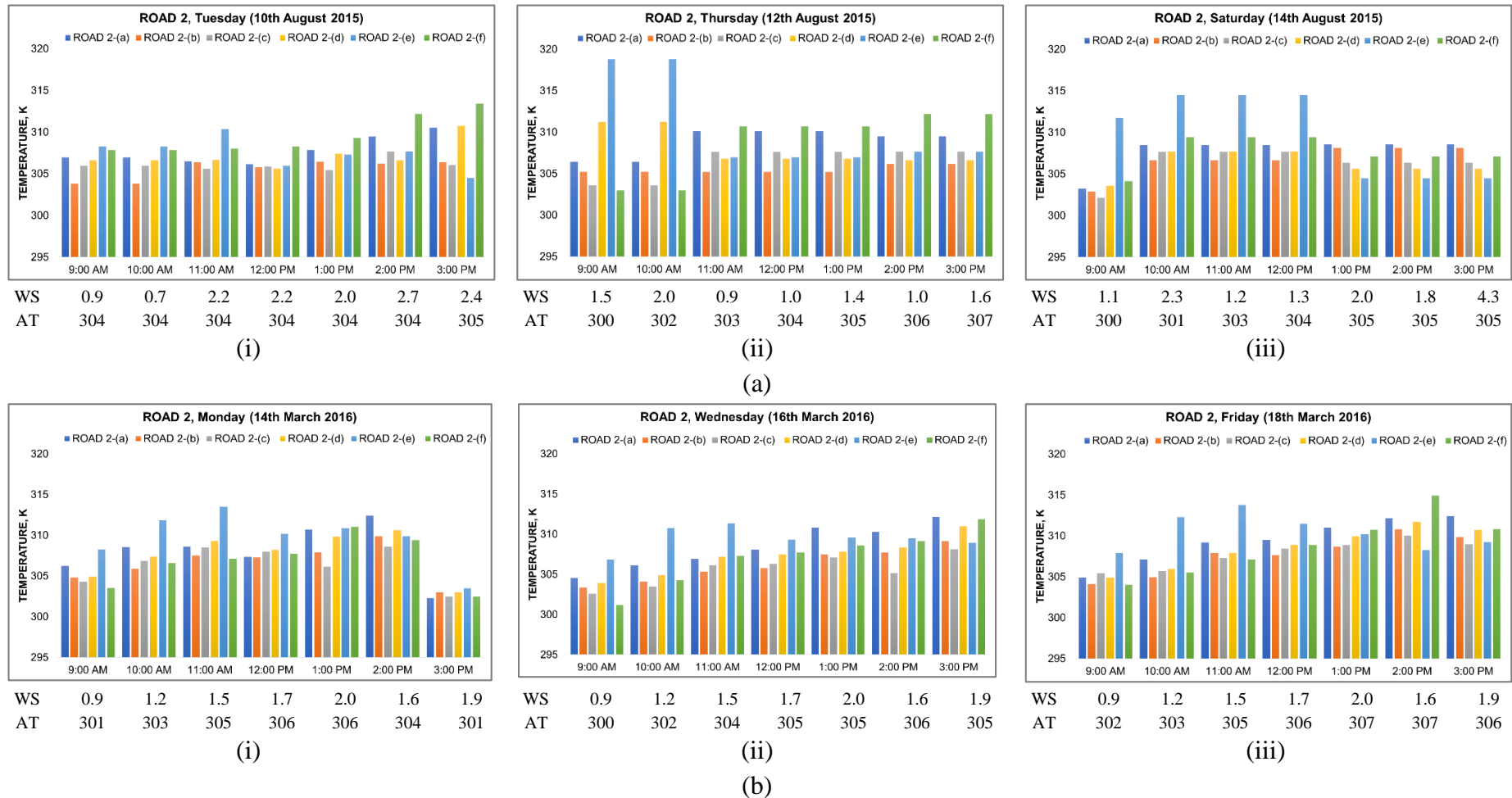


Figure 5.15 Average values calculated from thermal images of ROAD 2 consisting (a) façade temperature combining Side 1 and Side 2 during August 2015 (b) façade temperature combining Side 1 and Side 2 during March 2016. It should be noted that WS was indicated as wind speed in m/s and AT was indicated as ambient temperature in K.

Figure 5.15 shows the façade temperature for the buildings in ROAD 2. The second set of data collection which is on 14th, 16th and 18th March 2016 (refer to Figure 5.15(b)) followed the similar temperature trend as Figure 5.14(b) which low temperature was observed in the early morning hours and reached the temperature peak during 14:00 hour. It was observed that the façade temperature measured on 14th March 2016 at 15:00 hour dropped approximately 16 % or ± 6 °C from 14:00 hour. This trend was different than the temperature trend on the second day (16th March 2016) and the third day (18th March 2016). It was observed that the façade temperature during March 2016 did not change significantly from the data collection of the previous year (Figure 5.15(a)). In Figure 5.15(a), the temperature trend was observed dissimilar to the second set of data collection, which means there was insignificantly difference between the temperature during the early morning hours, during noon hours and after the noon hours. It was also observed that the façade temperature at Section 2-(e) exceeded the normal temperature range, ± 5 -7 °C higher than the other sections in ROAD 2.

Figure 5.16 and Figure 5.17 show the temperature of road surface with local wind speed and ambient temperature, respectively for ROAD 1 and ROAD 2 in three interval days of August 2015 and of March 2016 based on hourly intensity. For ROAD 1 as refer to Figure 5.16(a), the first set of data collection during August 2015 showed a large variance in the temperature trend according to hourly intensity between the data on 4th August 2015 and on 6th and 8th August 2015. During 4th August 2015 data collection, the road surface obtained the temperature peak at 12:00 hour noon with large variance in the temperature value between the early noon hour (09:00) and the noon hour (12:00), approximately 50 % increase in the temperature. The road surface temperature of ROAD 1 dropped almost 40 % from 12:00 noon to 15:00 hour. On 6th and 8th August 2015, the temperature peak

was observed during the afternoon hours (after 14:00 hour). During the second day data collection (6th August 2015), the highest obtained temperature was approximately 20 % less than the highest obtained temperature during the first and third day data collection.

In Figure 5.16(b), it was observed with similar temperature trend according to hourly intensity between 7th, 9th and 11th March 2016, 3-6 °C temperature increase in the interval hours from 09:00 hour to 13:00 hour. It was observed that the road surface temperature after 13:00 hour did not significantly change. Overall; between the data collection in August 2015 and in March 2016, it was observed with the temperature increase by approximately 10-22 % during the early morning hour (09:00), 30-45 % during the noon hours and 25-60 % during the late afternoon hour (15:00).

For ROAD 2 as shown in Figure 5.17, there was a unique temperature trend comparing the first data collection in the month of August 2015. The first day data collection (4th August 2015) showed an agreement with the influence of solar intensity on the road surface temperature with the temperature peak at 14:00 hour, following the trend of the previous façade temperature data collection. On the second day data collection (6th August 2015), the temperature peak was observed between 11:00 hour and 13:00 hour with insignificant temperature drop afterward. During this day, large temperature variance was observed between the morning hours (09:00 – 10:00) and the temperature peak, approximately 60 % due to rainy condition in the early morning before the beginning of the data collection. On 8th August 2015, it showed that the temperature trend was almost similar to the trend during 4th August, except for the temperature values in Section 2-(a) and 2-(b) outburst the normal range, $\pm 6-9$ °C higher than the other sections.

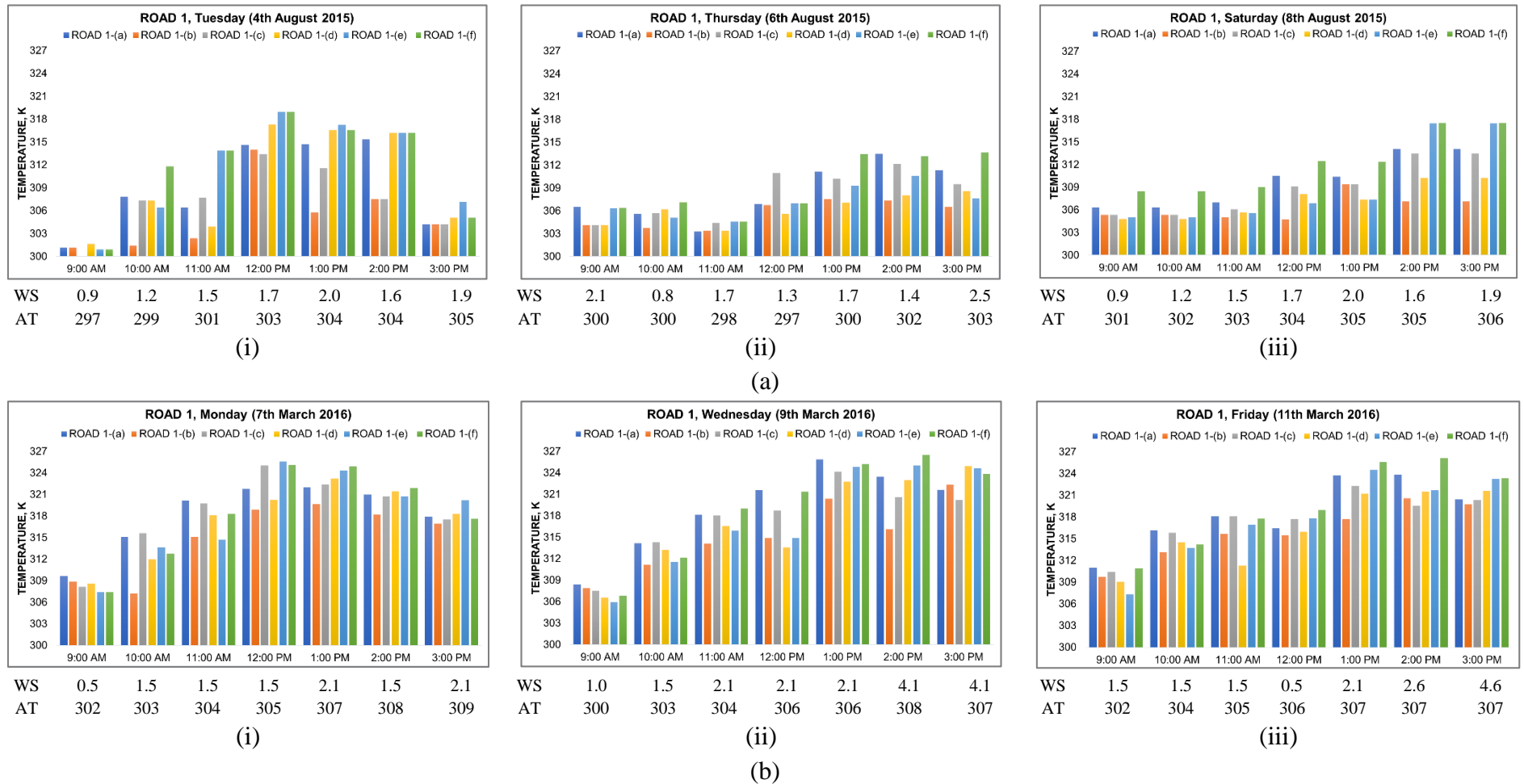


Figure 5.16 Average values calculated from thermal images of ROAD 1 consisting (a) road surface temperature combining Side 1 and Side 2 during August 2015 (b) road surface temperature combining Side 1 and Side 2 during March 2016. It should be noted that WS was indicated as wind speed in m/s and AT was indicated as ambient temperature in K.

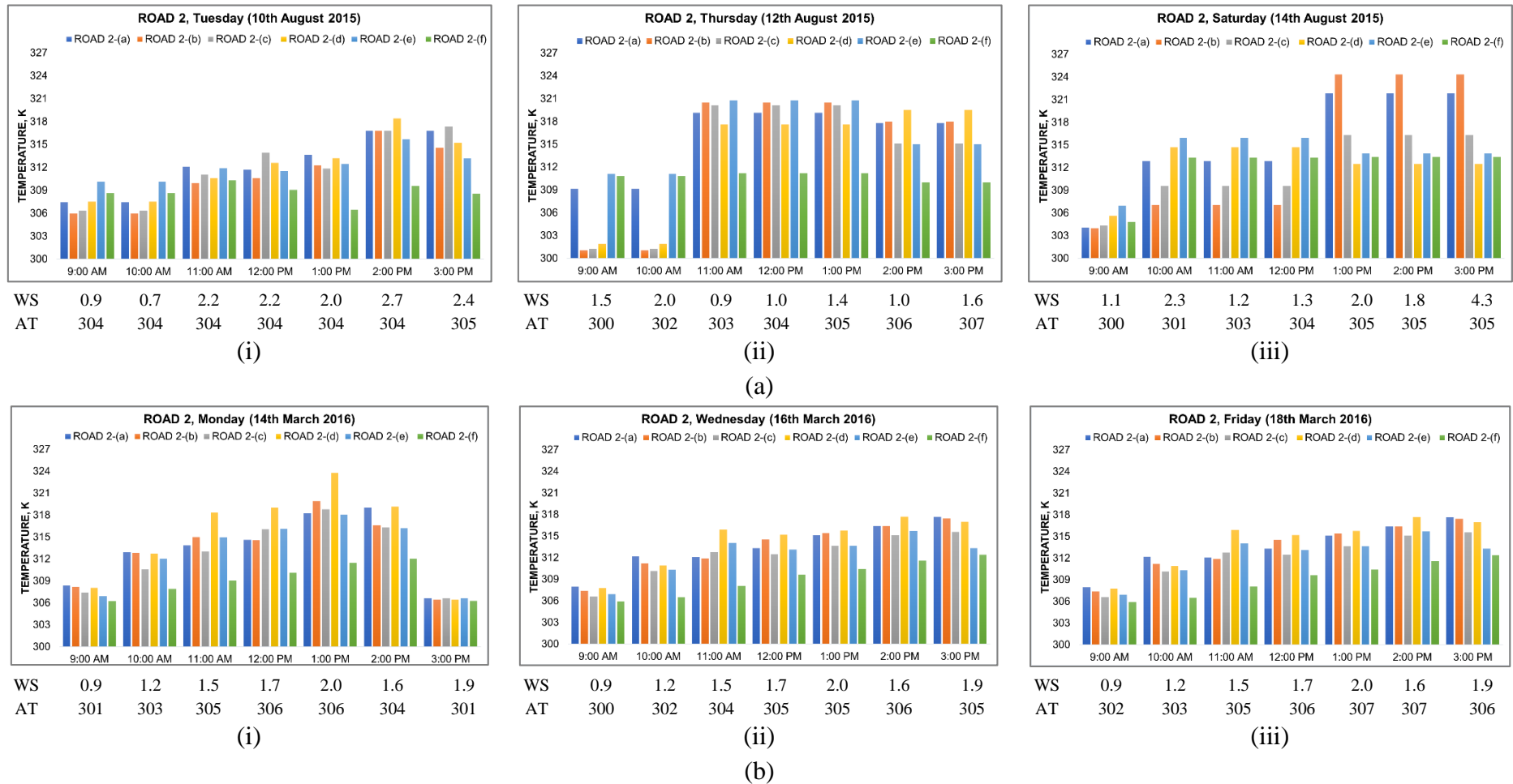


Figure 5.17 Average values calculated from thermal images of ROAD 2 consisting (a) road surface temperature combining Side 1 and Side 2 during August 2015 (b) road surface temperature combining Side 1 and Side 2 during March 2016. It should be noted that WS was indicated as wind speed in m/s and AT was indicated as ambient temperature in K.

The first day data collection in March 2016 as in Figure 5.17(b)-i showed a similar temperature trend with the façade temperature of ROAD 2 (Figure 5.15(b), except for the temperature peak was observed during 13:00 hour peak at 12:00 noon with approximately 32 % low in the temperature in the early morning hour (09:00) and in the late afternoon hour (15:00). Overall; the data collection in March 2016 did not change significantly from the data collection in August 2015, except for pronounce higher temperature during noon hours in comparing the data collection of 14th March 2016 as compared to the data collection of 10th August 2015 and the pronounce higher temperature during noon hours comparing the data collection of 12th August 2015 as compared to the data collection of 16th March 2016.

Based on the local weather condition of ambient temperature and wind speed which were included in Figure 5.14, Figure 5.15, Figure 5.16 and Figure 5.17; it was observed with low ambient temperature during morning hours and with higher ambient temperature during noon hours. Meanwhile in most of the day, it was observed with the increase in wind speed during noon hours from the morning hours. With higher wind speed, the local ambient temperature was expected to reduce. Nevertheless, it was difficult to observe the trend of local wind speed to influence the local ambient temperature and the data collection of ROAD 1 and ROAD 2. Thus, it was strongly agreed that the local weather condition and the temperature measurement were most probably to be influenced by the position of the sun and the cloud cover condition during the time and the date of the data collection.

5.4.2 Influence of street canyon aspect ratio on surface temperatures

In this section, the observation on the surface temperature based on street canyon aspect ratio was carried out by comparing: (a) the internal street canyon sections of ROAD 1 between the measurement in August 2015 and the measurement in March 2016 – Section 5.4.2.1, (b) the internal street canyon sections of ROAD 2 between the measurement in August 2015 and the measurement in March 2016 – Section 5.4.2.1, (c) average façade temperature and road surface temperature between the measurement in August 2015 and the measurement in March 2016 – Section 5.4.2.2, and (d) the average surface temperatures between ROAD 1 with average aspect ratio of 3 and ROAD 2 with average aspect ratio of 1 – Section 5.4.2.3.

Figure 5.18 shows the mean ambient temperature and the wind speed according to the dates of data collection involving ROAD 1 and ROAD 2. This data was referred to Appendix A.5 of the thesis. From Figure 5.19, it can be observed that the mean ambient temperature of ROAD 1 during March 2016 was higher than the temperature during August 2015, meanwhile an insignificant difference was observed to compare the ambient temperature during August 2015 and during March 2016. The daily wind speed during March 2016 was observed 27-50 % lower than during August 2015 in ROAD 1 and ROAD 2. There was a reduction in the daily wind speed of ROAD 1 on 6th August 2015, approximately 50-60 % lower than on 4th August 2015 and 8th August 2015; meanwhile a difference of 18 % in the daily wind speed of ROAD 2 on 12th August 2015 as compared to the other two dates (10th August 2015 and 14th August 2015). From the weather data of ambient temperature and wind speed, it shows that weather condition in March 2016 was indeed hotter than in August 2016. This data was incorporated in the next sections (Section 5.4.2, 5.4.3, 5.4.4) of this chapter.

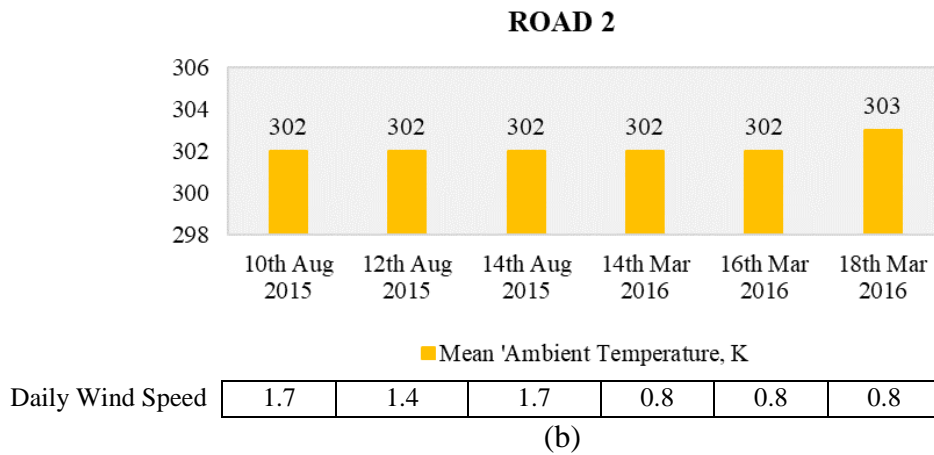
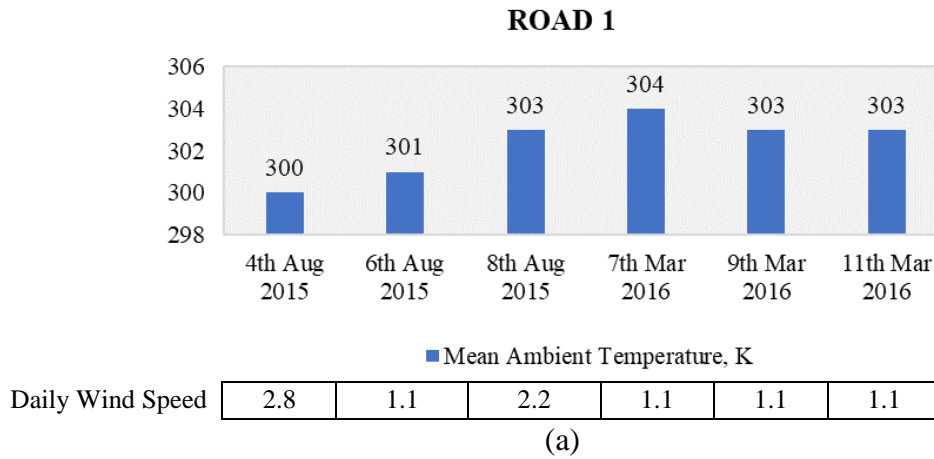
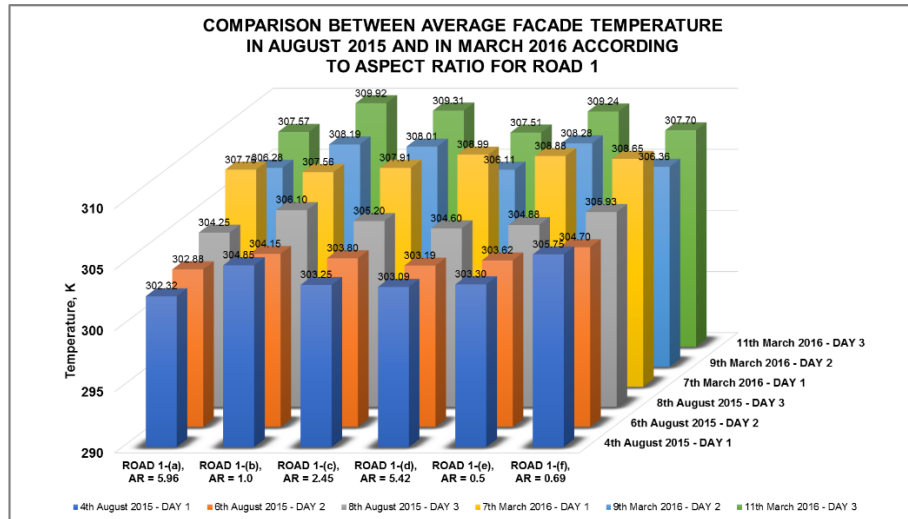


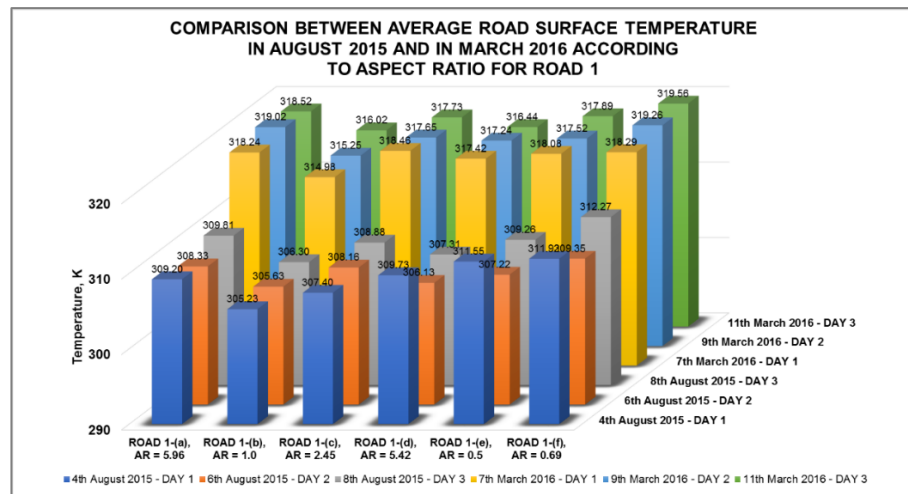
Figure 5.18 Mean ambient temperature and daily wind speed according to date for (a) ROAD 1 and for (b) ROAD 2. It should be noted that the mean wind speed was calculated in m/s unit.

5.4.2.1 Comparison between street canyon sections in ROAD 1 and ROAD 2

For this comparison, average temperature values were obtained from the average of temperature values plotted in individual period, from 09:00 hour and 15:00 hour. In addition, the trend of the temperature plotted for all six street canyon sections (from Section (A) to Section (F)) was observed in 6 data dates, the first three dates were carried out in August 2015 and the three later dates were carried out in March 2016, see the temperature comparison based on building façade and road surface in Figure 5.19.



(a)



(b)

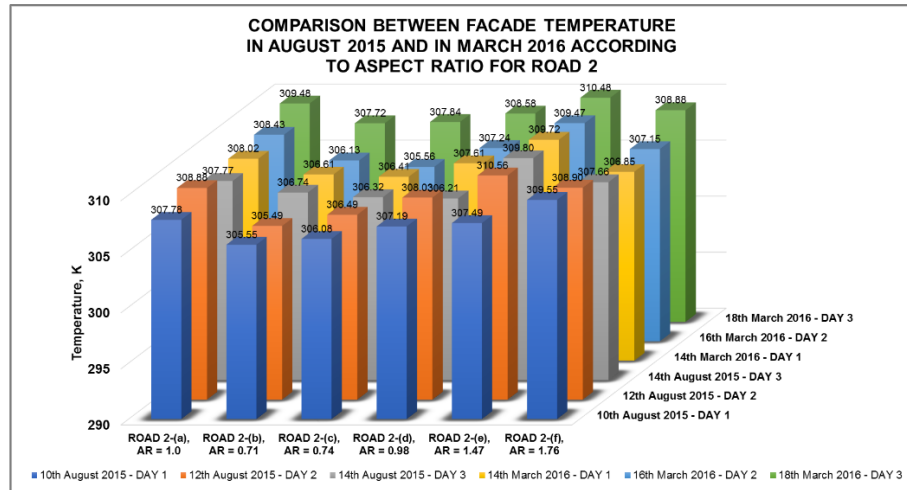
Figure 5.19 Average temperature comparing the street canyon sections of ROAD 1 (a) façade temperature (b) road surface temperature. The comparison included the data collection during August 2015 and during March 2016.

As refer to Figure 5.19, the comparison between the ROAD 1 sections was carried out based on the indication of $AR < 1$, $AR = 1$ and $AR > 1$. In Figure 5.19(a), the façade temperature in ROAD 1 was compared in 6 street canyon sections; which is between Section 1-(a) and Section 1-(f). It was observed with similar trend between 4th August 2015, 6th August 2015 and 8th August 2015 that the façade temperatures for $AR < 1$ and $AR = 1$ did not show significant difference between the two categories and obtained higher temperature as compared to $AR > 1$. The highest aspect ratio in ROAD 1, Section

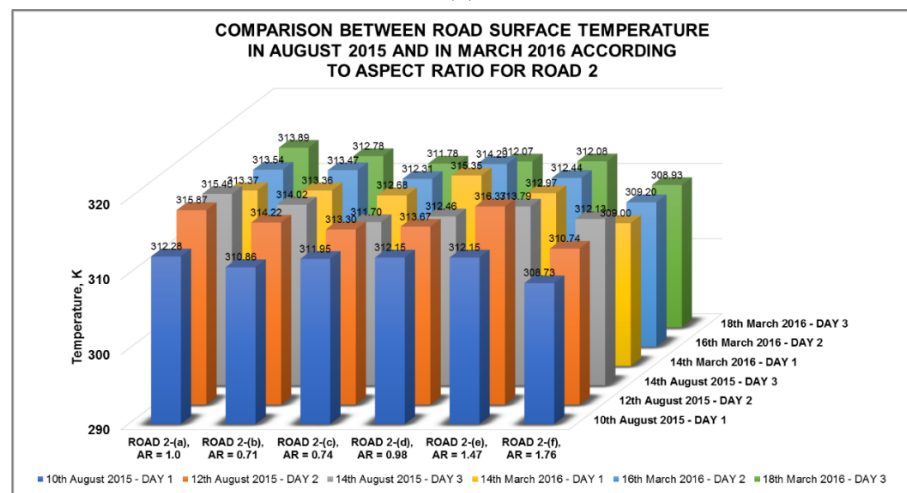
1-(a) obtained lowest temperature in all three dates in August 2015 as compared to the other sections. The data collection for the three days of March 2016 showed a different trend than the previous year. On 7th March 2016, higher façade temperature was found to be obtained by $AR > 1$ as compared to the temperature obtained by $AR < 1$ and $AR = 1$; meanwhile on 9th March 2016 and 11th March 2016, the temperature trend followed the temperature trend based on the previous year. To correlate Figure 5.19 and Figure 5.19, it can be agreed that the significant reduction in daily wind speed on 6th August 2015 did not significantly reduce the façade temperature of ROAD 1 on 6th August 2015 according to the aspect ratio of the canyon as compared to 4th August 2015 and 8th August 2015.

In Figure 5.19(b), the graph showed that the street canyon Section 1-(b) which has the average aspect ratio of 1 obtained lowest road surface temperature during all data collection dates, meanwhile the temperature values of the sections comparing $AR < 1$ and $AR > 1$ could not be detected with any significant. The significant temperature values can be observed in comparing the data collection of August 2015 and the data collection of March 2016, which demonstrated with the increase in the road surface temperature $\pm 8-9$ °C or approximately 24 %. For road surface temperature, the increased temperature rate shown in the data collection of March 2016 was 17 % more than the year before. Additionally, it was difficult to detect the influence of wind speed on road temperature comparing the street canyon sections, following the trend showed in Figure 5.19(a).

Like ROAD 1, the average façade temperature and road surface temperature comparing the 6 canyon sections in ROAD 2 were obtained from the average of temperature values plotted in individual period, from 09:00 hour and 15:00 hour; see the results in Figure 5.20.



(a)



(b)

Figure 5.20 Average temperature comparing the street canyon sections of ROAD 2 (a) façade temperature (b) road surface temperature. The comparison included the data collection during August 2015 and during March 2016.

As refer to Figure 5.20(a), results demonstrated that the canyon sections with $AR > 1$ obtained highest façade temperature in most of the dates in both 2015 and 2016 followed by the canyon sections with $AR = 1$. This means, low aspect ratio with $AR < 1$ within ROAD 2 obtained lowest façade temperature and this trend was against the trend for ROAD 1. In comparing the temperature difference over the two different months and years, there was no significant difference for ROAD 2, except for insignificant higher temperature in all canyon sections during the third data collection date of March 2016.

For road surface temperature (refer to Figure 5.20(b)), it was observed that the canyon sections with $AR < 1$ obtained highest temperature in most of the data collection both 2015 and 2016 as compared to the sections with $AR = 1$ and $AR > 1$. This means that the temperature trend between the dates, the months and the years was not significant to compare; which is against the increased trend for ROAD 1 between August 2015 and August 2016. Additionally, it was observed that the average façade and road surface temperature in ROAD 1 and ROAD 2 did not significantly increase or reduce; possibly due to the influence of stable ambient temperature and low daily wind speed.

5.4.2.2 Comparison of average temperature between August 2015 and March 2016

Average surface temperature obtained from the street canyon ROAD 1 and ROAD 2 was carried out comparing the data collection during August 2015 and during March 2015, see Figure 5.21 and Figure 5.22. Overall, the results showed in Figure 5.21 and Figure 5.22 were found proportion to the condition of mean ambient temperature during 6 days in the month of August 2015 and in the month of March 2016.

In Figure 5.21, result suggested that the average façade temperature calculated from the combined temperatures of all six canyon sections of ROAD 1 in March 2016 was $\pm 17\%$ higher than the temperature obtained in August 2015; meanwhile for the road surface temperature, the temperature increased $\pm 26\%$. For ROAD 1, it demonstrated that the temperature increase in facades was proportion to the temperature increase in road surfaces; however, the road surfaces obtained on average 13 % and 26 % higher in the temperature as compared to the façade temperature during the month of August 2015 and March 2016, respectively.

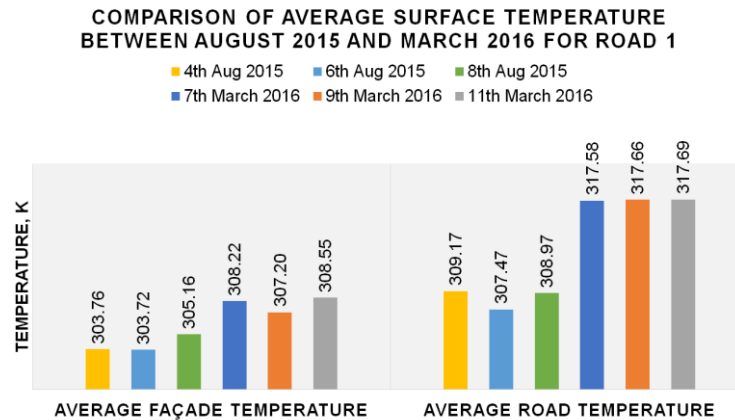


Figure 5.21 Comparison of average surface temperature between August 2015 and March 2016 for ROAD 1

As refer to Figure 5.22, result demonstrated that the average façade temperature of ROAD 2 obtained in August 2015 and in March 2016 was nearly similar and did not change significantly. Dissimilar trend was observed for road surface temperature of ROAD 2 with a slight decrease in the temperature values from the month of August 2015 to the month of March 2016, however the comparison was still insignificant. Overall, it can be agreed that the road surface temperature obtained on average 23 % higher than the façade temperature, similarly to ROAD 1.

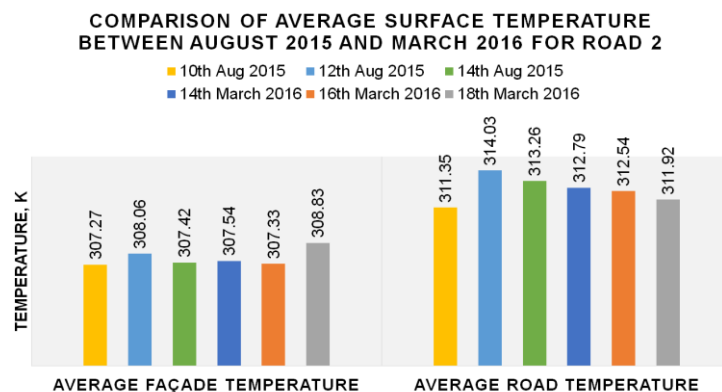


Figure 5.22 Comparison of average surface temperature between August 2015 and March 2016 for ROAD 2

This study confirmed the previous published works which reported higher temperature obtained by the ground and road surfaces than the temperature of building facades.

5.4.2.3 Comparison of average temperature between ROAD 1 and ROAD 2

Two dissimilar street canyon configurations with different aspect ratio, ROAD 1 and ROAD 2 were compared based on the average facades and road surface temperatures in three measured days, see Figure 5.23 and Figure 5.24 below. In Figure 5.23; results suggested that with the configuration of straight and deep street canyon, ROAD 1, the facade temperature and road surface temperature obtained during the three measured days in the month of August 2015 was on average 13 % and 11 %, respectively lower than the configuration of curvy and shallow street canyon ROAD 2.

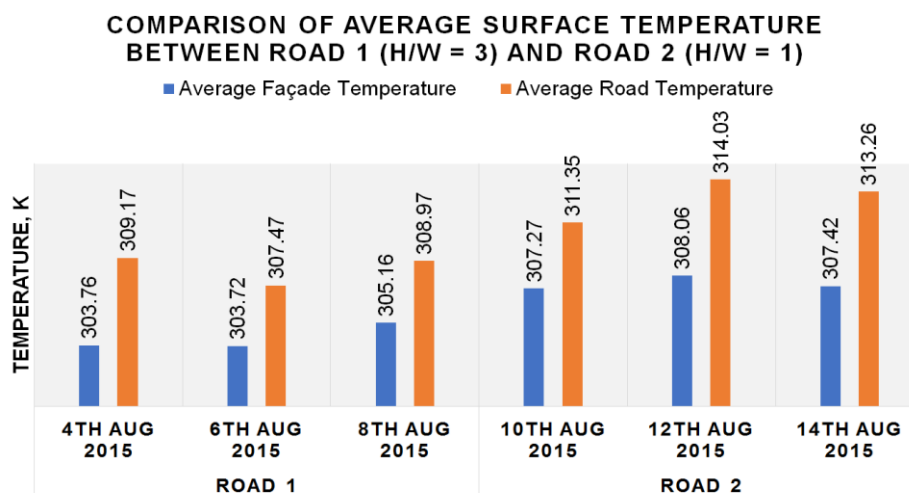


Figure 5.23 Comparison of average surface temperature based on different street canyon configuration and aspect ratio, ROAD 1 and ROAD 2 in August 2015

The trend of façade temperature and road surface temperature for ROAD 1 and ROAD 2 was found proportion, given by $\pm 3\text{-}4\text{ }^{\circ}\text{C}$ temperature gap between the two surface types. Meanwhile, the data collection of façade temperature and road surface temperature during the month of March 2016 showed an opposite trend, see Figure 5.24. The figure

demonstrated that the road surface temperature of ROAD 1 was on average 13 % higher than the surface temperature of ROAD 2, meanwhile insignificant difference in the façade temperature was found to compare between ROAD 1 and ROAD 2.

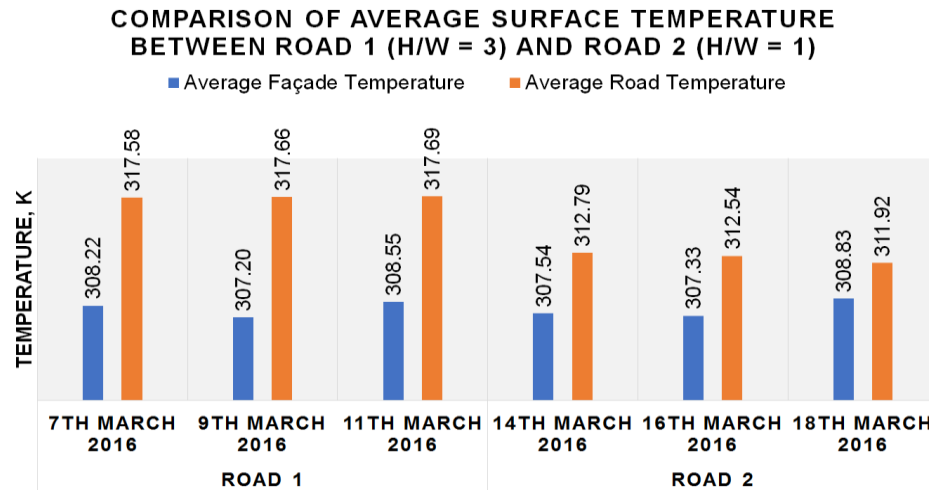


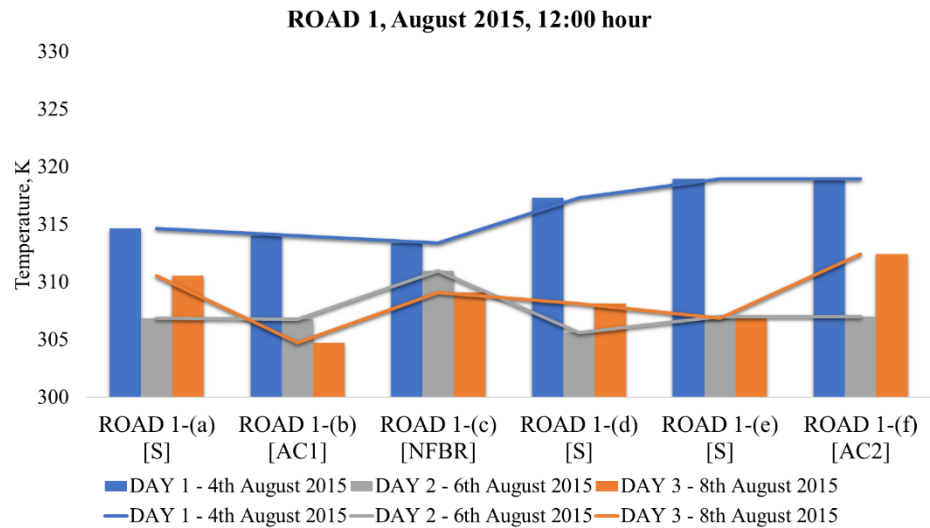
Figure 5.24 Comparison of average surface temperature based on different street canyon configuration and aspect ratio, ROAD 1 and ROAD 2 in March 2016

The temperature trend for building facades was disproportion to the temperature for road surface. With higher road surface temperature in ROAD 1, it was observed with insignificant impact on the temperature of building facades. The temperature gap between the road surface and the building facades in ROAD 1 was $\pm 9^{\circ}\text{C}$ or 26 %, meanwhile for ROAD 2, the temperature gap was $\pm 4^{\circ}\text{C}$ or 11 %.

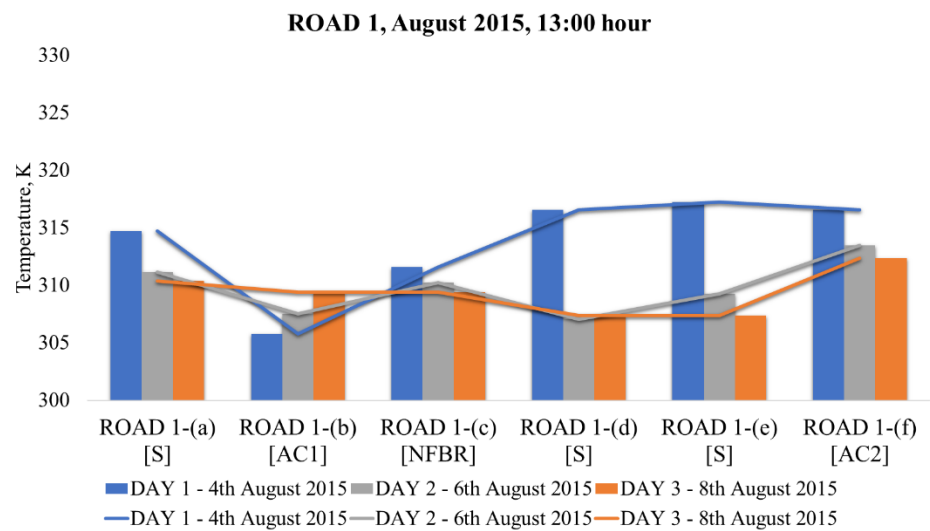
5.4.3 Influence of canyon configuration on road temperature

The influence of canyon configuration on road surface temperature was investigated concerning the straight canyon layout, ROAD 1 during the noon and afternoon hours (12:00 hour, 13:00 hour and 14:00 hour) comparing three data collection dates in the month of August 2015 and in the month of March 2016. It should be noted that the wind speed for all dates was between 1.3 m/s and 2.7 m/s with predominant wind direction from the south towards the street length of ROAD 1. The 6 canyon sections within ROAD 1 consist of 4 configuration types: (i) [S] for symmetrical canyon height – Section 1-(a), 1-(d), 1-(e), (ii) [AC1] for asymmetrical canyon height Type 1 – Section 1-(b), (iii) [AC2] for asymmetrical canyon height Type 2 – Section 1-(f) and (iv) [NFBR] for no first building row – Section 1-(b). The correlation between the results based on this study and the results based on the simulation model is explained and discussed in Chapter 6 Section 6.4. For this study, results are displayed in Figure 5.25 and Figure 5.26 below.

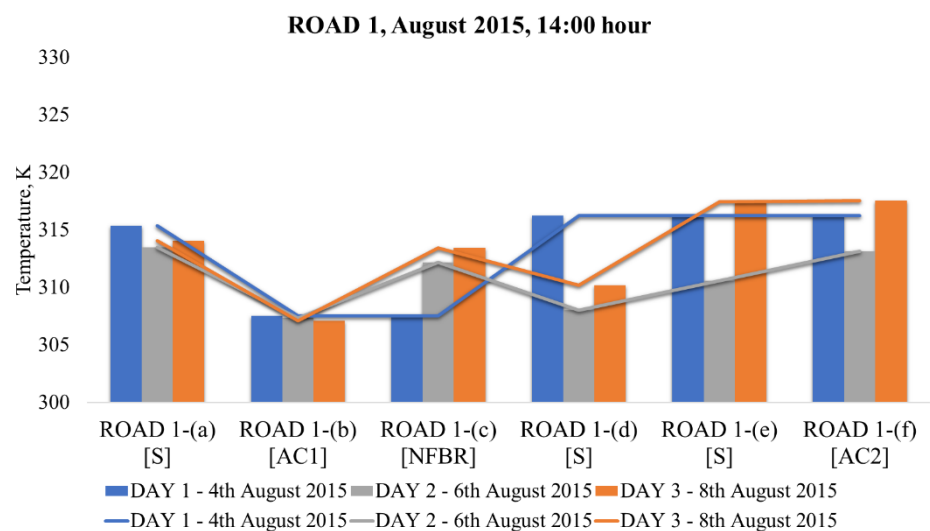
In overall, it was observed that the canyon configuration with asymmetrical canyon height Type 1 obtained lowest road surface temperature in most days and time as compared to other canyon configurations. In Figure 5.25, the temperature for the canyon sections within symmetrical height was found to be consistently high during 12:00, 13:00 and 14:00 hour of 4th August 2015; however, the trends for 6th and 8th August 2015 at 12:00 and 13:00 hour were in contrast. It was evidenced with lower road surface temperature with symmetrical canyon height of Section 1-(d) and 1-(e). The temperature obtained for Section 1-(f) did not show a significant difference than the other canyon sections with symmetrical height during 4th August 2015 but clearly higher in the temperature during 6th and 8th August 2015 at 12:00 and 13:00 hour.



(a)



(b)



(c)

Figure 5.25 Influence of canyon configurations on road temperature - August 2015

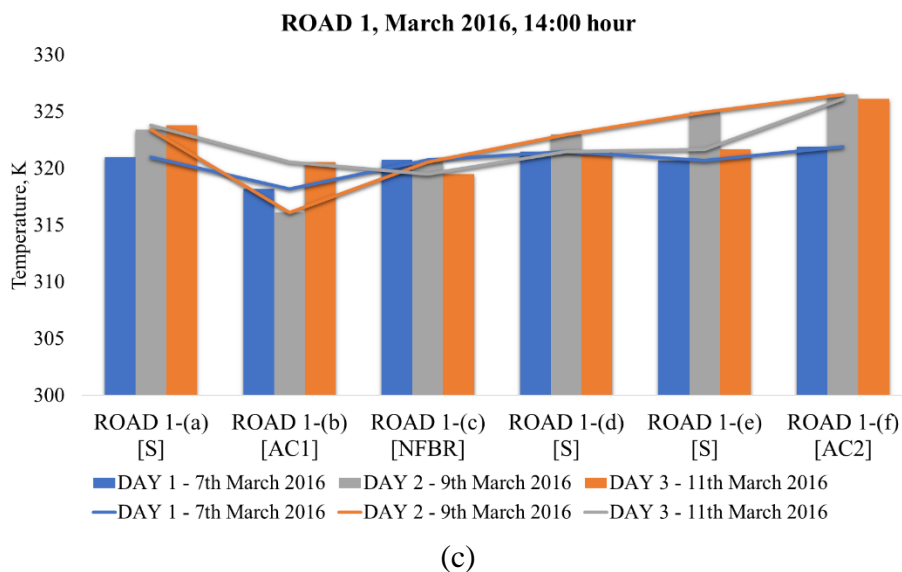
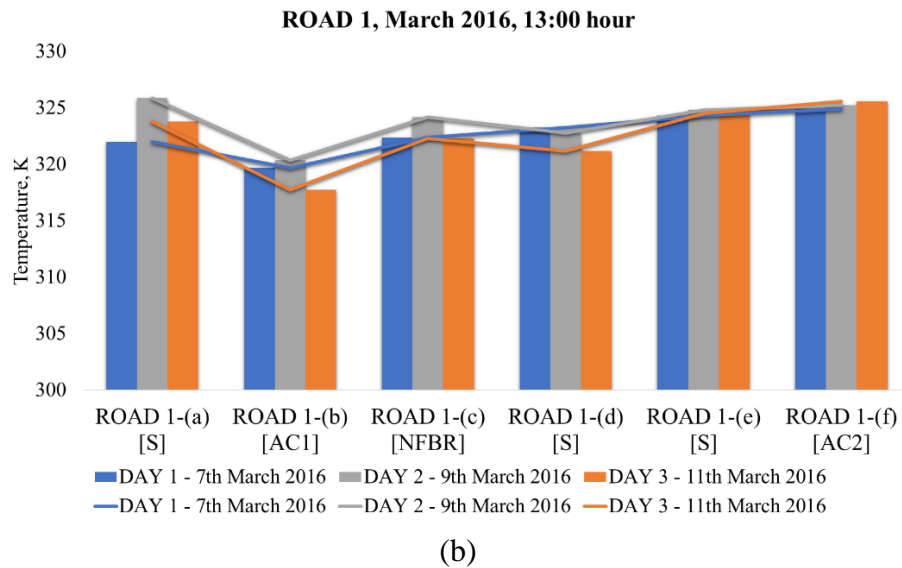
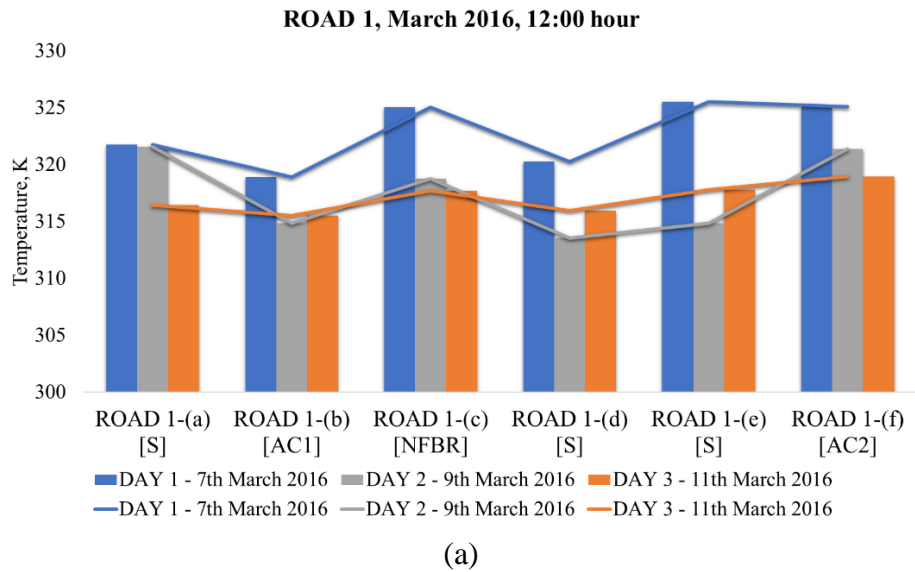


Figure 5.26 Influence of canyon configurations on road temperature - March 2016

As refer to Figure 5.26, a consistent trend of high temperature was obtained by road surfaces in the canyon sections with symmetrical height in three days of March 2016 at 12:00, 13:00 and 14:00 hour. Meanwhile, the road surface temperature for Section 1-(b) with asymmetrical canyon height obtained lowest in most of the date and time, following the trend during the month of August 2015. Similarly, the temperature values obtained by ROAD 1 Section 1-(f) did not show a significant difference from the temperature values of symmetrical canyon height.

5.4.3.1 External factors contributing to influence the road surface temperature

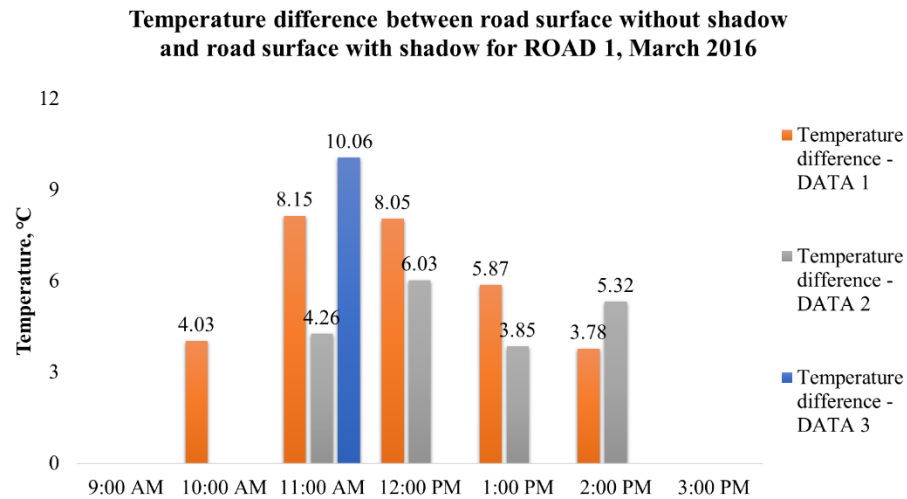
It should be highlighted that urban climate and surfaces are complex, thus the data collection of surface temperatures was depending on the condition of the daylight, solar intensity, ambient temperature, wind condition, humidity and precipitation apart from the canyon configuration and aspect ratio. In Section 5.4.1, it can be observed that the solar intensity during the month of August 2015 demonstrated its major influence on determining the road surface temperature. Low solar intensity was observed during the noon hours of 6th and 8th August 2015 as compared to the solar intensity during the noon hours of 4th August 2015. This variation created inconsistency in the temperature trend by the factor of canyon configurations influencing the surface temperature. A more consistent trend was observed for month of March 2016, which was reported with a consistent occurrence of heat wave and hot air temperature all over the month including weak daily speed as compared to the month of August 2015.

Furthermore, it should be emphasised on the shadow effects from buildings, trees and vehicles in the afternoon hours. From Figure 5.25 and Figure 5.26, the comparison between the canyon sections with higher aspect ratio (Section 1-(a) and Section 1-(d))

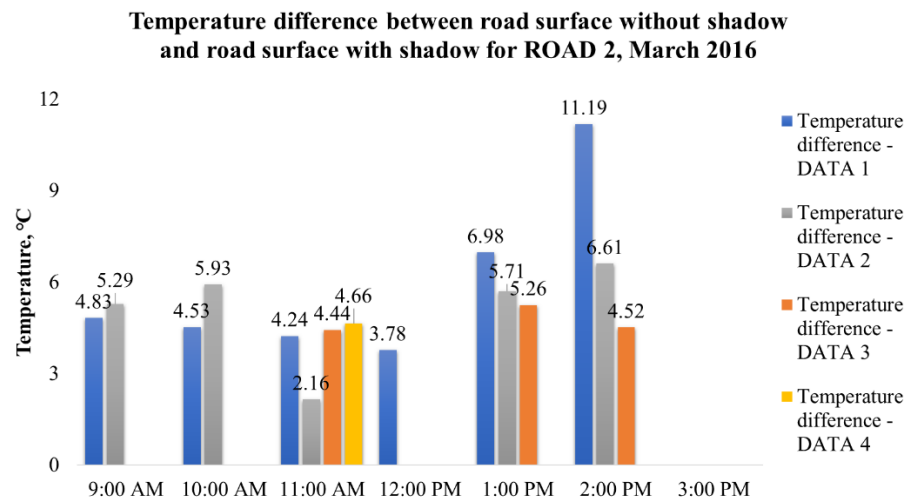
and the canyon section with lower aspect ratio (Section 1-(e)) did not show a consistent trend. Both Section 1-(a) and Section 1-(d) with symmetrical canyon height have the average aspect ratio, AR more than 5, thus the penetration of solar radiation into the canyon may be intruded due to building blocks that creating shadows on the road surfaces.

From the data collection carried out on ROAD 1 and ROAD 2, the comparison in the temperature values plotted for the road surfaces with and without shadows from buildings, trees and vehicles was carried out for the data of March 2016 and results displayed in Appendix A.12 are summarised in Figure 5.27. It should be noted that 'DATA 1', 'DATA 2', 'DATA 3' and 'DATA 4' means the representation of road surface temperature with and without shadow in different sets of data, which were found giving different values during the data collection in ROAD 1 and ROAD 2.

As refer to Figure 5.27, the temperature difference between the exposed road surface (no shadow) and the road surface with shadow is displayed for ROAD 1 and ROAD 2 regardless the canyon aspect ratio and canyon configuration. In Figure 5.27(a), the minimum reduction in the road surface temperature due to shadow effect was 3.78 °C meanwhile the maximum reduction achieved up to 10.06 °C; on average the reduction in the temperature was 5-6 °C. For ROAD 2 as shown in Figure 5.27(b), the maximum reduction in the road surface temperature due to shadow effect achieved up to 11.19 °C and the minimum temperature reduction was 2.16 °C. Similarly, the average temperature reduction for ROAD 2 was 5-6 °C. Thus; based on the results, it can be concluded that the shadow effects on road surfaces within ROAD 1 and ROAD 2 were compatible.



(a)



(b)

Figure 5.27 Influence of canyon configurations on road surface temperature

5.4.3.2 Validation of surface temperature with shadow effect

In Section 4.7.1 and Figure 4.24 of Chapter 4, the validation of ground surface temperature closer to Building B against the published work showed a significant difference due to the thesis's implementation of DO radiation with Solar Load Model. Based on the Figure 5.27, results demonstrated that the reduction in the surface temperature in two realistic urban street canyon studies due to shadowing was on average 5-6 °C and can be as maximum as 11.19 °C. The temperature difference between the

surface temperature without building shadow and the surface temperature with building shadow based on the simulation model used for this thesis was 8-20 °C, which the values were not far off the temperature difference obtained from the field measurement works of this thesis. Thus, it can be agreed that the simulation model of Standard $k - \varepsilon$ RANS with DO radiation and Solar Load Model is validated and compatible with the realistic urban surface condition.

5.4.4 Modelling investigation and validation against data collection

Figure 5.28 displays the complex geometry of the buildings including the street canyon studies of ROAD 1 and ROAD 2.

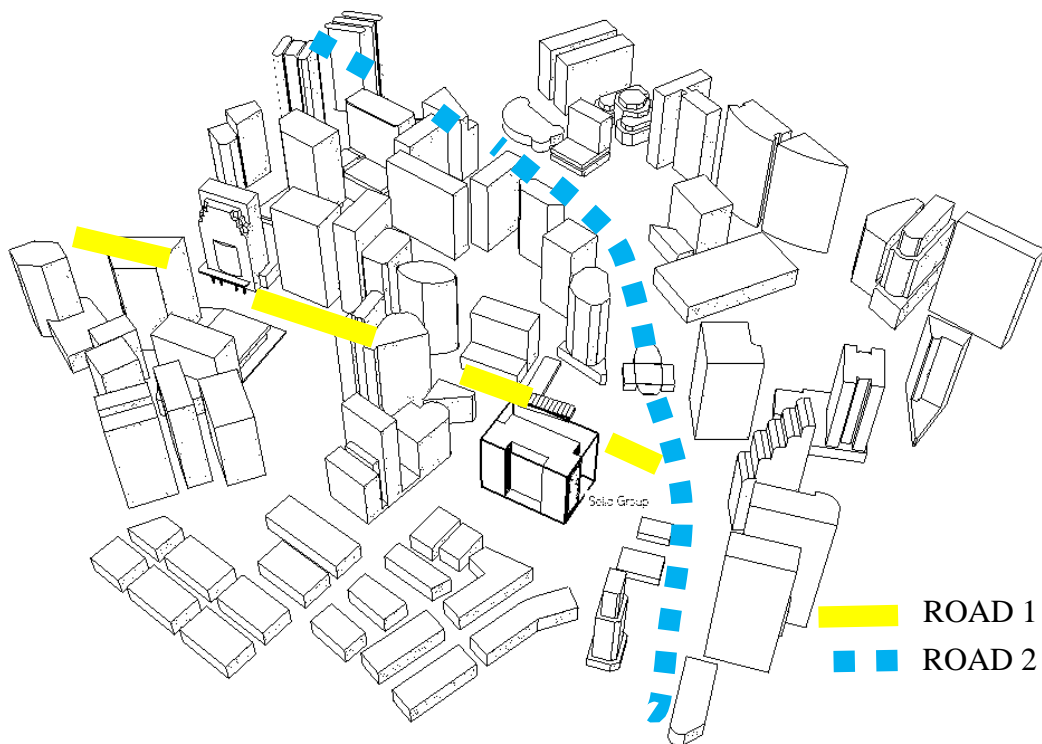


Figure 5.28 Geometry construction in Google Sketchup 2015 with Solid Inspector

The domain sizing was calculated based on the following criteria: (i) the five times height above the tallest building roof top – ($H_{TB} + 5H_{TB}$), (ii) the length from the most end of the

building facade to the east and to the west directions ($5H_{TB}$), (iii) the length from the most end of the building facade to the inlet plane ($5H_{TB}$), and (iv) the length from the most end of the building façade to the outlet plane with three times the length to the inlet plane ($15H_{TB}$). The criteria were set as a standard in several published works of with generic constant height urban form. In this study, ‘height’ of the building for non-generic form was emphasised based on the ‘tallest height’ in the flow domain. Figure 5.29 describes the detailed dimension of the domain in overall perspectives.

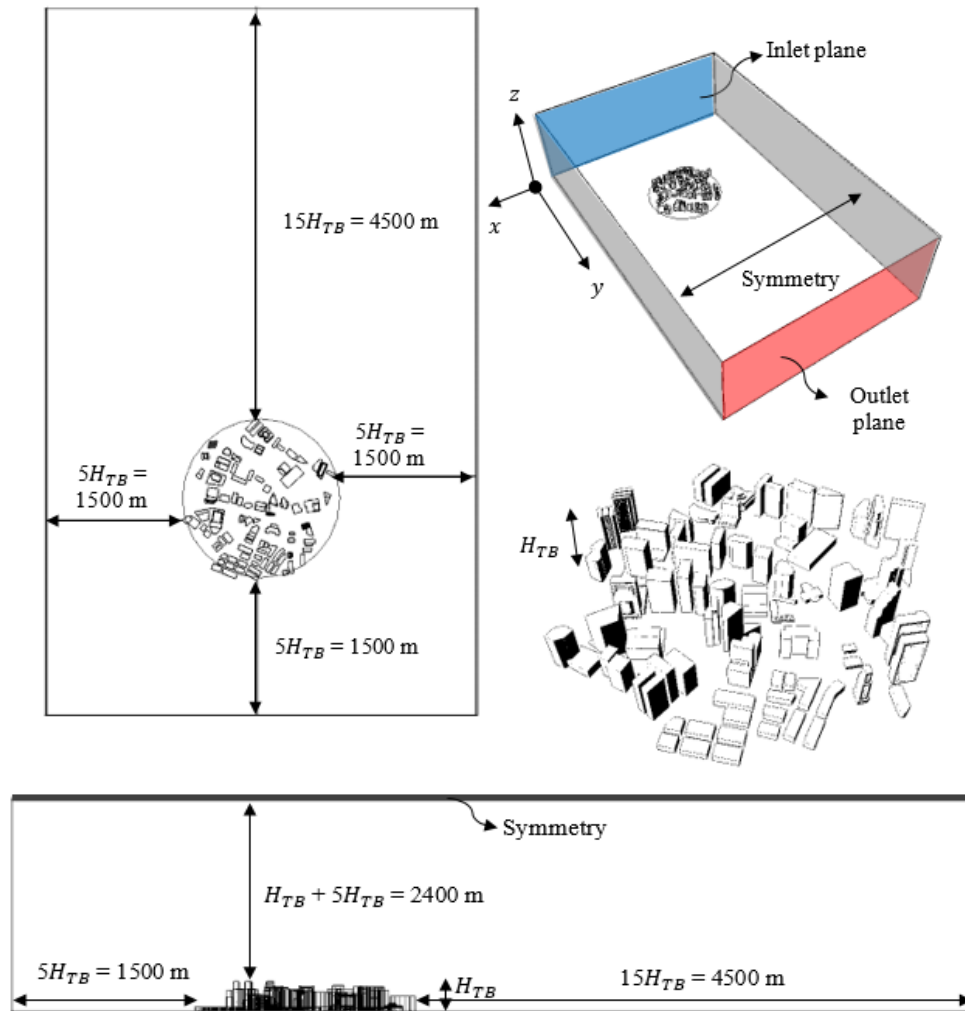


Figure 5.29 Dimension of the flow domain based on $H_{TB} = 300$ m

For daytime simulation, the sky condition was considered 75% in cloudiness (National Weather Service 2017) following the monthly weather data record thus the sunshine factor of 0.25 was set representing the average 25 % of the daylight hour. A logarithmic air velocity profile was refined based on the u^* at z -axis = 60 m above the ground. In ANSYS Fluent, the simulation of air velocity towards y -axis was set with a PROFILE velocity and z -height data. The variation in the mean wind speed with height was derived based on Rossby by assuming the roughness of fully rough flow affects the mixing-scale in the region where the z and z_0 are comparable; see Equation 5.1 as below:

$$z_h = \frac{u^*}{\kappa} \ln \left(\frac{z+z_0}{z} \right) \quad \text{Equation 5.1}$$

u^* is friction velocity and κ is Von Karman constant with the value of $\cong 0.4$. In calculating the value of u^* , this study requires the transport variable value of turbulent kinetic energy k and the standard version of k -epsilon model C_μ with the value of 0.09 by the derived equation as Equation 5.2 below:

$$u^* = k^{1/2} C_\mu^{1/4} \quad \text{Equation 5.2}$$

Additional equations were derived to find the value of k and the value of turbulent dissipation rate ϵ based on the velocity of the air U , turbulent intensity I (in %) and turbulent length-scale l ; see Equation 5.3 and Equation 5.4 below.

$$k = \frac{3}{2} U^2 I^2 \quad \text{Equation 5.3}$$

$$\epsilon = C_{\mu}^{3/4} k^{3/2} l^{-1} \quad \text{Equation 5.4}$$

The turbulent intensity I was calculated depending on the dimensionless Reynolds number Re of the air passing through the surface and whether the flow is in the steady state or in the turbulent state will be determined based on U , l and the fluid viscosity ν ; see Equation 5.5 and Equation 5.6.

$$I = 0.16 Re^{-1/8}, \text{ where } Re = \frac{U \cdot l}{\nu} \quad \text{Equation 5.5}$$

$$l = 0.07 d_f, \text{ where } d_f = 2 \frac{w \cdot h}{w + h} \quad \text{Equation 5.6}$$

Simplification was carried out in this study to prioritise the capability of CFD modelling in validating the temperature measurement studies within the minimum requirement. Thus, only the day and the time with south airflow direction was considered in the study. Also, it was assumed that all ground surfaces representing the pavements and road surfaces at ground level to be treated in one material. This is the same for all building facades. It should be noted that in realistic urban environment, urban surfaces require very complex measurement.

Table 5.5 summarises the wind speed and air temperature based on date and time when the measurement was carried out for ROAD 1 and ROAD 2 and details of the material properties used for the model. The airflow and heat transfer simulation of ROAD 1 and ROAD is shown as an example as per the temperature contour developed in ANSYS Fluent as Figure 5.30.

Table 5.5 Boundary condition for temperature validation of ROAD 1 and ROAD 2

DATE AND TIME	CASE STUDY	WIND SPEED & DIRECTION	AIR TEMPERATURE	
09 th March 2016 at 14:00 hr	ROAD 1	4.1 m/s, south	308 K	
Retrieved from: (WeatherUnderground 2016a)				
14 th March 2016 at 11:00 hr	ROAD 2	1 m/s, south	305 K	
Retrieved from: (WeatherUnderground 2016a)				
SURFACE DESCRIPTION	THERMAL CONDUCTIVITY (W/m·K)	SPECIFIC HEAT CAPACITY (W·kg/K)	DENSITY (kg/m³)	EMISSIONITY
Road materials (asphalt)	0.75	920	2360	0.94
Building materials	0.78	870	2050	0.94

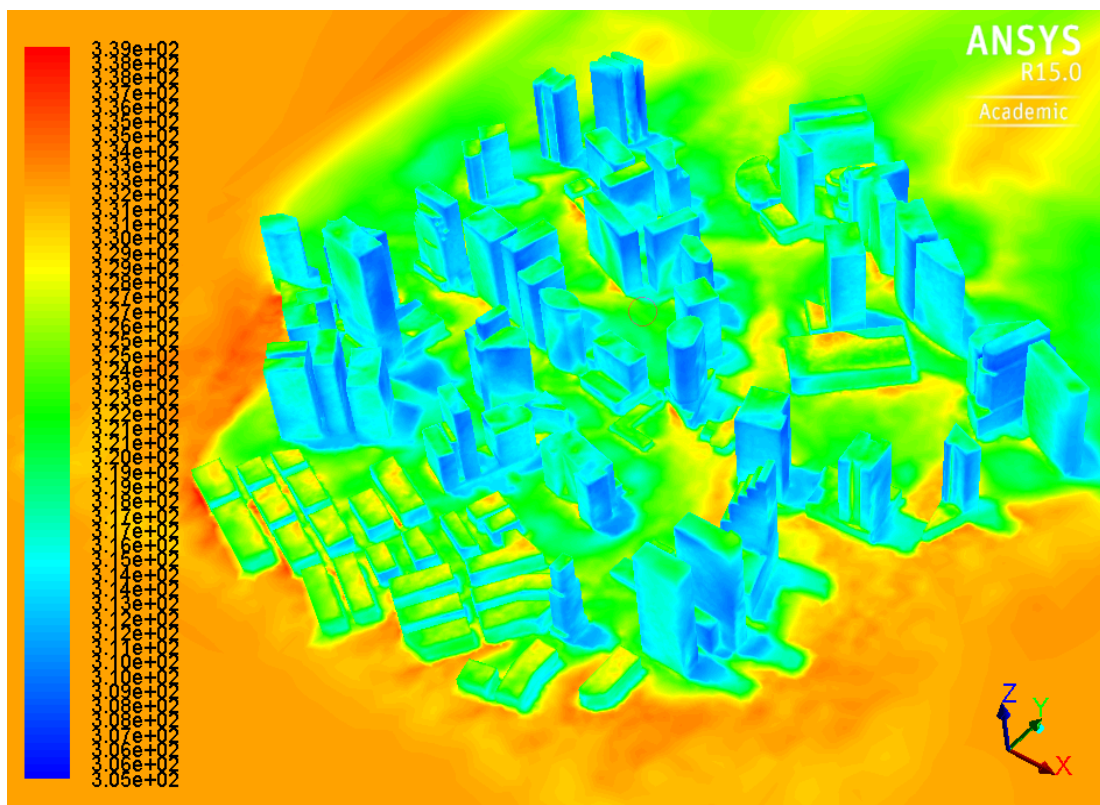


Figure 5.30 3D simulation consists of ROAD 1 and ROAD 2 with the setting of urban airflow, solar radiation and surface properties

Validation of façade temperature and road surface temperature is displayed in Figure 5.31 and Figure 5.32, respectively. In both figures, the comparison was based on the simulation results at six sections (Section (A) – Section (F)) according to the measured data

collection on 9th March 2016 at 14:00 hr for ROAD 1 and 14th March 2016 at 11:00 hour for ROAD 2. With the simplification of the modelling with simplified boundary condition set for both case studies, it was observed that both façade and road surface temperatures were closely validated against the results based on FLIR T650sc thermal images. Based on Figure 5.31, it was observed that the simulation date and time for façade temperature of ROAD 1 (9th March 2016 at 14:00 hour) obtained a better validation as the trend of temperature plotted across the street canyon was compatible with the data collection based on thermal imaging, with the error of percentage on average 16.5 % of the simulated temperatures to the temperatures of the thermal images.

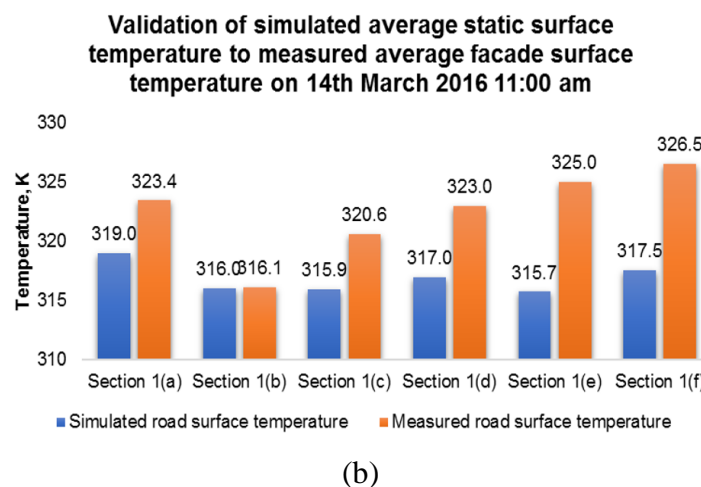
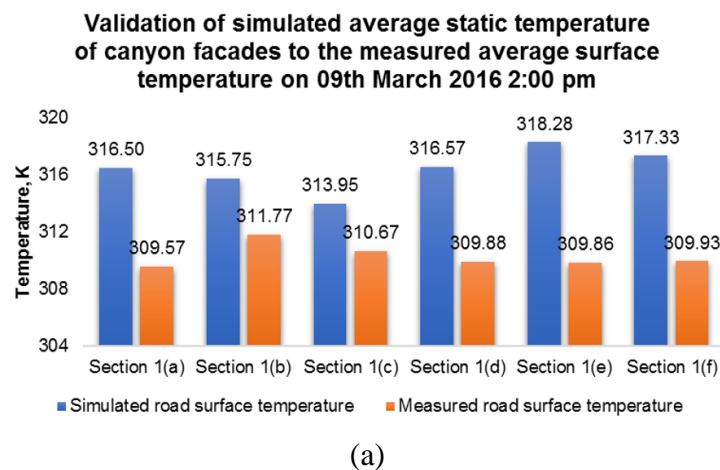
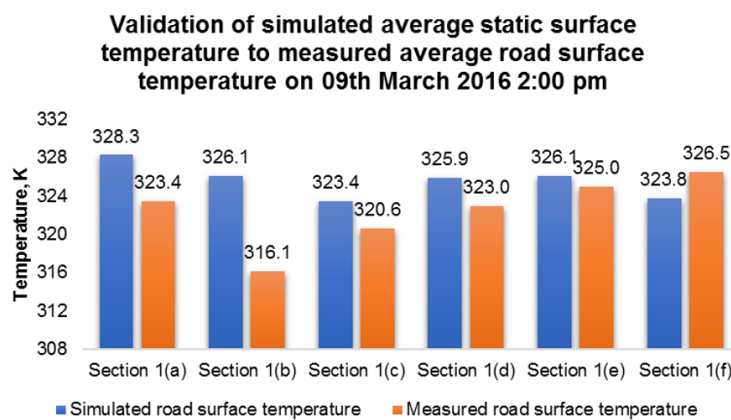
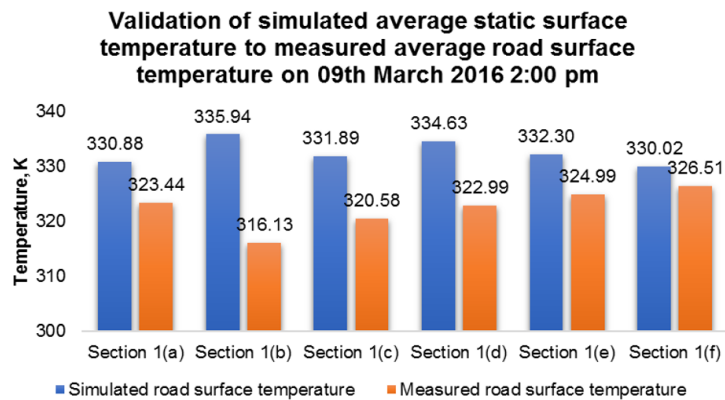


Figure 5.31 Validation of static façade temperature against thermal imaging results for (a) ROAD 1 during 9th March 2016 at 14:00 hour (b) ROAD 2 during 14th March 2016 at 11:00 hour

Figure 5.32 shows the validation of road surface temperature based on simulation to the measured road surface temperature based on thermal imaging. Like the previous result based on Figure 5.31, a better validation was observed during 9th March 2016 at 14:00 hour, with the error of percentage on average of the simulation to the thermal imaging was 8.65 %. For ROAD 2, the error of percentage of the simulation to the thermal imaging was on average 21.4 %.



(a)



(b)

Figure 5.32 Validation of static road surface temperature against thermal imaging results for (a) ROAD 1 during 9th March 2016 at 14:00 hour (b) ROAD 2 during 14th March 2016 at 11:00 hour

It should be noted in determining the outdoor temperature for urban environment can be complicated due to unpredicted weather within the time frame of conducting data collection. Meanwhile the simulation results are fixed with the boundary condition

applied. Thus, simulation of outdoor environment with simplification of the model boundary condition with 8-21 % average error of percentage for façade temperature and average 10-17 % error of percentage for road surface temperature (from in Figure 5.31 and Figure 5.32) seem satisfied the validation of modelling method against the outdoor field measurement using FLIR T650sc infrared thermal camera.

5.5 Summary

In summary, Chapter 5 introduced and explained the experimental data collection method used to investigate the thermal effects from building facades and road surfaces within two selected urban street canyons. Indoor-outdoor calibration and validation tests were carried out by factoring the distance of the images; which were taken from several distances towards an object for temperature reading. Simplification of the building facades and geometries was carried out to validate CAD modelling. Based on the modelling results, the model's temperature values were validated with the temperature values of data collection. Further discussion to correlate the temperature results based on urban canyons and the simulation modelling of the hydronic RPSC performance within several urban canyon is detailed in Chapter 6.

CHAPTER 6

Results and discussion

6.0 Introduction

Chapter 6 presents the result analysis and discussion that were structured based on the aim and objectives of this study, which was stated in Chapter 1. Section 6.1 presents the first three objectives (Objective 1-3) to evaluate the CFD simulation of hydronic RPSC system in performing surface temperature reduction (STR) and potential temperature collection (PTC) within urban environment. Section 6.2 presents the results and discussion for the Objective 4, 5 and 6 to evaluate the performance of hydronic RPSC within urban configuration with several adjustments of the system parameters. Section 6.3 presents the results and discussion for Objective no 7 and 8 in evaluating the after effect of hydronic RPSC application on urban temperatures (road surface temperature and air temperature at pedestrian level) which involved several configurations of urban street canyon. Section 6.4 presents and discusses the comparison based on the result and analysis from the experimental studies as per Chapter 5 and from the simulation modelling at once to discuss the validation of the model. In Section 6.5, a summary of the works based on each section is highlighted.

6.1 CFD analysis of RPSC performance based on urban configuration

For the first investigation, the comparison of the hydronic RPSC performance within an urban street canyon domain, shortened as ‘urban macro domain’ was carried out with the system performance within an opened space (flat surface), shortened as ‘rural/flat macro domain’. Both domain geometries were based on the settings described in Chapter 4 Section 4.2.1. The default setting of the comparison was during the midday (13:00) of hot summer month, 21st June in Milan city centre at longitude 9.18 °E, latitude 45.47°N and UTC +1 with 303 K ambient temperature and wind speed, 2 m/s. The wind direction was perpendicular to the length of the canyon buildings. For Figure 6.1 shows the comparison of the road surface within an urban macro domain and within flat/rural macro domain.

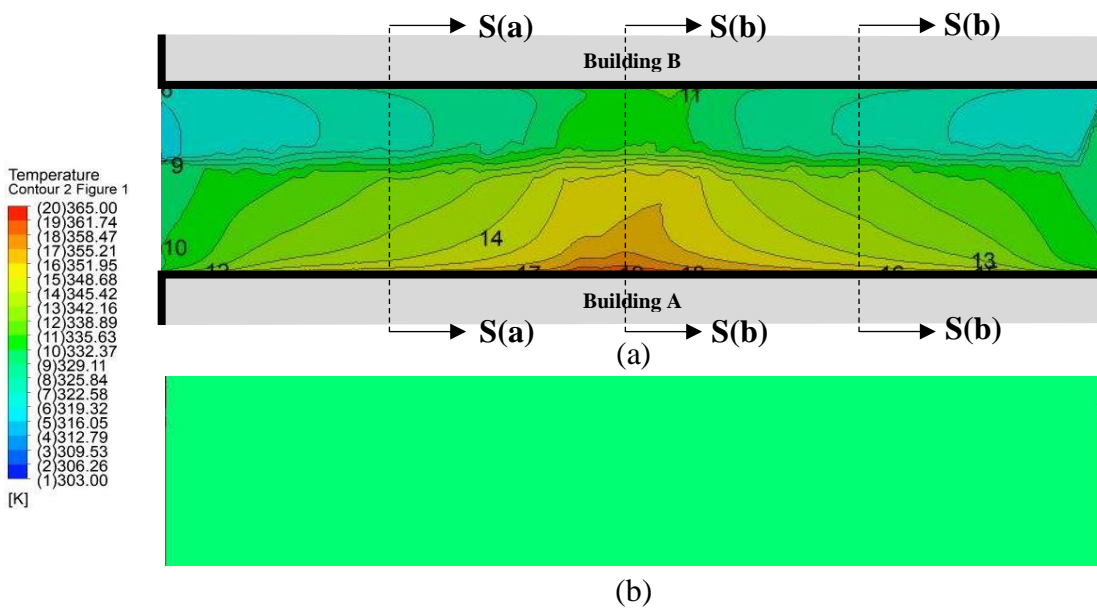


Figure 6.1 Simulation result of static surface temperature for (a) urban street canyon of urban macro domain (b) flat surface of rural/flat macro domain. Sectional air velocity indicated as S-S(a), S-S(b) and S-S(c) is detailed in Appendix A.13

Figure 6.1(a) shows the temperature contour of canyon road surface due to the effect of predominant airflow from the inlet plane across the first building (Building A) and

penetrated the canyon area from the sides and top of the canyon. Additional information on air velocity vector occurred at different locations can be referred to Appendix A.13. Results based on urban macro domain demonstrated that the temperature contours across the surface with hotter temperature observed at the centre of the surface area. The existing Building A and B influenced to include the effect of shadow on the surface area closer to Building B. From the centre of the surface, lower temperature contours spread from the centre and the hotter surface area (closer to Building A) to the left and right surface areas of the canyon openings where the air can access to street canyon. At the side of Building B where the surface was shaded, the temperature contour did not obviously diverse.

Additionally, the ambient temperature set for the inlet boundary condition, 303 K (30 °C) was also high to represent a hot summer day in the month of June. Unequal solar heat flux distribution was observed at the simulation time on the canyon road surface, causing the sideway of Building A was directly heated by the solar radiation. The low air speed during solar peak hour caused low rate of solid-air heat convection to occur, plus with the condition of the building canyon that acted as the blockage to the movement of predominant airflow. Section of air temperature within the street canyon of urban macro domain in Figure 6.2 demonstrates higher air temperature closer to the ground level. The temperature difference between the two surfaces in two different domain configurations is quantified based on area-weighted average of ground surface temperature above 9 pipes located as explained in Chapter 4 of the thesis, see Figure 6.3. Based on the Figure 6.3, it was confirmed that the temperature of road surface for the urban macro domain with street canyon AR 1 obtained temperature diversity from the measurement point closer to Building A (Point A-5) to the measurement point closer to Building B (Point B-5).

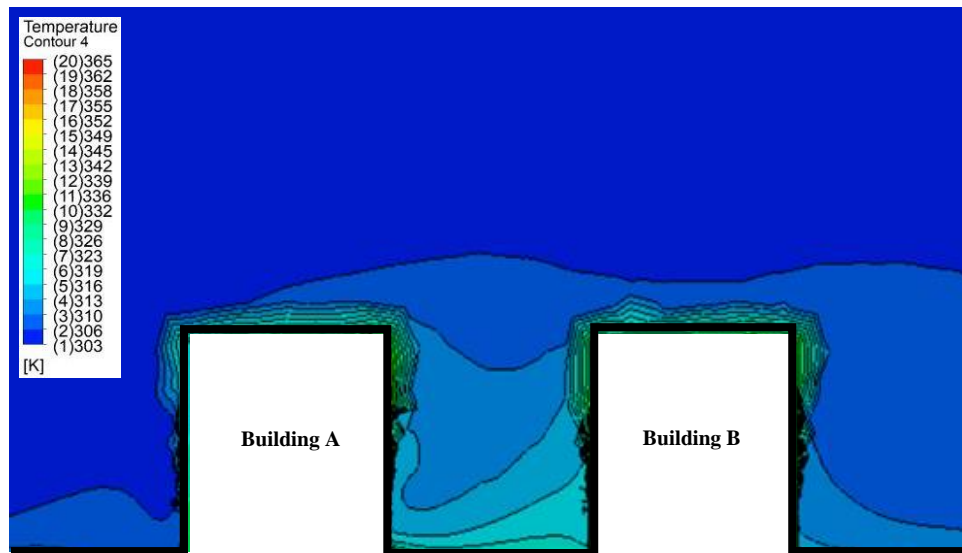


Figure 6.2 Air temperature at the centre of street canyon of urban macro domain

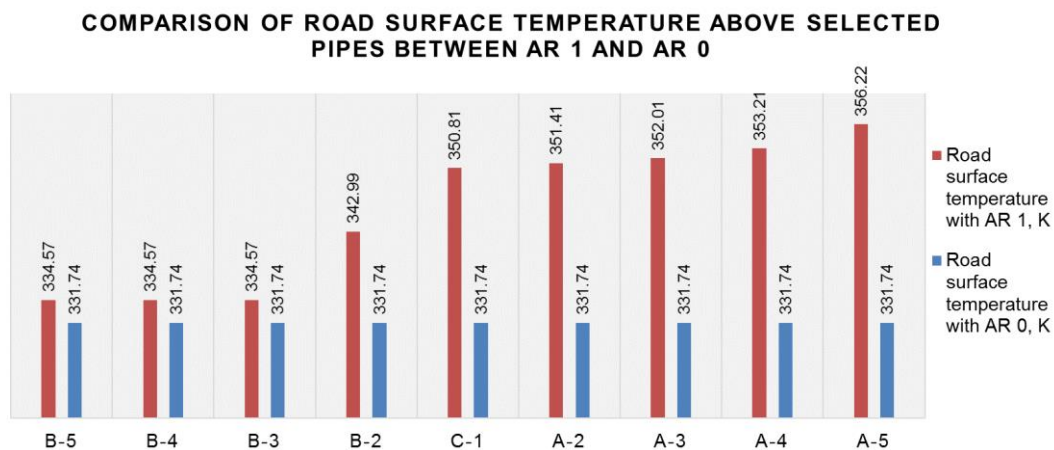


Figure 6.3 Area-weighted average road surface temperature 0.15m above selected pipe location at 13:00 hour for urban macro domain with street canyon AR 1 and for rural/flat macro domain without building (AR 0)

The unequal solar heat flux distribution during 13:00 hour due to several factors (direction of solar radiation, building orientation) caused the refraction of the solar angle and the shadow effect on road surfaces. This trend was observed vice-versa for the road surface of rural/flat macro domain where the surface obtained similar temperature values at the measurement points. The values of average surface temperature at each selected point were applied as the boundary condition of micro domain model for calculating each

temperature difference (Delta T) of inlet-outlet water condition, PTC and STR in unit percentage, refer to Section 6.1.1.

6.1.1 Effect of urban canyon on RPSC performance

The stitched graphic of road surface temperature at 9 pipe locations after the simulation of hydronic RPSC system in Figure 6.4 displays a clear influence of building canyon on its road surface based on its unequal surface temperature distribution as compared to the road surface exposed without buildings. In this study, the RPSC with urban canyon was termed as RPSC-1 and the RPSC without urban canyon was termed as RPSC-0.

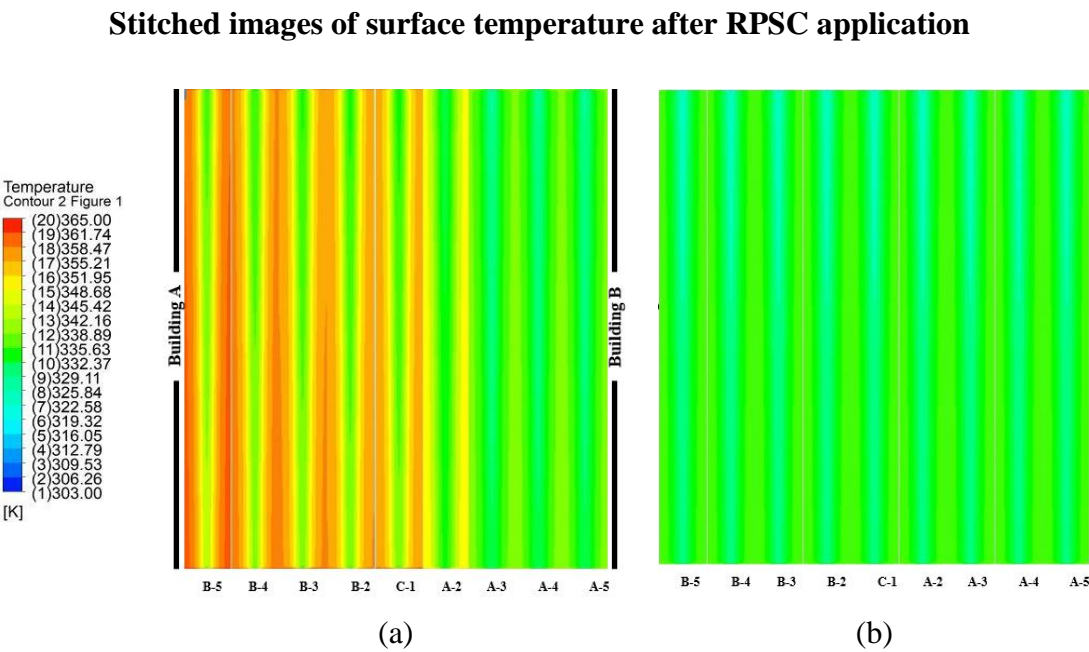


Figure 6.4 Surface temperature after RPSC simulation at 0.15m below pipes for (a) urban macro domain or RPSC-1 (b) rural/flat macro domain or RPSC-0

Full result of Delta T, PTC and STR comparing RPSC-1 and RPSC-0 is displayed in Table 6.1. Based on Table 6.1, overall efficiency of RPSC-1 was on average 35.76 % for potential temperature collection and on average 9.25 % for surface temperature reduction. With building shadow, the STR performance of RPSC-1 was reduced between 16.82 %

and 34.27 %. Based on the result, it can be observed that urban surfaces were in various temperature as compared to rural surfaces due to a strong influence of the street canyon configuration.

Table 6.1 Calculated Delta T, PTC and STR values at 13:00 hour on 21st June

DESCRIPTION	$T_{w(i)}$ (K)	$T_{w(o)}$ (K)	<i>Delta T</i> (K)	PTC, %	STR, %
RPSC-0 for all pipes	292.99	301.52	8.53	42.67	51.45
RPSC-1 for all pipes	292.99	304.57	11.58	57.93	56.21
A-5	292.99	306.91	13.92	69.63	59.25
A-4	292.99	306.24	13.25	66.28	58.56
A-3	292.99	305.98	12.99	64.98	58.26
A-2	292.99	305.85	12.86	64.33	58.10
C-1	292.99	305.71	12.72	63.63	57.96
B-2	292.99	303.99	11.00	55.03	55.72
B-3	292.99	302.14	9.15	45.77	52.67
B-4	292.99	302.14	9.15	45.77	52.67
B-5	292.99	302.14	9.15	45.77	52.67
*** PTC = Potential Temperature Collection, STR = Surface Temperature Reduction					

6.1.1.1 Effect of solar intensity on RPSC performance

Investigation on comparing the RPSC-1 to the hydronic RPSC-0 is displayed in this section. Figure 6.5 displays the values of outlet water temperature of RPSC system involving three selected pipe locations (Pipe A-5, C-1 and B-5) to evaluate the effect of solar intensity on both RPSC-1 and RPSC-0. It was noted that the three selected pipes were based on the closest pipe to Building A (Pipe A-5), the centre pipe (C-1) and the closest pipe to Building B (B-5). Based on the figure, it was noted that the plotted graph showing the outlet water temperature of RPSC-1 and RPSC-0 was in bell curve shape with lower temperature was obtained during the morning hours. The temperature then gradually increased accordingly to time and achieved its peak at noon hours (between 12:00 and 14:00 hour) before the temperature began to fall towards evening. It can be agreed that the graph trend in Figure 6.5 satisfied the graph trend of the plotted façade

and road surface temperatures based on the thesis' data collection as explained in Chapter 5 Section 5.4.1. In the previous data collection, the peak temperature time was measured mostly at 14:00 hour and the temperature began to fall on the latter hours.

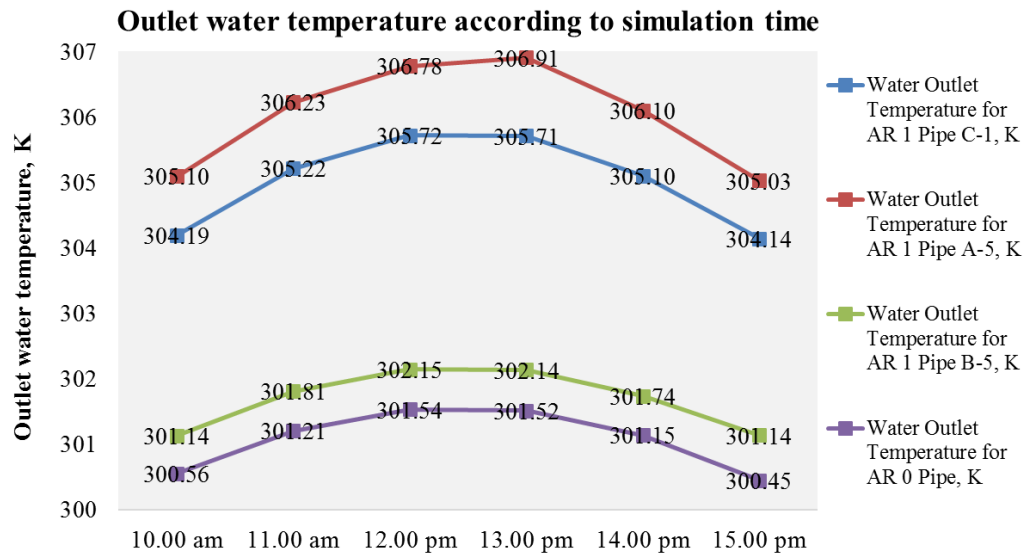


Figure 6.5 Effect of hourly solar intensity on the RPSC outlet water temperature

6.1.1.2 Effect of wind velocity during summertime on RPSC performance

Figure 6.6 demonstrates the plotted surface temperature, outlet water temperature and Delta T for Pipe C-1 (due to its location at the centre of canyon) by wind velocity. In Chapter 2, it was highlighted that wind velocity is one of main parameters to influence the microclimate condition, see Section 2.2.1. This section evaluates performance of hydronic RPSC system within urban macro domain when strong and weak wind condition was applied. Based on Figure 6.6 the simulation suggested that with lower wind velocity, higher Delta T can be obtained by RPSC system. This means the reduction in the Delta T reached up to 55.78 % (less 8.45 K / °C) when the velocity changed from 1 m/s to 10 m/s. The air velocity vector within the canyon comparing 1 m/s, 2 m/s, 5 m/s and 10 m/s is further explained in Appendix A.14.

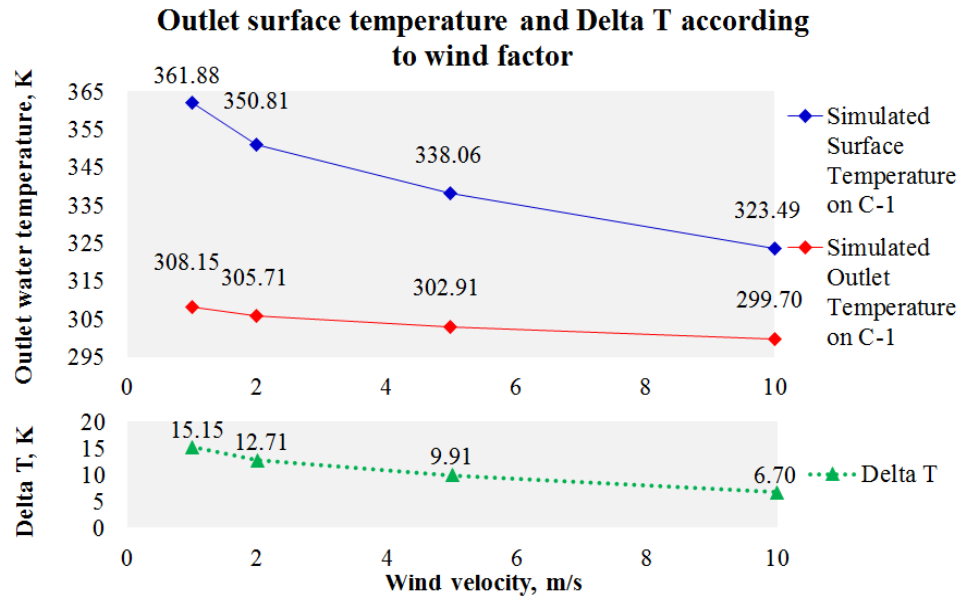


Figure 6.6 Result of inlet outlet temperature difference, Delta T of RPSC performance based on wind factor

6.1.1.3 Seasonal effect on RPSC performance

The effect of changing seasons on RPSC performance was studied based on every 21st day during the months of (i) Spring March, (ii) Summer June, (iii) Autumn September (iv) Winter December (WeatherUnderground 2014). Figure 6.7 shows the predicted values of outlet water temperature and Delta T for Pipe C-1 of RPSC-1 simulated based seasons. Based on Figure 6.7, it can be agreed that summertime provides high solar intensity, thus causing the road surface to obtain highest temperature value as compared to other months and seasons. Seasonal change from 21st June to 21st September shows the reduction in the surface temperature by on average 30 %. The highest reduction can be predicted when summertime was changed to winter time (21st December), by on average 62 %. During 21st March, the plotted temperature value shows on average 40 % behind the value plotted during 21st June. Based on the figure, values obtained for the simulated surface temperature according to the four seasons seem consistent with Delta T. This means, higher surface temperature value causes higher Delta T was obtained from the

simulation. Effects of surface temperature based on seasonal changes was referred to Appendix A.15.

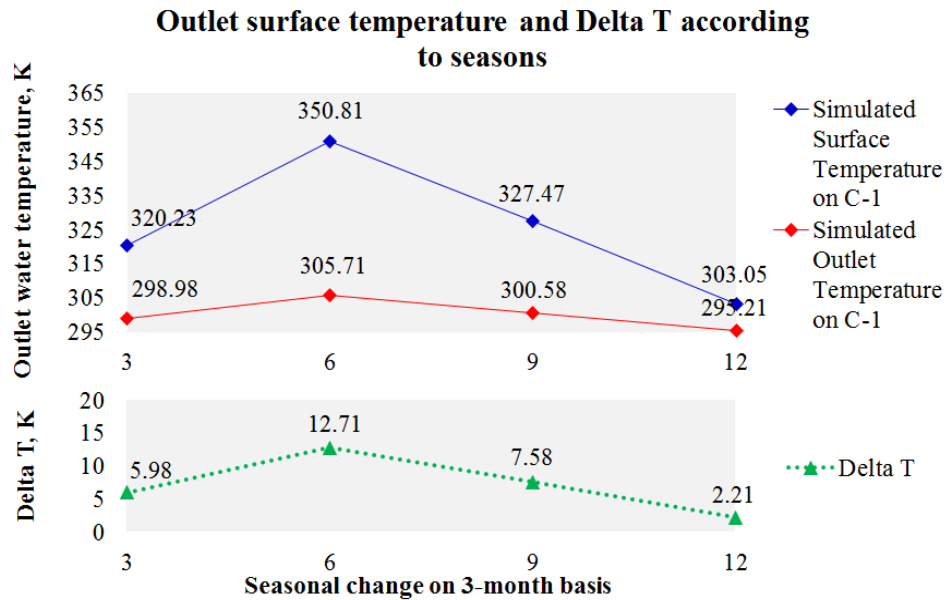


Figure 6.7 Predicted Delta T of RPSC performance based on seasonal changes

6.1.2 Effect of canyon aspect ratio on RPSC performance

In this section, results are presented in three sub sections. Section 6.1.2.1 discusses the effect of the canyon aspect ratio on road surface temperature. Section 6.1.2.2 presents the results of the simulation of micro domain (RPSC pipes) in urban canyon with various aspect ratio AR 1, 2, 3 and 4. Section 6.1.2.3 displays the effect of leeward façade temperature based on the simulation of macro domain with AR 1, 2, 3 and 4. Section 6.1.2.4 discusses the effect of canyon aspect ratio on the performance RPSC in terms of Delta T, PTC and STR.

6.1.2.1 Effect of aspect ratio on surface temperature

Figure 6.8 shows the comparison of temperature contour of road surface in four aspect ratios (AR 1, 2, 3 and 4).

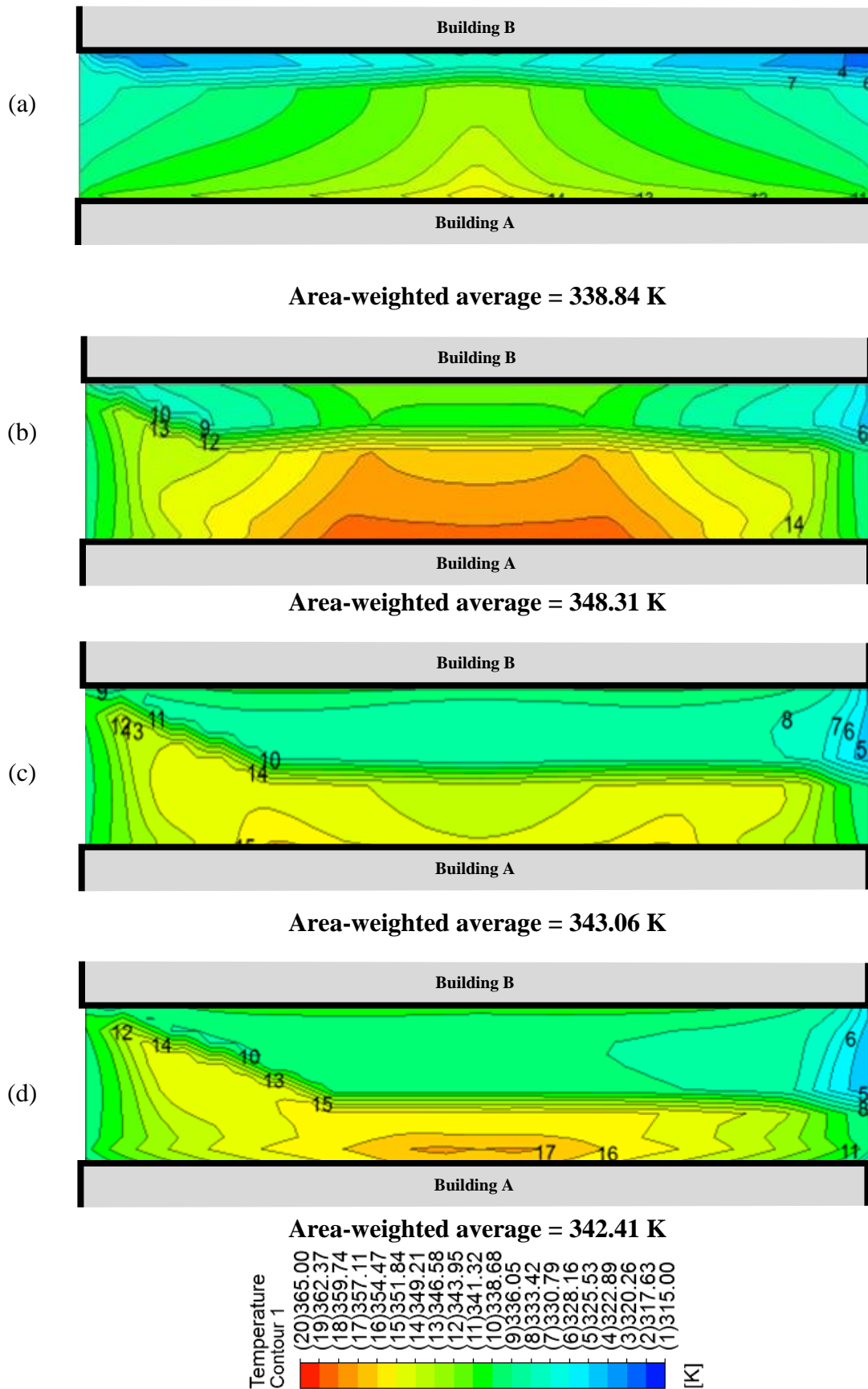
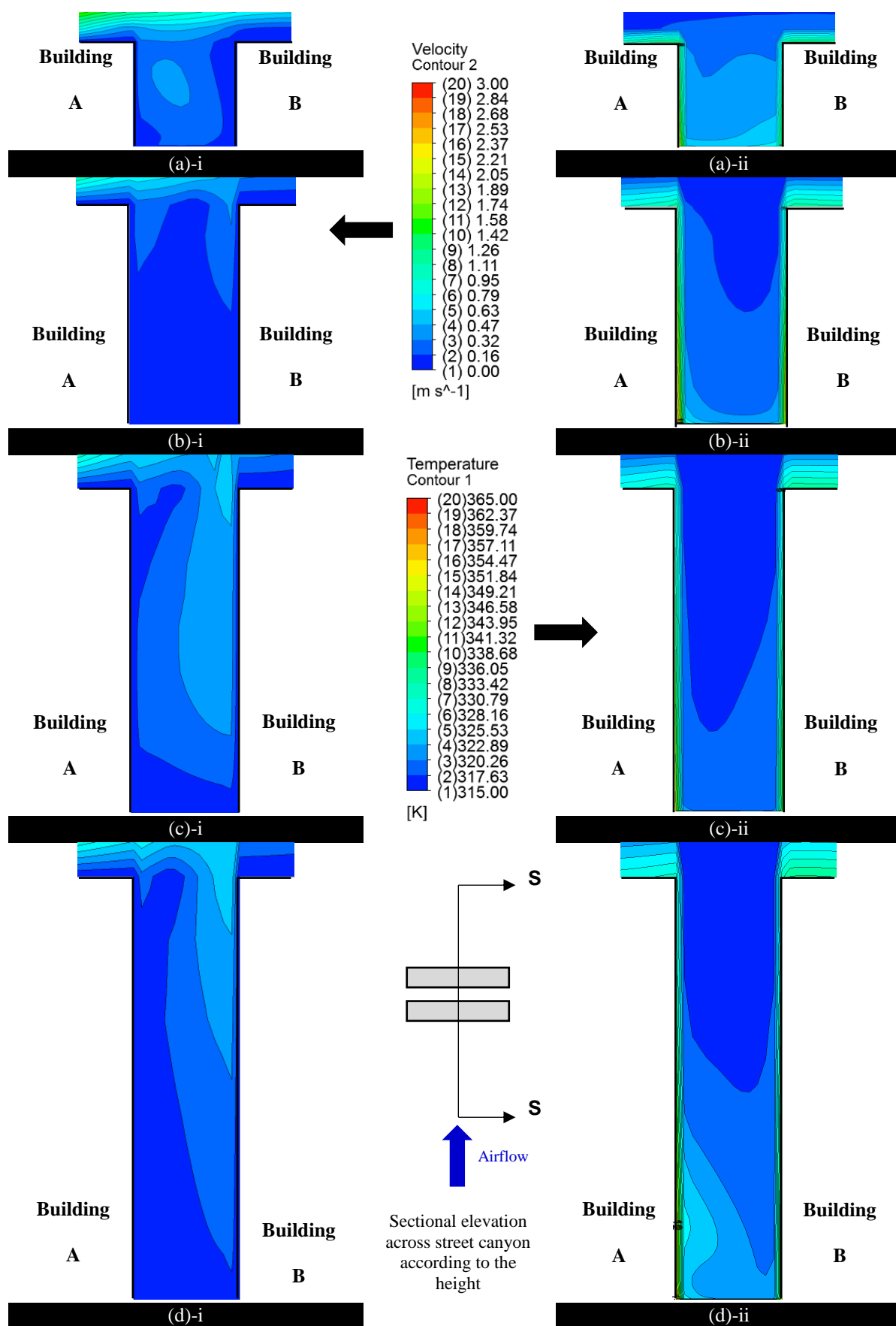


Figure 6.8 Surface temperature contour of street canyon comparing its effect based on the configuration of aspect ratio (a) AR 1 (b) AR 2 (c) AR 3 (d) AR 4

It should be reminded that the simulation was carried out during summer, 21st June at 13:00 hour with 303 K ambient temperature and 2 m/s wind speed. The wind direction was similarly set to the previous AR 1 and AR 0 settings; which was perpendicular to the length of the canyon buildings. For all aspect ratios, it can be observed that due to the angle of the direct solar radiation and shadow of Building B, lower surface temperature was obtained near the Building B as compared to Building A. In addition, it was highlighted that the depth of shadow kept increasing with higher aspect ratio. Meanwhile, the surface temperature near Building A obtained higher temperature specifically at the middle of the canyon. However, it could also be observed that the surface temperature did not only increase according to the aspect ratio. As observed in Figure 6.8, AR 2 obtained the highest surface temperature as compared to the other aspect ratios particularly at midway of Building A, 363 K. Based on average surface temperature as detailed in Figure 6.8, it showed that the value obtained by AR 2 was followed by AR 3, 4 and 1. Section 6.1.2.2 further discusses the influence of aspect ratio and air temperature on the surface temperature of street canyon.

6.1.2.2 Effect of aspect ratio and air temperature on road surface temperature

Sections of air velocity and air temperature at the middle of the street canyon (290 m from x -axis, between 420 m and 440 m from the y -axis) are shown in Figure 6.9; see Section S-S labelled (a), (b), (c) and (d) for AR 1, AR 2, AR 3 and AR 4, respectively. As observed, the airflow at 2 m/s with the temperature 303 K (30 °C) has crossed over the street canyon perpendicular to the wind flow direction which caused rotating airflow with low air speed inside the street canyon. As the building height increased from 20 m (AR 1) to 40 m (AR 2), it was observed that the circulation of air inside the street canyon was reduced particularly in AR 2.



Thus, the combined effect of direct solar radiation and low speed airflow helped to elevate the temperature of the surface. Although the street canyon had openings on the right, left and top; the air movement was insufficient to reduce the surface temperature, particularly the middle surface.

As can be seen from Figure 6.9(b), lower temperature contours were found near the canyon openings but higher towards the middle surface. In general, the air temperature distribution within the street canyon was observed to be lower near the rooftop and higher towards the surface. By increasing the aspect ratio from AR 2 to AR 3, it was found that the effect of shadow from Building B has increased and thus further lowered the heat from the road surface. From AR 3 to AR 4; it was observed that the increase in the street canyon height has slightly reduced the average surface temperature due to the increased shadow of Building B. Additionally, the increase in the aspect ratio from AR 3 to AR 4 also caused the reduction of air penetrating all openings more than AR 3, causing higher air temperature closer to Building A due to low air velocity, see Figure 6.9(d).

6.1.2.3 Effect of aspect ratio on leeward façade temperature

Figure 6.10 displays the result of façade temperature contour of Leeward Wall by Building A facing canyon according to the aspect ratio of 1, 2, 3 and 4. Based on Figure 6.10, it was noted that the Leeward Wall of Building A for all aspect ratios obtained higher temperature contour closer to the ground level. The refraction of solar radiation directed from behind the Building B has majorly influenced the rise in the façade temperature. The increased temperature was more prominent when comparing the Leeward Wall of Building A between AR 1 and AR 2. However, above the aspect ratio of 2, the shadow effect from Building B played a major influence in reducing the heating

of Leeward Wall, with cooler contours on Leeward Wall of AR 3 and AR 4 as compared to Leeward Wall of AR 2. In comparing the façade temperature between the four aspect ratios, it should be highlighted that the Leeward Wall of AR 2 was affected the most.

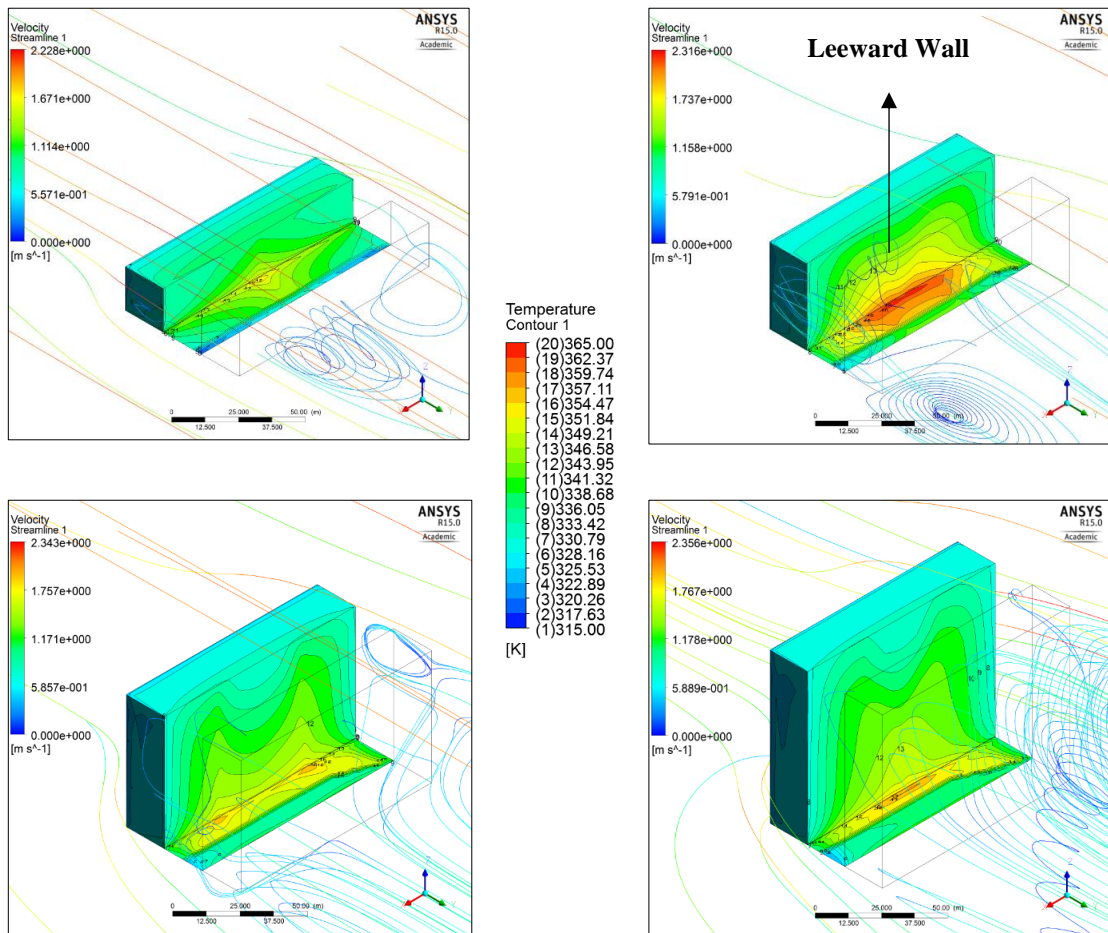


Figure 6.10 Temperature contour of Leeward Wall (façade of Building A facing canyon) and 3D air streamlines of (a) AR 1 (b) AR 2 (c) AR 3 (d) AR 4

6.1.2.4 Effect of urban aspect ratio on RPSC Delta T, PTC and STR

Additional results of road surface temperature plotted along the length of the street canyon comparing AR 1, 2, 3 and 4 are displayed in Appendix A.16, conforming the previous explanation on the major effects of solar radiation and wind blocking from Building B. The temperature plot was varied at three y-axis: (i) C-1 - middle of street canyon, 430 m

from inlet plane in y-axis; (ii) A-5 - 1.0 m from Building A and (iii) B-5 - 1 m from Building B. Figure 6.11 shows 6 additional locations added in between A-5, C-1 and B-5 for measuring the surface temperature, which was utilised as the boundary condition for the micro domain simulations.

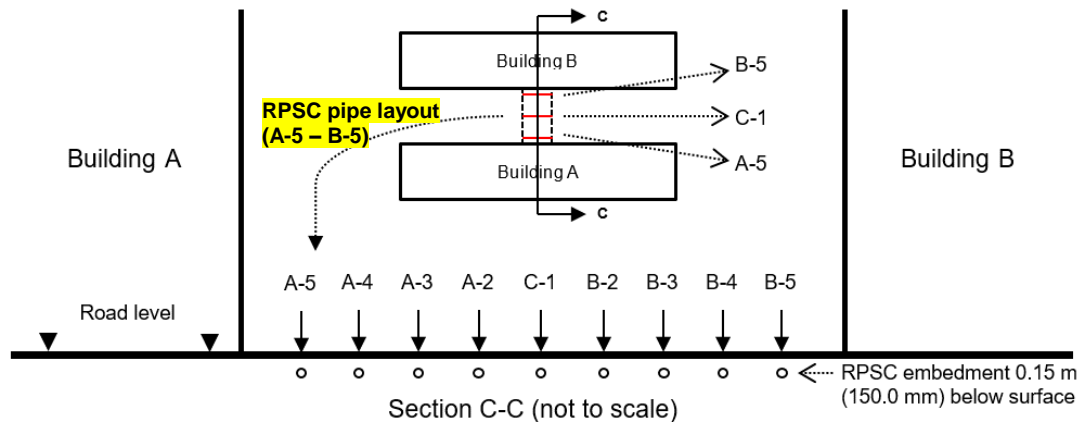


Figure 6.11 Details on 9 locations of average surface temperature from macro domain to be exported to micro domain

Table 6.2 shows the average temperature values measured from the locations detailed in Figure 6.11 and the outlet water temperature obtained based on micro domain simulation. These results were used to obtain RPSC performance in terms of Delta T, PTC and STR.

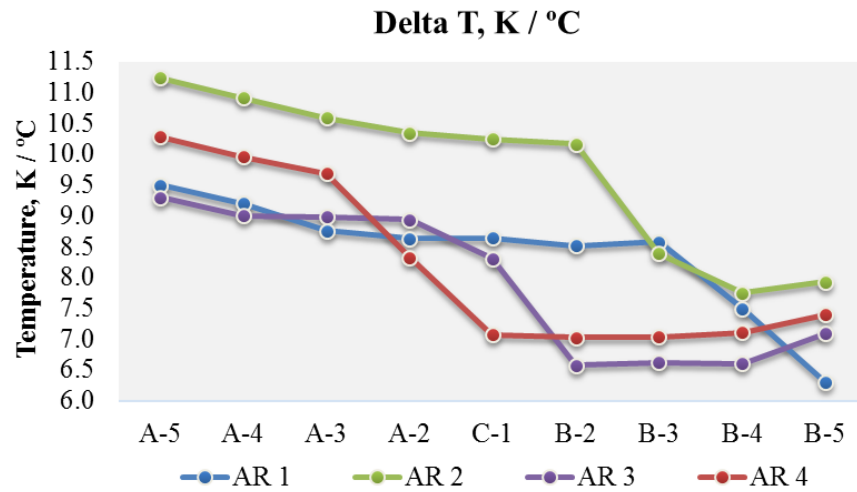
Table 6.2 Average surface temperature and outlet water temperature during 13:00 hour

Description	Surface temperature based on area-weighted average, Kelvin (K)								
	A5	A4	A3	A2	C1	B2	B3	B4	B5
AR 1	351.00	359.32	347.76	346.74	346.07	345.67	345.65	339.51	332.78
AR 2	361.74	359.91	358.34	357.29	356.62	356.23	345.30	341.27	343.09
AR 3	351.08	349.43	348.59	348.07	344.25	339.91	333.62	333.82	336.44
AR 4	356.84	354.60	353.06	344.57	337.03	336.53	336.29	336.41	338.54
Description	Outlet water temperature based on area-weighted average, Kelvin (K)								
	A5	A4	A3	A2	C1	B2	B3	B4	B5
AR 1	302.56	302.22	301.95	301.76	301.63	301.55	301.53	300.51	299.38
AR 2	304.36	304.00	303.70	303.50	303.36	303.27	301.47	300.78	301.04
AR 3	302.44	302.18	302.04	301.95	301.33	299.65	299.60	299.64	300.06
AR 4	303.38	303.02	302.77	301.39	300.16	300.08	300.04	300.06	300.41

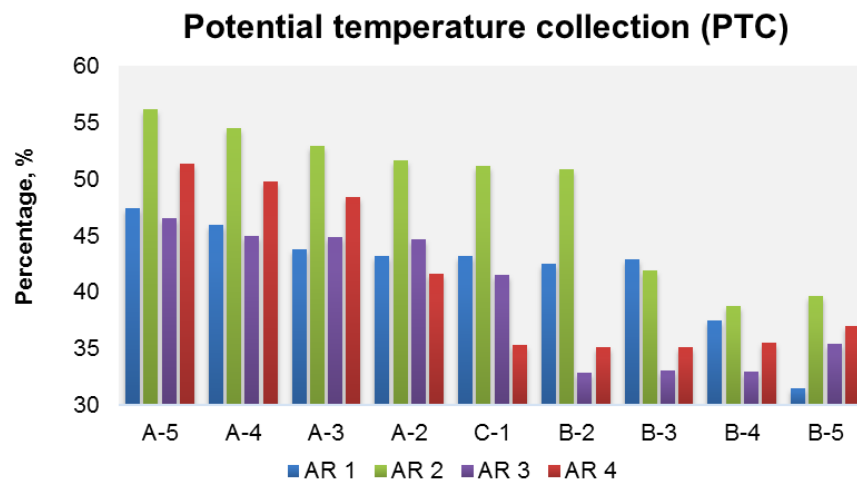
Figure 6.12 shows the RPSC performance in terms of Delta T, PTC and STR. In Figure 6.12(a), the Delta T was plotted according to the location of pipe embedment, demonstrating higher Delta T based on location was obtained by the pipes closer to Building A and vice-versa for the pipes closer to Building B. The highest Delta T was obtained by pipe A-5 within the aspect ratio of 2, with 11.24 °C; followed by pipe A-5 of AR 4 (10.28 °C), AR 1 (9.5 °C) and AR 3 (9.3 °C). With the shadow effect from Building B, the lowest Delta T obtained by pipe B-5 was AR 1 with 6.3 °C, followed by AR 3 (7.01 °C), AR 4 (7.34 °C) and AR 2 (7.93 °C). These results were observed tally to the obtained surface temperature on Section 6.1.2.1 and 6.1.2.2.

Based on Figure 6.12(a), it was expected that the obtained PTC values were parallel to the obtained Delta T values, showing the highest average PTC of RPSC system was based on the configuration of AR 2, with 16.0-23.0 % higher than other aspect ratios. It can be observed that the obtained PTC values for AR 2 at pipe location between A-5 and B-5 were significant against other aspect ratios, meanwhile the values were significantly dropped when building shadow dominated the surface area, see Figure 6.12(b).

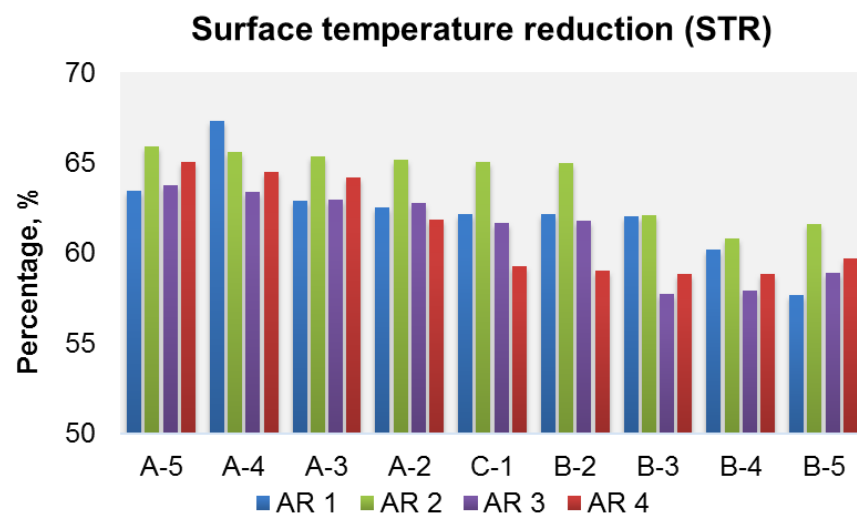
Similarly applied to the other aspect ratios, the trend of the obtained PTC values was majorly influenced by both canyon buildings that were adjacent to one another; either the surface temperature to be shaded, received the effect of solar refraction or to be blocked by predominant airflow. Inversely, the trend for STR values were insignificant to compare the four aspect ratios, see Figure 6.12(c). On average; although AR 2 has still dominated the result, the STR for AR 2 was higher than AR 1, AR 4 and AR 3 by 2.81 %, 4.38 % and 4.46 %, respectively.



(a)



(b)



(c)

Figure 6.12 Performance of RPSC based on street canyon aspect ratio showing (a) Delta T (b) PTC, % (c) STR, %

6.1.3 Effect of urban topologies on RPSC performance

Four sub-sections are presented in this section. Section 6.1.3.1 compares and discusses the temperature distribution of canyon surface in three canyon settings – one with symmetrical canyon height ($H/W = 1$) and two with asymmetrical canyon height – Type 1 and Type 2. Section 6.1.3.2 discusses the comparison of sectional air velocity at the centre of the canyon between the three canyons meanwhile Section 6.1.3.3 displays and analyses the temperature effect on the building facades. Section 6.1.3.4 presents the analysis of RPSC performance based on PTC and STR in percentage.

6.1.3.1 Comparative analysis on temperature of canyon road surface

Figure 6.13 displays the surface temperature contour of road surface within three street canyon configurations – symmetrical canyon height, asymmetrical canyon height Type 1 and asymmetrical canyon height Type 2. As mentioned in the previous sections of this chapter, Building B acted as the obstacle to the direct solar radiation towards façade and road surfaces within street canyon. Due to this, the refraction of solar radiation was observed towards the façade and sideway of Building A. Building B also caused the sideway nearby the building to be shaded. As referred to the previous boundary condition set for the simulations in Section 6.1.1 and 6.1.2, the simulation was carried out during summer, 21st June at 13:00 hour with 303 K ambient temperature and 2 m/s wind speed. The wind direction was similarly set to the previous AR 1 and AR 0 settings; which was perpendicular to the length of the canyon buildings. With the modification of the street canyon, it can be observed that the effects of surface temperature contour of each configuration were significant.

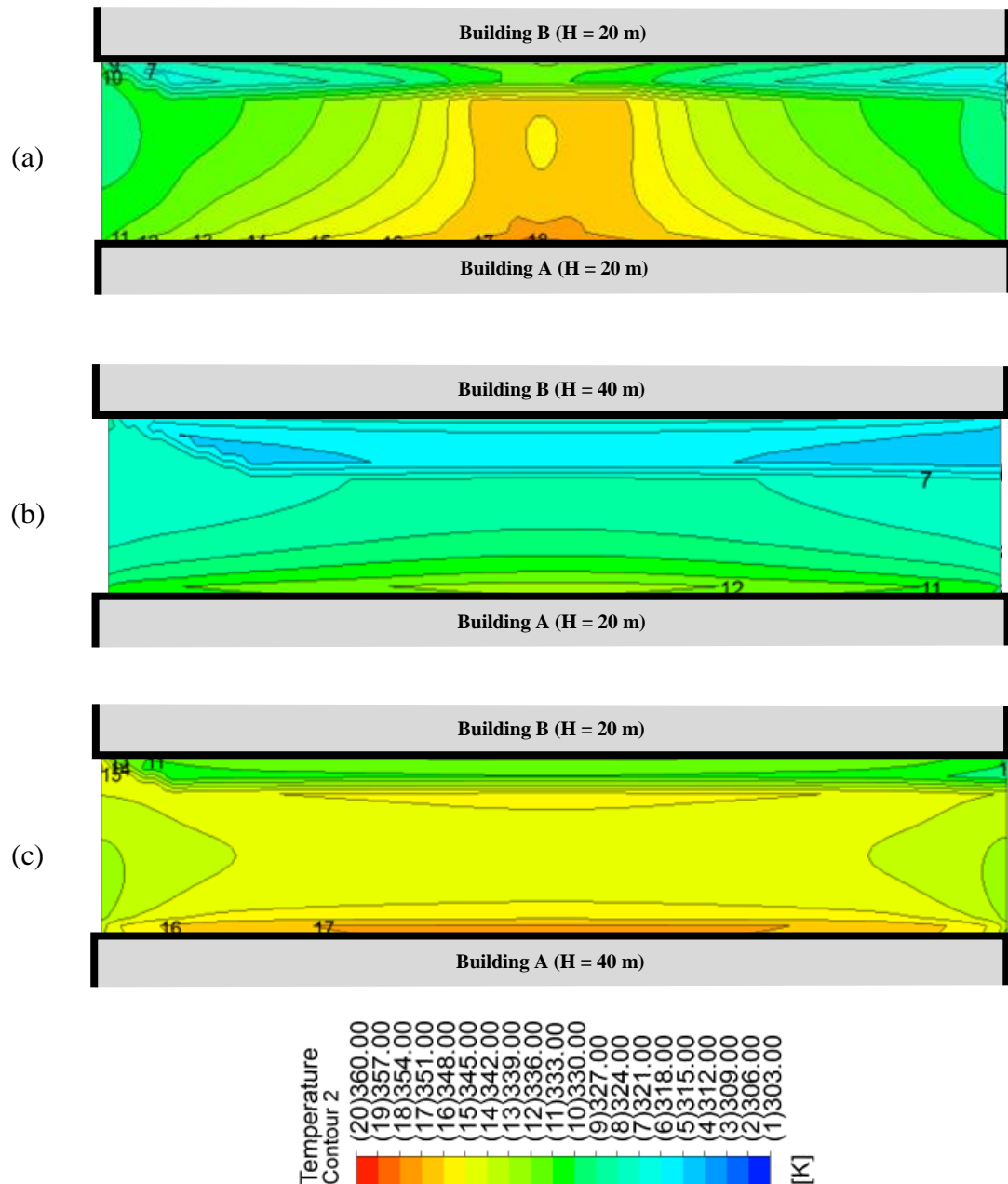


Figure 6.13 Temperature contour of canyon road surface comparing (a) Symmetrical canyon height (b) Asymmetrical canyon height Type 1 (c) Asymmetrical canyon height Type 2

As refer to Figure 6.13(a), the contour trend conforms the previous simulation of urban street canyon AR 1, where lower temperature was observed near the left and right canyon openings meanwhile the centre of the canyon surface obtained higher temperature, see hotter temperature contours at the centre of the road surface. In Figure 6.13(b), it can be

observed that larger shadow has superimposed the road surface within asymmetrical canyon height Type 1 due to double the height of Building B ($H = 40$ m), causing much lower surface temperature obtained by Type 1 as compared to other two canyon settings. Additionally, refraction of solar radiation conforms the similar trend as symmetrical canyon height, causing the surface area closer to Building A to obtain higher temperature than other surface areas.

For asymmetrical Type 2 which is shown in Figure 6.13(c), lower building height on the second canyon row (Building B) imitated similar shadow effect closer to Building B as the previous simulations with symmetrical canyon height. However, it was observed that the temperature of the surface at the centre of canyon towards left and right canyon openings did not vary significantly and seemed almost identical. Also, it was observed with insignificant higher temperature contours at the sideway of Building A. Further investigation involving 3D air velocity streamlines in Section 6.1.3.2 provides further explanation on the significant difference in the surface temperature contour when the canyon height was modified.

6.1.3.2 Comparative analysis on air velocity streamlines

Analysis of 3D air velocity streamlines with effects of forward and backward is carried out in this section to compare the three street canyon settings, see Figure 6.14. For all types, the first façade of the first building row facing canyon (Building A) acted as the blockage to the predominant airflow that caused airflow to cross over the building and to disperse around the canyon edges to avoid the vertical obstacle, Building A. Simultaneously, airflow penetrated the canyon from both canyon openings and from the

top opening. It was also observed that asymmetrical canyon height has significantly modified the airflow movement.

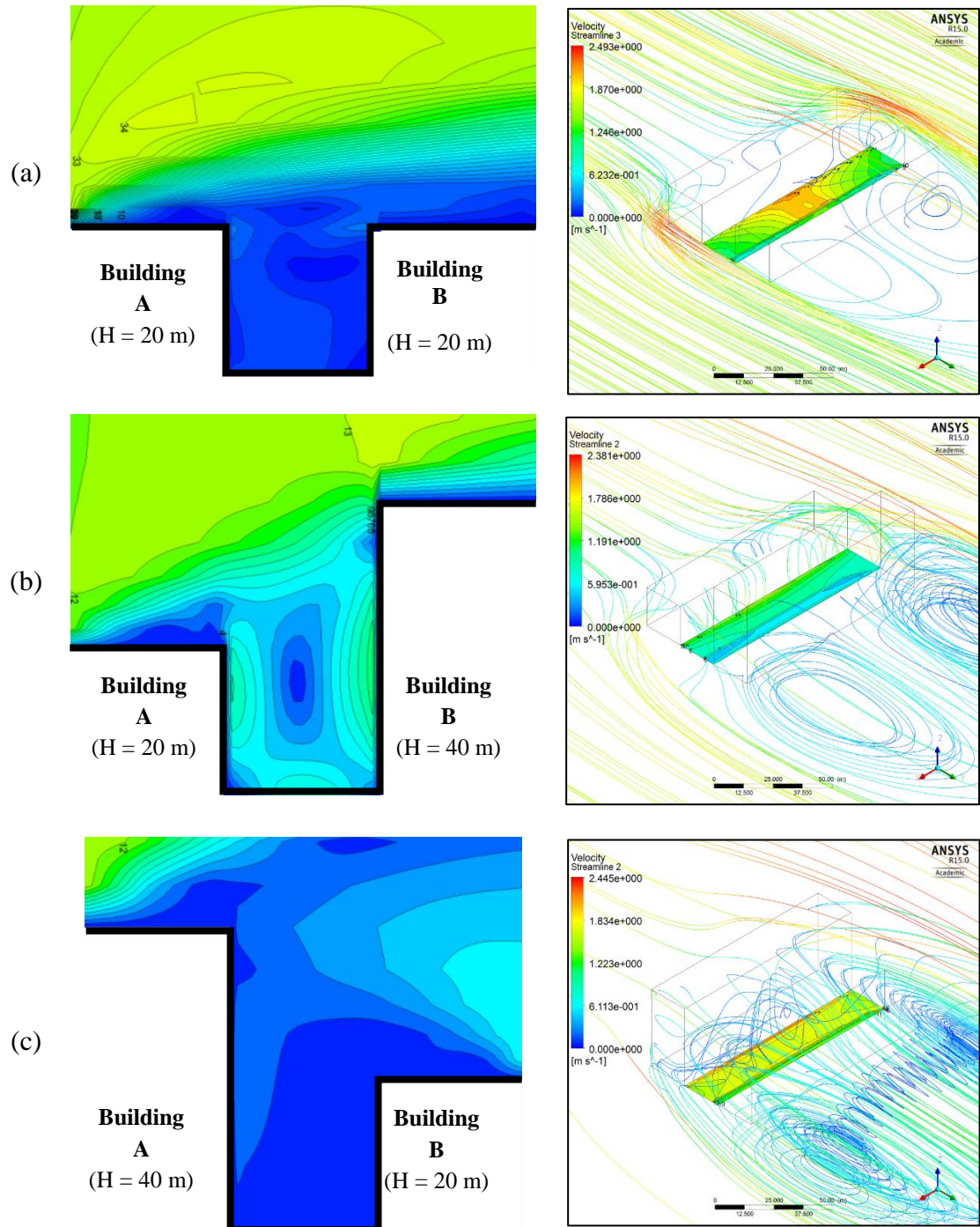


Figure 6.14 Air velocity contour comparing (a) Symmetrical canyon height (b) Asymmetrical canyon height Type 1 (c) Asymmetrical canyon height Type 2

Figure 6.14(b) which represents the airflow movement for Type 1 demonstrated the easier penetration of airflow into the canyon space from the upper openings as compared to Type 2. With a taller height of Building B, it became the obstacle to the entering airflow and swirling air effect was seen to exist and to be directed down to the canyon road surface, indirectly assisting in cooling the surface temperature. Additional effects of shadow from Building B assisted the increased cooling effect of the temperature.

Based on Figure 6.14(c), Building A caused larger swirling air passed over Building B as the air moved from high to low pressure, causing low air velocity at the downside of the street canyon Type 2. The airflow which penetrated the canyon openings (all directions) also occurred but has a little impact on reducing the deep-down canyon space and road surface temperature. Additionally, it was observed that the temperature contour classified as (15) has dominated almost 60 % of the total surface area of asymmetrical canyon height Type 2, see the temperature range. For symmetrical canyon height, swirling air was more visible at the side openings of the canyon, which influenced on the uneven temperature distribution of the road surface, see Figure 6.14(a). Further explanation on the correlation between street canyon height, street canyon road surface and canyon façade temperature is available in Section 6.1.3.3.

6.1.3.3 Comparative analysis on façade temperature

Figure 6.15 displays the temperature façades facing street canyon (Leeward Wall for Building A and Windward Wall for Building B) for the three canyon settings. In overall, it was observed that all façade temperatures have gradually increased according to the height. It was observed that hotter temperature contours were situated closer to the ground as compared to the upper locations.

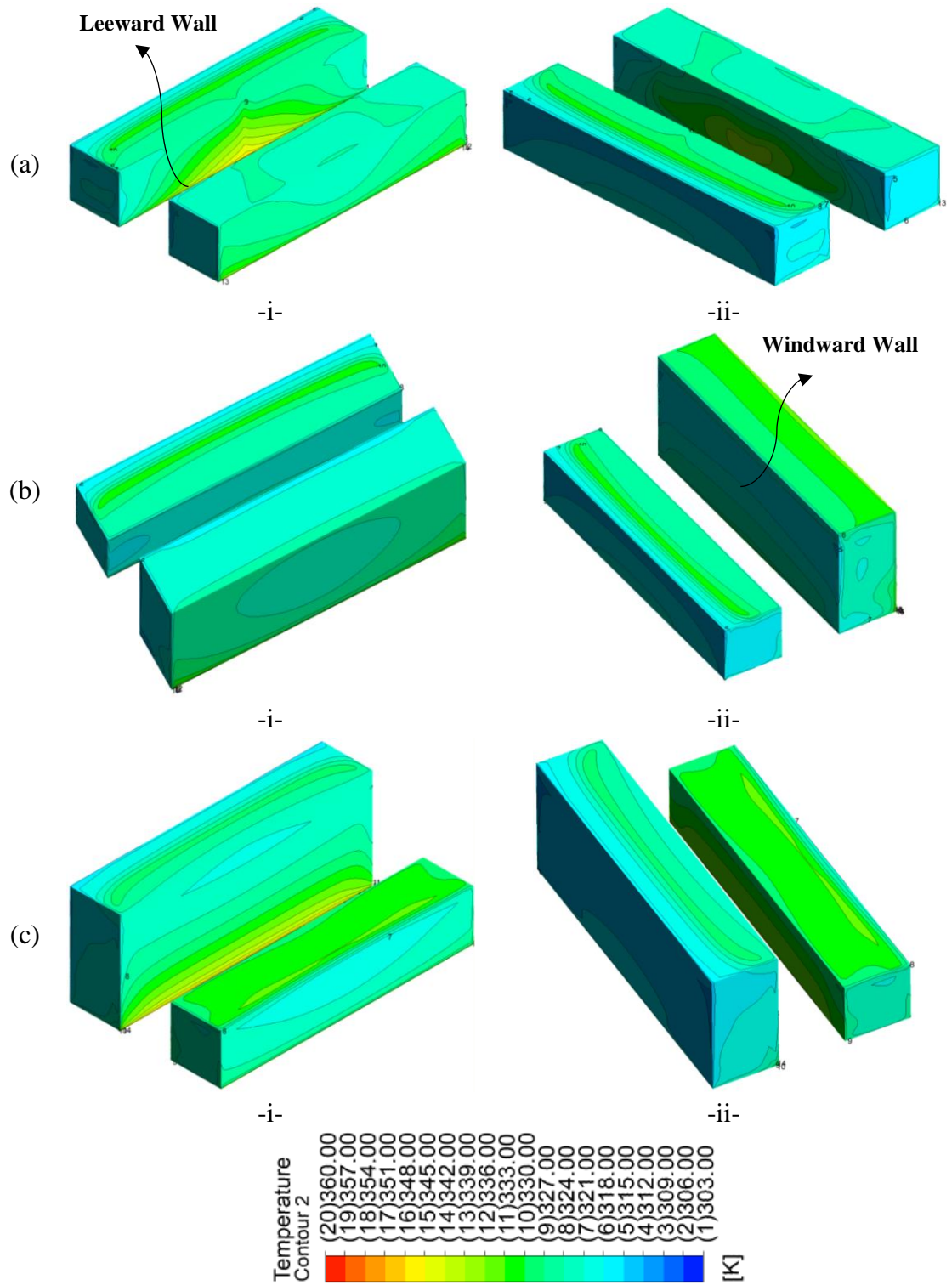


Figure 6.15 Façade temperature comparing (a) Symmetrical canyon height – i & ii (b) Asymmetrical canyon height Type 1 – i & ii (c) Asymmetrical canyon height Type 2 – i & ii

In the case of symmetrical canyon height, it was found with hotter temperature contours at the centre of the facades closer to the ground level, following the trend of road surface temperature for symmetrical canyon height; see Figure 6.15(a)-i and Figure 6.15(a)-ii. For asymmetrical canyon height Type 1 based on Figure 6.15(b)-i and Figure 6.15(b)-ii, lower temperature was observed for both Leeward Wall and Windward Wall as compared to the other two canyon settings. Obstruction of solar radiation from Building B and the building shadow influenced the obtained temperature of Leeward Wall 1 to be identically low with insignificant temperature difference (hotter spots) at the left and right canyon openings.

For the Leeward Wall 1 of asymmetrical canyon height Type 2, it was observed that the temperature contours which were diverse according to the height were identically distributed from the left canyon opening to the right canyon opening, please refer to Figure 6.15(c-i). For Windward Wall 2 as Figure 6.15(c-ii), approximately 50 % of the surface area closer to the ground level obtained the temperature value 342 K, see contour under the classification (14). It was mentioned before that due to the taller height of Building A, large swirling air has passed over Building B, reducing the penetration of airflow from left and right canyon openings. Thus, the Windward Wall 2 for asymmetrical Type 2 obtained almost identical temperature end to end of the facades.

6.1.3.4 RPSC performance in PTC and STR based on canyon configuration

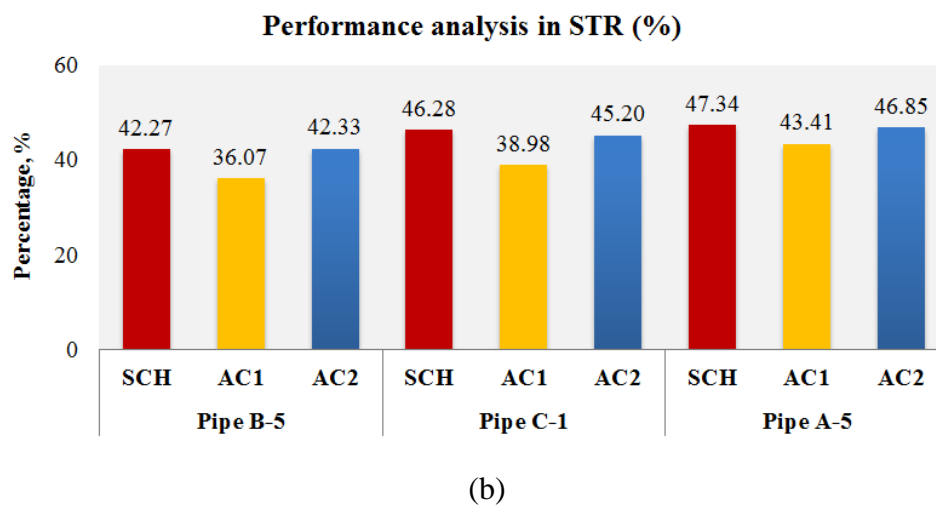
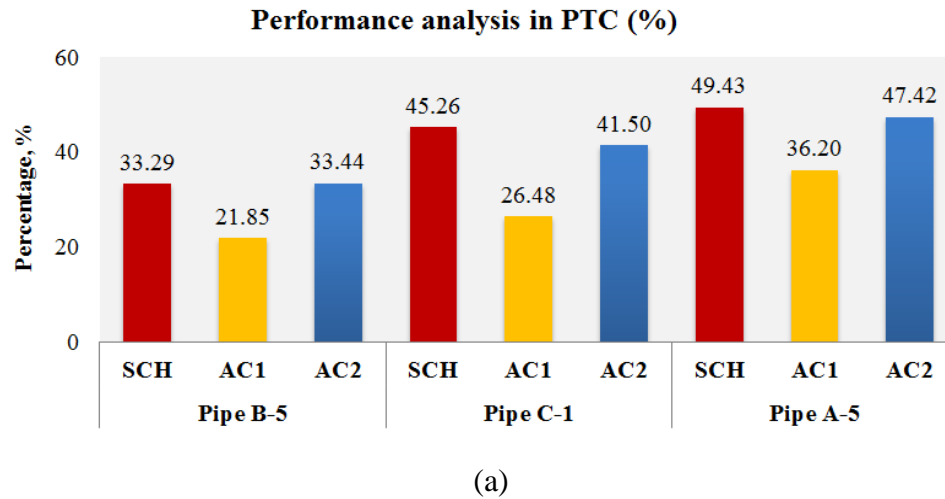
In this section, analysis of simulated hydronic RPSC system based on three urban macro domains with height modification is further discussed. Average surface temperature $T_{s,initial}$ was calculated based on the average of the plotted temperature values for three pipes (C, A-5 and B-5) in the three canyon settings as the boundary pavement temperature

set for the micro domain simulation, see Appendix A.17. The final temperature $T_{s,final}$ was obtained based on the simulation of micro domain, see Table 6.3 below.

Table 6.3 Calculation of average surface temperature according to pipe locations

Description	Pipe B-5			Pipe C-1			Pipe A-5		
	SCH	AC1	AC2	SCH	AC1	AC2	SCH	AC1	AC2
Average $T_{s,initial}$, K	333.94	319.88	334.13	348.66	344.04	344.04	353.79	337.52	351.32
Average $T_{s,final}$, K	308.18	302.97	308.25	313.64	305.08	311.93	315.55	309.51	314.63
SCH = Symmetrical Canyon Height, AC1 = Asymmetrical Canyon Height Type 1, AC2 = Asymmetrical Canyon Height Type 2									

Hydronic RPSC performance in PTC and STR was calculated based on the inlet-outlet water temperature difference (Delta T). Figure 6.16 demonstrates the comparison of PTC and STR values in percentage between symmetrical canyon height, asymmetrical canyon height Type 1 and asymmetrical canyon height Type 2. Based on Figure 6.16; for all three canyon settings, RPSC system performed not less than 20 % and not more than 50 % in obtaining potential temperature collection (PTC); however, the PTC of RPSC system based on symmetrical canyon height obtained the highest percentage, which was 53.26 % and 4.58 % more than asymmetrical canyon height Type 1 and asymmetrical canyon height Type 2, respectively. The calculation of STR in overall suggested that the RPSC system performed in reducing the surface temperature not less than 35 % and not more than 50 %. For the RPSC system with asymmetrical canyon height Type 1, the obtained STR value has approximately 15 % less than the STR value in the other two canyon settings. Conversely, insignificant difference in the STR value between symmetrical canyon height and asymmetrical canyon height Type 2, on average 1.2 %.



SCH = Symmetrical Canyon Height, AC1 = Asymmetrical Canyon Height Type 1,
AC2 = Asymmetrical Canyon Height Type 2

Figure 6.16 RPSC performance calculated in (a) potential temperature collection (PTC) and (b) surface temperature reduction (STR)

6.2 CFD analysis of RPSC performance with system adjustment

In this section, evaluation of hydronic RPSC system within urban configuration was carried out based on the adjustment of several system parameters. Five parameters were classified into three parts. The first part involved with the adjustment of two parameters in minimising/maximising the surface areas of temperature reduction: (i) pipe depth (ii) inlet water temperature. The second part involved with the adjustment of two parameters

in minimising/maximising the flow rate of the system for the similar reason, which are: (i) inlet water velocity (ii) pipe diameter. The third part presents the adjustment based on both surface area and flow rate involving the changes in RPSC layouts. Except for changes in pipe layout, all simulations involved system adjustment was based on AR 1 canyon during 21st June at 13:00 hour. This section was referred to Table 4.8 in Chapter 4 Section 4.4.2.

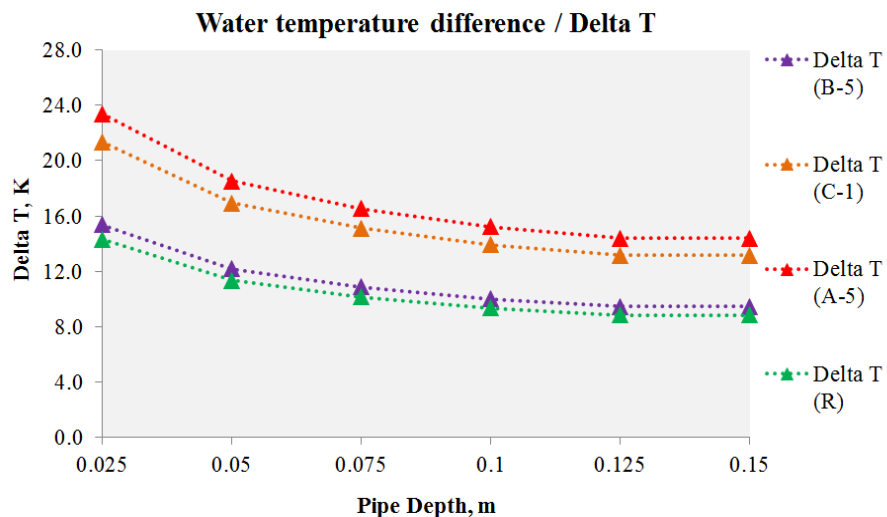
6.2.1 Minimising/maximising surface area on RPSC performance

In this section, two parameters related to the hydronic RPSC system were investigated which the changes determine the surface area of RPSC performance. It was noted that all simulations in this section are based on continuous water flow within pipelines and not within the time-basis. The results were presented based on the plotted Delta T, PTC and STR values at three measured pipe locations (A-5, C-1 and B-5) of AR 1. In the previous sub-section, it was mentioned that the area-weighted average of surface temperature for road surface without building was similar in all locations of the selected pipes. Thus, the Delta T, PTC and STR at the three pipe locations A-5, C-1 and B-5 for RPSC system without building was classified as R.

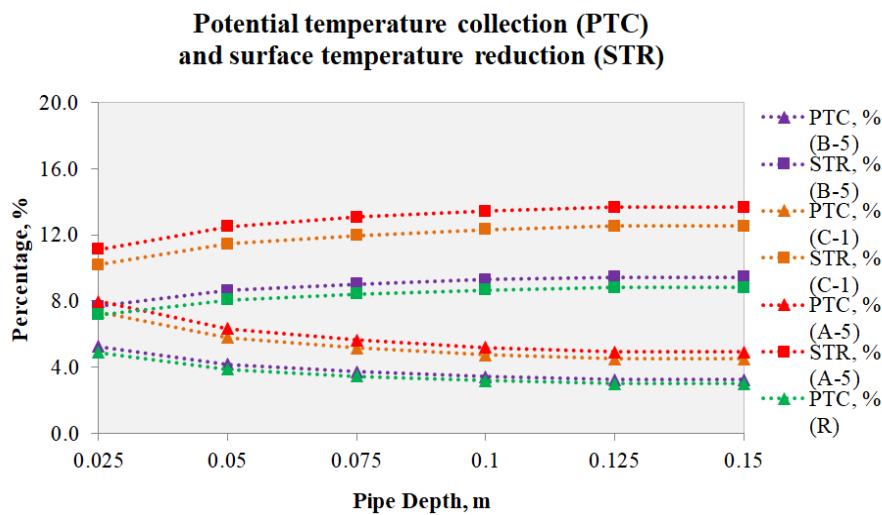
6.2.1.1 Effect of changing the depth of RPSC pipes

This section explains the investigation of the effect of changing RPSC pipe embedment depth in Delta T, PTC and STR, see Figure 6.17. Based on the graphs, it can be observed with significant drop in the effort of RPSC to reduce surface temperature, approximately 60 % when the depth of pipe embedment was reduced from deepest depth 0.15 m to shallowest depth 0.025 m. This means, deeper depth required the RPSC system for extra efforts to enlarge the cooling effect from the surface. For Delta T and PTC, it showed

improvement in the performance when shallower depth was set. Conversely, a significant drop in Delta T and PTC was observed when the depth was increased to 0.05 m from the shallowest depth 0.025 m. For all pipes, a gradual reduction trend was observed when the pipe depth was kept increasing, but as not as noticeable as changing the pipe diameter.



(a)

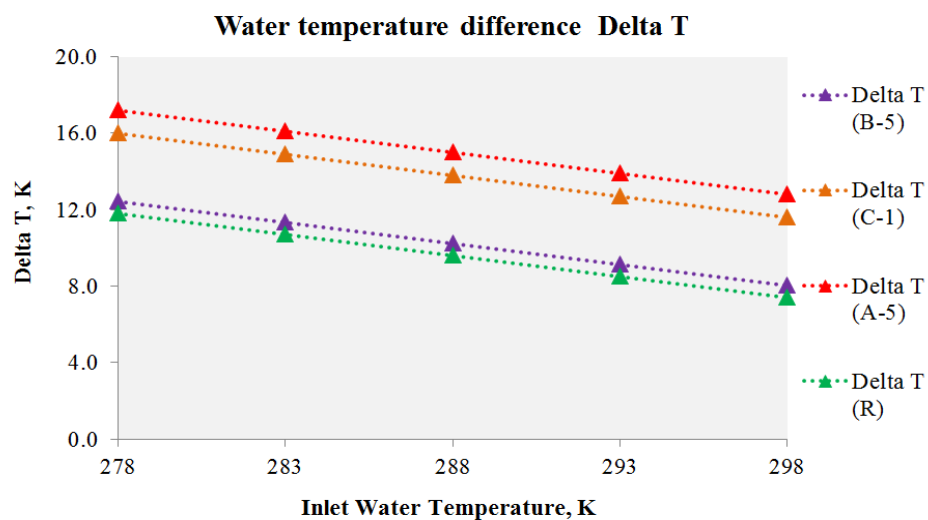


(b)

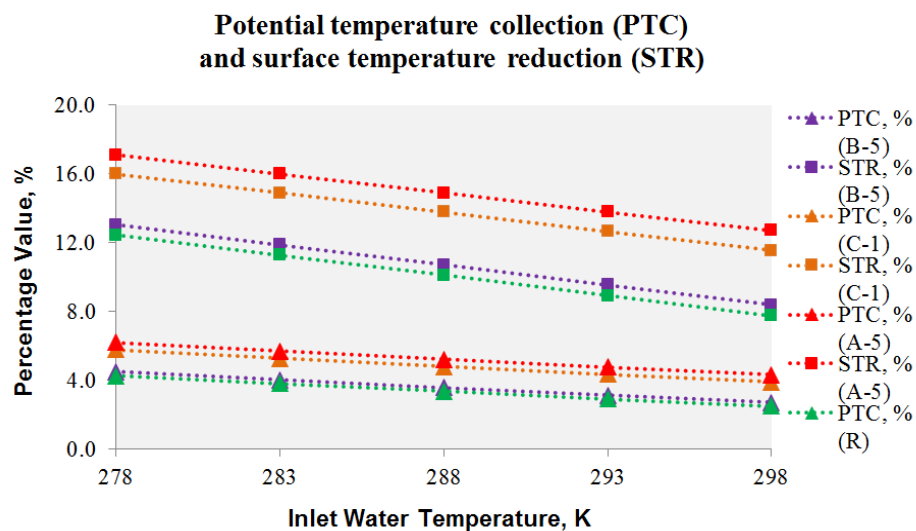
Figure 6.17 RPSC performance based on pipe depth in (a) Delta T (b) PTC and STR

6.2.1.2 Effect of changing inlet water temperature

In this study, the effect of inlet water temperature on Delta T, PTC and STR between the range of 278 K (5 °C) and 298 K (25 °C) was investigated, see Figure 6.18. As Figure 6.18, it was observed that the graph trend plotted for Delta T and PTC was parallel to the plot for STR. This means higher inlet temperature reduces the temperature difference between inlet and outlet water temperatures.



(a)



(b)

Figure 6.18 RPSC performance based on inlet water temperature in (a) Delta T (b) PTC and STR

Also, higher inlet temperature reduces the potential of the system to cool the surface temperature due to small amount of temperature difference will be obtained. The increase in inlet water temperature increases the loss in Delta T, PTC and STR accordingly and in a constant steep trend. In comparing the result based on the simulation of RPSC-1 and RPSC-0, it was observed that higher surface temperature obtained from RPSC-1 caused the steep temperature trend meanwhile the effect from RPSC-0 was indeed less steep.

6.2.2 Minimising/maximising mass flow rate on RPSC performance

Higher inlet water flow velocity with larger pipe diameter increases the cooling effect of a heated road surface temperature. In this study, the adjustment in the parameters was carried out using diverse range to evaluate the maximum and minimum performance of RPSC in Delta T, PTC and STR. Also, the plotted graph trend determines the optimum values to be used for the system to avoid unnecessarily too low or too high settings when the system performance does not significantly improve.

6.2.2.1 Effect of changing the inlet water velocity of RPSC pipes

Inlet velocity values were ranged between 0.1 m/s and 2 m/s and the graph was plotted comparing the Delta T, PTC and STR values between pipe location, see Figure 6.19. According to this figure, it was found that a significant drop in Delta T and PTC up to 60 % when the inlet velocity was changed from 0.1 m/s to 0.5 m/s. For the later velocity range, the drop was in gradual until insignificant drop can be observed when the adjustment in the water velocity was done from 0.75 m/s to 2 m/s.

The calculated STR graph trend was completely vice-versa to Delta T and PTC which the improvement in STR performance can be seen when higher inlet velocity was used until

it was observed that the performance became stagnant due to the dominant of volume of water flow with the temperature achieved its equilibrium state conforming the temperature of its surroundings. Thus, after 0.75 m/s, it was unnecessary to use high-speed water velocity as insignificant increase in the surface temperature reduction by RPSC system can be observed.

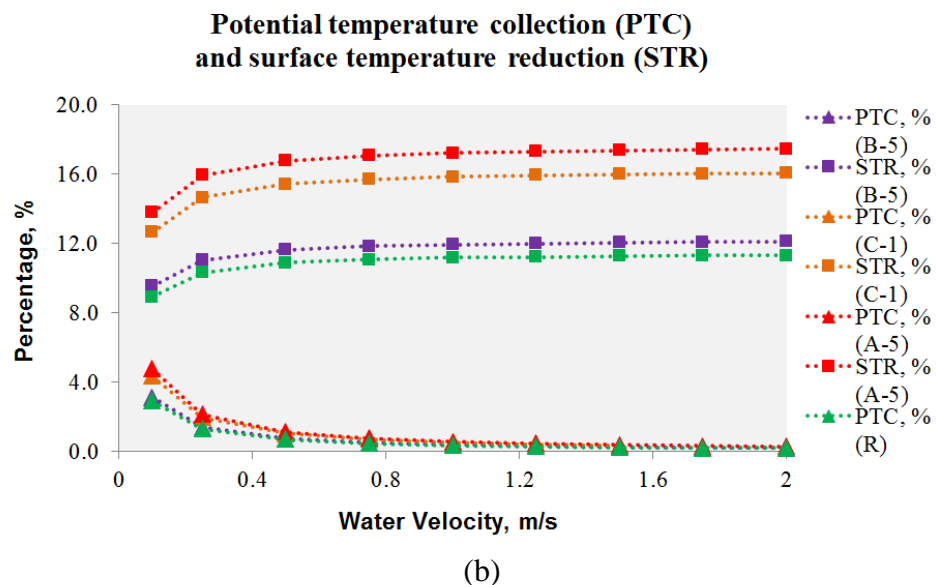
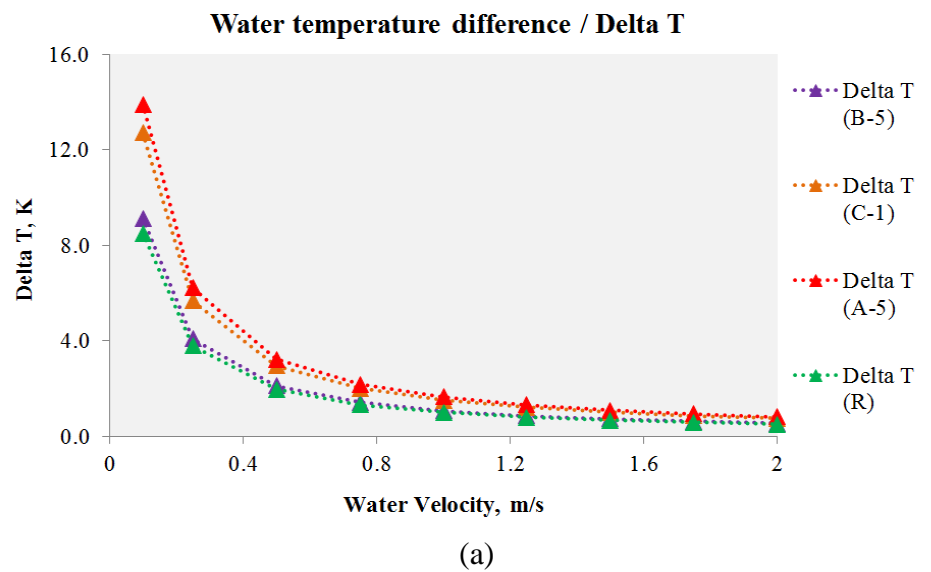
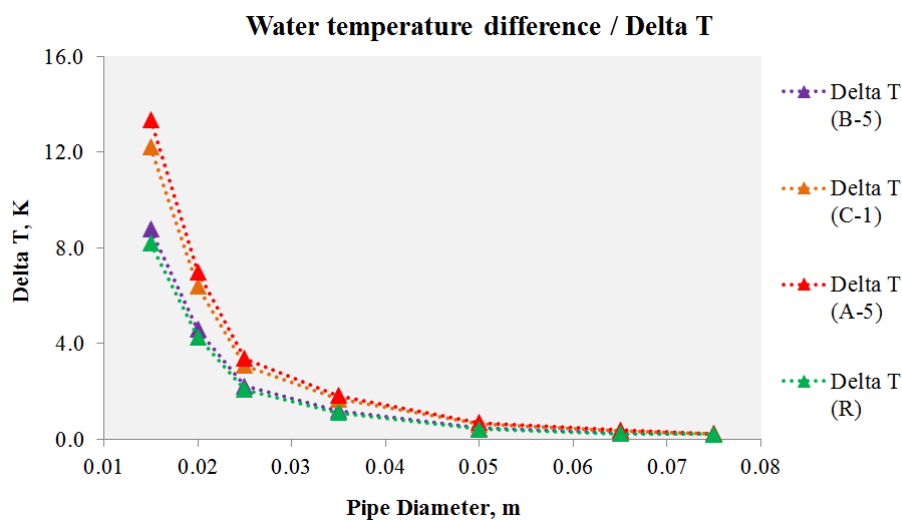


Figure 6.19 RPSC performance based on water velocity in (a) Delta T (b) PTC and STR

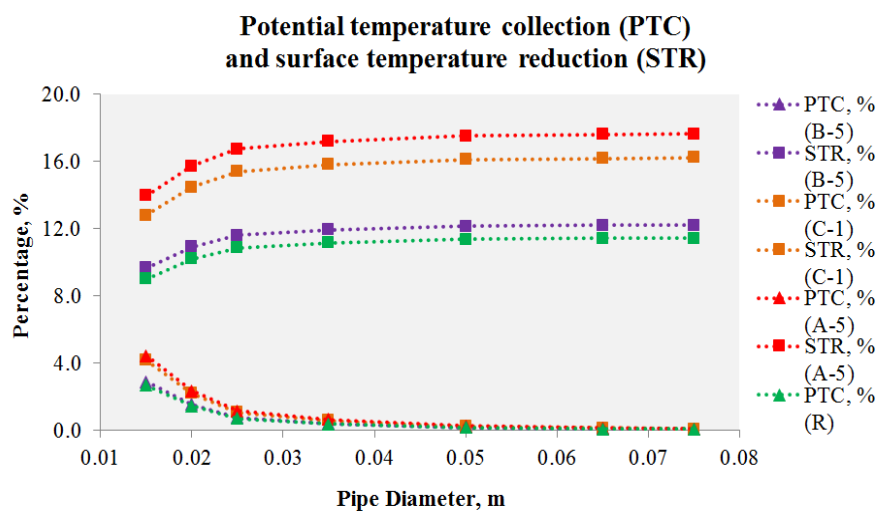
6.2.2.2 Effect of changing the diameter of RPSC pipes

Effect of changing diameter of RPSC pipes was carried out within the range between 0.015 m (15 mm) and 0.075 m (75 mm) according to its water velocity as in Table 4.8.

Figure 6.20 displays the RPSC performance in Delta T, PTC and STR according to the diameter of RPSC pipes. Based on the values plotted for RPSC-1 and RPSC-0 as Figure 6.20, it can be observed that higher STR can be obtained with larger pipe diameter and vice-versa with smaller pipe diameter, demonstrating the contrast between the two aspects.



(a)



(b)

Figure 6.20 RPSC performance based on pipe diameter in (a) Delta T (b) PTC and STR

In Figure 6.20(a), the highest Delta T was obtained by the smallest pipe diameter at all locations, on average 8-13.35 K. The plotted PTC trend was observed to be parallel to the plotted Delta T. When the pipe with diameter 0.015 m (15 mm) was replaced with second smallest pipe diameter, 0.02 m (20 mm), the performance of RPSC in Delta T and PTC was approximately 50 %. The reduction in the Delta T according to the increase in the pipe diameter can be observed in gradual movement until a half-curve bell shape graph trend was obtained. In Figure 6.20(b), the plotted STR values showed the inverse trend against the trend of PTC, thus the performance drop in PTC by 50 % becomes 50 % increase in the RPSC performance in term of STR. Due to continuous water flow inside the pipelines, it was observed that the road surface with larger pipe diameter will experience higher surface temperature reduction. The reason was due to the continuous water flow within large pipe diameter that carried lower temperature in large volume.

6.2.3 Combined effect of surface area and flow rate on RPSC system

In this section, CFD analysis of investigating the effect of two RPSC pipe layouts with two inlet water velocities on the system Delta T, PTC and STR was carried out using the temperature data of Kuala Lumpur urban canyon. As explained in Chapter 5, the road surface temperature based on ROAD 1 on the date of 6th August 2015 by 12:00 noon was used as the boundary condition of the simulation.

6.2.3.1 Effect of RPSC layout on surface temperature reduction

Figure 6.21 displays the plotted surface temperature at the centre of RPSC pipes comparing serpentine layout (RPSC Type SPP) and straight layout (RPSC Type STP) using inlet water velocity 0.1 m/s. The surface temperature was plotted along the 9 m length of the road surface with gap 0.5 m from the inlet-outlet plane.

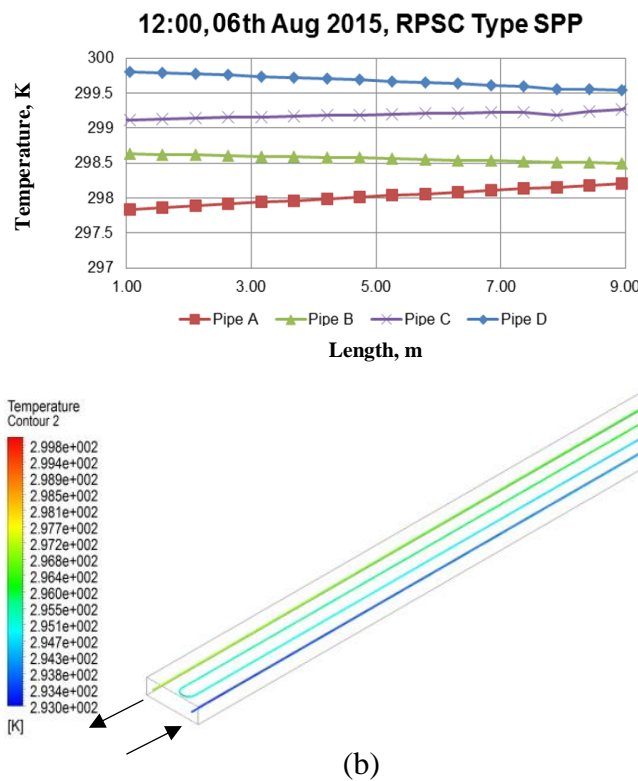
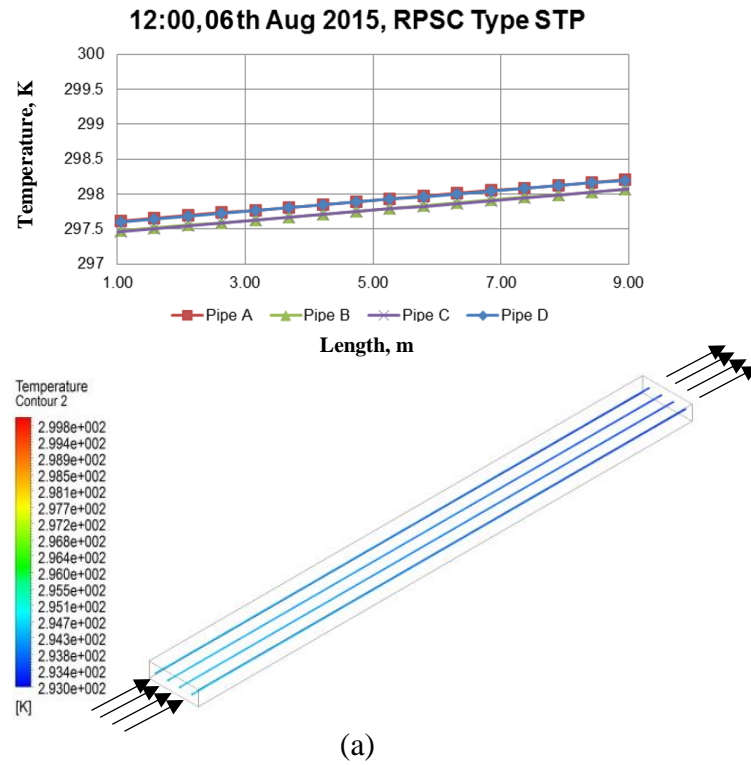


Figure 6.21 Surface temperature plotted across four locations and pipe wall surface temperature based on 0.1 m/s inlet water velocity simulation comparing (a) Type STP (b) Type SPP

Based on Figure 6.21(a), it was observed that surface temperature trend of RPSC Type STP in 9 m length showed insignificant increase in the temperature closer to the water

outlet location. Similar trend was observed to compare Pipe A, B, C and D of Type STP. For RPSC Type SPP, the temperature trend at the similar location of Pipe A, B, C and D as RPSC Type STP was observed more diverse, demonstrating highest surface temperature plotted for Pipe D and lowest water temperature plotted for Pipe A; see Figure 6.21(b).

It was noted that RPSC Type SPP had the layout of 40 m length, which was bended into the shape of four continuous pipelines with half-sphere corners. Meanwhile for RPSC Type STP, four straight pipes to be lined up within similar pipe gap with Type SPP. The flowing water inside RPSC Type STP which carried lower temperature has larger capacity to dominant the temperature of surroundings by the help of shorter inlet-outlet length and indirectly reduced more surface temperature as compared to RPSC Type SPP. Conversely, the flowing water inside RPSC Type SPP had to move within 40 m non-stop causing uneven surface temperature comparing the locations with further higher closer to the outlet of the pipe. Based on Figure 6.21; it was noted that the temperature difference between the outlet of RPSC Type STP and of Type SPP was 1.5 °C, showing 5.95 % higher in terms of the temperature value using Type SPP over Type STP.

6.2.3.2 Effect of increasing RPSC flow rate on surface temperature reduction

Figure 6.22 displays the simulation of RPSC Type SPP and RPSC Type STP using higher inlet water velocity, 0.25 m/s. It was observed that with RPSC Type STP, the surface temperature at all locations were expected to receive similar reduction trend but the reduction was insignificant.

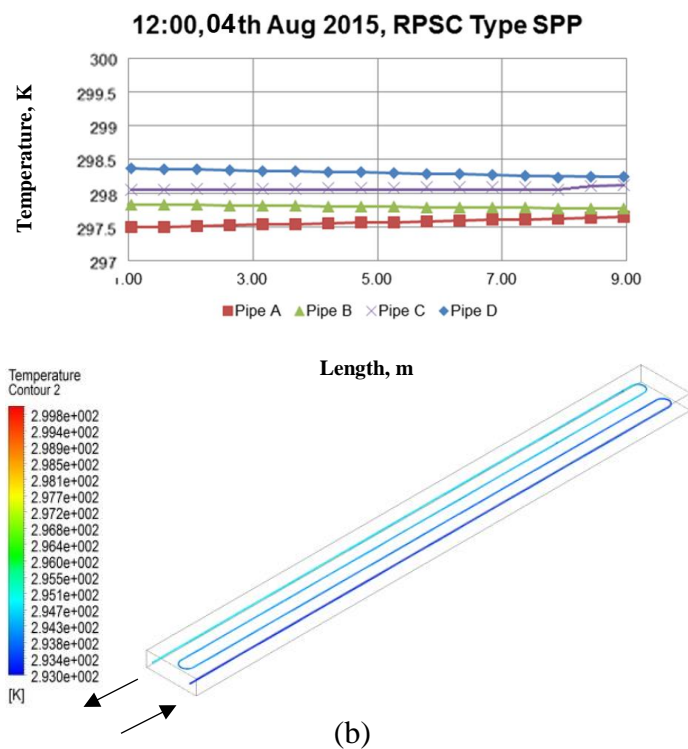
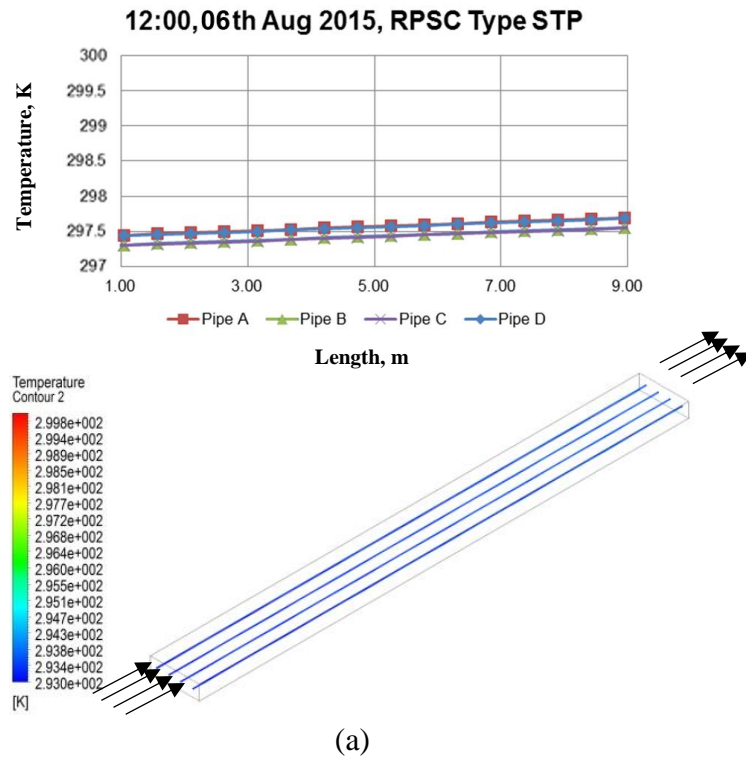
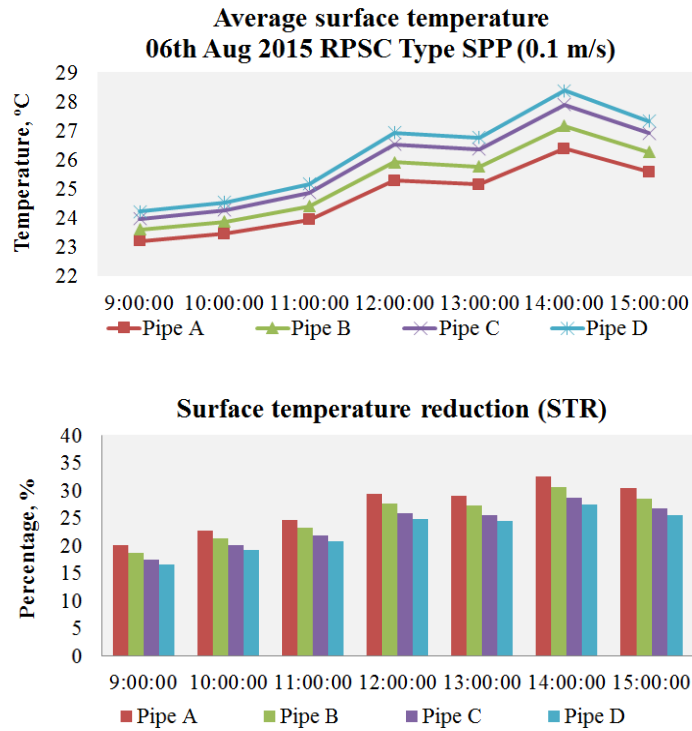


Figure 6.22 Surface temperature plotted across four locations and pipe wall surface temperature based on 0.25 m/s inlet water velocity simulation comparing (a) Type STP (b) Type SPP

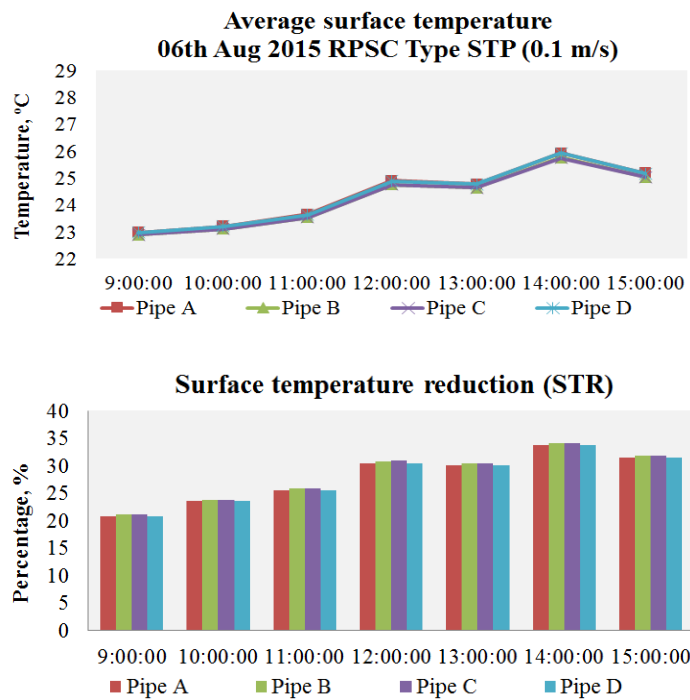
Contrariwise, the 0.25 m/s inlet water velocity assisted in the significant reduction of surface temperature at all locations in the simulation of RPSC Type SPP. This means RPSC Type SPP becomes more effective with higher water velocity, meanwhile for RPSC Type STP, 0.1 m/s is enough for the system to perform without additional setting of inlet water velocity.

Simulation results of surface temperature at four pipe locations (Pipe A, B, C and D) involving RPSC Type SPP and RPSC Type STP from 09:00 hour to 15:00 hour with two inlet velocity values are presented in Figure 6.23 and Figure 6.24. For Type STP with 0.1 m/s water velocity, it was observed that the percentage of STR based on every location was very similar. In overall hours, the surface temperature was reduced in between 20 % and 35 %. Switching the inlet velocity to 0.25 m/s did not significantly increase the STR percentage, with on average 1.33 % or 0.32 °C increase in all simulations and locations; see Figure 6.23.

For Type SPP, a significant difference in the STR was observed between the surface locations. The temperature of the pavement surface located nearby the inlet point (Pipe A) was reduced not less 19 % (at 9:00 hour) and not more 33 % (at 14:00 hour). Conversely, the temperature of pavement surface located nearby the outlet plane (Pipe D) as presented in Figure 6.23 was reduced the least by 15 % at 09:00 hour and the most by 28 % at 14:00 hour. With higher solar radiation, it was observed that more heat was absorbed to the pipe body and the water inside. Thus, the surface temperature gap became gradually broader due to insufficient water capacity to facilitate the increasing surface temperature.

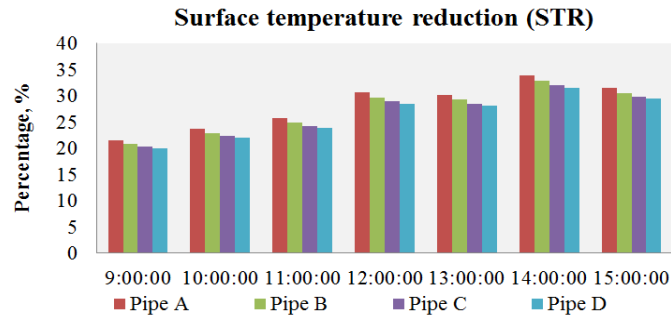
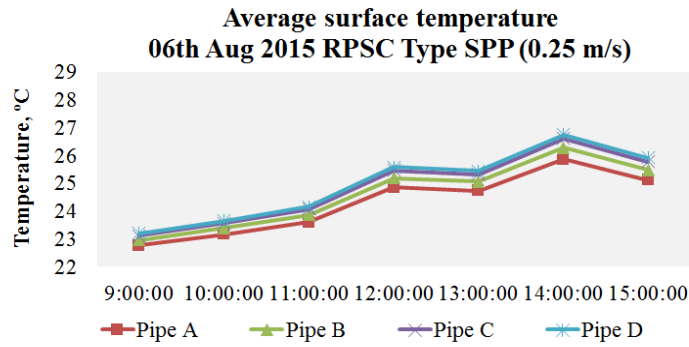


(a)

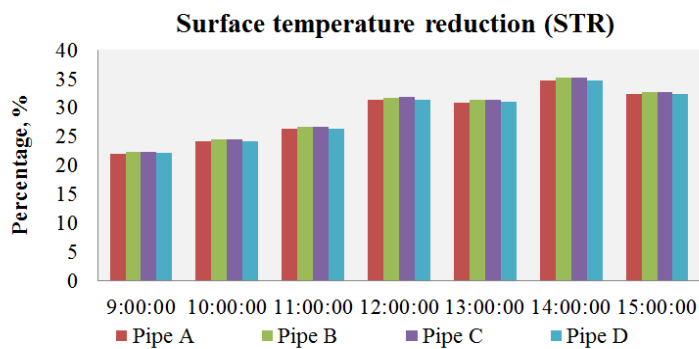
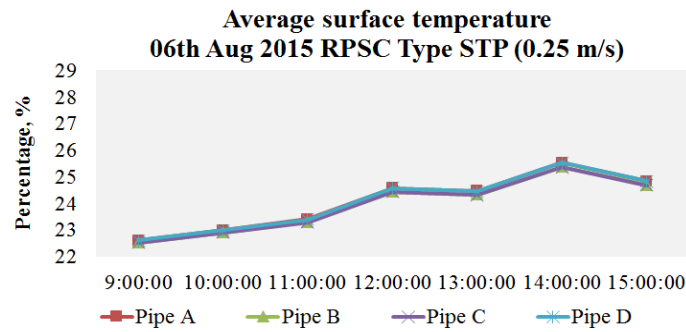


(b)

Figure 6.23 Average surface temperature based on hourly simulation (09:00 – 15:00) and percentage of surface temperature reduction (%) comparing: (a) Type SPP with 0.1 m/s (b) Type STP with 0.1 m/s



(a)



(b)

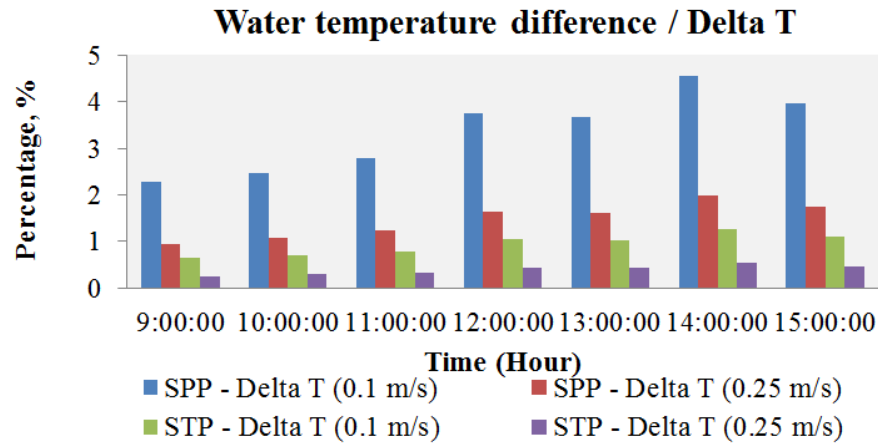
Figure 6.24 Average surface temperature based on hourly simulation (09:00 – 15:00) and percentage of surface temperature reduction (%) comparing: (a) SPP with 0.25 m/s (b) Type STP with 0.25 m/s

By switching the velocity value to 0.25 m/s (see Figure 6.24), a significantly less temperature gap between each location was observed especially in the afternoon. The calculated STR was observed to be increased according to the surface location. At location Pipe A, the increase in the STR value was not less than 1.2 % at 9:00 hour and not more than 2 % at 14:00 hour meanwhile at Pipe D location, the STR value was increased as high as 5.71 % at 14:00 hour and as low as 3.56 % at 9:00 hour.

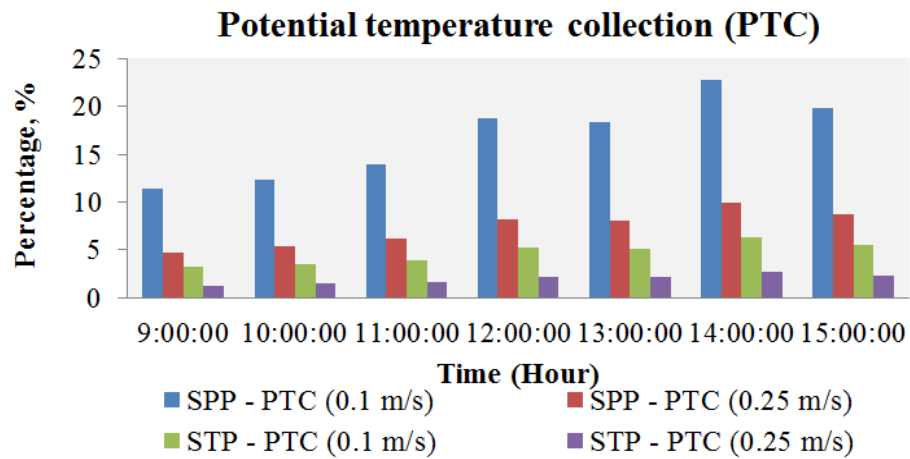
6.2.3.3 Calculation of Delta T, PTC and STR comparing SPP and STP

Based on the result in Figure 6.23 and Figure 6.24, the Delta T based on area-weighted average temperature difference between inlet and outlet was calculated, resulting the reduction in Delta T with the increased inlet water velocity; see Figure 6.25. Results showed that RPSC Type STP had obtained Delta T not less than 0.6 °C (9:00 hour) and not more than 1.5 °C (14:00 hour) with inlet velocity 0.1 m/s. Contrariwise, Delta T based on RPSC Type SPP seems more significant than RPSC Type STP, which obtained as high as 4.55 °C (14:00 hour) and as low as 2.28 °C (9:00 hour). It was noted that the PTC values were calculated based on the obtained Delta T, thus Figure 6.25 suggested that the graph trend plotted from 09:00 to 15:00 of Delta T and PTC was relatively comparable.

With high performance of RPSC Type STP in temperature collection (using inlet velocity 0.1 m/s), the highest PTC can be obtained was 6.36 % during the hottest simulation hour in the afternoon (14:00 hour) meanwhile the lowest PTC can be obtained was 3.2 % during the coolest simulation hour in the morning (9:00 hour). On average, based on 7-hour simulation; RPSC Type STP performs 4.69 % in terms of potential temperature collection.



(a)



(b)

Figure 6.25 RPSC performance comparing SPP and STP based on hourly simulation (09:00 – 15:00) with 0.1 m/s and 0.25 m/s inlet velocity in (a) Delta T (b) PTC

Using similar setting, the RPSC Type SPP had a PTC as high as 22.74 % during the hottest simulation hour (14:00 hour). Conversely, in the early simulation hour (09:00 hour), PTC for RPSC Type SPP was 11.42 %. On average, the RPSC Type SPP was performed 72.02 % more than RPSC Type STP in terms of potential temperature collection. By switching the system setting to 0.25 m/s inlet velocity, it was observed that the loss percentage in *Delta T* and PTC for both models was almost at par; on average 59.12 % for Type STP and 56.68 % for Type SPP which were calculated within the 7-hour simulation. Based on Figure 6.26, the highest thermal performance of the RPSC

Type STP in terms of surface temperature reduction (using 0.25 m/s inlet velocity) was during 14:00 hour with 47.51 % reduction; meanwhile for the RPSC Type SPP, the reduction was 43.76 %. During the coolest simulated hour (at 09:00 hour with 0.1 m/s inlet velocity), RPSC Type STP surface temperature reduction was 28.83 % while the RPSC Type SPP surface temperature reduction was 23.16 %. Based on the 7-hour simulation, the pavement surface can be potentially cooled 30-36.4 % and 37-39.5 % with RPSC Type SPP and Type STP, respectively, showing insignificant difference when comparing the two types of RPSC pipe layout.

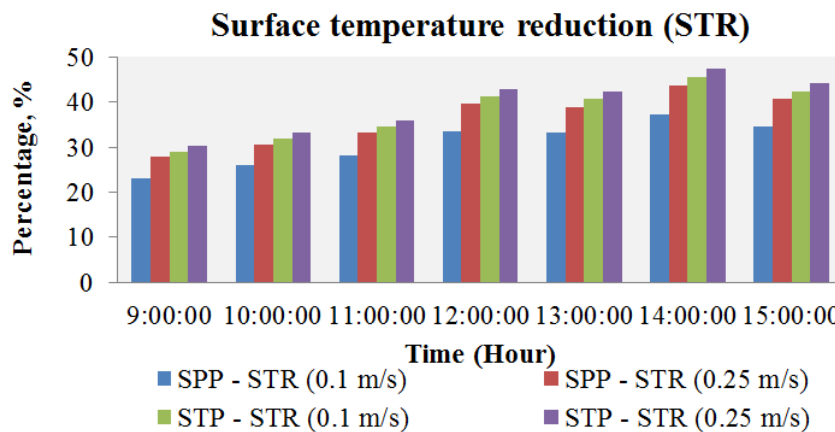


Figure 6.26 RPSC performance comparing SPP and STP based on hourly simulation (09:00 – 15:00) with 0.1 m/s and 0.25 m/s inlet velocity in terms of STR

6.3 Effect of RPSC application on outdoor temperature condition

This section investigates the effect of the application of RPSC on the surface temperature, air velocity and temperature profiles. In this study, the configuration of street canyon comparing several aspect ratios was only based on symmetrical canyon height due to the highest surface temperature at the centre of the canyon with symmetrical canyon as compared to asymmetrical canyon configurations, see Section 6.1.3. After the simulation of RPSC system using micro domain model, area-weighted average temperature at 0.15

m (150 mm) below road surface based on 9 selected pipe locations was obtained and was assumed to be applied for the whole road surface area of the street canyon. The average temperature has accounted for both internal water temperature (in the centre of pipe) and the surrounding road layer temperature affected or not affected by RPSC system. This data became the temperature condition for the macro domain model comparing AR 1, 2, 3 and 4, see Table 6.4.

Table 6.4 Exported average temperature at 0.15 m below surface to macro domain

Description	Pavement temperature at 0.15 m depth based on area-weighted average (K)								
	A5	A4	A3	A2	C1	B2	B3	B4	B5
AR 1	315.4	314.5	313.8	313.4	313.1	312.9	312.9	310.5	307.9
	Average temperature = 312.7								
AR 2	319.5	318.6	317.9	317.5	317.1	316.9	312.7	311.1	311.7
	Average temperature = 315.9								
AR 3	315.0	314.4	314.1	313.9	312.4	308.5	308.4	308.5	309.5
	Average temperature = 311.6								
AR 4	317.2	316.3	315.8	312.5	309.7	309.5	309.4	309.4	310.3
	Average temperature = 312.2								

The after effect of surface temperature contour for all aspect ratios is detailed in Appendix A.18. In Figure 6.27, STR which was calculated from the average surface temperature (see Figure 6.8) before and after RPSC application is presented. Based on Figure 6.27, it was expected that high surface temperature reduction was proportional to high temperature difference, dominated by AR 2 (20.93 °C Delta T or 27.79 % STR) followed by AR 3, AR 4 and AR 1 with 19.75 °C (28.19 %), 19.04 °C (27.43 %) and 15.94 °C (24.21 %), respectively. The calculated STR resulted nominal difference in the value obtained by AR 2, 3 and 4 with 3-4 % higher than AR 1. See also Appendix A.19.

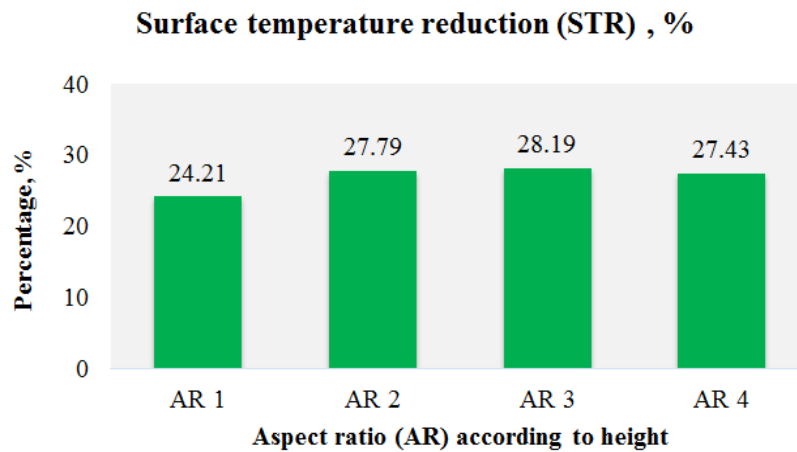


Figure 6.27 Performance of RPSC in dissipating heat from road surface according to street canyon aspect ratio in terms of STR

Additional information on the dimensionless air temperature between 0.5 m and 5 m above road level to evaluate the effect of RPSC before and after its application on the air temperature at pedestrian level can be referred to Appendix A.20. Overall, results demonstrated that the highest air temperature reduction was within the AR 1 street canyon, followed by AR 4, AR 2 and AR 3. In terms of temperature variance according to height, AR 1 dominated the result. AR 2 obtained second highest temperature variance followed by AR 3 and AR 4, however the air temperature reduction of AR 2 was indeed lower than AR 4. This result can be seen tally to the analysis in Section 6.1.2.2 based on Figure 6.10. The temperature reduction in air temperature across the height combining the results of all four aspect ratios is displayed in Figure 6.28.

Based on Figure 6.28, the reduction in the air temperature across the height at 13:00 hour with 303 K (30 °C) air temperature on 21st June was found largest in the configuration of AR 1 with RPSC, which was 4.67 °C at 0.5 m above ground level and 3.08 °C at 5 m above ground level; meanwhile the least variance in the temperature across height was observed for configuration AR 4 with RPSC, which was 2.47 °C at the 0.5 m height and

2.12 °C at 5 m height. The least temperature reduction by RPSC system was observed for AR 3 with maximum reduction was 1.74 °C at 0.5 m height and minimum reduction was 0.82 °C at 5 m height.

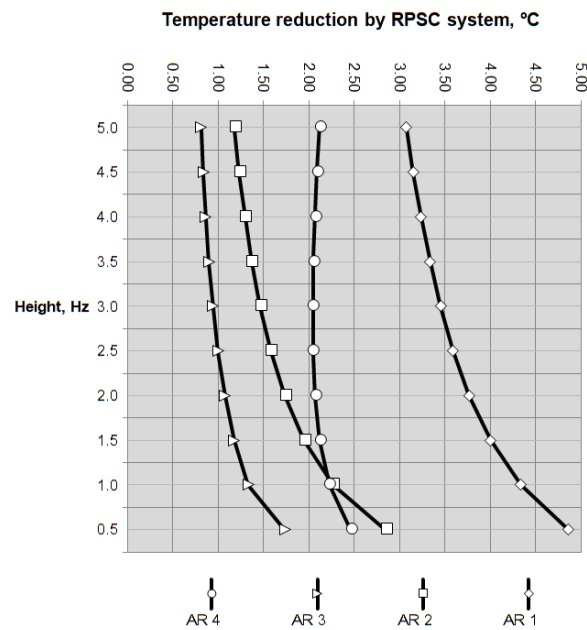


Figure 6.28 Temperature reduction (in °C) comparing the aspect ratio of 1, 2, 3 and 4

Although AR 2 obtained second lowest temperature reduction after AR 3, result based on the analysis suggested that the road surface of AR 2 obtained highest average temperature among all simulated aspect ratios, thus requires highest priority. In Figure 6.27, it can be observed with insignificant difference in the STR value between AR 2, 3 and 4. Thus, the current setting of RPSC system (inlet water velocity 0.1 m/s, pipe diameter 0.2 m, inlet water temperature 293 K and pipe depth 0.15 m) requires adjustment for optimum air temperature reduction that can be at par or better than the obtained air temperature reduction of AR 4. For AR 3, result suggested that unnecessary to further the adjustment of RPSC system specifically closer to the ground level as the current RPSC setting did not significantly change the air temperature across height.

6.3.1 Calculation of Heat Index (HI) using air temperature

Overall, the air temperature at 0.5 m to 2.0 m in all aspect ratios after the RPSC application was 33-37 °C with the reduction in air temperature by 1 °C, 2 °C, 2.1 °C and 4 °C. Based on these air temperature values, the calculation of Heat Index or Humiture can be obtained as this indicator is to determine the human-perceived equivalent temperature or to be simplified as how hot is the air temperature is felt when humidity is considered. The human body can be cooled by sweating or perspiration, which the heat from the body will be removed through evaporation of the sweat. However, with humidity, the evaporation rate or the rate of removing heat from the body is decreased. US National Ocean and Atmospheric Administration (NOAA) under National Weather Service has established a Heat Index table to calculate the ‘feel like’ temperature with the information of relative humidity in percentage and air temperature in Fahrenheit, see Figure 6.29.

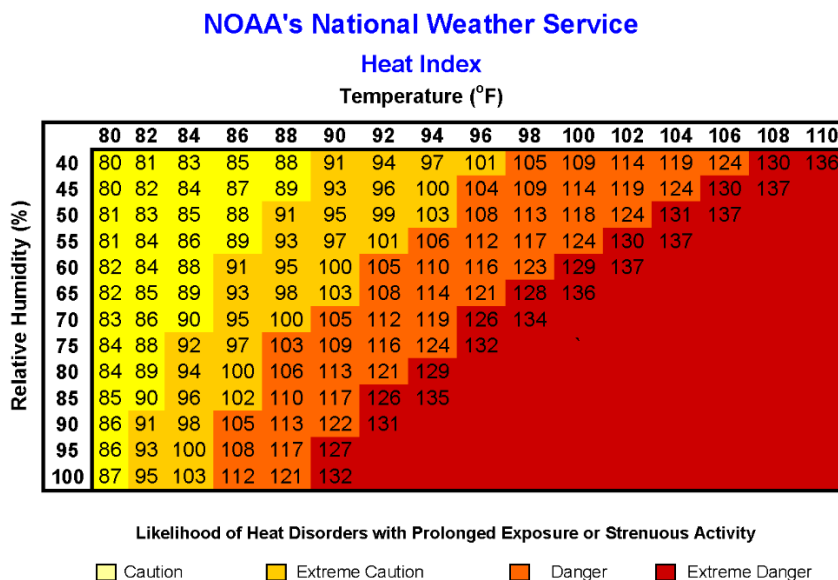


Figure 6.29 Table of Heat Index (HI) developed by NOAA's National Weather Service. 20th September 2017. Retrieved from:
http://www.nws.noaa.gov/om/heat/heat_index.shtml.

Based on the temperature values obtained from the simulation, which are 33-37 °C (91.4-98.6 F) with 75 % relative humidity, it was highlighted that the obtained ‘feel like’ temperature was 46.7-55.6 °C (116-132 F), which falls under danger and extreme danger categories. According to NOAA’s National Weather Service, the human body which is exposed to these categories will experience with heat cramps, heat exhaustion and as extreme as heat stroke to occur. This means, the air temperature reduction using RPSC system at the current setting requires further investigation to reduce the ‘feel like temperature’ to 20-29 °C in achieving little or no discomfort to human body.

6.3.2 Effect on energy load based on urban air temperature

Based on the air temperature reduction 1-4 °C, the potential of the reduction in the building air-conditioning unit can achieve up to quadruple the reduction of 500 megawatts per 1 °C (approximately 2000 megawatts) or approximately quadruple the electric cost of USD 100,000 per hour for the usage of 1-1.5 megawatts in the urban area. This was based on the literature from the previous works (see Chapter 2) which have discussed on the effect of increase in 1 °C to the electric loads under the urban case study carried out by (Akbari & Matthews 2012; Akbari et al. 2001; Elsayed & Ilham S. M. Elsayed 2012; Elsayed 2012c).

6.4 Comparative analysis on experimental and simulation results

The simulation analysis displayed in Section 6.1 highlighted the effect of street canyon configurations in urban areas on ground surface temperature situated within the street canyon, specifically during midday hours. Results were analysed based on an elongated street canyon with the openings to the canyon were from two corners, left and right and from the top of the canyon. Several canyon configurations were studied:

- (i) symmetrical with aspect ratio 1 – building rows adjacent to the street canyon were in symmetrical height configuration and the height of the buildings was similar to the canyon width,
- (ii) symmetrical with higher aspect ratio – double, triple and quadruple the building height to the canyon width,
- (iii) asymmetrical Type 1 – shorter height of the first building row and compared to the second row, and
- (iv) asymmetrical Type 2 – taller height of the first building row as compared to the second row.

Two urban street canyons of Kuala Lumpur metropolitan, ROAD 1 and ROAD 2 were studied to determine the effects of canyon configuration and aspect ratio on the temperature of the building facades and the temperature of road surface in between the canyons. Each street canyon consists of 6 urban canyon sections (detailed in Chapter 5), which was initially carried out to calculate the average aspect ratio of the building heights and the width of the canyons. The description on street canyons based on both simulation model and experiments is summarised in Table 6.5 below:

Table 6.5 Exported average temperature at 0.15 m below surface to macro domain

DESCRIPTION	CONFIGURATION	ASPECT RATIO	REMARK
SIMULATION MODEL			
AR 0	No building	0	Straight layout 1 canyon row with side openings (left and right)
AR 1	Symmetrical	1	
AR 2	Symmetrical	2	
AR 3	Symmetrical	3	
AR 4	Symmetrical	4	
AC1	Asymmetrical Type 1	First row = 1, Second row = 2	
AC2	Asymmetrical Type 2	First row = 2, Second row = 1	
EXPERIMENTAL DATA COLLECTION			
ROAD 1 – AVERAGE ASPECT RATIO = 3			
Section 1-(a)	Almost symmetrical	5.96	Straight layout and having spacing between buildings
Section 1-(b)	Asymmetrical Type 1	1.00	
Section 1-(c)	No first building row	2.45	
Section 1-(d)	Almost symmetrical	5.42	
Section 1-(e)	Almost symmetrical	0.5	
Section 1-(f)	Asymmetrical Type 2	0.69	
ROAD 2 – AVERAGE ASPECT RATIO = 1			
Section 2-(a)	Asymmetrical Type 2	1	Curvy layout in quarter circle and having spacing between buildings
Section 2-(b)	Asymmetrical Type 2	0.71	
Section 2-(c)	No second building row	0.74	
Section 2-(d)	Asymmetrical Type 2	0.98	
Section 2-(e)	No second building row	1.47	
Section 2-(f)	No first building row	1.76	

6.4.1 Similarities in the simulation data set and experimental data set

Both simulation and experimental data were set during hot daytime with high mean air temperature. For the simulation, the inlet air temperature was set to 303 K (30 °C) meanwhile the mean air temperature from the weather data of Kuala Lumpur during the month of August 2015 and the month of March 2016 was 302 K (29 °C) and 303 K (30 °C). Both simulation studies and experimental studies investigated the configuration of elongated and straight urban canyon layout perpendicular to the predominant wind speed

and direction. The effect of solar intensity on the road surface temperature within urban canyon was carried out within similar 7 interval hours, from 9 am (09:00 hour) to 3 pm (15:00 hour).

6.4.2 Differences in the simulation data set and experimental data set

The simulation model resembled an urban area with temperate climate condition during summer month meanwhile the experimental data collection was carried out in an urban area with hot humid climate condition during southwest monsoon and northeast monsoon. Additional urban canyon with no straight canyon layout, named ROAD 2 was carried out for its comparison to a straight urban canyon layout, named ROAD 1. Both ROAD 1 and ROAD 2 have 9-11 buildings per canyon row became 6 canyon sections with different aspect ratios and different configurations. Meanwhile, the simulation model shaped the elongated street canyon to be 1 canyon row and 1 configuration (symmetrical).

Overall, higher surface temperature values were observed from the simulation as compared to the values from the experimental data collection. In the work of simulation model, the wind speed was set low with default air temperature 303 K (30 °C) to resemble the hot summer day with constant calm wind condition, 2 m/s. Meanwhile, the data collection for the wind speed, wind direction and ambient temperature was not carried out within the canyon areas; This means the data from the nearby local weather station was referred for the case studies. In reality, the gust wind speed and its direction also involve to influence the wind speed at the local condition.

6.4.3 Temperature results based on aspect ratio

Analysis in comparing the road surface temperature between the simulation model and the experimental data was carried out by ensuring the compatibility of the street canyon configuration between both studies. In the case of experimental street canyon, the selection was considered only for ROAD 1 with almost symmetrical height, which is Section 1-(a) consisting AR = 5.96, Section 1-(d) consisting AR = 5.42 and Section 1-(e) consisting AR = 0.5. The data set for the experiment should be compared based on 1 pm (13:00) following the simulation data set. Figure 6.30 compares the temperature analysis according to canyon aspect ratio between the simulation and experimental results.

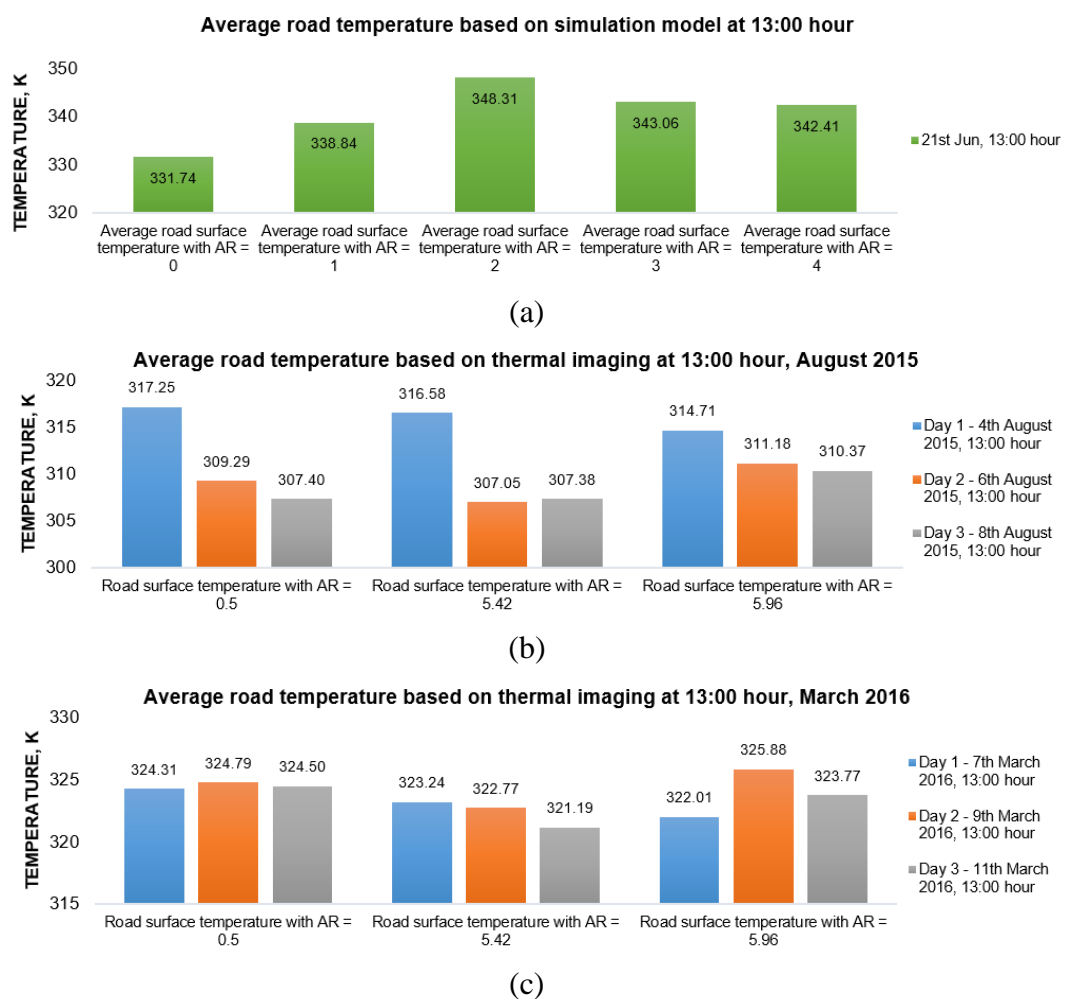


Figure 6.30 Effect of canyon aspect ratio on road temperature based on (a) simulation modelling (b) thermal imaging in August 2015 (c) thermal imaging in March 2016

Based on the comparison it was summarised that during hot summertime 13:00 hour as Figure 6.30(a); the simulation results of symmetrical street canyon demonstrated on average higher temperature of road surface within the street canyon with the aspect ratio more than 1, however the temperature variance was not significant above than AR 2 as compared to the temperature variance from AR 1 to AR 2. The road surface temperature closer to Leeward Building Wall obtained higher value due to the refraction of solar radiation and lower road surface temperature closer to Windward Wall due to high convection rate and shadow effect.

During 13:00 hour for both data collections of August 2015 and March 2016, the experimental data demonstrated an inconsistent trend as compared to the simulation, see Figure 6.30(b). There were days showed higher temperature was obtained with $AR > 1$ and there were days showed higher temperature was obtained with $AR < 1$. Results suggested with major influence of solar intensity in determining the road temperature based on the dissimilar temperature trends obtained according to time and day. Results demonstrated the reduction in the road surface temperature caused by shadows as maximum as 11.19 °C. Thus, the influence of shadow on the surfaces which shown in the simulation studies are validated against the experiments.

6.4.4 Temperature results based on street canyon configuration

The effect of street canyon configurations (symmetrical height, asymmetrical heights) on the road surface temperature was investigated and compared between the simulation model and the experimental data collection on ROAD 1. Analysis based on the results is shown in Figure 6.31 and Figure 6.32 based on different month and date.

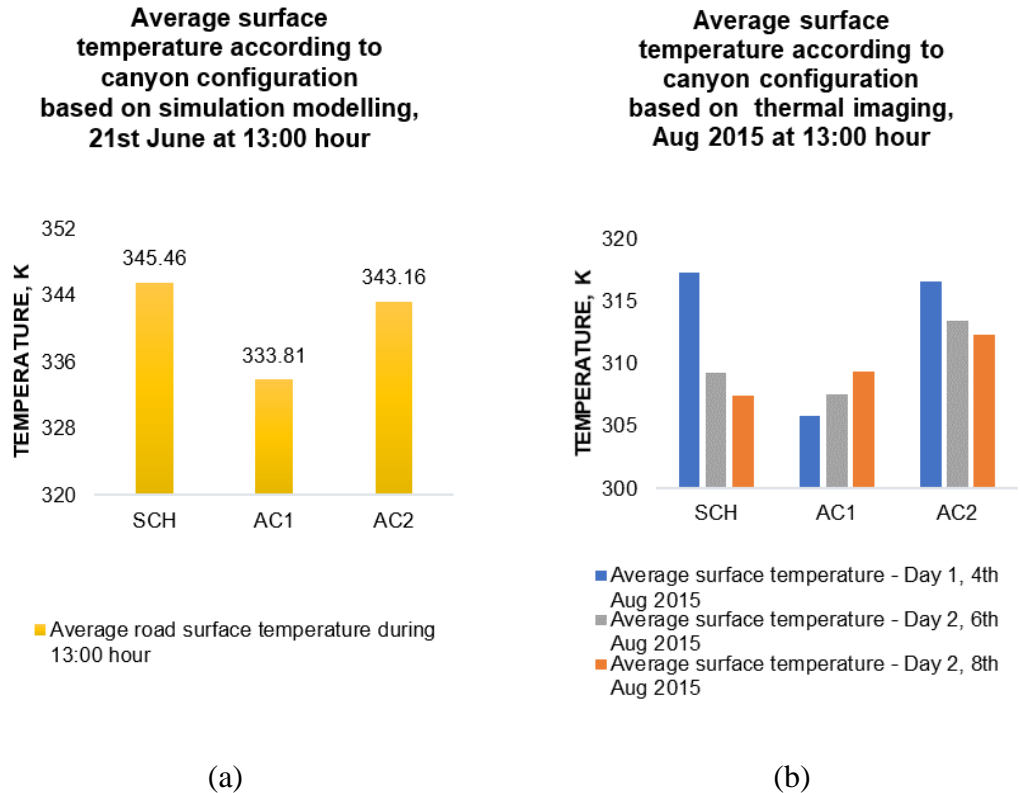


Figure 6.31 Effect of canyon configuration on road temperature based on (a) simulation modelling (b) thermal imaging in August 2015

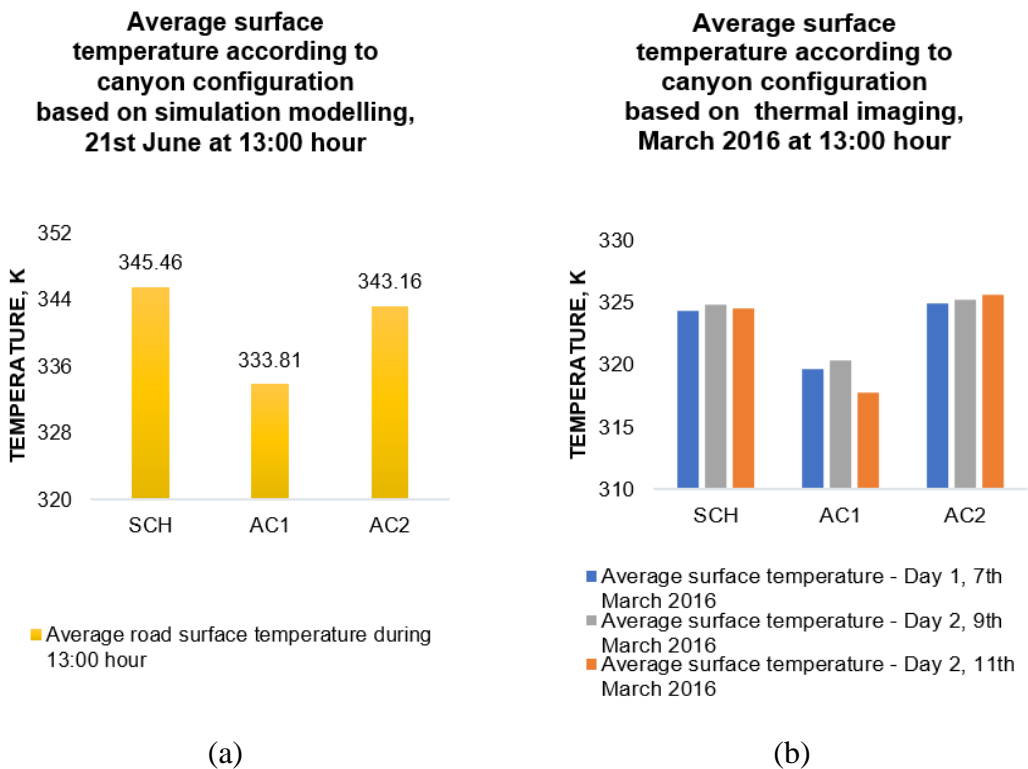


Figure 6.32 Effect of canyon configuration on road temperature based on (a) simulation modelling (b) thermal imaging in March 2016

The simulation results of 13:00 hour as shown in Figure 6.31 and Figure 6.32 demonstrated with higher wind velocity within the street canyon with asymmetrical height Type 1 as compared to the street canyons with symmetrical height and asymmetrical height Type 2. Due to this effect, the road surface within asymmetrical canyon Type 1 obtained lower temperature on average as compared to the other two configurations. Simulation results demonstrated with insignificant temperature difference comparing the road surface within symmetrical canyon height and within asymmetrical canyon height Type 2. However, it was observed that the road surface within symmetrical canyon height obtained a slightly higher temperature than the road surface within asymmetrical canyon height Type 2.

During 13:00 hour on most of the days of data collection (August 2015 and March 2016) as shown in Figure 6.32, the road surface within asymmetrical canyon height Type 2 (Section 1-(b)) obtained lowest temperature as compared to other canyon configurations, validating the results calculated from the simulation model. Based on the data collection of 4th August 2015 at noon hours, the road surface temperature within asymmetrical canyon Type 2 (ROAD 1 Section 1-(f)) did not significantly change from the surface temperature within symmetrical canyon height. However, the values were clearly higher during the noon hours of 6th and 8th August 2015. Results of the following year showed a repeated trend as the result of 4th August 2015.

The effect of street canyon configuration over the road surface temperature showed the correlation between the SCH, AC 1 and AC2 in the simulation results with the realistic urban configuration of ROAD 1, thus validated the trend of the temperature obtained in the simulation results.

6.4.5 Temperature results based on wind-blocking canyon condition

The results from the simulation and experimental studies were compared for the temperature of building facades and road surfaces.

6.4.5.1 Effect of façade temperature

Based on the simulation results, the temperature of Windward Wall was lower than the temperature of Leeward Wall due to receiving high convection rate from the predominant wind. The solar radiation which directed from the behind of Building B caused the creation of building shadows on the canyon road and the adjacent building facades, reducing the surface temperature. Furthermore, solar refraction caused certain surface areas to obtain higher temperature. Deeper canyon with symmetrical height increased the shadow effect on the façade surfaces thus reduced more temperature (AR 3 obtained lower temperature than AR 2). For the canyon with asymmetrical height Type 1, the facade temperature was indeed lower due to high convection.

Based on the data collection of August 2015 and March 2016, it was observed that the building facades of Section 1-(b) which is configured as asymmetrical canyon height Type 1 with aspect ratio of 1 obtained slightly higher temperature at most of the hour and day as compared to other sections. Other types of canyon configuration did not significantly influence the façade temperature, thus the temperature variance between the sections was minimal. It was observed that the building facades for the canyon sections with symmetrical height obtained lower temperature as compared to the other sections, thus validating the simulation result.

6.4.5.2 Effect of road surface temperature

Simulation results demonstrated its correlation with wind-blocking to increase road surface temperature specifically the surface area closer to Leeward Wall. The temperature variance between the road surface temperature without shadow and the road surface with shadow (334.57 °C) was determined based on two pipes location: (i) at location Pipe A-5, the variance was 21.65 °C (ii) at location Pipe C-1, the variance was 18.84 °C.

Based on the experimental results; In ROAD 1, it can be observed that the road surface temperature was disproportion to the façade temperature, showing lower road surface temperature obtained by Section 1-(b), which obtained highest façade temperature. The temperature variance between the road surface temperature without shadow and the road surface temperature with shadow was on average 5-6 °C, minimum variance was 3.78 °C and the maximum variance was 10.06 °C.

6.4.6 Analysis based on the potential UHI occurrence and mitigation

The results from the simulation and the experimental studies were expanded to summarise the individual analysis by highlighting the potential UHI occurrence and mitigation. In this section, for experimental works, the analysis included the data of ROAD 2 meanwhile for simulation works, the analysis included the performance of hydronic RPSC system in PTC, STR and in reducing air temperature. Table 6.6 displays the summary of analysis based on the above comparing the simulation modelling and the experimental studies.

Table 6.6 Potential UHI and mitigation comparing simulation and experiments

POTENTIAL UHI OCCURRENCE	
Analysis based on simulation	Analysis based on thermal imaging
Parameter 1: Aspect ratio	
It was found that deep street canyon (aspect ratio > 1) within symmetrical canyon condition blocked the predominant wind penetrating the street canyon, thus enhances the warming effect within the urban canopy and increases the electricity of mechanical ventilation and air-conditioning.	For ROAD 1, it was observed that the façade temperature and the road surface during the data collection in the month of March 2016 were $\pm 17^{\circ}\text{C}$ and $\pm 26^{\circ}\text{C}$, respectively higher than the data collection in August 2015 due to heat wave. For ROAD 2, the façade temperature and the road surface temperature based on August 2015 and March 2016 did not change significantly.
Parameter 2: Urban configuration / topology	
Symmetrical canyon conditions worsen the air circulation within the street canyon, which then increases the surface temperatures as well. Asymmetrical canyon height Type 1 showed an improvement of reducing surface temperature due to the higher air volume penetrating the canyon space and to cool down the hot surface temperatures.	In comparing ROAD 1 and ROAD 2, the data collection of August 2015 showed that the façade temperature and road surface temperature for ROAD 1 were on average 13 % and 11 %, respectively lower than the temperatures for ROAD 2. Meanwhile, ROAD 1 obtained on average 13 % higher in the road surface temperature over the road surface temperature of ROAD 2 during the data collection of March 2016.
POTENTIAL UHI MITIGATION	
Analysis based on simulation	Analysis based on thermal imaging
Application of hydronic RPSC system	
Using the default setting of hydronic RPSC system, the air temperature for pedestrian level within the canyon of 1, 2, 3 and 4 was potentially reduced 2-4 $^{\circ}\text{C}$; however, the obtained comfort temperature was 46.7-55.6 $^{\circ}\text{C}$ (116-132 F), which falls under danger and extreme danger category. Optimisation of hydronic RPSC system by increasing surface area of temperature reduction and to use an optimised water flow rate increase the performance of RPSC system for UHI mitigation.	Due to time constraint, the projection of hydronic RPSC system in mitigating surface temperatures within ROAD 1 and ROAD 2 could not be carried out using ANSYS CFD modelling. In Section 6.2.3, the RPSC domain comparing Type STP and Type SPP applied the boundary condition based on the data collection on ROAD 1, 4 th August 2015. Result suggested that RPSC performed 30-39 % in surface temperature reduction and 56-59 % performance in potential temperature collection.

6.5 Summary

Overall, Chapter 6 analysed and discussed the aim and objectives of the thesis based on computational results of RPSC performance in mitigating Urban Heat Island (UHI) effect. The thesis introduced the simulation of 3D de-coupled CFD modelling which the output from macro domain (to represent the microclimate environment above ground level) as the boundary condition for micro domain (to represent RPSC system for mitigating UHI effect). Simplification on the urban configuration was carried out for the thesis which only used a street canyon configuration with the orientation to be perpendicular to the predominant airflow as an urban environment.

Several configurations were investigated based on the modification of the canyon height and aspect ratio. Despite the simplification of the macro domain model, the results obtained for the study objectives have shown the significant of urban configuration on the performance of RPSC system in terms of inlet-outlet temperature difference (Delta T), surface temperature reduction (STR) and potential temperature collection (PTC). The results based on the simulation were compared with the results of experimental works explained in Chapter 5 and several agreements and disagreements were discussed. The use of RPSC system in mitigating surface-air UHI effects require further investigations in optimising the surface area of temperature reduction with optimum temperature collection to achieve low air temperature for low outdoor thermal discomfort and low indoor electricity load.

CHAPTER 7

Conclusion and future work

Overall, aim of the study was to investigate the application and the performance of hydronic RPSC in mitigating urban heat island (UHI) effect by introducing 3D ‘de-coupled’ simulation modelling of dynamic heat and airflow in ANSYS Fluent. Three main investigations have been carried out and were analysed based on the simulation works that have been done. Also, the supported validation based on previously published works and based on the data collection of temperature measurement studies of Kuala Lumpur street canyon were carried out. Thus, the analysis based on the results and discussion in Chapter 6 have led to the derivation of several conclusions which were structured according to the study objectives.

1. Determine the effect of urban canyon on RPSC system/performance

- i. Average road surface temperature within urban street canyon was 332.32 K or 59.32 °C meanwhile the average surface temperature without buildings (flat surface) was 327.92 K or 54.92 °C, resulting an average of 8.02 % higher in the performance of the urban surface in heat absorption against the surface temperature of flat surface.

- ii. Based on the simulation, the performance of RPSC system in an urban street canyon with two building rows and with perpendicular orientation to the predominant airflow was 35.76 % and 9.25 % more in terms of PTC and STR than the system application without buildings (flat surface).
- iii. Other factors also influenced the efficiency/deficiency of RPSC application. By changing the air velocity from the lowest setting which is 1 m/s to the highest setting which is 10 m/s, the performance of RPSC system in term of PTC was reduced up to 55.78 %; resulting the deficiency of using RPSC system during strong wind as this factor dominates the increased rate of convection heat transfer from the heated road surface.
- iv. The simulation of RPSC performance according to four seasons demonstrated the highest heat dissipation using RPSC system was during summer months due to high solar intensity as compared to other seasons. During these months, the temperature of the road surface can be 62 %, 40 % and 30 % higher than the months of winter, spring and autumn, respectively.
- v. Results based on the data collection using thermal infrared camera on ROAD 1 and ROAD 2 showed the solar intensity as the prominent factor to determine the surface temperatures. From the data collection, the highest solar intensity between 09:00 hour and 16:00 hour was observed during 14:00 hour in the afternoon, causing the temperature peaked at this time. Furthermore, the temperature values during the month of March 2016 for ROAD 1 showed approximately 20 % higher than the temperature values during the month of August 2015. Based on these results, it can be agreed that the simulation results of road surface temperature based on different intensity and seasonal changes were validated.

2. Determine the effect of canyon aspect ratios on RPSC performance

- i. The result of average road surface temperature from the simulation demonstrated 14.38 % increase in the temperature when the building height increased from AR 1 to AR 2; however, it was observed that no constancy in the temperature increase according to the increase in aspect ratio. An approximate of 7-8 % reduction in the surface temperature when the building height increased from AR 2 to AR 3 and AR 4.
- ii. Based on the simulation results of road surface temperature for all aspect ratios, it was expected that the obtained PTC and STR within the configuration of AR 2 was 16-23 % and 2-4.5 % respectively over AR 1, 3 and 4. Overall, an obvious higher performance was obtained with higher surface temperature and vice-versa in the trend with the obtained lower surface temperature.
- iii. From the data analysis of Kuala Lumpur hot humid urban canyons, inconsistency in the trend of façade and road surface temperatures were found in comparing the individual street canyon sections (Section (A) – Section (F)). For ROAD 1, the canyon sections with $AR > 1$ obtained lowest temperature values in the month of August 2015 meanwhile it obtained highest in the month of March 2015. For ROAD 2, a consistent trend was observed, which the building facades of the canyon sections with $AR < 1$ obtained lowest for both 2015 and 2016 data collections. For road surfaces, the temperature comparing individual street canyon sections for both ROAD 1 and ROAD 2 did not show any significant difference.
- iv. The data collection showed that ROAD 1 with average aspect ratio 3 obtained road temperature 11 % lower than ROAD 2 with average aspect ratio 1 in the month of August 2015. However; in the month of March 2016, road temperature in ROAD 1 obtained on average 13 % higher than ROAD 2.

3. Determine the effect of urban topologies on RPSC performance

- i. Results based on the simulation demonstrated that the asymmetrical canyon height Type 2 obtained on average 60 % identically high road surface temperature throughout the surface area, thus RPSC system can potentially obtain optimum steady temperature almost all over the street canyon surface.
- ii. Simulation based on the average surface temperature calculated on the three street canyon configurations, it was found that the RPSC system within symmetrical canyon height has significantly performed in terms of PTC on average 53.26 % more than asymmetrical canyon height Type 1 and insignificant higher in PTC on average 4.58 % more than asymmetrical canyon height Type 2.
- iii. The RPSC performance within symmetrical canyon height in terms of STR was on average not more than 40 %, demonstrating significant higher in STR, approximately 50 % than asymmetrical canyon height Type 2. Like PTC, the average STR value obtained by asymmetrical canyon height Type 2 did not differ significantly from the average STR value obtained by symmetrical canyon height, approximately 15 % lower.
- iv. Results from data collection showed with a consistent lowest temperature obtained by ROAD 1 canyon section with asymmetrical canyon height Type 1. It was also observed that canyon sections with symmetrical canyon height obtained higher temperature as compared to the other canyon configurations during the first day of data collection in August 2015. However, similar results were observed from the data collection in March 2016 due to a constant heat wave incidence with hot air temperature throughout the month. Also, an insignificant difference was found to compare the temperature results between the symmetrical canyon height and the asymmetrical canyon height Type 2. The data trend validated the simulation trend.

4. Determine the effect based on minimising/maximising surface area on RPSC performance

- i. The simulation results have shown an improvement in Delta T and PTC, up to 60 % when the pipe depth was reduced from 0.15 m (15 mm) to 0.025 m (25 mm) or approximately 83 % depth reduction. This means that the obtained Delta T of the shallowest depth can be as maximum as 23 °C with hotter pavement surface and as minimum as 14 °C with colder pavement surface (due to shadow effect).
- ii. With lowest inlet water temperature, RPSC pipe obtained as high as 17.0 °C in term of Delta T meanwhile with highest inlet water temperature, RPSC pipe obtained Delta T as low as 7.5 °C, approximately 56 % performance loss in term of PTC. By reducing the Delta T and the PTC values, the STR value dropped steadily and constantly. Thus, with approximate 56 % performance loss in PTC, performance loss in STR with approximate 56 % was also obtained.

5. Determine the effect based on minimising/maximising mass flow rate on RPSC performance

- i. Based on the analysis, it showed that a significant drop in Delta T and PTC up to 60 % when the inlet velocity was changed from the lowest tested water velocity, 0.1 m/s to higher tested velocity, 0.5 m/s. For the later velocity range, the drop was gradual until insignificant drop can be observed with the adjustment in the water velocity from 0.75 m/s to 2 m/s. The calculated STR graph trend was completely vice-versa to Delta T and PTC, which the improvement in STR performance can be observed when higher inlet velocity was used until the performance improvement became stagnant due to the dominant of volume of water flow with the temperature achieved its equilibrium state conforming the temperature of its surroundings. Thus,

after 0.75 m/s, it was suggested with unnecessary to use high-speed water velocity as insignificant increase in the surface temperature reduction by RPSC system can be observed.

- ii. When the pipe with diameter 0.015 m (15 mm) was replaced with second smallest pipe diameter, 0.02 m (20 mm), the performance of RPSC in terms of Delta T and PTC was -reduced up to 50 % meanwhile the drop in the performance as maximum as 84 % was found when smallest pipe diameter was changed to largest pipe diameter.

6. Determine the effect based on minimising/maximising surface area and mass flow rate on RPSC performance

- i. With low simulation water velocity (0.1 m/s), RPSC straight pipe (Type STP) obtained 20-35 % between 09:00 hour and 15:00 hour with similar reduction in the surface temperature (STR) was observed above all pipe locations. Like Type STP, the performance in STR using RPSC serpentine pipe (Type SPP) was observed significant comparing the surface area above pipe locations. The surface temperature above Pipe A was reduced approximately 19-33 % between 09:00 hour and 15:00 hour meanwhile the reduction in the surface temperature above Pipe D was lower than Pipe A, approximately 15-28 % within the 7-hour simulation.
- ii. When higher inlet water velocity was applied (0.25 m/s), RPSC performance in term of STR was increased to 28-48 % for Type STP and to 23-44 % for Type SPP, demonstrating insignificant difference in the STR value to compare both pipe layouts from the lowest tested water velocity to the highest tested water velocity (0.1 m/s to 0.25 m/s).

- iii. At 0.1 m/s inlet water velocity, simulation results demonstrated that RPSC performance in Delta T and PTC for Type SPP was observed significant, 72.02 % higher in the performance as compared to Type STP. With 0.25 m/s inlet water velocity, although both layouts have loss in the performance of Delta T and PTC by approximately 55-60 %, RPSC Type SPP still dominated the performance over RPSC Type STP.

7. Determine the condition of comfort temperature after RPSC application

Evaluation on mitigating air UHI effect at street canyon pedestrian level was conducted based on the application of RPSC system on the road surface within symmetrical canyon height in four ratios. The following conclusions were drawn:

- i. Application of RPSC system for surface-air UHI mitigation was investigated, showing the average reduction in road surface temperature at all aspect ratios approximately 16-21 %. Based on the simulation analysis after the RPSC application, it was found that RPSC system has assisted in reducing air temperature within the street configuration of AR 1, AR 2, AR 3 and AR 4 by 3.68 °C (9.30 %), 1.69 °C (4.64 %), 1.07 °C (3.11 %) and 2.13 °C (5.62 %), respectively.
- ii. Overall, the air temperature at pedestrian level in all aspect ratios was 33-37 °C with air temperature reduction 1-4 °C when RPSC system was applied. Based on 33-37 °C (91.4-98.6 F) with 75 % relative humidity, it was highlighted that the obtained ‘feel like’ temperature based on the table of Heat Index (HI) was 46.7-55.6 °C (116-132 F), which falls under danger and extreme danger categories. According to the investigation of National Ocean and Administration (NOAA) under National Weather Service, the ‘feel like’ temperature fall under these categories has the potential to harm human body with heat cramps, heat exhaustion and as extreme as

heat stroke. It was reported that the 'feel like' temperature with little or no discomfort to human body should fall to 20-29 °C.

8. Determine the impact on energy consumption for thermal comfort after RPSC application

- iii. The air temperature reduction 1-4 °C has the potential in the reduction of using air-conditioning unit double to quadruple the usage of 500 megawatts and approximately double to quadruple the electric cost of USD 100,000 per hour for the usage of 1-1.5 megawatts.

Limitation of study

The limitation of the research conducted in the thesis was found within the applied boundary condition on the computational results involving macro domain and micro domain. Future recommendation for the model of RPSC performance within urban configuration can be improved by:

- i. Comparing the orientation of street canyon configuration that the current study has only considered based on its perpendicular orientation to the predominant airflow to the orientation of street canyon with parallel orientation to the predominant airflow.
- ii. Analysing the RSPC performance based on the adjustment in the surface materials involving both macro domain and micro domain i.e. building facades, road materials, RPSC pipe materials, RPSC fluid material.

- iii. Comparing the model configuration used in ANSYS Fluent. For example, the viscosity model of Standard $k - \varepsilon$ model can be compared to Realizable $k - \varepsilon$ model to monitor how significant the viscosity model to affect the temperature results.
- iv. Carrying out investigation of RPSC optimisation in obtaining optimum Delta T, PTC and STR together with its effect on air temperature and 'feel like' air temperature following Heat Index (HI).

Future work

Research also experienced with time constraint to fully analyse the data collection based on the microclimate urban street canyon studies involving ROAD 1 and ROAD 2 of Kuala Lumpur conurbation centre. Future investigation can improve to include:

- i. The analysis in terms of horizontal and vertical temperatures which compare data collection of ROAD 1 and ROAD 2 with the non-generic simulation modelling involving canyon aspect ratio of 1 and 3 based on the realistic configuration of ROAD 1 and ROAD 2 according to month, day and hour.
- ii. Prediction study of air-surface UHI effect based on the data collection by the application of ANSYS Fluent model.
- iii. Prediction study of mitigating road temperatures of ROAD 1 and ROAD 2 with hydronic RPSC system.
- iv. Prediction of the impact on indoor comfort with excessive outdoor temperatures with low wind speed according to aspect ratio and urban topology / configuration using simulation modelling with the boundary condition based on the data collection.

LIST OF REFERENCES

- Abd Razak, A. et al., 2013. Analysis of airflow over building arrays for assessment of urban wind environment. *Building and Environment*, 59, pp.56–65. Available at: <http://dx.doi.org/10.1016/j.buildenv.2012.08.007>.
- Ahmad, K., Khare, M. & Chaudhry, K.K., 2005. Wind tunnel simulation studies on dispersion at urban street canyons and intersections - A review. *Journal of Wind Engineering and Industrial Aerodynamics*, 93(9), pp.697–717.
- Ahmad, S. & Hashim, N., 2007. Effects of Soil Moisture on Urban Heat Island Occurrences : Case of Selangor , Malaysia. *Humanity & Social Sciences Journal*, 2(2), pp.132–138.
- Akbari, H., 2005. Energy Saving Potentials and Air Quality Benefits of Urban Heat Island Mitigation. *Solar Energy*, pp.1–19. Available at: <http://escholarship.org/uc/item/4qs5f42s.pdf>.
- Akbari, H. & Matthews, H.D., 2012. Global cooling updates: Reflective roofs and pavements. *Energy and Buildings*, 55, pp.2–6. Available at: <http://dx.doi.org/10.1016/j.enbuild.2012.02.055>.
- Akbari, H., Pomerantz, M. & Taha, H., 2001. Cool surfaces and shade trees to reduce energy use and improve air quality in urban areas. , 70(3), pp.295–310.
- Al-Saad, M.A., Jubran, B.A. & Abu-Faris, N.A., 1994. Development and testing of concrete solar collectors. *International Journal of Solar Energy*, 16(1), pp.27–40. Available at: <http://dx.doi.org/10.1080/01425919408914264>.
- Alchapar, N.L., Correa, E.N. & Cantón, M.A., 2014. Classification of building materials used in the urban envelopes according to their capacity for mitigation of the urban heat island in semiarid zones. *Energy and Buildings*, 69, pp.22–32. Available at: <http://linkinghub.elsevier.com/retrieve/pii/S0378778813006580> [Accessed March 28, 2014].
- Ali-toudert, F. et al., 2005. Outdoor thermal comfort in the old desert city. , 28(1993), pp.243–256.

- Ali-Toudert, F. & Mayer, H., 2006. Numerical study on the effects of aspect ratio and orientation of an urban street canyon on outdoor thermal comfort in hot and dry climate. *Building and Environment*, 41(2), pp.94–108. Available at: <http://linkinghub.elsevier.com/retrieve/pii/S0360132305000120> [Accessed March 26, 2014].
- Allegrini, J., Dorer, V. & Carmeliet, J., 2012. Analysis of convective heat transfer at building facades in street canyons and its influence on the predictions of space cooling demand in buildings. *Journal of Wind Engineering and Industrial Aerodynamics*, 104–106, pp.464–473. Available at: <http://dx.doi.org/10.1016/j.jweia.2012.02.003>.
- Allegrini, J., Dorer, V. & Carmeliet, J., 2015. Coupled CFD, radiation and building energy model for studying heat fluxes in an urban environment with generic building configurations. *Sustainable Cities and Society*, 19, pp.385–394. Available at: <http://dx.doi.org/10.1016/j.scs.2015.07.009>.
- Ansys, 2009. ANSYS Fluent Tutorial. , (April).
- April, F.S., 1999. Comment : Human Contribution. , 80(33).
- Arnfield, A.J., 2003. Review two decades of urban climate research : a review of turbulence , exchanges of energy and water , and the urban heat island. , 26, pp.1–26.
- Arnfield, A.J., 1990. Street design and urban canyon solar access. *Energy and Buildings*, 14(2), pp.117–131.
- Arnfield, a. J. & Grimmond, C.S.B., 1998. An urban canyon energy budget model and its application to urban storage heat flux modeling. *Energy and Buildings*, 27(1), pp.61–68.
- Benson, J. et al., 2008. Global sensitivity analysis of a 3D street canyon model—Part II: Application and physical insight using sensitivity analysis. *Atmospheric Environment*, 42(8), pp.1874–1891. Available at: <http://linkinghub.elsevier.com/retrieve/pii/S135223100701062X> [Accessed March 30, 2014].
- Berdahl, P. & Bretz, S.E., 1997. Preliminary survey of the solar reflectance of cool roofing materials. , 25, pp.149–158.
- Bilgen, E. & Richard, M.-A., 2002. Horizontal concrete slabs as passive solar collectors. *Solar Energy*, 72(5), pp.405–413.

- Blocken, B., Carmeliet, J. & Stathopoulos, T., 2007. CFD evaluation of wind speed conditions in passages between parallel buildings-effect of wall-function roughness modifications for the atmospheric boundary layer flow. *Journal of Wind Engineering and Industrial Aerodynamics*, 95(9–11), pp.941–962.
- Blocken, B., Stathopoulos, T. & Carmeliet, J., 2007. CFD simulation of the atmospheric boundary layer: wall function problems. *Atmospheric Environment*, 41(2), pp.238–252.
- Bobes-Jesus, V. et al., 2013. Asphalt solar collectors: A literature review. *Applied Energy*, 102, pp.962–970. Available at: <http://linkinghub.elsevier.com/retrieve/pii/S030626191200637X>.
- Bottillo, S. et al., 2014. Fluid dynamic and heat transfer parameters in an urban canyon. *Solar Energy*, 99, pp.1–10. Available at: <http://linkinghub.elsevier.com/retrieve/pii/S0038092X13004611> [Accessed March 30, 2014].
- Bozonnet, E., Belarbi, R. & Allard, F., 2005. Modelling solar effects on the heat and mass transfer in a street canyon, a simplified approach. *Solar Energy*, 79(1), pp.10–24.
- Bretz, S., Akbari, H. & Rosenfeld, A., 1997. Practical issues for using solar-reflective materials to mitigate urban heat islands. , 32(1).
- Carnielo, E. & Zinzi, M., 2013. Optical and thermal characterisation of cool asphalts to mitigate urban temperatures and building cooling demand. *Building and Environment*, 60, pp.56–65. Available at: <http://dx.doi.org/10.1016/j.buildenv.2012.11.004>.
- Cengel, Y.A. & Boles, M.A., 2015. *Thermodynamics An Engineering Approach* Eighth Edi., Mc Graw Hill Education.
- Cengel, Y.A. & Ghajar, A.J., 2015. *Heat and Mass Transfer Fundamental & Applications* Fifth Edit., Mc Graw Hill Education.
- Chapman, L., Azevedo, J.A. & Prieto-Lopez, T., 2013. Urban heat & critical infrastructure networks: A viewpoint. *Urban Climate*, 3, pp.7–12. Available at: <http://dx.doi.org/10.1016/j.uclim.2013.04.001>.
- Chen, M. et al., 2011. Study of ice and snow melting process on conductive asphalt solar collector. *Solar Energy Materials and Solar Cells*, 95(12), pp.3241–3250. Available at: <http://linkinghub.elsevier.com/retrieve/pii/S0927024811004168> [Accessed March 30, 2014].

- Chiasson, A. & Spitler, J., 2001. Modeling Approach to Design of a Ground-Source Heat Pump Bridge Deck Heating System. *Transportation Research Record*, 1741(1), pp.207–215.
- Christen, A. & Vogt, R., 2004. Energy and radiation balance of a central European City. *International Journal of Climatology*, 24(11), pp.1395–1421.
- Chudnovsky, a., Ben-Dor, E. & Saaroni, H., 2004. Diurnal thermal behavior of selected urban objects using remote sensing measurements. *Energy and Buildings*, 36(11), pp.1063–1074. Available at: <http://linkinghub.elsevier.com/retrieve/pii/S03787778804000854> [Accessed March 30, 2014].
- CIMSS, 2017. WXWISE Urban Heat Islands. Available at: <http://cimss.ssec.wisc.edu/wxwise/heatisl.html> [Accessed March 12, 2018].
- Comarazamy, D.E., Gonzalez, J.E. & Luvall, J.C., 2015. Quantification and mitigation of long-term impacts of urbanization and climate change in the tropical coastal city of San Juan, Puerto Rico. *International Journal of Low-Carbon Technologies*, 10(1), pp.87–97.
- Coutts, A.M. et al., 2016. Thermal infrared remote sensing of urban heat: Hotspots, vegetation, and an assessment of techniques for use in urban planning. *Remote Sensing of Environment*, 186, pp.637–651. Available at: <http://dx.doi.org/10.1016/j.rse.2016.09.007>.
- Eliasson, I. et al., 2006. Wind fields and turbulence statistics in an urban street canyon. *Atmospheric Environment*, 40(1), pp.1–16.
- Elsayed, I.S.M., 2012a. Effects of Population Density and Land Management on the Intensity of Urban Heat Islands : A Case Study on the City of.
- Elsayed, I.S.M., 2012b. Mitigation of the urban heat island of the city of Kuala Lumpur, Malaysia. *Middle East Journal of Scientific Research*, 11(11), pp.1602–1613. Available at: <http://www.scopus.com/inward/record.url?eid=2-s2.0-84868622933&partnerID=tZOtx3y1>.
- Elsayed, I.S.M., 2012c. Mitigation of the Urban Heat Island of the City of Kuala Lumpur , Malaysia. , 11(11), pp.1602–1613.
- Elsayed, I.S.M., 2006. The effects of urbanization of the intensity of the urban heat island: A case study on the city of Kuala Lumpur. , PhD.
- Elsayed, I.S.M. & Ilham S. M. Elsayed, 2012. a Study on the Urban Heat Island of the City of Kuala Lumpur, Malaysia. *Journal of King Abdulaziz University*, 23(2), pp.121–134.

- Erell, E. et al., 2013. Effect of high-albedo materials on pedestrian heat stress in urban street canyons. *Urban Climate*. Available at: <http://linkinghub.elsevier.com/retrieve/pii/S2212095513000539> [Accessed March 30, 2014].
- Feng, T. & Feng, S., 2012. A numerical model for predicting road surface temperature in the highway. *Procedia Engineering*, 37(Cems), pp.137–142.
- Fluent, 2009. ANSYS Fluent 12.0 user's guide. *Ansys Inc*, 15317(November), pp.1–2498. Available at: <http://scholar.google.com/scholar?hl=en&btnG=Search&q=intitle:ANSYS+FLUENT+User'+s+Guide#1>.
- Franke, J. et al., 2007. *Best practice guideline for the CFD simulation of flows in the urban environment*,
- Gao, Q. et al., 2010. Experimental study of slab solar collection on the hydronic system of road. *Solar Energy*, 84(12), pp.2096–2102. Available at: <http://dx.doi.org/10.1016/j.solener.2010.09.008>.
- Giannaros, T.M. & Melas, D., 2012. Study of the urban heat island in a coastal Mediterranean City: The case study of Thessaloniki, Greece. *Atmospheric Research*, 118, pp.103–120. Available at: <http://linkinghub.elsevier.com/retrieve/pii/S0169809512001810> [Accessed March 26, 2014].
- Gilbert, H., Mandel, B.H. & Levinson, R., 2016. Keeping California cool: Recent cool community developments. *Energy and Buildings*, 114, pp.20–26. Available at: <http://dx.doi.org/10.1016/j.enbuild.2015.06.023>.
- Giridharan, R., Ganesan, S. & Lau, S.S.Y., 2004. Daytime urban heat island effect in high-rise and high-density residential developments in Hong Kong. *Energy and Buildings*, 36(6), pp.525–534.
- Giridharan, R., Lau, S.S.Y. & Ganesan, S., 2005. Nocturnal heat island effect in urban residential developments of Hong Kong. *Energy and Buildings*, 37(9), pp.964–971.
- Green Power, 2012. Report on Urban Heat Island Effect in Hong Kong. Available at: <http://studylib.net/doc/7524843/preliminary-study-on-the-urban-heat-island-effect-in-hong...> [Accessed March 12, 2018].
- Gülten, A., Aksoy, U.T. & Öztop, H.F., 2016. Influence of trees on heat island potential in an urban canyon. *Sustainable Cities and Society*, 26, pp.407–418.

- Hall, M.R. et al., 2012. Influence of the Thermophysical Properties of Pavement Materials on the Evolution of Temperature Depth Profiles in Different Climatic Regions. *Journal of Materials in Civil Engineering*, 24(1), pp.32–47.
- Harman, I.N. & Belcher, S.E., 2006. The surface energy balance and boundary-layer over urban street canyons. , pp.2749–2768. Available at: <http://dx.doi.org/10.1256/qj.05.185>.
- Hasebe, M, Yamikawa, Y and Meiarashi, S., 2006. Thermoelectric generators using solar thermal energy in heated road pavement. ... , 2006. *ICT'06. 25th* ..., pp.697–700. Available at: http://ieeexplore.ieee.org/xpls/abs_all.jsp?arnumber=4133389.
- Hiung, T.J. & Ahmad, M.H., 2006. Possibility of Using Computational Fluid Dynamics (CFD) for Urban Canyon Studies in Tropical Climate. , (1).
- van Hove, L.W.A. et al., 2015. Temporal and spatial variability of urban heat island and thermal comfort within the Rotterdam agglomeration. *Building and Environment*, 83, pp.91–103. Available at: <http://linkinghub.elsevier.com/retrieve/pii/S0360132314002881>.
- Hu, Z. et al., 2012. Numerical investigation on the urban heat island in an entire city with an urban porous media model. *Atmospheric Environment*, 47, pp.509–518. Available at: <http://dx.doi.org/10.1016/j.atmosenv.2011.09.064>.
- Ito, S. et al., 2005. Measurement of the thermal environment in urban canyons and prediction by CFD simulation. *Ninth International IBPSA Conference*, (August 2003), pp.475–482.
- Kantzioura, A., Kosmopoulos, P. & Zoras, S., 2012. Urban surface temperature and microclimate measurements in Thessaloniki. *Energy and Buildings*, 44(1), pp.63–72. Available at: <http://dx.doi.org/10.1016/j.enbuild.2011.10.019>.
- Karachaliou, P., Santamouris, M. & Pangelou, H., 2016. Experimental and numerical analysis of the energy performance of a large scale intensive green roof system installed on an office building in Athens. *Energy and Buildings*, 114, pp.256–264. Available at: <http://dx.doi.org/10.1016/j.enbuild.2015.04.055>.
- Kennedy, C. & Corfee-Morlot, J., 2013. Past performance and future needs for low carbon climate resilient infrastructure- An investment perspective. *Energy Policy*, 59, pp.773–783. Available at: <http://dx.doi.org/10.1016/j.enpol.2013.04.031>.
- Kershaw, T. et al., 2010. Estimation of the urban heat island for UK climate change projections. , 3, pp.251–263. Available at: <http://dx.doi.org/10.1177/0143624410365033>.

- Kim, J.J. & Baik, J.J., 2004. A numerical study of the effects of ambient wind direction on flow and dispersion in urban street canyons using the RNG k- ϵ turbulence model. *Atmospheric Environment*, 38(19), pp.3039–3048.
- Kleerekoper, L. et al., 2015. Creating drafts in urban settings through coloured façades: Exploring a new climate adaptation measure based on thermal stratification. *Urban Climate*, 14, pp.290–300. Available at: <http://dx.doi.org/10.1016/j.uclim.2015.09.002>.
- Kleerekoper, L., van Esch, M. & Salcedo, T.B., 2012. How to make a city climate-proof, addressing the urban heat island effect. *Resources, Conservation and Recycling*, 64, pp.30–38. Available at: <http://linkinghub.elsevier.com/retrieve/pii/S0921344911001303> [Accessed March 23, 2014].
- Kolokotroni, M. et al., 2012. London's urban heat island: Impact on current and future energy consumption in office buildings. *Energy and Buildings*, 47, pp.302–311. Available at: <http://dx.doi.org/10.1016/j.enbuild.2011.12.019>.
- Kolokotroni, M. & Giridharan, R., 2008a. Urban heat island intensity in London: An investigation of the impact of physical characteristics on changes in outdoor air temperature during summer. *Solar Energy*, 82(11), pp.986–998. Available at: <http://linkinghub.elsevier.com/retrieve/pii/S0038092X08001084> [Accessed March 26, 2014].
- Kolokotroni, M. & Giridharan, R., 2008b. Urban heat island intensity in London: An investigation of the impact of physical characteristics on changes in outdoor air temperature during summer. *Solar Energy*, 82(11), pp.986–998.
- Landsberg, H.E., 1981. *The Urban Climate* 1st Editio., New York: Academic Press.
- Lemonsu, A. & Masson, V., 2002. Simulation of a summer urban breeze over paris. , (October 2001), pp.463–490.
- Levermore, G. & Cheung, H., 2012. A low-order canyon model to estimate the influence of canyon shape on the maximum urban heat island effect. *Building Services Engineering Research and Technology*, 33(4), pp.371–385.
- Lin, T. et al., 2010. Effect of pavements albedo on long-term outdoor thermal comfort. In *Proceedings of the 7 th Conference on Biometeorology*. pp. 497–503. Available at: https://www.researchgate.net/profile/Andreas_Matzarakis/publication/259475542_Proceedings_of_the_7th_Conference_on_Biometeorology_Albert-Ludwigs-University_of_Freiburg_Germany_12-14_April_2010/links/0deec533fc3df68709000000/Proceedings-of-the-7th-Conferen.

- Lin, T.P., Ho, Y.F. & Huang, Y.S., 2007. Seasonal effect of pavement on outdoor thermal environments in subtropical Taiwan. *Building and Environment*, 42(12), pp.4124–4131.
- Loomans, M. et al., 2003. Design tool for the thermal energy potential of asphalt pavements. , pp.745–752.
- Mallick, R.B., Chen, B.-L. & Bhowmick, S., 2009. Harvesting energy from asphalt pavements and reducing the heat island effect. *International Journal of Sustainable Engineering*, 2(3), pp.214–228. Available at: <http://www.tandfonline.com/doi/abs/10.1080/19397030903121950> [Accessed March 30, 2014].
- Memon, R.A. & Leung, D.Y.C., 2011. On the heating environment in street canyon. *Environmental Fluid Mechanics*, 11(5), pp.465–480.
- Memon, R.A., Leung, D.Y.C. & Liu, C.H., 2009. An investigation of urban heat island intensity (UHII) as an indicator of urban heating. *Atmospheric Research*, 94(3), pp.491–500. Available at: <http://dx.doi.org/10.1016/j.atmosres.2009.07.006>.
- Memon, R.A., Leung, D.Y.C. & Liu, C.H., 2010. Effects of building aspect ratio and wind speed on air temperatures in urban-like street canyons. *Building and Environment*, 45(1), pp.176–188. Available at: <http://dx.doi.org/10.1016/j.buildenv.2009.05.015>.
- Mills, G., 2008. Luke Howard and The Climate of London. *Weather*, 63(6). Available at: <http://www.theurbanclimatologist.com/uploads/4/4/2/5/44250401/post6lukehoward.pdf> [Accessed February 26, 2018].
- Mirzaei, P. a. & Haghighat, F., 2012. A procedure to quantify the impact of mitigation techniques on the urban ventilation. *Building and Environment*, 47(1), pp.410–420. Available at: <http://dx.doi.org/10.1016/j.buildenv.2011.06.007>.
- Montávez, J.P. & Jiménez, J.I., 2000. A MONTE CARLO MODEL OF THE NOCTURNAL SURFACE TEMPERATURES IN URBAN CANYONS. , pp.433–452.
- National Weather Service, 2017. Appendix A: Anatomy of a Zone Forecast. Available at: <https://www.weather.gov/media/pah/ServiceGuide/A-forecast.pdf> [Accessed January 20, 2018].
- Nazarian, N. & Kleissl, J., 2015. CFD simulation of an idealized urban environment: Thermal effects of geometrical characteristics and surface materials. *Urban Climate*, 12, pp.141–159. Available at: <http://dx.doi.org/10.1016/j.uclim.2015.03.002>.

- Niachou, K., Livada, I. & Santamouris, M., 2008. Experimental study of temperature and airflow distribution inside an urban street canyon during hot summer weather conditions. Part II: Airflow analysis. *Building and Environment*, 43(8), pp.1393–1403.
- O'Malley, C. et al., 2015. Urban Heat Island (UHI) mitigating strategies: A case-based comparative analysis. *Sustainable Cities and Society*, 19, pp.222–235. Available at: <http://dx.doi.org/10.1016/j.scs.2015.05.009>.
- Ojima, T., 1990. Changing Tokyo Metropolitan Area and its Heat Island Model. , 16, pp.191–203.
- Oke, T.R., 1987a. *Boundary Layer Climates* Second Edi. Taylor & Francis e-Library, ed., Methuen & Co. Ltd.
- Oke, T.R., 1987b. *Boundary Layer Climates* Second Edi., Methuen & Co. Ltd.
- Oke, T.R., 1981. Canyon geometry and the nocturnal urban heat island. , 1, pp.237–254.
- Oke, T.R., 1988. Street design and urban canopy layer climate. *Energy and Buildings*, 11(1–3), pp.103–113.
- Owen, T.W., Carlson, T.N. & Gillies, R.R., 1998. An assessment of satellite remotely-sensed land cover parameters in quantitatively describing the climatic effect of urbanization. , 19(9), pp.1663–1681.
- Pan, P. et al., 2015. A review on hydronic asphalt pavement for energy harvesting and snow melting. *Renewable and Sustainable Energy Reviews*, 48, pp.624–634. Available at: <http://dx.doi.org/10.1016/j.rser.2015.04.029>.
- Panão, M.J.N.O., Gonçalves, H.J.P. & Ferrão, P.M.C., 2006. A Matrix Approach Coupled with Monte Carlo Techniques for Solving the Net Radiative Balance of the Urban Block. *Boundary-Layer Meteorology*, 122(1), pp.217–241. Available at: <http://link.springer.com/10.1007/s10546-006-9088-y> [Accessed March 30, 2014].
- Pascual-Muñoz, P. et al., 2013. Thermal and hydraulic analysis of multilayered asphalt pavements as active solar collectors. *Applied Energy*, 111, pp.324–332.
- Priyadarsini, R., Hien, W.N. & Wai David, C.K., 2008. Microclimatic modeling of the urban thermal environment of Singapore to mitigate urban heat island. *Solar Energy*, 82(8), pp.727–745.
- Qin, Y. & Hiller, J.E., 2011. Modeling temperature distribution in rigid pavement slabs: Impact of air temperature. *Construction and Building Materials*, 25(9), pp.3753–3761. Available at: <http://dx.doi.org/10.1016/j.conbuildmat.2011.04.015>.

- Radhi, H., Assem, E. & Sharples, S., 2014. On the colours and properties of building surface materials to mitigate urban heat islands in highly productive solar regions. *Building and Environment*, 72, pp.162–172. Available at: <http://dx.doi.org/10.1016/j.buildenv.2013.11.005>.
- Radhi, H., Fikry, F. & Sharples, S., 2013. Impacts of urbanisation on the thermal behaviour of new built up environments: A scoping study of the urban heat island in Bahrain. *Landscape and Urban Planning*, 113, pp.47–61. Available at: <http://linkinghub.elsevier.com/retrieve/pii/S0169204613000200> [Accessed March 19, 2014].
- Robinson, D., 2006. Urban morphology and indicators of radiation availability. *Solar Energy*, 80(12), pp.1643–1648.
- Rosenfeld, A.H. et al., 1995. Mitigation of urban heat islands: materials, utility programs, updates. , 22, pp.255–265.
- Rossi, F. et al., 2014. Analysis of retro-reflective surfaces for urban heat island mitigation: A new analytical model. *Applied Energy*, 114, pp.621–631. Available at: <http://dx.doi.org/10.1016/j.apenergy.2013.10.038>.
- Rotach, M.W., 1995. Profiles of turbulence statistics in and above an urban street canyon. *Atmospheric Environment*, 29(13), pp.1473–1486.
- Rübenkönig, O., The Finite Volume Method (FVM) – An introduction. Available at: http://www.imtek.uni-freiburg.de/simulation/mathematica/IMSweb/imsTOC/Lectures and Tips/Simulation I/FVM_introDocu.html [Accessed May 28, 2017].
- Sailor, D.J. & Fan, H., 2002. Modeling the diurnal variability of effective albedo for cities. *Atmospheric Environment*, 36(4), pp.713–725.
- Saneinejad, S., Moonen, P. & Carmeliet, J., 2014. Coupled CFD, radiation and porous media model for evaluating the micro-climate in an urban environment. *Journal of Wind Engineering and Industrial Aerodynamics*, 128, pp.1–11. Available at: <http://dx.doi.org/10.1016/j.jweia.2014.02.005>.
- Sani, S., 1984. Urban Development And Changing Patierns Of Night Time Temperatures In The Kuala Lumpur-Petaling Jaya Area Malaysia. *Jurnal Teknologi*, 5(1), pp.27–35.
- Santamouris, M., 2012. Cooling the cities – A review of reflective and green roof mitigation technologies to fight heat island and improve comfort in urban environments. *Solar Energy*. Available at: <http://linkinghub.elsevier.com/retrieve/pii/S0038092X12002447> [Accessed March 23, 2014].

- Santamouris, M., 2015. Regulating the damaged thermostat of the cities — Status , impacts and mitigation challenges. *Energy & Buildings*, 91, pp.43–56. Available at: <http://dx.doi.org/10.1016/j.enbuild.2015.01.027>.
- Shaopeng, W., Mingyu, C. & Jizhe, Z., 2011. Laboratory investigation into thermal response of asphalt pavements as solar collector by application of small-scale slabs. *Applied Thermal Engineering*, 31(10), pp.1582–1587. Available at: <http://linkinghub.elsevier.com/retrieve/pii/S1359431111000378> [Accessed August 8, 2014].
- Smith, C. & Levermore, G., 2008. Designing urban spaces and buildings to improve sustainability and quality of life in a warmer world. *Energy Policy*, 36(12), pp.4558–4562. Available at: <http://linkinghub.elsevier.com/retrieve/pii/S0301421508004825> [Accessed March 26, 2014].
- Stavrakakis, G.M. et al., 2012. A computational methodology for effective bioclimatic-design applications in the urban environment. *Sustainable Cities and Society*, 4(1), pp.41–57. Available at: <http://dx.doi.org/10.1016/j.scs.2012.05.002>.
- Streutker, D.R., 2003. Satellite-measured growth of the urban heat island of Houston , Texas. , 85, pp.282–289.
- Synnefa, A. et al., 2011. Experimental testing of cool colored thin layer asphalt and estimation of its potential to improve the urban microclimate. *Building and Environment*, 46(1), pp.38–44. Available at: <http://linkinghub.elsevier.com/retrieve/pii/S0360132310002039> [Accessed March 30, 2014].
- Taha, H., Sailor, D. & Municipal, S., 1992. High-Albedo Materials for Reducing Building Cooling Energy Use. *Energy*.
- Taleghani, M., 2017. Outdoor thermal comfort by different heat mitigation strategies- A review. *Renewable and Sustainable Energy Reviews*, (March), pp.1–8. Available at: <http://dx.doi.org/10.1016/j.rser.2017.06.010>.
- Tan, S.-A. & Fwa, T.-F., 1992. Influence of pavement materials on the thermal environment of outdoor spaces. *Building and Environment*, 27(3), pp.289–295.
- Tian, W. et al., 2007. Effect of urban climate on building integrated photovoltaics performance. *Energy Conversion and Management*, 48(1), pp.1–8.
- Toparlar, Y. et al., 2015. CFD simulation and validation of urban microclimate: A case study for Bergpolder Zuid, Rotterdam. *Building and Environment*, 83, pp.79–90. Available at: <http://dx.doi.org/10.1016/j.buildenv.2014.08.004>.

- Uehara, K. et al., 2000. Wind tunnel experiments on how thermal stratification affects flow in and above urban street canyons. *Atmospheric Environment*, 34(10), pp.1553–1562.
- Utlu, Z., Aydin, D. & Kincay, O., 2014. Comprehensive thermodynamic analysis of a renewable energy sourced hybrid heating system combined with latent heat storage. *Energy Conversion and Management*, 84, pp.311–325. Available at: <http://dx.doi.org/10.1016/j.enconman.2014.04.024>.
- Vardoulakis, S. et al., 2003. Modelling air quality in street canyons: a review. *Atmospheric Environment*, 37(2), pp.155–182. Available at: <http://linkinghub.elsevier.com/retrieve/pii/S1352231002008579>.
- Vasiliev, L.L., 1988. Heat pipes for ground heating and cooling. *Heat Recovery Systems and CHP*, 8(2), pp.125–139.
- Voogt, J.A. & Oke, T.R., 2003. Thermal remote sensing of urban climates. , 86, pp.370–384.
- Wang, H. et al., 2010. Numerical simulation on the thermal response of heat-conducting asphalt pavements. *Phys. Scr*, 14041, pp.11–14.
- WeatherUnderground, 2014. Cavaria con Premezzo Weather | Personal Weather Station: IVARESEC3 by Wunderground.com | Weather Underground. Available at: <https://www.wunderground.com/personal-weather-station/dashboard?ID=IVARESEC3#history/s20140921/e20141021/mmonth> [accessed 17.08.15] [Accessed February 26, 2018].
- WeatherUnderground, 2016a. Weather History for Kuala Lumpur Aziz, MY | Weather Underground. Available at: https://www.wunderground.com/history/airport/WMSA/2016/3/9/DailyHistory.html?req_city=Sultan+Abdul+Aziz+Shah-Subang&req_state=&req_statename=Malaysia&reqdb.zip=00000&reqdb.magic=390&reqdb.wmo=WWMSA [Accessed January 20, 2018].
- WeatherUnderground, 2016b. Weather History for Kuala Lumpur Aziz, MY | Weather Underground - 07th March 2016. Available at: https://www.wunderground.com/history/airport/WMSA/2016/3/7/DailyHistory.html?req_city=&req_state=&req_statename=&reqdb.zip=&reqdb.magic=&reqdb.wmo= [Accessed March 16, 2018].
- WeatherUnderground, 2016c. Weather History for Kuala Lumpur Aziz, MY | Weather Underground - 09th March 2016. Available at: https://www.wunderground.com/history/airport/WMSA/2016/3/9/DailyHistory.html?req_city=&req_state=&req_statename=&reqdb.zip=&reqdb.magic=&reqdb.wmo= [Accessed March 16, 2018].

- WeatherUnderground, 2016d. Weather History for Kuala Lumpur Aziz, MY | Weather Underground - 11th March 2016. Available at:
https://www.wunderground.com/history/airport/WMSA/2016/3/11/DailyHistory.html?req_city=&req_state=&req_statename=&reqdb.zip=&reqdb.magic=&reqdb.wmo= [Accessed March 16, 2018].
- WeatherUnderground, 2016e. Weather History for Kuala Lumpur Aziz, MY | Weather Underground - 14th March 2018. Available at:
https://www.wunderground.com/history/airport/WMSA/2016/3/14/DailyHistory.html?req_city=&req_state=&req_statename=&reqdb.zip=&reqdb.magic=&reqdb.wmo= [Accessed March 16, 2018].
- WeatherUnderground, 2016f. Weather History for Kuala Lumpur Aziz, MY | Weather Underground - 16th March 2016. Available at:
https://www.wunderground.com/history/airport/WMSA/2016/3/16/DailyHistory.html?req_city=&req_state=&req_statename=&reqdb.zip=&reqdb.magic=&reqdb.wmo= [Accessed March 16, 2018].
- WeatherUnderground, 2016g. Weather History for Kuala Lumpur Aziz, MY | Weather Underground - 18th March 2018. Available at:
https://www.wunderground.com/history/airport/WMSA/2016/3/18/DailyHistory.html?req_city=&req_state=&req_statename=&reqdb.zip=&reqdb.magic=&reqdb.wmo= [Accessed March 16, 2018].
- Wilby, R.L., 2003. Past and projected trends in London ' s urban heat island. , 58(August 1999), pp.251–260.
- Yusuf, Y.A., Pradhan, B. & Idrees, M.O., 2014. Spatio-temporal Assessment of Urban Heat Island Effects in Kuala Lumpur Metropolitan City Using Landsat Images. *Journal of the Indian Society of Remote Sensing*, 42(December), pp.829–837.
- Ziehn, T. & Tomlin, a. S., 2008. Global sensitivity analysis of a 3D street canyon model—Part I: The development of high dimensional model representations. *Atmospheric Environment*, 42(8), pp.1857–1873. Available at:
<http://linkinghub.elsevier.com/retrieve/pii/S1352231007010643> [Accessed March 30, 2014].

APPENDICES

Appendix A.1

Google Sketchup Pro is a user-friendly 3D modelling computer program that has been widely used for different applications (i.e. architecture, urban spaces and engineering) and has the function to import and export common 2D and 3D formats. To create the geometry of an urban street canyon within a fluid domain, an outer shell (to be known as enclosure) of the airflow volume should be built with two solid buildings. However, only the inflow and outflow planes require no enclosure; see Figure A.1. 1.

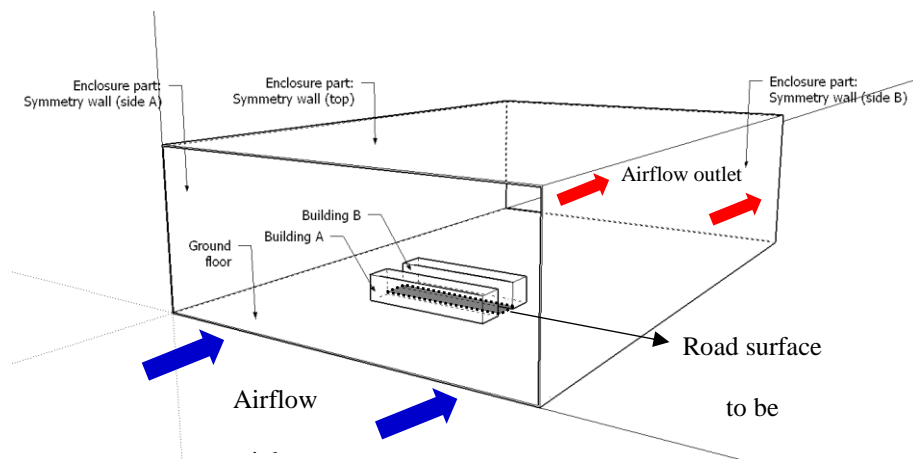


Figure A.1. 1 Creation of geometry of macro domain consisting enclosure and buildings in Google Sketchup Pro

In Google Sketchup Pro, a plane or a surface that is extruded will automatically become a solid. To ensure that the export of the 3D component from Google Sketchup Pro is successful, all solid components (enclosure and buildings) and surfaces should be exploded. This is due to most CAD programs have dissimilarity in interpreting solid components from other 3D modelling programs. Thus, the explosion of solid components

and surfaces is required before the information of 3D Sketchup file (.skp file) can be transferred into the 3D Autodesk Education AutoCAD drawing file, to be known as .dwg file. The .dwg file is a proprietary binary file format that stores the information of 2D and 3D design data and metadata. This means, the model configuration of the airflow domain with enclosure and buildings built in Google Sketchup Pro is still be kept as original in .dwg file before this file is exported into Initial Graphics Exchange Specification (IGES), a compatible geometry file which can be opened in ANSYS 15.0 Academic Research DesignModeler.

IGES file or .iges file is a neutral file format that is used to transfer the 2D and 3D drawing data between dissimilar CAD systems; in this case between Google Sketchup Pro and Autodesk AutoCAD. IGES however, has the limitation in translating all entities in .dwg file as per the original .skp file. During the processing of IGES file in ANSYS DesignModeler, unnecessary lines at the whole domain body were generated which caused one face was divided in several number of faces. In ANSYS DesignModeler, 'Body Operation' was used to clean the unnecessary lines and to simplify the domain from multiple bodies to one body; see Figure A.1. 2.

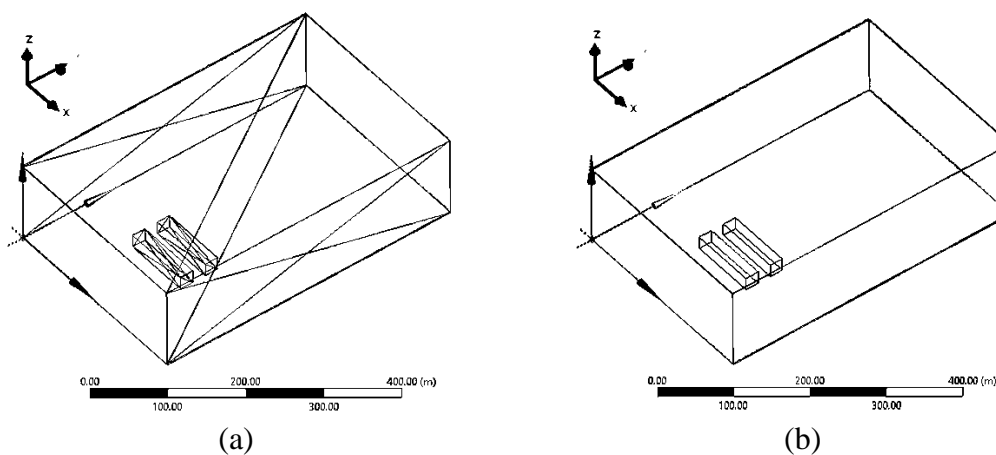


Figure A.1. 2 Comparison of the domain geometry (a) before 'body operation' tool was used, and (b) after 'body operation' tool was used

The enclosure body of the domain should be disappeared to create fluid body which contains air for the simulation of an urban environment. Before using ‘Fill’ tool to discard the enclosure body, two inlet and outlet surfaces had to be created to establish the airflow body. It should be noted that the two solid buildings also were automatically subtracted from the domain to ensure the analysis is simplified only based on the fluid flow and the shape of street canyon without additional influences from the interior of the buildings. Furthermore, this study did not account for the effects of building interiors to the air and surface temperatures within the domain. Figure A.1. 3(a) and Figure A.1. 3(b) show the disappearance of the enclosure body before and after ‘Fill’ tool was used meanwhile Figure A1.3(c) shows the selected ground surface with the subtracted building floors.

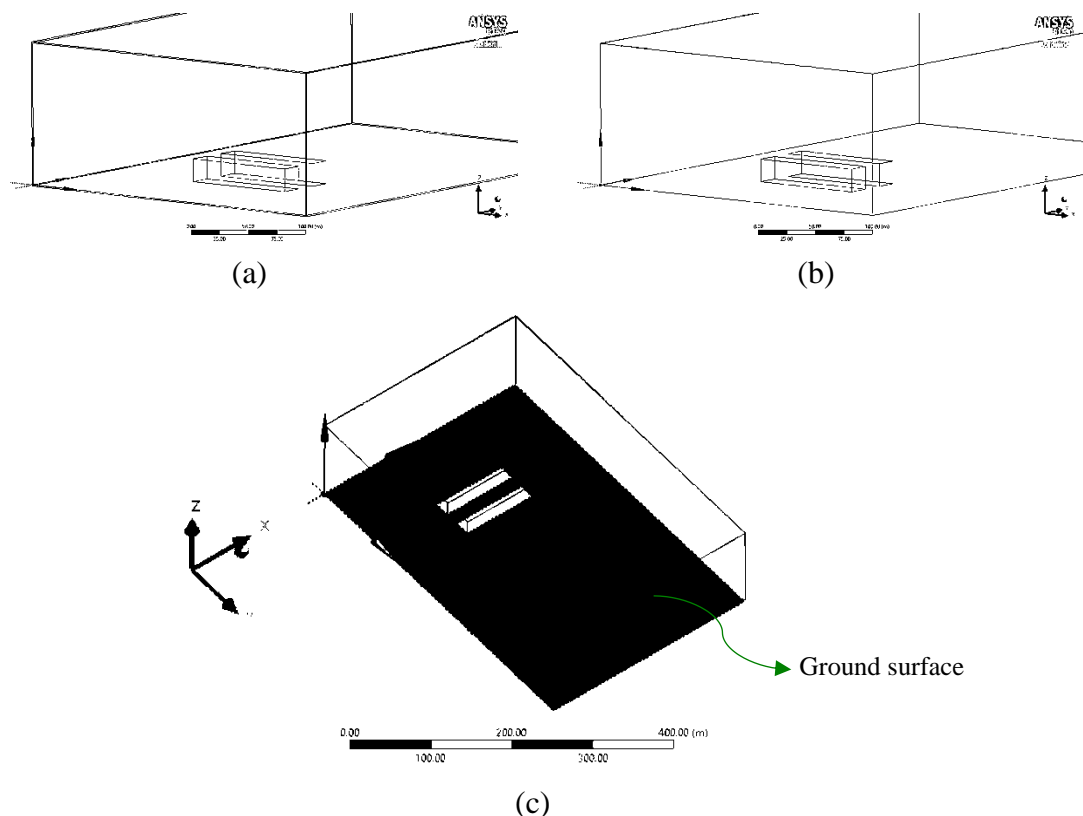


Figure A.1. 3 Comparison of the macro domain (a) before creation of inlet-outlet faces and using ‘fill’ tool (b) disappearance enclosure solid and building interiors. Effect of subtraction of building floors from the ground surface is shown in (c)

Appendix A.2

Based on Figure 4.15 in Chapter 4; slicing on the volume of macro domain was carried out based on: (i) buildings' rooftop wall became the reference plane for separating the above rooftop region and the below rooftop region; (ii) the buildings' side walls (opposing symmetry walls) became the reference plane for separating the regions without blockage (without buildings) and the region with blockage (with buildings); (iii) the buildings' walls across its length (opposing inlet plane and outlet plane) became the reference plane to separate the upstream region (towards inlet plane) and the downstream region (towards outlet plane); and (iv) additional slicing was done to separate the region consists of street canyon with the region consists of buildings. Figure A.2. 1 shows the plan, sectional elevation and 3D vies of structured mesh for AR 1.

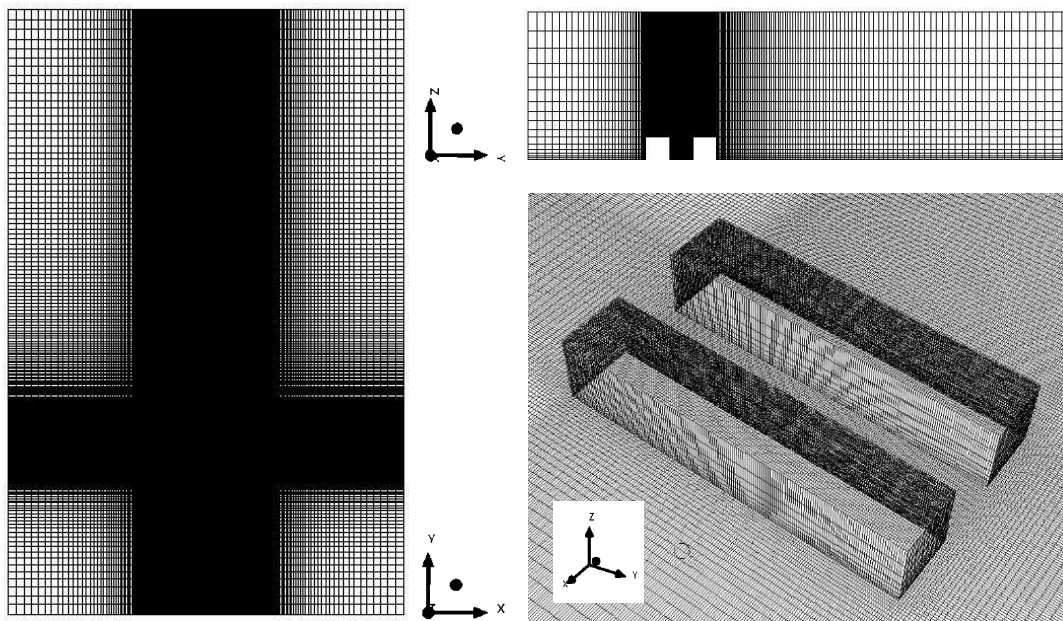


Figure A.2. 1 Plan, sectional elevation and 3D view of structured mesh for AR 1

In total, 28 sliced bodies were produced using slicing tool in ANSYS DesignModeler and the bodies excluded the interior volume of the two buildings. By using slicing tool, similar edge sizing can be created for the bodies with similar height. This becomes the opportunity to set bias on the size of the edge to refine cells at necessary regions, leaving other cells in larger size so that excessive time consumed for the computation can be avoided. Figure A.2. 2 highlights edge sizing and inflated mesh generation for macro domains with asymmetrical height.

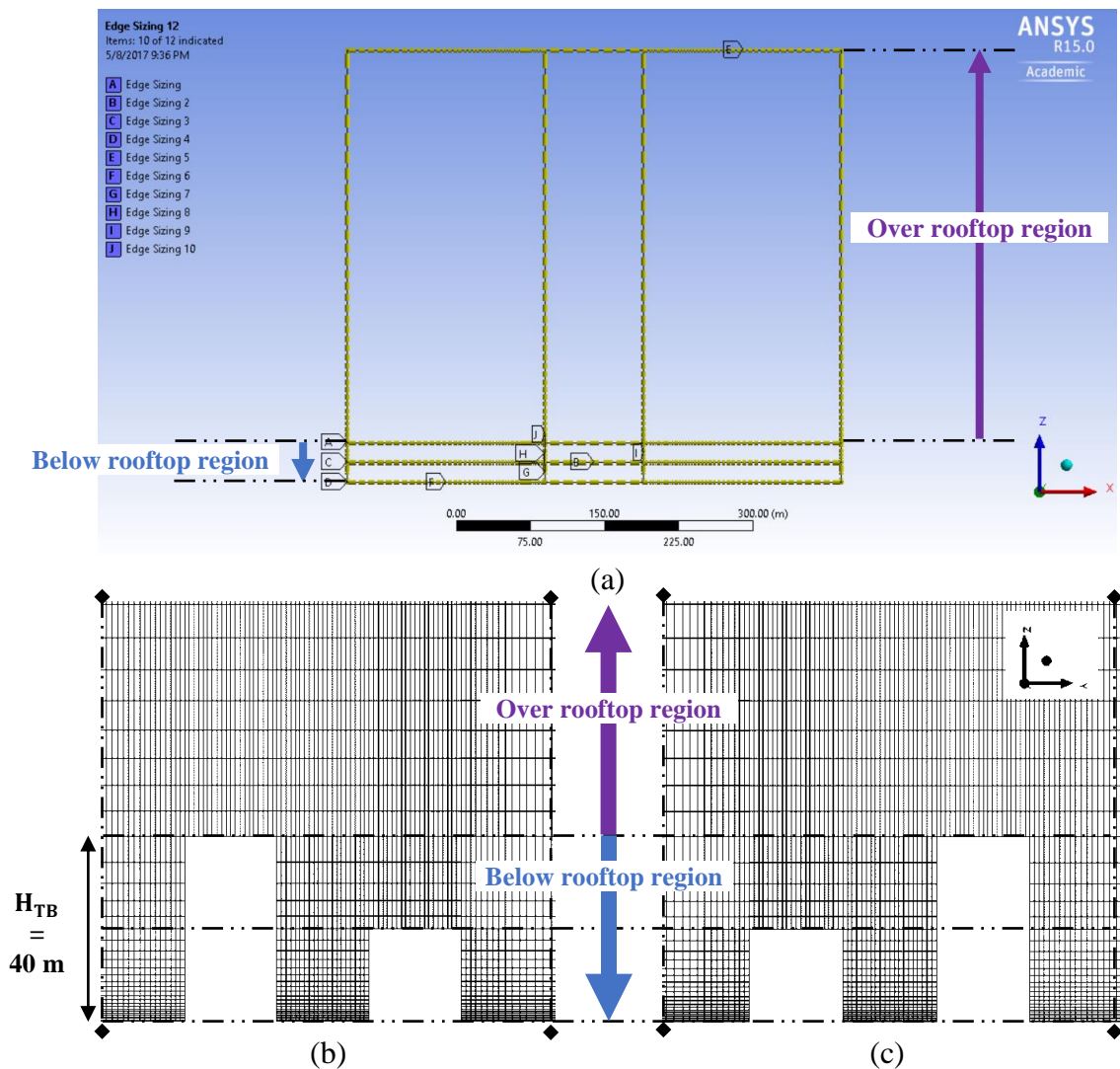


Figure A.2. 2 Bias setting for edge sizing helps to (a) distinguish the cell size according to the study priority i.e. fine cells were generated closer to street canyon ground and building walls (b) generate structured mesh for asymmetrical street canyon Type 1 (c) asymmetrical street canyon Type 2

The slicing technique, edge sizing and bias were similarly applied on other macro domain geometries (asymmetrical canyon height and different aspect ratios); however, the sizing and bias values were set different depending on the configuration of the buildings (due to different height) and the size of the domain (for the case of $H = H_{TB}$). For the canyon aspect ratio with more than 1 (AR 2, 3 and 4), the domain region below rooftop level was sliced every 20 m height until it reached the rooftop level. As shown in Figure A.2. 2, the tallest building height within the domain was 40 m, thus the rooftop walls for the shortest building height (20 m) became the reference to divide the volume at that height in equal. The reason of slicing the building height in every 20 m was to ensure the refinement in the cell size generated for the street canyon including building walls below rooftop region.

Appendix A.3

Based on Figure 4.18 in Chapter 4, the pipe body was forced with 0.02 m (20 mm) for the sizing of the cell, which means every edge of the cell became 0.02 m (20 mm). Additional sizing was determined for the pavement body. The length of the pavement, 10 m was divided into 2000 elements; forcing the edge of one cell to be 0.005 m (5 mm). The Automatic Meshing Method has successfully generated the micro domain with major hexahedral mesh for the upper and lower layers of the pavement body meanwhile smaller cell size was generated closer to the pipe body.

Similar meshing technique was applied on the micro domain with four pipes of Type STP and Type SPP as per the setting for the micro domain with one pipe. However, both types were divided into three sub-volumes where the centre pipe embedment region was separated from the upper and below pavement layers. Hard behaviour was set for the edge sizing of pavement body meanwhile the edge sizing for the centre region was set with soft behaviour to allow the influence of the mesh of pipe body over the centre region. Following the setting made for RPSC domain with one pipe, the cells of pipe bodies of Type STP and Type SPP were forced to size in 0.02 m (20 mm), ensuring the cells generated for the pipes are finer as compared to the cells generated for the pavement body.

Appendix A.4

Data regarding the weather station and average relative humidity and air temperature values was obtained from Weather Underground, a commercial weather service which provides worldwide data coverage of real-time forecast and history weather information via the internet using BestForecast™ system. BestForecast™ system of Weather Underground has the spatial resolution of 4 KM grid or one forecast every 4 KM, which means it performs 36 % more forecasts than NWS system. Temporal resolution of the system is updated every 15 minutes with hourly forecast generation frequency.

Source: <https://www.wunderground.com/about/data>

Retrieved by: 08/11/2107

Appendix A.5

Table A.5. 1 Ambient air temperature for the month of August 2015

Wind speed data in August 2015 from Petaling Jaya Station (3° 06' 07" N, 101° 38' 42" E) at level 58.6 m						
09:00	10:00	11:00	12:00	13:00	14:00	15:00
4th August 2015						
24 °C (297 K)	26 °C (299 K)	28 °C (301 K)	30 °C (303 K)	31 °C (304 K)	31 °C (304 K)	32 °C (305 K)
Mean temperature: 27 °C / 300 K						
6th August 2015						
27 °C (300 K)	27 °C (300 K)	25 °C (298 K)	26 °C (297 K)	27 °C (300 K)	29 °C (302 K)	30 °C (303 K)
Mean temperature: 28 °C / 301 K						
8th August 2015						
28 °C (301 K)	29 °C (302 K)	30 °C (303 K)	31 °C (304 K)	32 °C (305 K)	32 °C (305 K)	33 °C (306 K)
Mean temperature: 30 °C / 303 K						
10th August 2015						
31 °C (304 K)	31 °C (304 K)	31 °C (304 K)	31 °C (304 K)	31 °C (304 K)	31 °C (304 K)	32 °C (305 K)
Mean temperature: 29 °C / 302 K						
12th August 2015						
27 °C (300 K)	29 °C (302 K)	30 °C (303 K)	31 °C (304 K)	32 °C (305 K)	33 °C (306 K)	34 °C (307 K)
Mean temperature: 29 °C / 302 K						
14th August 2015						
27 °C (300 K)	28 °C (301 K)	30 °C (303 K)	31 °C (304 K)	32 °C (305 K)	32 °C (305 K)	31 °C (305 K)
Mean temperature: 29 °C / 302 K						
* Wind direction & speed were retrieved from: Malaysia Meteorological Department						

Table A.5. 2 Ambient air temperature for the month of March 2016

Wind speed data in March 2016 from Sultan Abdul Aziz Airport (3.13 °N 101.55 °E)						
09:00	10:00	11:00	12:00	13:00	14:00	15:00
7th March 2016						
29 °C (302 K)	30 °C (303 K)	31 °C (304 K)	32 °C (305 K)	34 °C (307 K)	35 °C (308 K)	36 °C (309 K)
Mean temperature: 31 °C / 304 K						
9th March 2016						
27 °C (300 K)	30 °C (303 K)	31 °C (304 K)	33 °C (306 K)	33 °C (306 K)	35 °C (308 K)	34 °C (307 K)
Mean temperature: 30 °C / 303 K						
11th March 2016						
29 °C (302 K)	31 °C (304 K)	32 °C (305 K)	33 °C (306 K)	34 °C (307 K)	34 °C (307 K)	34 °C (307 K)
Mean temperature: 30 °C / 303 K						
14th March 2016						
28 °C (301 K)	30 °C (303 K)	32 °C (305 K)	33 °C (306 K)	33 °C (306 K)	31 °C (304 K)	28 °C (301 K)
Mean temperature: 29 °C / 302 K						
16th March 2016						
27 °C (300 K)	29 °C (302 K)	31 °C (304 K)	32 °C (305 K)	32 °C (305 K)	33 °C (306 K)	32 °C (305 K)
Mean temperature: 29 °C / 302 K						
18th March 2016						
29 °C (302 K)	30 °C (303 K)	32 °C (305 K)	33 °C (306 K)	34 °C (307 K)	34 °C (307 K)	33 °C (306 K)
Mean temperature: 30 °C / 303 K						
* Wind direction & speed were retrieved from: Sultan Abdul Aziz Airport-Subang;						
07 th March 2016 - (WeatherUnderground 2016b)			14 th March 2016 - (WeatherUnderground 2016e)			
09 th March 2016 - (WeatherUnderground 2016c)			16 th March 2016 - (WeatherUnderground 2016f)			
11 th March 2016 - (WeatherUnderground 2016d)			18 th March 2016 - (WeatherUnderground 2016g)			

Table A.5. 3 Wind speed data and direction for the month of August 2015

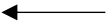

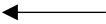




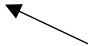







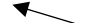
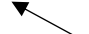







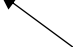









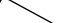

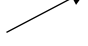

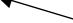



Wind speed data in August 2015 from Petaling Jaya Station (3° 06' 07" N, 101° 38' 42" E) at level 58.6 m						
09:00	10:00	11:00	12:00	13:00	14:00	15:00
4th August 2015						
 90 ° 0.9 m/s	 70 ° 1.2 m/s	 90 ° 1.5 m/s	 150 ° 1.7 m/s	 200 ° 2.0 m/s	 190 ° 1.6 m/s	 220 ° 1.9 m/s
6th August 2015						
 120 ° 2.1 m/s	 130 ° 0.8 m/s	 240 ° 1.7 m/s	 200 ° 1.3 m/s	 230 ° 1.7 m/s	 170 ° 1.4 m/s	 140 ° 2.5 m/s
8th August 2015						
 110 ° 1.5 m/s	 120 ° 2.6 m/s	 130 ° 2.0 m/s	 150 ° 1.6 m/s	 140 ° 2.0 m/s	 190 ° 2.0 m/s	 220 ° 2.3 m/s
10th August 2015						
 110 ° 0.9 m/s	 110 ° 0.7 m/s	 130 ° 2.2 m/s	 140 ° 2.2 m/s	 150 ° 2.0 m/s	 140 ° 2.7 m/s	 140 ° 2.4 m/s
12th August 2015						
 100 ° 1.5 m/s	 70 ° 2.0 m/s	 50 ° 0.9 m/s	 180 ° 1 m/s	 230 ° 1.4 m/s	 190 ° 1.0 m/s	 130 ° 1.6 m/s
14th August 2015						
 240 ° 1.1 m/s	 250 ° 2.3 m/s	 190 ° 1.2 m/s	 120 ° 1.3 m/s	 170 ° 2.0 m/s	 230 ° 1.8 m/s	 250 ° 4.3 m/s
* Wind direction & speed were retrieved from: Malaysia Meteorological Department						

Table A.5. 4 Wind speed data and direction for the month of March 2016



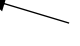
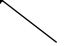




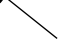
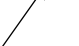
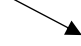

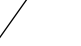
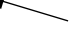
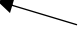

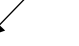

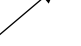

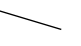


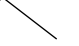
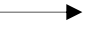
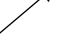
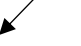
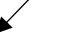
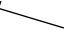
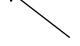


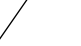

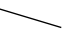

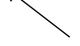
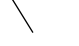

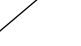

Wind speed data in August 2015 from Sultan Abdul Aziz Airport (3.13 °N 101.55 °E)						
7th March 2016						
09:00	10:00	11:00	12:00	13:00	14:00	15:00
 157.5 ° 0.5 m/s	 180 ° 1.5 m/s	 112.5 ° 1.5 m/s	 135 ° 1.5 m/s	 90 ° 2.1 m/s	 225 ° 1.5 m/s	 90 ° 2.1 m/s
9th March 2016						
(Calm) (Calm)	 45 ° 1.0 m/s	 135 ° 1.5 m/s	 225 ° 2.1 m/s	 292.5 ° 2.1 m/s	 180 ° 4.1 m/s	 225 ° 4.1 m/s
11th March 2016						
 112.5 ° 1.5 m/s	 112.5 ° 1.5 m/s	 180 ° 1.5 m/s	 45 ° 0.5 m/s	 180 ° 2.1 m/s	 247.5 ° 2.6 m/s	 225 ° 4.6 m/s
14th March 2016						
 112.5 ° 0.5 m/s	 157.5 ° 1.0 m/s	 157.5 ° 1.0 m/s	 135 ° 1.5 m/s	 270 ° 4.1 m/s	 247.5 ° 3.6 m/s	 45 ° 3.1 m/s
16th March 2016						
 45 ° 0.5 m/s	 112.5 ° 1.0 m/s	 135 ° 1.5 m/s	 180 ° 2.1 m/s	 157.5 ° 1.5 m/s	 225 ° 1.5 m/s	 180 ° 3.1 m/s
18th March 2016						
 112.5 ° 1.0 m/s	 90 ° 1.0 m/s	 135 ° 2.1 m/s	 157.5 ° 2.1 m/s	 225 ° 2.6 m/s	 247.5 ° 3.1 m/s	 202.5 ° 5.1 m/s
* Wind direction & speed were retrieved from: Sultan Abdul Aziz Airport-Subang;						
07 th March 2016 - (WeatherUnderground 2016b)			14 th March 2016 - (WeatherUnderground 2016e)			
09 th March 2016 - (WeatherUnderground 2016c)			16 th March 2016 - (WeatherUnderground 2016f)			
11 th March 2016 - (WeatherUnderground 2016d)			18 th March 2016 - (WeatherUnderground 2016g)			

Table A.5. 5 Cloud cover condition for the month of August 2015

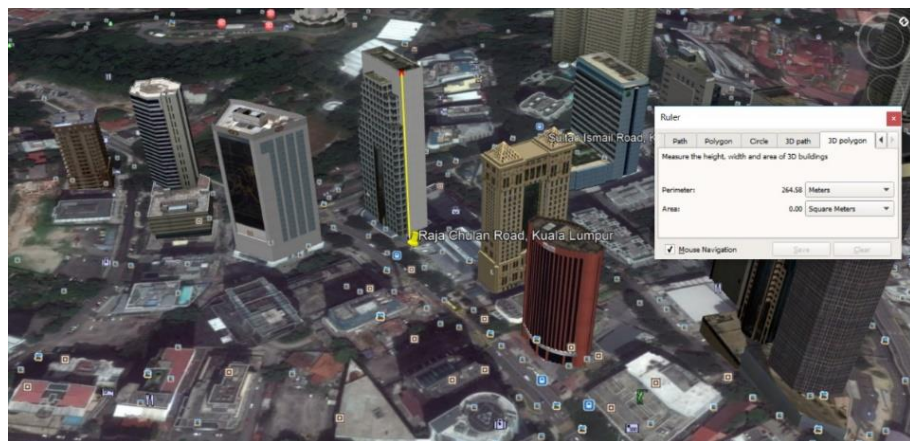
Wind speed data in August 2015						
from Petaling Jaya Station (3° 06' 07" N, 101° 38' 42" E) at level 58.6 m						
09:00	10:00	11:00	12:00	13:00	14:00	15:00
4th August 2015						
7 oktas Most Cloudy 70-87 %	7 oktas Most Cloudy 70-87 %	7 oktas Most Cloudy 70-87 %	7 oktas Most Cloudy 70-87 %	7 oktas Most Cloudy 70-87 %	7 oktas Most Cloudy 70-87 %	7 oktas Most Cloudy 70-87 %
6th August 2015						
7 oktas Light Rain Showers 70-87 %	7 oktas Light Rain Showers 70-87 %	7 oktas Most Cloudy 70-87 %	7 oktas Most Cloudy 70-87 %	7 oktas Most Cloudy 70-87 %	7 oktas Most Cloudy 70-87 %	7 oktas Most Cloudy 70-87 %
8th August 2015						
7 oktas Most Cloudy 70-87 %	7 oktas Most Cloudy 70-87 %	7 oktas Most Cloudy 70-87 %	7 oktas Most Cloudy 70-87 %	7 oktas Most Cloudy 70-87 %	7 oktas Most Cloudy 70-87 %	7 oktas Most Cloudy 70-87 %
10th August 2015						
7 oktas Most Cloudy 70-87 %	7 oktas Most Cloudy 70-87 %	7 oktas Most Cloudy 70-87 %	7 oktas Most Cloudy 70-87 %	7 oktas Most Cloudy 70-87 %	7 oktas Most Cloudy 70-87 %	7 oktas Most Cloudy 70-87 %
12th August 2015						
7 oktas Most Cloudy 70-87 %	6 oktas Partly Sunny 51-69 %	6 oktas Partly Sunny 51-69 %	7 oktas Most Cloudy 70-87 %	7 oktas Most Cloudy 70-87 %	7 oktas Most Cloudy 70-87 %	7 oktas Most Cloudy 70-87 %
14th August 2015						
7 oktas Most Cloudy 70-87 %	7 oktas Most Cloudy 70-87 %	7 oktas Most Cloudy 70-87 %	7 oktas Most Cloudy 70-87 %	7 oktas Most Cloudy 70-87 %	7 oktas Most Cloudy 70-87 %	7 oktas Most Cloudy 70-87 %
* Wind direction & speed were retrieved from: Malaysia Meteorological Department * Determination of 'Cloud Cover' percentage (%) was based on National Weather Service. Retrieved from: https://www.weather.gov/media/pah/ServiceGuide/A-forecast.pdf						

Table A.5. 6 Cloud cover condition for the month of March 2016

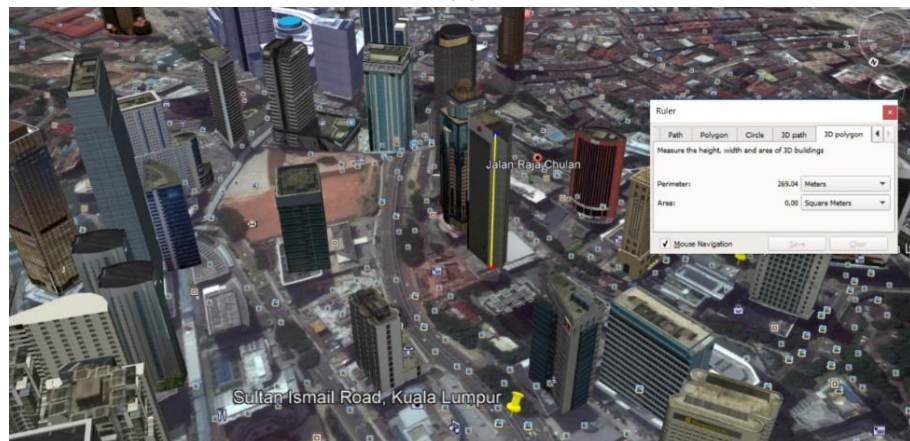
Wind speed data in August 2015 from Sultan Abdul Aziz Airport (3.13 °N 101.55 °E)						
09:00	10:00	11:00	12:00	13:00	14:00	15:00
7th March 2016						
Most Cloudy 70-87 %	Most Cloudy 70-87 %	Most Cloudy 70-87 %	Most Cloudy 70-87 %	Most Cloudy 70-87 %	Most Cloudy 70-87 %	Most Cloudy 70-87 %
9th March 2016						
Most Cloudy 70-87 %	Most Cloudy 70-87 %	Most Cloudy 70-87 %	Most Cloudy 70-87 %	Most Cloudy 70-87 %	Most Cloudy 70-87 %	Most Cloudy 70-87 %
11th March 2016						
Most Cloudy 70-87 %	Most Cloudy 70-87 %	Most Cloudy 70-87 %	Most Cloudy 70-87 %	Most Cloudy 70-87 %	Most Cloudy 70-87 %	Most Cloudy 70-87 %
14th March 2016						
Haze 70-87 %	Most Cloudy 70-87 %	Most Cloudy 70-87 %	Most Cloudy 70-87 %	Most Cloudy 70-87 %	Light Rain Showers 88-100 %	Rain, Thunder 88-100 %
16th March 2016						
Most Cloudy 70-87 %	Most Cloudy 70-87 %	Most Cloudy 70-87 %	Most Cloudy 70-87 %	Most Cloudy 70-87 %	Most Cloudy 70-87 %	Most Cloudy 70-87 %
18th March 2016						
Most Cloudy 70-87 %	Most Cloudy 70-87 %	Most Cloudy 70-87 %	Most Cloudy 70-87 %	Most Cloudy 70-87 %	Most Cloudy 70-87 %	Most Cloudy 70-87 %
<p>* Wind direction & speed were retrieved from: Sultan Abdul Aziz Airport-Subang;</p> <p>07th March 2016 - (WeatherUnderground 2016b) 14th March 2016 - (WeatherUnderground 2016e) 09th March 2016 - (WeatherUnderground 2016c) 16th March 2016 - (WeatherUnderground 2016f) 11th March 2016 - (WeatherUnderground 2016d) 18th March 2016 - (WeatherUnderground 2016g)</p> <p>* Determination of 'Cloud Cover' percentage (%) was based on National Weather Service. Retrieved from: https://www.weather.gov/media/pah/ServiceGuide/A-forecast.pdf</p>						

Appendix A.6

In determining the exact height of the buildings, Google Earth Pro was referred as the system is updated with mostly information of 3D buildings and terrains. An exact dimension according to the satellite map is available in Google Earth Pro, allowing the measurement of length, width, building height, and surface area with exact dimension. For the building height that is not available in the application, rough estimation based on cross-sectional elevation as described in the previous Figure 5.4 was determined. Figure A.6. 1(a) and Figure A.6. 1(b) show the terrains of ROAD 1 and ROAD 2, respectively.



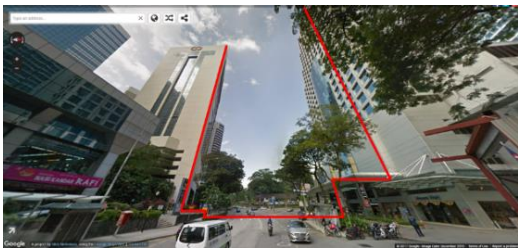
(b)



(a)

Figure A.6. 1 3D terrains with the information of building height and road width for
(a) ROAD 1 (b) ROAD 2

Appendix A.7



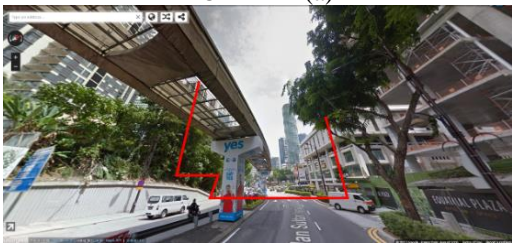
ROAD 1 – (a)



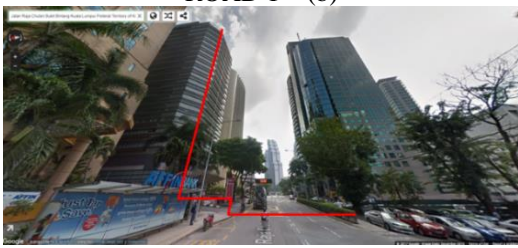
ROAD 2 – (a)



ROAD 1 – (b)



ROAD 2 – (b)



ROAD 1 – (c)



ROAD 2 – (c)



ROAD 1 – (d)



ROAD 2 – (d)



ROAD 1 – (e)



ROAD 2 – (e)



ROAD 1 – (f)



ROAD 2 – (f)

Figure A.7. 1 Cross-sectional elevation as per described in Figure 5.4

Appendix A.8

Compilation of thermal infrared images based on hourly basis was based on the files and documents labelled as below which is available in the supplementary materials of the thesis:

ROAD 1 – AUGUST 2015

- DATA COLLECTION ON 4TH AUGUST 2015
 - Every hour basis, 09:00 – 15:00
- DATA COLLECTION ON 6TH AUGUST 2015
 - 09:00 – 15:00
 - Every hour basis, 09:00 – 15:00
- DATA COLLECTION ON 8TH AUGUST 2015
 - 09:00 – 15:00
 - Every hour basis, 09:00 – 15:00

ROAD 1 – MARCH 2016

- DATA COLLECTION ON 07TH MARCH 2016
 - 09:00 – 15:00
- DATA COLLECTION ON 9TH MARCH 2016
 - 09:00 – 15:00
- DATA COLLECTION ON 11TH MARCH 2016
 - 09:00 – 15:00

ROAD 2 – AUGUST 2015

- DATA COLLECTION ON 10TH AUGUST 2015
 - 09:00 – 15:00
- DATA COLLECTION ON 12TH AUGUST 2015
 - 09:00 – 15:00
- DATA COLLECTION ON 14TH AUGUST 2015
 - 09:00 – 15:00

ROAD 2 – MARCH 2016

- DATA COLLECTION ON 14TH MARCH 2016
 - 09:00 – 15:00
- DATA COLLECTION ON 16TH MARCH 2016
 - 09:00 – 15:00
- DATA COLLECTION ON 18TH MARCH 2016
 - 09:00 – 15:00

Appendix A.9

Pico TC-08 is an eight-channel high resolution temperature data logging device developed by Pico Technology with the range of temperature is between -270 °C and 1820 °C. The data logger has the capability to read up to 10 measurements per second and the data can be derived and analysed using an installed PicoLog data logger software before the device is connected to a computer. Example of the device is shown in Figure A.9. 1 below.



Figure A.9. 1 Pico TC-08 data logging device to be connected to PicoLog software installed in a computer by using USB cable.

Source:

<http://www.picotech.com/data-logger/tc-08/thermocouple-data-logger>

<http://www.industrial-needs.com/technical-data/temperature-datalogger-pico-tc-08.htm>

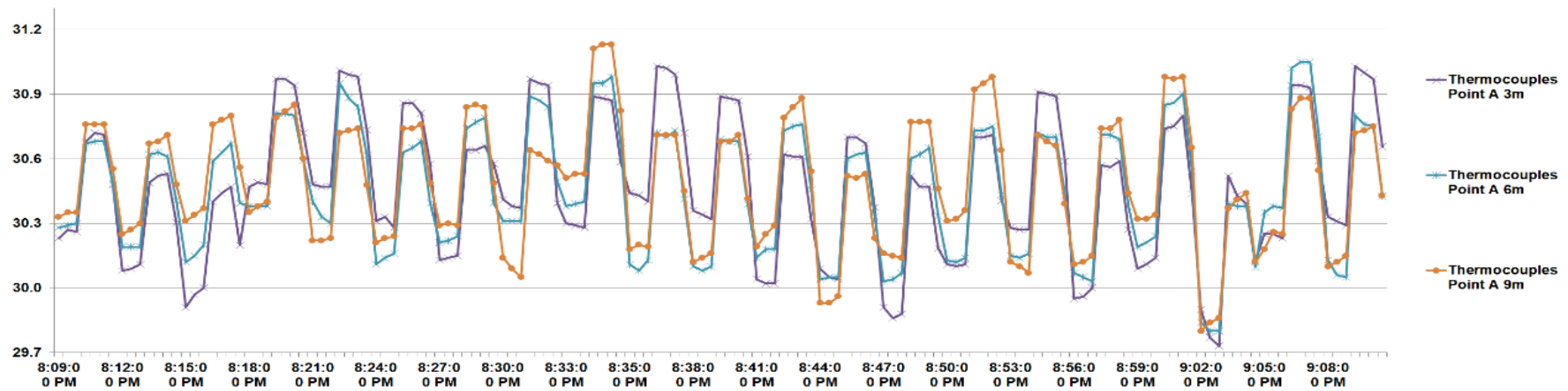
Retrieved by: 08/11/2017

Appendix A.10

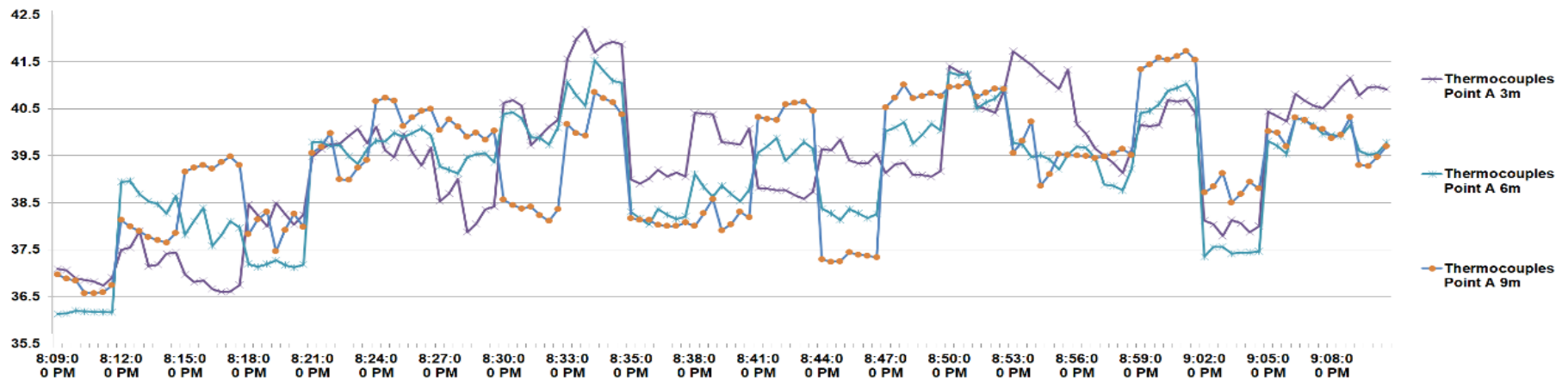
INDOOR CALIBRATION: UNIVERSITY OF SHEFFIELD, UNITED KINGDOM

4 thermocouples Type K were stitched to the sand paper using double-sided tape and to be connected to data logging device and a notebook DELL Precision M4700. Point A and Point B were indicated as the two spots that were used for the comparison of the obtained values with the thermal camera. The calibration work did not start immediately to stabilise the temperature reading for the first 9 minutes or 540 seconds afterward. The first capture of thermal image began at 20:09 pm. The interval time between the first thermal imaging to the second one was 3 minutes or 180 seconds.

For Point A, it was observed that within an hour measurement, the surface temperature did not fluctuate above and below the range between 29.7 °C and 31 °C, showing that the stability of the temperature was achieved before 20:09 pm. For Point B, the stability in the temperature was observed after 20:24 pm, ranged between 36.5 °C and 42 °C. Lower temperature was observed to be obtained by the thermocouple before this time. Figure A.10. 1 shows the obtained surface temperature at Point A and Point B. After obtaining the results from thermal images according to the distance, FLIR ResearchIR was used to ensure the temperature sports captured earlier were at the right location of thermocouples specifically Point A and Point B.

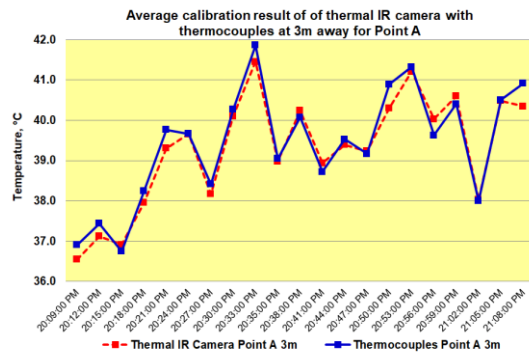


(a)

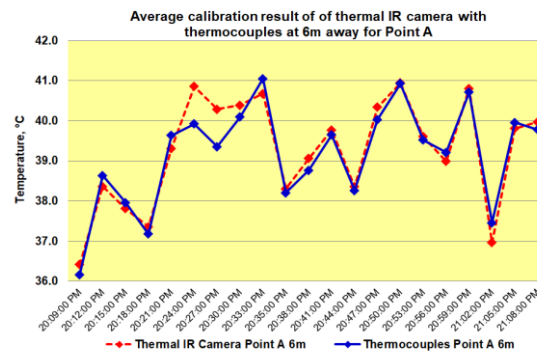


(b)

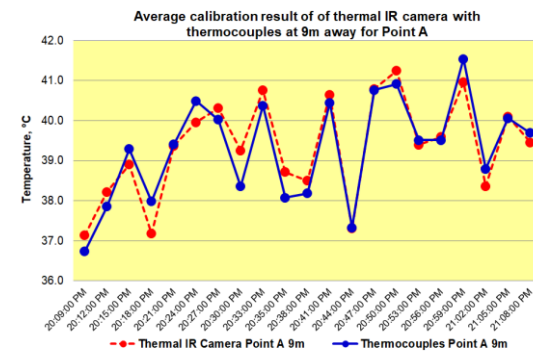
Figure A.10. 1 Temperature results using thermocouples Type K between 20:09 pm and 21:08 pm at (a) Point A (b) Point B



3 m distance

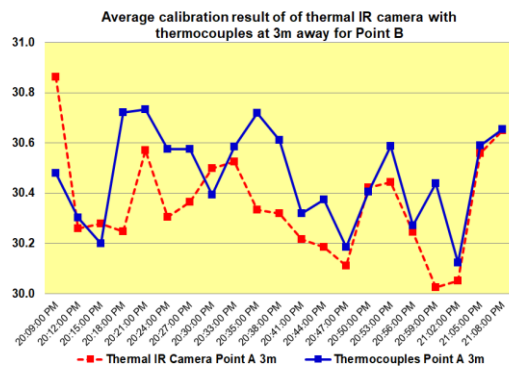


6 m distance

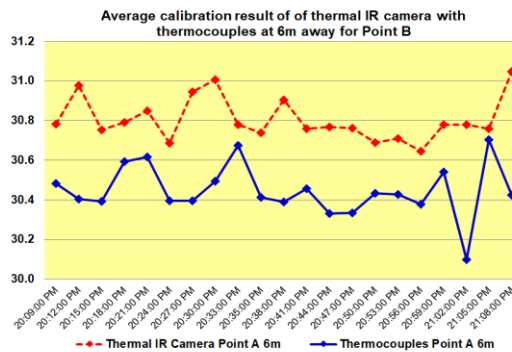


9 m distance

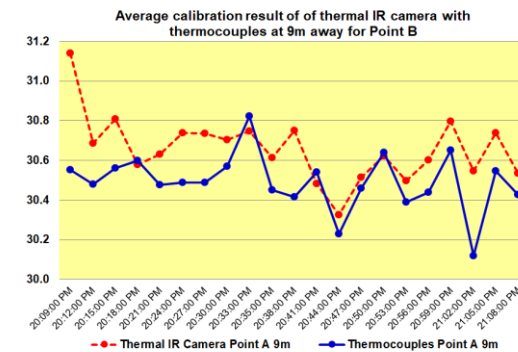
Point A



3 m distance



6 m distance



9 m distance

Point B

Figure A.10. 2 Comparative temperature results obtained by thermocouples and FLIR T650sc infrared thermal camera

In this study, three locations were compared to the results of thermocouple reading: (i) 3 m distance, (ii) 6 m distance, and (iii) 9 m distance from the heated surface. This means, the comparison for 3 m distance was 9 seconds after the measurement began meanwhile for 6 m and 9 m, the temperature values should be obtained at 18th second and 27th second, respectively. The comparative temperature results between thermocouples and FLIR T650sc infrared thermal camera are displayed in Figure A.10. 2.

Based on Figure A.10. 2, it was observed that the temperature values obtained from the camera for Point A have carefully followed the trend obtained from the thermocouple, resulting the temperature values of all measured period and location (3 m, 6 m and 9 m) were comparable to one another. For Point B, it should be highlighted that the trend can be observed satisfied with minimal higher and lower temperatures were obtained by the camera from the results based on thermocouples. Larger difference was observed at Point B, 6 m distance from the heated surface as compared to other locations. Error percentage of FLIR T650sc to the results of thermocouples is displayed in **Figure A.10. 3**.

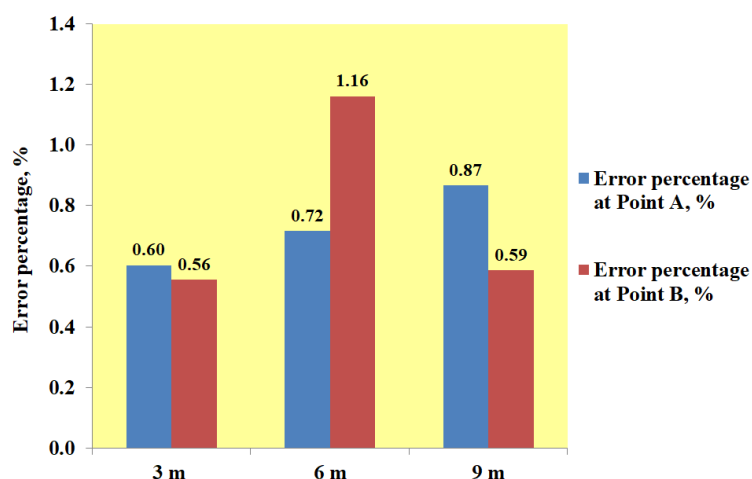


Figure A.10. 3 Percentage of error, % comparing the temperature results of FLIR T650sc thermal camera and thermocouples at Point A and Point B

Figure A.10. 3 satisfied the results shown in Figure A.10. 2, which demonstrating the percentage error for the location afar from the heated surface was still below than 1.2 %. The limitation of this calibration study was the maximum length of the tested room was 10 m. Additionally, the room temperature was controlled from the beginning of the test. For outdoor measurement, it should be highlighted that various parameter will be involved to influence the temperature results. Thus, another calibration involved with outdoor setting were done during hot tropical day on 28th March 2016 in Malaysia.

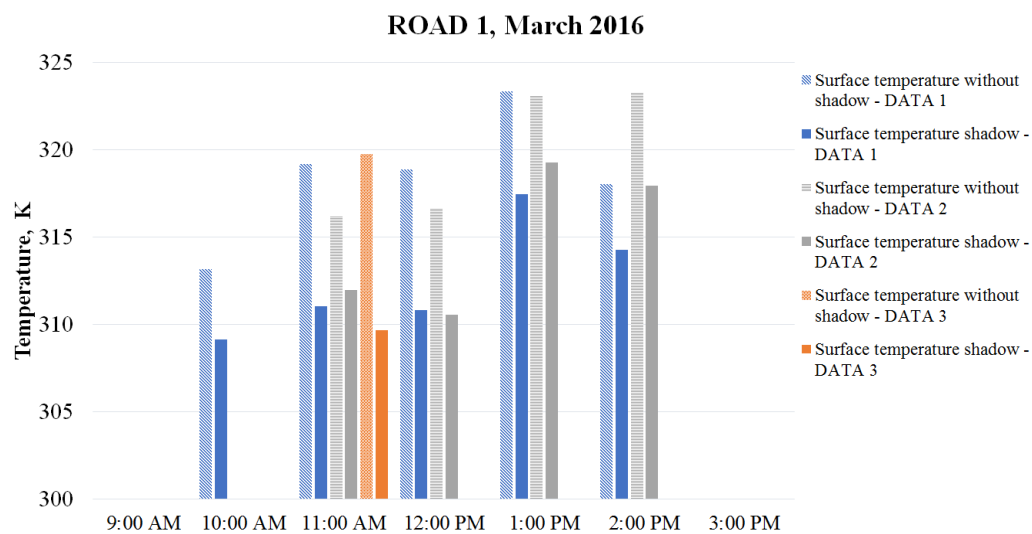
Appendix A.11

OUTDOOR CALIBRATION STUDY IN HOT HUMID CITY, MALAYSIA

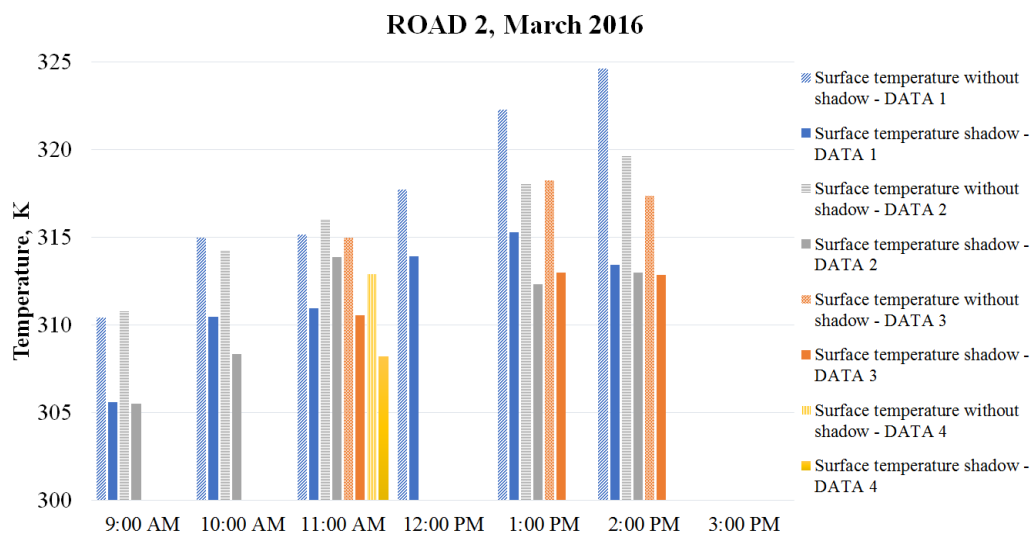
It should be noted that the thermal imaging work had only begun at 13:20 hour and was ended at 14:20 hour due to the instability in the temperature data with significant fluctuation was observed during the first 20 minutes. It was unexpected that within the period of the measurement, strong wind occurred intermittently.

Appendix A.12

Comparison between road surface temperature with and without shadow effect in the street canyon of ROAD 1 and ROAD 2 based on month of March 2016.



(a)



(b)

Figure A.12. 1 Comparison between road surface temperature without shadow and with shadow for (a) ROAD 1 in March 2016 (b) ROAD 2 in March 2016

Appendix A.13

Three cross-sections which were plotted at 120 m, 150 m and 180 m in the x -axis in Figure 6.2 demonstrates the comparison of the air velocity vector in the three plotted sections within the street canyon. Based on all sections in Figure A.13. 1; it was observed that a low air speed closer to the ground of street canyon in urban macro domain mainly due to Building A that acted as the blocking wall against the predominant airflow. In comparing the result of air velocity vectors at the three cross-sections, it was observed with clear air circulation in the section closer to the canyon openings (120 m and 180 m in the x -axis) as the outside airflow contained higher velocity carrying lower temperature, which explains the reduction in the surface temperature closer to the canyon openings as in Figure A.13. 1.

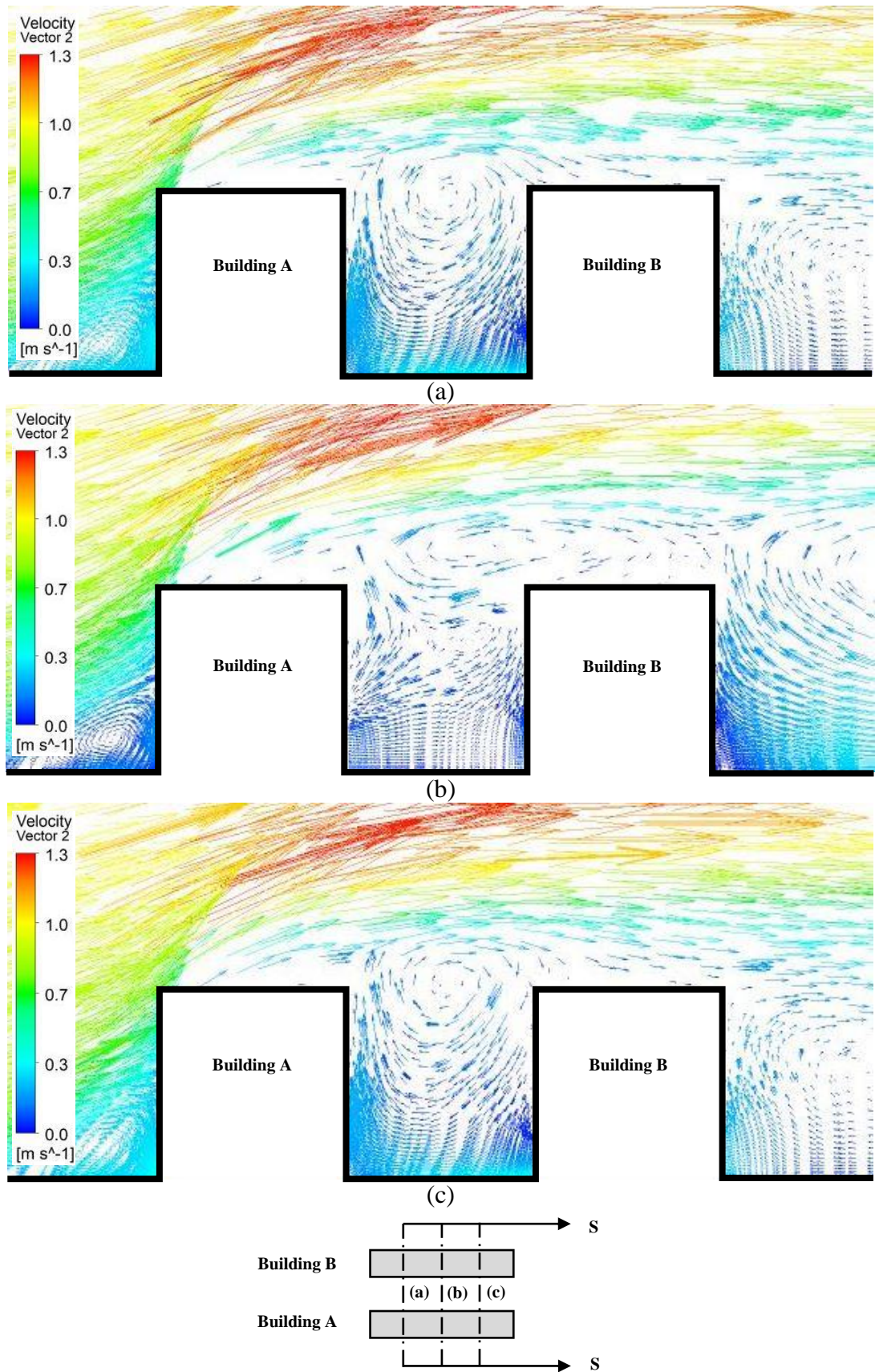


Figure A.13. 1 Air velocity vector at 13:00 hour across street canyon at section S-S
 (a) 120 m in x-axis (b) 150 m in x-axis (c) 180 m in x-axis

Appendix A.14

Further explanation is displayed in Figure A.14. 1 which shows the comparative airflow vector profile for 1 m/s, 2 m/s, 5 m/s and 10 m/s at 150 m in the x -axis. Based on Figure A.14. 1, vortex air rotation was observed to occur within the canyon when higher wind velocity was applied. By applying the highest wind velocity (10 m/s), the highest velocity at the pedestrian level can reach up to 2.2 m/s meanwhile with the lowest wind velocity (1 m/s), the wind velocity at the pedestrian level was less than 0.2 m/s. Effective cooling will be obtained during days with higher wind velocity. With this condition, any cooling device will not be efficient for its application. This means, hydronic RPSC system requires the installation during hot and less windy climate condition to optimise its performance in PTC and STR.

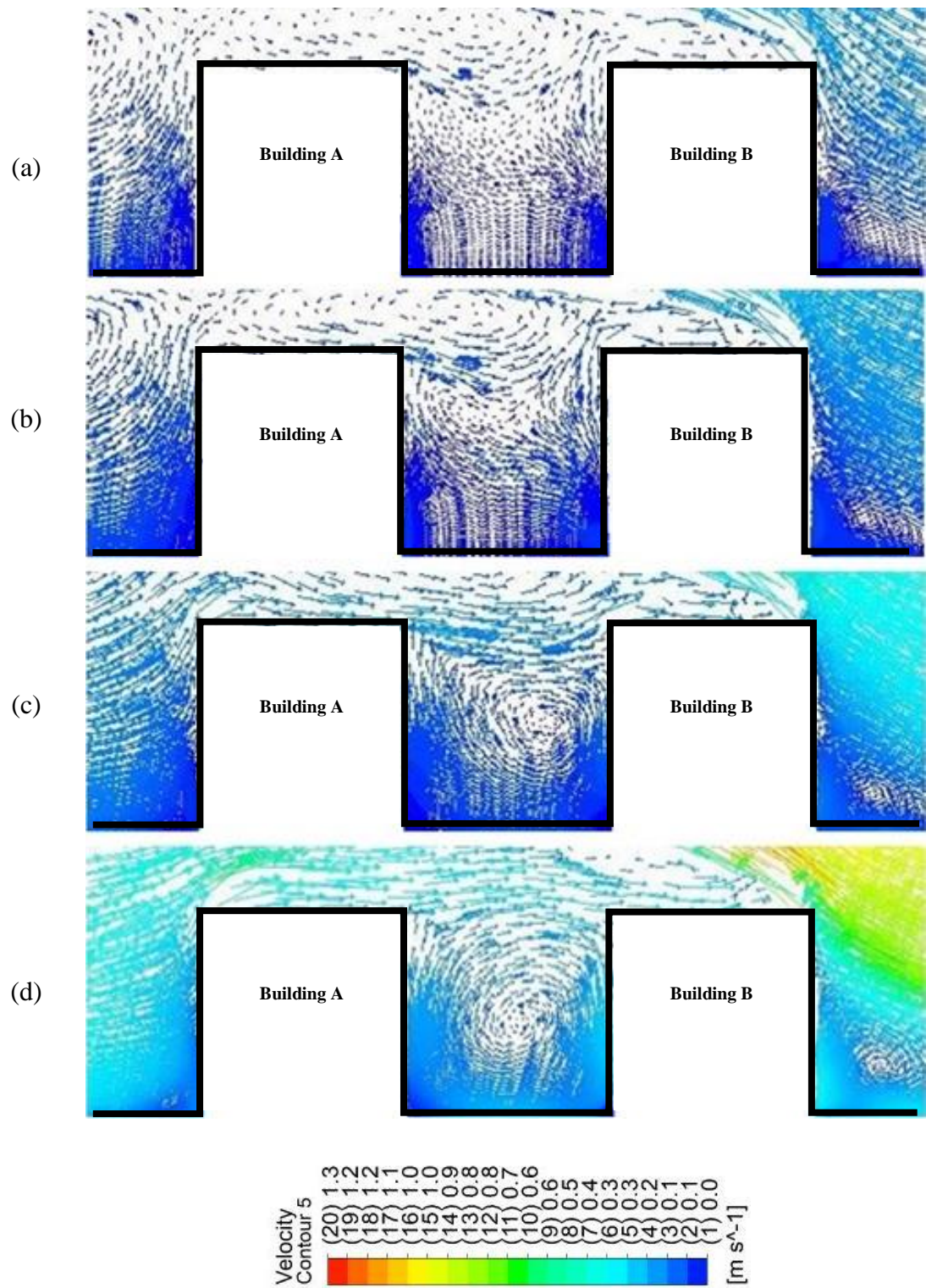


Figure A.14. 1 Cross-sectional plane of velocity vector inside canyon (a) 1 m/s (b) 2 m/s (c) 5 m/s (d) 10 m/s

Appendix A.15

Figure A.15. 1 compares the obtained surface temperature contour according to the seasons. It can be observed that all-seasonal surface temperatures obtained highest temperature at the centre of the canyon area. This can be agreed that the configuration of the canyon with the orientation perpendicular to the predominant wind has strongly affected the development of the temperature contour. In comparing the surface temperature according to the season, the main factor influencing the temperature values of the canyon road surface was the solar position and its irradiance which affect the ambient temperature of the canyon. The lowest temperature obtained during 21st December was due to the low solar irradiance to the surface and vice-versa during 21st June. With this result, it can be agreed that hydronic RPSC system will be mostly efficient during summer days with low wind velocity condition for optimum Delta T, PTC and STR.

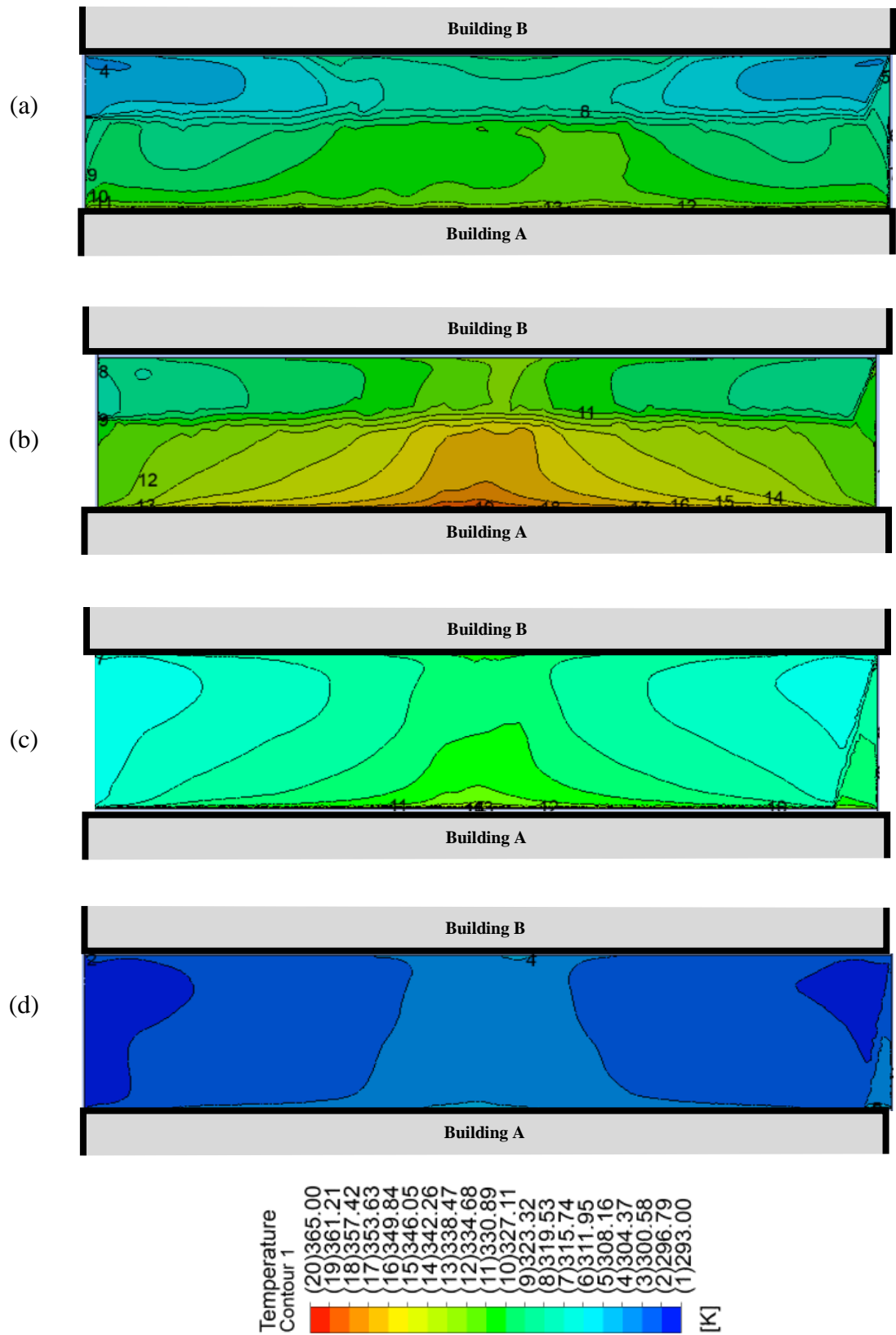
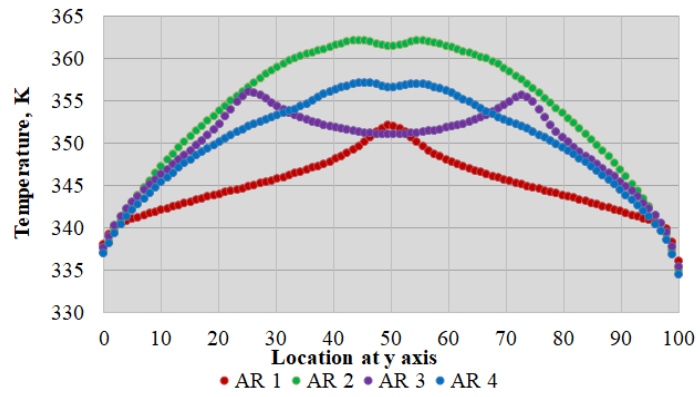


Figure A.15. 1 Urban simulation by factoring season: (a) Spring (b) Summer (c) Autumn (d) Winter

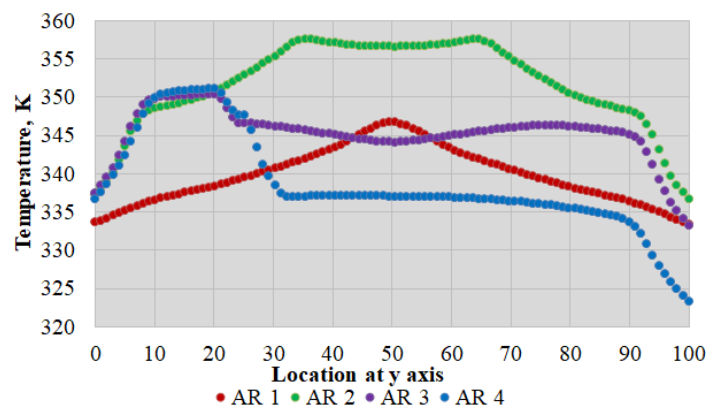
Appendix A.16

Figure A.16. 1(a), Figure A.16. 1(b) and Figure A.16. 1(c) shows the plot of the temperature of road surface across the length of the street canyon (100 m; between 240 m and 340 m location in x -axis) in three locations: (i) C-1 - middle of street canyon, 430 m from inlet plane in y -axis; (ii) A-5 - 1.0 m away from Building A, 421 m from inlet plane in y -axis; and (iii) B-5 - 1 m away from Building B, 439 m from inlet plane in y -axis. Based on Figure A.16. 1, it can be observed that the surface temperature for AR 1 and AR 2 peaked at the middle of the road surface in all plotted locations (C-1, A-5 and B-5) with lower temperature contours closer to the left and right canyon openings.

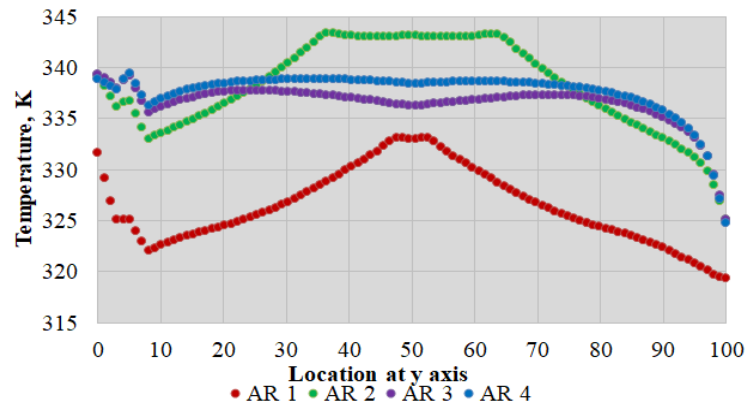
Similarly, for AR 3 and AR 4; a gradual increase in the surface temperature was observed from both openings. For AR 3, a drop in the temperature trend at the middle of the surface was observed. At location A-5, a downward curve trend of the surface temperature occurred between 25 m and 75 m in x -axis. At location C-1 and B-5; with the influence of shadow from Building B, it can be observed that the surface temperature plotted at the middle of the street canyon for AR 3 and AR 4 did not significantly change except for a slight drop between 35 m and 65 m in x -axis. At these locations, an obvious difference in the temperature was found between the surface that obtained direct solar radiation and the surface that obtained shadow from Building B. In comparing the aspect ratio of 1, 2, 3 and 4, it was observed that the road surface of AR 2 absorbed highest temperature at all locations (C-1, A-5 and B-5).



(a)



(b)

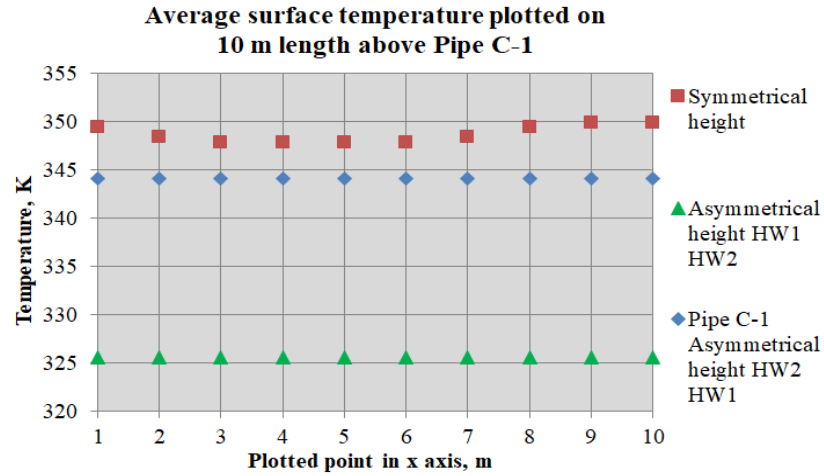


(c)

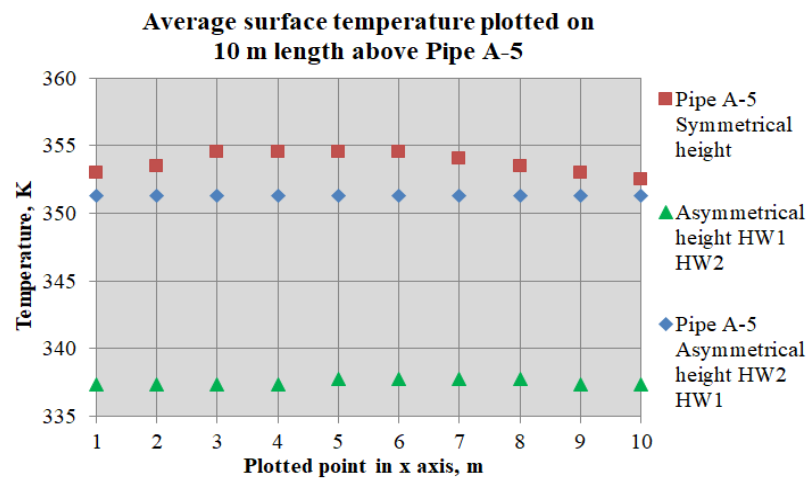
Figure A.16. 1 Plotted temperature across the length of the street canyon surface comparing different location (a) A-5 (b) C-1 (c) B-5

Appendix A.17

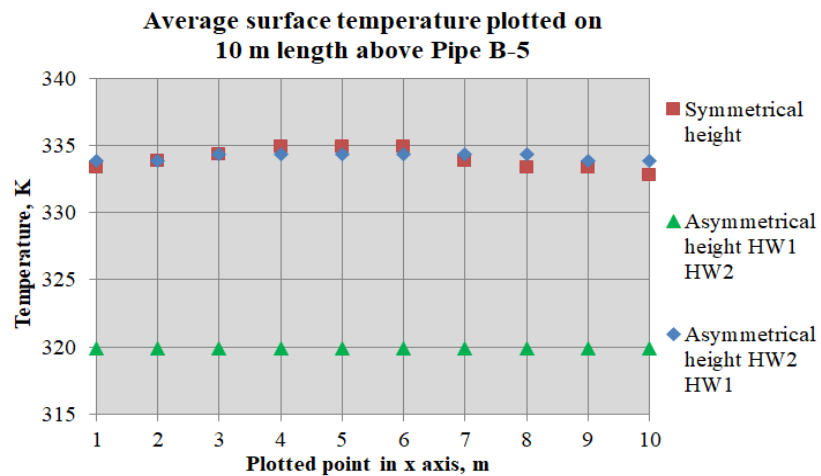
Based on the three locations, 10 temperature points were determined according to every 1 m gap (due to the length of pipe embedment was 10 m, see Chapter 4) and the area-weighted average of the values was obtained for each pipe point. The plotted temperature of 10 temperature points between location 245 m and location 255 m in x -axis is displayed in Figure A.17. 1. Based on Figure A.17. 1, result suggested that the surface temperature of symmetrical canyon height plotted for Pipe C-1 and A-5 was 25.21-43.93 % and 3.15-6.51 % higher than the surface temperature within asymmetrical canyon height Type 1 and asymmetrical canyon height Type 2, respectively. For Pipe B-5, the plotted temperature value has an insignificant 0.3 % higher than the values plotted for symmetrical canyon height and leaving the asymmetrical canyon height Type 1 behind both canyon settings, on average 20.14-23.08 % lower in the temperature values.



(a)



(b)



(c)

Figure A.17. 1 Surface temperature values plotted on 10 points comparing symmetrical canyon height, asymmetrical canyon height Type 1 and asymmetrical canyon height Type 2 at (a) location Pipe C-1 (b) location Pipe A-5 (c) location Pipe B-5

Appendix A.18

Figure A.18. 1 shows the temperature contour of street canyon surface comparing AR 1, 2, 3 and 4 after the application of RPSC system. Based on this figure, a significant reduction in the surface temperature was observed from the heated surface shown in Figure 6.8 of Section 6.1.2.1. For Figure A.18. 1(a), the temperature contour of AR 1 which was classified as (8) has dominated the surface temperature almost 60 %, meanwhile the temperature contour represented the shadow effect from Building B has been increasing from AR 3 to AR 4; see Figure A.18. 1(c) and Figure A.18. 1(d). For AR 2, the temperature contour classified as (10) was clearly observed dominated the centre of the canyon road surface.

Based on the area-weighted average calculated based on the road surface temperature of AR 1, 2, 3 and 4, the aspect ratio 2 has dominated the temperature against other aspect ratios by 8.24 %, 8.1 % and 7.96 % for AR 1, AR 3 and AR 4, respectively. Based on this, it can be observed with nominal difference in the average surface temperature of AR 1, 3 and 4, showing the RPSC performance capabilities within these three aspect ratios were equal. For AR 2, result suggested that the requirement for RPSC to perform at par to other aspect ratio was more than 8 % due to higher obtained temperature within the configuration of double the building height to the width of the canyon.

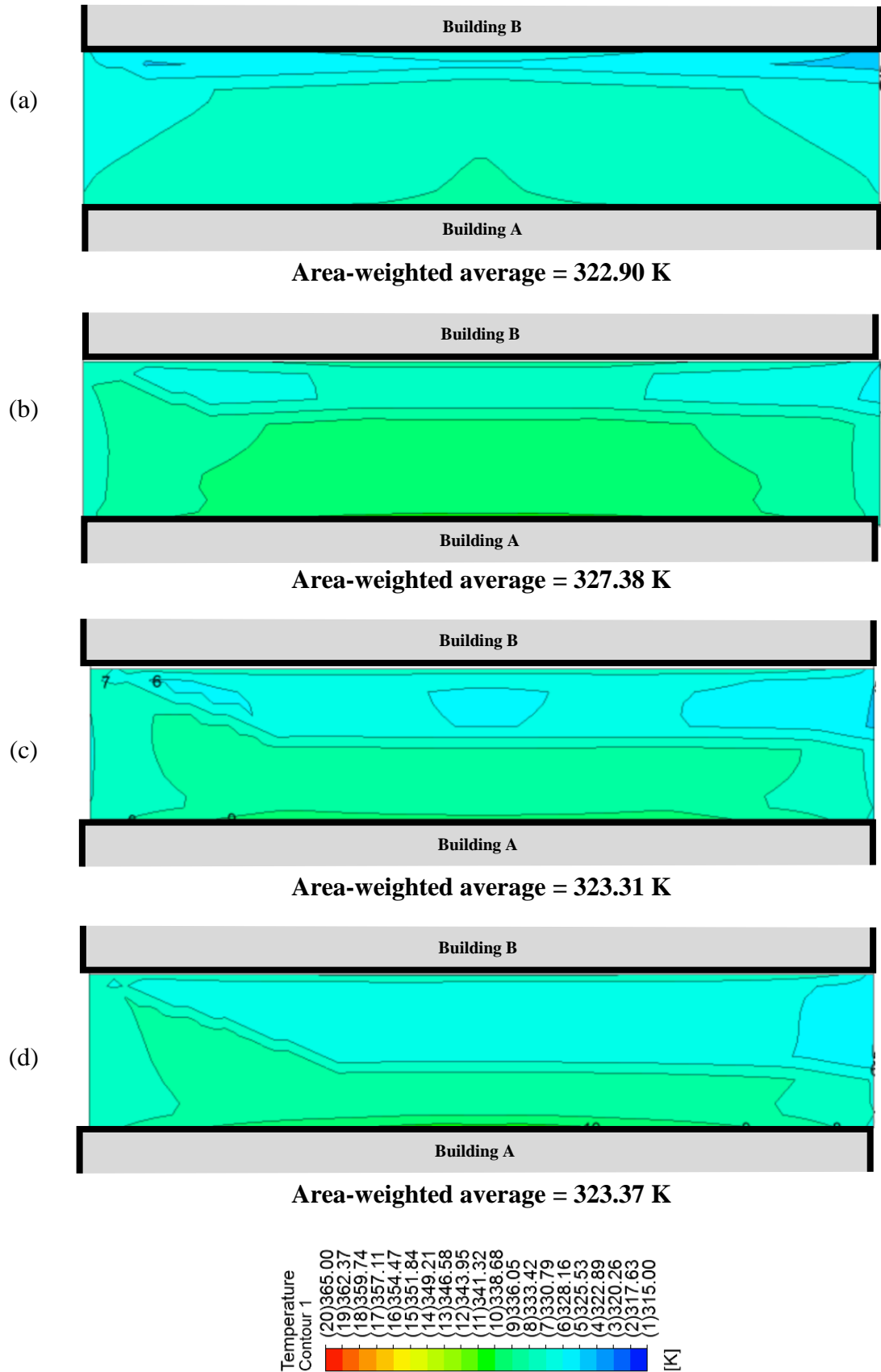


Figure A.18. 1 Surface temperature contour with RPSC application (a) AR 1 (b) AR 2 (c) AR 3 (d) AR 4

Appendix A.19

The temperature difference before and after the RPSC application is displayed in Figure A.19. 1; resulting the highest temperature difference was obtained by AR 2, followed by AR 3, AR 4 and AR 1.

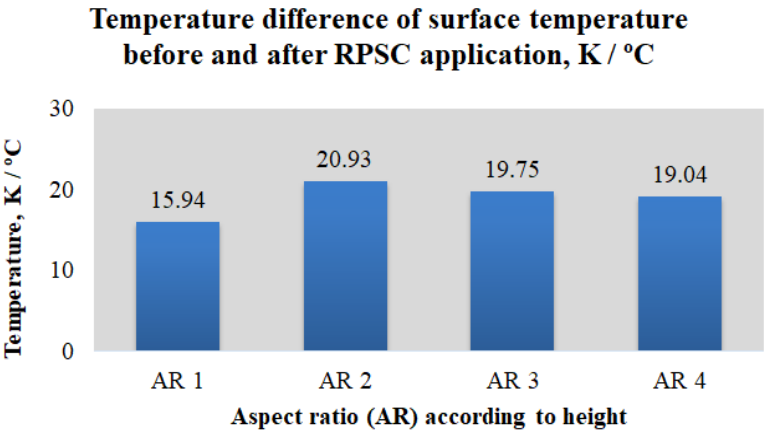


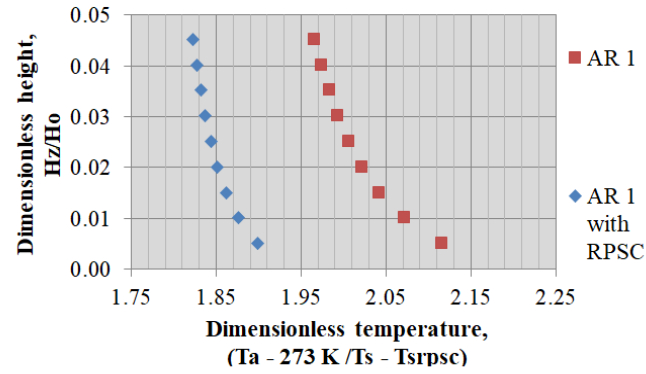
Figure A.19. 1 Performance of RPSC in dissipating heat from road surface according to street canyon aspect ratio in terms of temperature difference before and after RPSC application

Appendix A.20

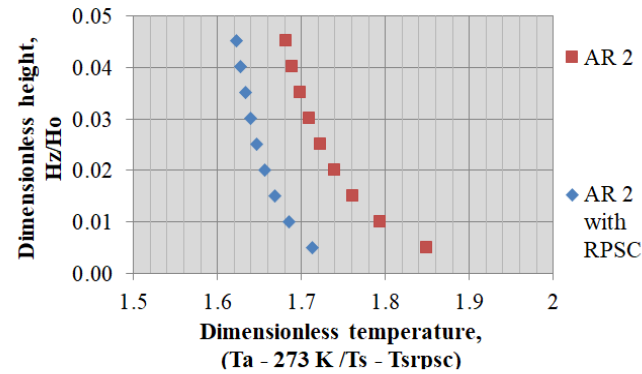
Figure A.20. 1 shows the dimensionless air temperature between 0.5 m and 5 m above ground level (in z-axis) for the analysis of temperature distribution in the pedestrian level, 1.5-2 m. In this study, the temperature profile in the middle of street canyon at 290 m in the x -axis and 430 m in the y -axis was plotted and compared. In overall, the lowest dimensionless air temperature value plotted closer to the ground was observed with the aspect ratio of 2, showing the highest reduction the RPSC system can perform, closely followed by AR 3, 1 and 4. However; between the four aspect ratios, the graph trend of AR 1 showed the highest reduction in the air temperature when RPSC system was used to dissipate heat from the road pavement. This was due to the configuration of AR 1 which had the shortest building height as compared to other aspect ratios and as the result of more air movement within AR 1 which easier the cooling effect of the air temperature from the RPSC system as well as the road surface.

Moreover, large variance in the plotted temperature values across height was found, showing lower air temperature closer to the rooftop as compared to the ground level. The second largest variance in plotting the air temperature comparing before and after the RPSC application was observed with the embedment of RPSC system in AR 4, followed by AR 2 and AR 3. However, the plotted vertical temperature profile of AR 4 in the z -axis did not vary significantly as compared to other aspect ratios. This can be due to the increase in the street canyon height, which was a major cause of low and insufficient air speed within the street canyon. It was concluded that the vertical temperature profile becomes narrower with the increase in the street canyon height.

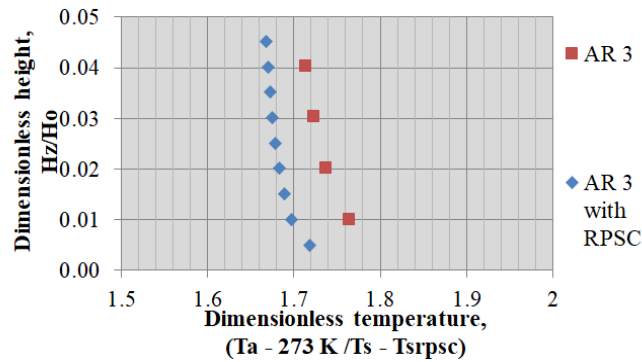
(a)



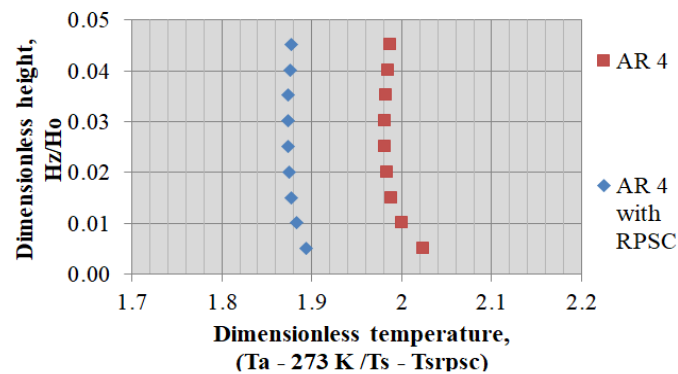
(b)



(c)



(d)



Note : Dimensionless height 0.00 – 0.05 = 0.00 m – 5 m

Figure A.20. 1 Dimensionless air temperature plotted across height in z-axis with different aspect ratio (a) AR 1 (b) AR 2 (c) AR 3 (d) AR 4

It was also observed from Figure A.20. 1 with almost no significant difference in the temperature variance across the height in z-axis between AR 1 and AR 2, only that the plotted dimensionless air temperature value closest to the ground level for AR 2 was lower than AR 2, causing the dimensionless air temperature after RPSC application for AR 2 was plotted lower than AR 1. For AR 3, the reduction in the air temperature by RPSC system was seen to be the least among other aspect ratios as the plotted dimensionless air temperature before the RPSC application was lowest among other aspect ratios. This can be due to the factor of the effect of shadow from Building B over AR 2 with better air movement than AR 4, causing more cooling effect at the centre of the AR 3 canyon before the system application. This means the system did not perform to cool down the street canyon air temperature as much as other aspect ratios.